

TMF4/P310(12)

**CHURN-ANNULAR GAS-LIQUID FLOWS IN LARGE
DIAMETER VERTICAL PIPES**

GERRIT PIETER VAN DER MEULEN

**Thesis submitted to the University of Nottingham
for the degree of Doctor of Philosophy**

JULY 2012

Abstract

This thesis presents an investigation on the churn to annular flow pattern boundary in an 11 m tall, 127 mm id vertical riser. Experimental data on film thickness, pressure drop and drop size and velocity was analysed and interpreted. Entrained fraction, interfacial and wall shear stresses and the interfacial friction were calculated from the experimental data.

A new churn-annular flow transition boundary was derived based on trends, and in particular changes of slopes, observed in film thickness, pressure drop and structure velocity data. This is supported by observations made using high speed photography. Minima in slopes are found in plots of film thickness and pressure gradient with gas superficial velocity at low liquid flow rates. These minima are however not clearly visible at higher liquid flow rates in the data obtained.

Dimensional analysis of this transition boundary and those proposed by other workers, using Froude and Weber numbers, resulted in a closer agreement between transition boundaries then was achieved till present. The correlation found, which describes the boundary, performs well for different pipe diameters, fluid properties and experimental flow conditions.

It was observed that existing models for the calculation of interfacial and wall shear stresses, including the interfacial friction factor, do not perform well in churn type flows. Their performance and agreement with the present data at high gas flow rates, thus annular flow, was however better. This indicated that these models do not take some of the characteristics of the flow into account, e.g., gas core density. It was found that the latter parameter plays an important role in churn flow since the gas core density increases steeply with decreasing

gas flow rate. New relationships for these parameters are suggested for a more accurate prediction in large diameter pipes.

The diameter, velocity, and entrained fraction of drops show similar trends to that of the liquid film thickness and pressure drop. The velocity and the entrained fractions show most profound information. The entrained fraction increases in churn flow with gas flow rate. It then shows a steep decrease in a transitional area. In this area it may be that the entrained fraction is more contained in large waves and wisps than in drops. At higher gas flow rates, the entrained fraction increases again, as is well reported by other researchers. Here the breakup and atomisation of large waves and wisps play an important role.

From comparison between drop fractions deposited by diffusion and direct impaction in the CFD and experimental results, there is evidence that in large diameter pipes a third deposition mechanism applies: Transitional deposition. Analysis shows that transitional impaction occurs at medium sized drops at medium gas flow rates. Around these conditions, large waves are present in the flow as described above. The third deposition mechanism probably occurs when the majority of entrained liquid is carried in large waves and wisps as reported above. Therefore, at the transition from churn to annular flow in large diameter vertical pipes, the behaviour of the flow is not typical to that observed in smaller diameter pipes.

Acknowledgements

“Good man, keep up the good work”

....that is the phrase that keeps coming back when I am working on something, whether in my professional career or work in my private life. I've heard it many times and it has been a very important driving factor to finish my PhD with Professor Barry Azzopardi. Many thanks go out to him for the opportunity, his support and sharing his knowledge in order to accomplish this journey.

I would also like to express my gratitude to my sponsors: the TMF participants^(*), their financial support made it possible for me to undertake this research project, explain it during sponsor-meetings and travel to conferences and meetings. Also the University of Nottingham Graduate School Travel Price Scheme participated in funding when I got the Travel Price awarded to travel to the ICMF conference in the USA.

Big thanks go out to my colleagues Phil, Mick, Melvin-John, Jim, Terry and Reg for their technical support and for their trust whilst I was working in the workshop, using tools and machinery.

I would also like to thank my colleagues in the department for the discussions on multiphase flow, collaboration during long experimental campaigns and academic papers. Special thanks go out to Kris and Piotr and their support while working with the PDA and CFD simulations. Domenico Strazza, to whom I owe big thanks for our long term and distance friendship.

Special thanks also go out to the Lincoln Hall Warden and tutors, it was a tremendous pleasure to share lovely moments during social events.

Thanks to my colleagues at INTECSEA B.V. for their patience during the times I had to work on my thesis.

I would like to thank my parents for their support in every sense of the word during this long journey. They have played a crucial factor in the whole process, bringing me back to the real world whenever that was necessary.

Last but not least, my girlfriend, my rock solid support whilst we both studied and lived in the UK. Looking for the right words to express my gratitude is quite impossible. Zeynep, thank you so much for everything!

Oostwold, September 2011.

(*) This work has been undertaken within the Joint Project on Transient Multiphase Flows and Flow Assurance. UK Engineering and Physical Sciences Research Council (EPSRC) and the following: - Advantica; BP Exploration; CD-adapco; Chevron; ConocoPhillips; ENI; ExxonMobil; FEESA; IFP; Institutt for Energiteknikk; Norsk Hydro; PDVSA (INTERVEP); Petrobras; PETRONAS; Scandpower PT; Shell; SINTEF; Statoil and TOTAL.

“Tough times do not last, tough people do, remember?” (Gregory Peck)

To my parents

Nomenclature

<i>A</i>	Area (m ²)
<i>B</i>	Constant in curve fitting (-)
<i>C</i>	Drag coefficient (-)
<i>c</i>	Constant (-)
<i>D</i>	Diameter (m)/Deposition
<i>D</i> ₃₂	Sauter mean diameter (μm)
<i>E</i>	Resistivity (-)/Entrainment (-)
<i>F</i>	Frictional pressure drop (Pa/m)/Force (N/m)
<i>Fr</i>	Froude number (-)
<i>G_e</i>	Dimensionless conductance (-)
<i>f</i>	Product modified Bessel function/Friction factor (-)/Frequency (Hz)
<i>g</i>	Gravitational constant (ms ⁻¹)
<i>h</i>	Height (mm)
<i>I</i>	Bessel functions/ Incident light (W/ m ²)
<i>K</i>	Apparent conductance Ω/Bessel functions
<i>k</i>	Elliptic integral (-)/Mass transfer coefficient (-)
<i>Ku</i>	Kutateladze number (-)
<i>L</i>	Length (m)
<i>m</i>	Mass flux (kg/m ² ·s)
<i>N</i>	Number
<i>Oh</i>	Ohnesorge number (-)
<i>P</i>	Pressure (Pa)
<i>R</i>	Resistance Ω
<i>R_e</i>	Reynolds number (-)
<i>S</i>	Slip velocity ratio (-)
<i>s</i>	Thickness or width (mm)
<i>t</i>	Time (s)
<i>U</i>	Velocity (ms ⁻¹)
<i>u</i>	Dimensionless gas number (-)
<i>V</i>	Voltage (V)
<i>v</i>	Velocity component (m/s)
<i>W_e</i>	Weber number (-)
Greek Letters	
<i>ρ</i>	Density (kg·m ⁻³)
<i>η</i>	Viscosity (Pa·s)
<i>σ</i>	Surface tension (N·m ⁻¹)
<i>θ, β</i>	Angle (°)/non dimensional time/fraction of liquid film (-)
<i>γ</i>	Liquid conductivity (S·m ⁻¹)/skewness (-)
<i>ε</i>	Fraction of fluid phase(-)
<i>δ</i>	Film thickness (mm)
<i>Φ</i>	Doppler burst
<i>τ</i>	Interfacial shear stress (N·m ⁻¹)
<i>Γ</i>	Equivalent to constant <i>e</i>
<i>α</i>	Dispersed phase hold-up (-)
<i>ζ</i>	Eddy lifetime (-)
<i>μ</i>	Kinematic viscosity (St)
<i>π</i>	Pi (-)

Subscripts

<i>app</i>	Apparent
<i>c</i>	Core
<i>cor</i>	corrected
<i>Diff</i>	diffusional
<i>d</i>	Drop/Drag
<i>f</i>	film
<i>full</i>	Full pipe
<i>g</i>	Gas/Gravitational
<i>gs</i>	Gas superficial
<i>i</i>	Interfacial/Intensity
<i>L</i>	Cross sectional area of liquid/wetted perimeter
<i>l</i>	Liquid
<i>ls</i>	Liquid superficial
<i>m</i>	Measuring volume
<i>max</i>	Maximum
<i>mix</i>	Mixture
<i>out</i>	Output
<i>Probe</i>	Probe resistance
<i>ref</i>	Reference resistance
<i>sm</i>	small
<i>s</i>	Blasius friction factor/frequency
<i>TP</i>	Two Phase
<i>t</i>	Transit time
<i>w</i>	Wave/Wall
<i>x</i>	Two phase flow resistance or voltage
<i>z</i>	Axial distance

Superscripts

*	Dimensionless gas number
---	--------------------------

Figure #	Table of Figures Description	Page #
1.1	Investigated area of flow conditions	5
2.1	Vertical gas-liquid flow patterns	9
2.2	Reproduced gas-liquid flow pattern map for vertical upward flow (Hewitt and Roberts, 1969)	10
2.3	Different flow pattern transitions to annular flow.	11
2.4	Concept of Whalley <i>et al.</i> (1974)	20
3.1	The 5 inch experimental facility	26
3.2	Labview data acquisition software user interface	29
3.3	The conductance probe pipe section	30
3.4	Impression of the calibration setup with the probe rings (in red), a water fragment (in blue) and the non-conducting cylinder (in grey).	33
3.5	Typical error for present study	35
3.6	Typical bubble distribution	36
3.7	Illustration of a pipe with insert only (lhs) and with insert and beads (rhs).	37
3.8	Conventional and bubbly flow probe calibration.	39
3.9	The resistive character of the probes	39
3.10	Annular flow calibration curve	40
3.11	Error between calibration procedures (note expanded axis)	40
3.12	The LDA/PDA and traverse setup	42
3.13	The optical access section. On the left hand side the laser beam transmitter.	42
3.14	Schematic of a typical two component LDA/PDA setup with three photo detectors.	44
3.15	Single beam scattering principle	44
3.16	Multiple beam scattering principle	45
3.17	Laser beam intersection, measuring volume and fringes.	46
3.18	Gaussian beam character	47
3.19	Sketch of mask C with small apertures for larger drop diameters	48
3.20	Doppler frequency shift due to the detector angular difference.	48
3.21	The Trajectory effect	50
3.22	Sketch of the principle suggested by Teixeira (1988)	51
3.23	Sketch of the principle from Saffman (1987)	52
3.24	The slit effect	53
3.25	Illustration of the WMS	55
3.26	Section of the total cross sectional area of the pipe, with receiver wires horizontally and transmitter wires vertically.	55
4.1	Typical film thickness time series for a liquid superficial velocity of 0.2 m/s. Interesting is the very large peak for gas superficial velocity of 3 m/s.	59
4.2	Data for 2 barg plotted on flow pattern map from Hewitt and Roberts (1969)	62
4.3	Annular flow. Gas superficial velocity 16 m/s, liquid superficial velocity 0.014 m/s. The non-coherence of the waves is clearly visible. The white ellipse marks a string of newly entrained drops from the marked wave.	63

4.4	Churn-annular flow. Gas superficial velocity 10 m/s, liquid superficial velocity 0.04 m/s. Waves are very irregular, moving “sideways” on the pipe wall. Also gas bubbles in the liquid film can be observed.	64
4.5	Film thicknesses for all experiments in the experimental matrix (conductance probes).	65
4.6	Film thickness for selected experiments. WMS denotes data obtained with the wire mesh sensor.	66
4.7	Frictional pressure drop for selected experiments.	67
4.8	Film thickness (a) and pressure drop (b), including higher liquid flow rates	68
4.9	Comparison of film thickness measured experimentally by conductance probes and WMS.	69
4.10	Wave heights for selected flow rates.	71
4.11	Structure velocities for selected experiments.	72
4.12	Effect of gas flow rate on correlation coefficient and correlograms.	73
4.13	Interfacial shear stress vs. film thickness.	75
4.14	Interfacial shear stress vs liquid superficial velocity	76
4.15	Components of the pressure drop for annular type flow	78
4.16	Components of the pressure drop for churn type flow	78
4.17	Comparison of interfacial shear stress equations	80
4.18	Comparison of interfacial shear stress minima	81
4.19	Comparison of interfacial friction factor equations	82
4.20	Comparison of calculated wall shear stress	83
4.21	Comparison of calculated wall vs. interfacial shear stress	84
4.22	Calculated wave pressure drop vs superficial gas velocity	86
4.23	Calculated pressure drop vs. measured pressure drop.	87
4.24	Wire mesh spatial results. Superficial gas velocity 10 m/s and liquid superficial velocity 0.04 m/s (a) and superficial gas velocity 7.85 and liquid superficial velocity 0.04 m/s (b)	89
4.25	Flow pattern map for the churn-annular transition in a 127 mm pipe. CP boundary is obtained from conductance probes, CF boundary is estimated from cine film.	91
4.26	Dimensional analysis of churn/annular transition data	94
4.27	Performance of Eq. 4.21 (solid lines) versus experimental churn to annular transition data from different authors (symbols).	95
4.28	Effect of gas density.	96
4.29	Effect of gas density on data from Szalenski <i>et al.</i> (2010)	97
5.1	Simplified break up mechanisms in vertical annular flow. Ligament break up (a) and bag break up (b)	102
5.2	Gas superficial velocity 16 m/s, Liquid superficial velocity 0.014 m/s	106
5.3	The velocity of a drop near the wall, a drop in the gas core and a disturbance wave.	107
5.4	Gas superficial velocity 13 m/s, liquid superficial velocity 0.014 m/s	108
5.5	The velocity of a drop breaking up near the wall, a drop reaching the gas core and a disturbance wave	109
5.6	$t = 0$ ms, drop travelling upwards near the wall. Liquid superficial velocity 0.04, gas superficial velocity 16 m/s.	110

5.7	The velocity of a drop breaking up near the wall, a drop reaching the gas core, a disturbance wave, bubble in the film and the average disturbance wave velocity obtained from the conductance probes (dashed line).	111
5.8	Cycle of disturbance wave and drop creation	112
5.9	Cartesian coordinates of measuring points across the pipe cross-section.	115
5.10	Example of corrected and uncorrected Sauter mean diameter at the pipe centreline.	119
5.11	Sauter mean diameters for all liquid velocities. Note expanded axis	120
5.12	Selected cases for the evolution of the Sauter mean diameter	121
5.13	Sauter mean diameter in relation to the pipe cross section. Closed symbols represent a gas superficial velocity of 18.3 m/s, open symbols those for 14.5 m/s.	123
5.14	Mean drop velocity for an average gas superficial velocity of 18 m/s. Open symbols represent the overall mean velocity, closed symbols represent tracer drops. The straight line is the overall averaged gas superficial velocity. Dashed line is gas velocity profile from simulations for a gas superficial velocity of 20 m/s.	124
5.15	Experimental mean drop velocities for various superficial gas velocities. Solid line represents the Star-CD data obtained for a gas superficial velocity of 20 m/s.	125
5.16	Mean drop velocity for an average gas superficial velocity of 14.5 m/s. Closed symbols represent the overall mean velocity. The straight line is the overall averaged gas superficial velocity.	126
5.17	Standard deviation for gas superficial velocities of 18.3 m/s (closed symbols) and 14.5 m/s (open symbols).	128
5.18	Comparison with previous work. Note that the data from Fore and Dukler (1995) and Teixeira (1988) is extended to negative r/R .	129
5.19	Overall mean drop velocity at the centreline and pipe wall. Marks represent data from Fore and Dukler (1995) for liquid superficial velocities from 0.015 to 0.045 m/s. Open symbols represent data from van 't Westende (2008) for liquid superficial velocities from 0.01 to 0.04 m/s	131
5.20	Normalised skewness of drop velocity distributions. Closed symbols represent the selected experiments; open symbols represent all other experiments.	133
5.21	The liquid film thickness for selected experiments. The Sauter mean diameter for liquid superficial velocity 0.0045 m/s is illustrated to examine the trends (open symbols).	136
5.22	Entrained fraction for selected experiments.	137
5.23	Comparison with the entrained fraction obtained by Azzopardi (1983) and Verbeek <i>et al.</i> (1992). Liquid superficial velocities are all 0.01 m/s.	138
5.24	Comparison of entrainment in churn flow	139
5.25	Comparison of entrainment in churn flow including others	140
5.26	Mean liquid film velocity	142
5.27	The structure velocity (closed symbols). The mean liquid film velocity for 0.0045 m/s is also plotted for illustration.	143

6.1	Example simulation of drop motion ((Andreussi and Azzopardi (1981)) ($D_t = 32$ mm, $U_t = 0.9$ m/s, $U_{gs} = 29$ m/s)	146
6.2	Initial Mesh	152
6.3	Refined mesh 2	152
6.4	Gas velocity profile in the 32 mm pipe	153
6.5	Gas velocity profile in the 127 mm pipe	153
6.6	Cross sections presented in scaled manner run 7 and run 4	155
6.7	Cross sections presented in scaled manner run 9 and run 3	156
6.8	Drop response time and the time required for a drop to travel radially at 0.7 m/s in a 32 mm and 127 mm pipe	157
6.9	Quantification of diffusion, L and δ are the approximate length and width of the bulk of drops	158
6.10	Volumetric fractional deposition rates in the 32 and 127 mm pipe. Superficial gas velocity, 29 m/s, drop ejection velocity, 0.7 m/s.	163
6.10	Volumetric fractional deposition rates in the 127 mm pipe including multiple angle drop injection. Gas superficial velocity is 20 m/s, drop ejection velocity is 0.7 m/s. Solid line is an experimental size distribution for gas and liquid superficial velocity 20.2 and 0.0045 m/s respectively.	164
6.11	Simple approach (a), more complex (b) and Gaussian (c) angular distributions	165
6.13	Lateral velocity, 32 mm pipe for one drop sample. Note for the 450 μ m drop the injection point was set at 3.5 m.	166
6.14	Lateral velocity, 127 mm pipe for one drop sample	167
6.15	Lateral velocity, 127 mm pipe for one drop sample	168
6.16	Lateral velocity, 127 mm pipe and multiple angle injection for one drop sample.	169
6.17	Axial velocity, 32 mm pipe for one drop sample. Note for the 450 μ m drop the injection point was set at 3.5 m.	170
6.18	Axial velocity, 127 mm pipe for one drop sample	170
6.19	Axial velocity 127 mm pipe, for one drop sample.	171
6.20	Axial velocity, 127 mm pipe and multiple angle injection for one drop sample.	171
6.21	Axial distance and axial velocity for runs 1, 3 and 4	172
6.22	Axial distance and axial velocity for runs 8, 9, 13, 15 and 16	173
6.23	Axial distance and axial velocity for runs 17 to 19. For comparison "A" is run 10 and "B" is run 16. Solid line and solid line with marks denote experimentally obtained drop velocity distributions for gas superficial velocities of 16.86 and 20.19 m/s. Liquid superficial velocity 0.0045 m/s	173
6.24	Typical drop trajectories in the 32 mm pipe for runs 1, 3 and 4	176
6.25	Typical drop trajectories in the 127 mm pipe for runs 17, 18, 19 and 8, 9 and 13	176
6.26	Effect of angle of injection on deposition distance.	177
6.27	Drop deposition fractions for various ejection angles (closed symbols) and diameters (open symbols)	178
6.28	Deposition coefficients for runs 8, 9 and 12 to 19	180
6.29	Drop fraction deposited by diffusion	181
6.30	Simulation and predicted drop deposition fractions. Simulation	182

results (squares), experimental results (circles) at gas superficial velocities of 20 and 11 m/s and boundaries between the expected deposition mechanisms (solid lines).

6.31 Pipe diameter effect 187

Table of Tables

Table #	Description	Page #
3.1	Relative error between bead diameters	41
5.1	Drop size and entrainment behaviour	113
5.2	Setup parameters of the Dantec PDA	116
5.3	Experimental conditions comparison	127
5.4	Probability distributions	134
6.1	Simulation conditions	148
6.2	Simulation results (Model, D_t , D_d , U_{gs} and U_I denote the turbulence model employed, pipe diameter, drop diameter, gas superficial velocity and drop ejection velocity respectively).	159

ABSTRACT	
ACKNOWLEDGEMENTS	
NOMENCLATURE	
TABLE OF FIGURES	
TABLE OF TABLES	
1 INTRODUCTION	1
1.1 Two-phase gas liquid flow risers	1
1.2 Aims	3
1.3 Objectives	4
1.4 Scope of thesis	5
2 LITERATURE SURVEY	7
2.1 Vertical gas-liquid flow	8
2.2 Structuring flow patterns	9
2.3 Dimensional analysis	12
2.4 Void fraction correlations: Examples of dimensionless numbers	15
2.5 Annular flow specific models	16
3 THE EXPERIMENTAL FACILITY, EQUIPMENT AND INSTRUMENTATION	24
3.1 The experimental facility	24
3.2 Differential pressure cell	27
3.3 Flow meters	27
3.4 Pressure transducers	27
3.5 Temperature	28
3.6 Data Acquisition	28
3.7 Conductance Probes	30
3.8 Probe Theory	30
3.9 Conventional Probe Calibration	33
3.10 Sources of discrepancy and improvements	35
3.11 Results	38
3.12 Laser Doppler Velocimetry and Phase Doppler Anemometry	42
3.13 Fundamentals of Laser Doppler Anemometry	43
3.14 Phase Doppler Anemometry	47
3.15 Sources of discrepancy	49
3.16 Wire Mesh Sensor	53
3.17 Sources of Discrepancy	55
4 LIQUID FILM CHARACTERISTICS	57
4.1 Background and motivation	57
4.2 Experimental outline	61
4.3 Results	62
4.4 The liquid Film	65
5 THE CREATION, BEHAVIOUR AND SIZES OF DROPS	101
5.1 Background on drops in gas-liquid flows	101
5.2 Experimental outline	104
5.3 Scoping experiments	105
5.4 Photography without the liquid film present	112
5.5 Phase Doppler Anemometry Results	114
5.6 The liquid film and entrained fraction	136

6	DROP SIMULATIONS	145
6.1	Previous work	145
6.2	Outline	147
6.3	Numerical drop trajectory experiments	149
6.4	Results	154
6.5	Quantitative information	166
7	CONCLUSIONS AND RECOMMENDATIONS	189
7.1	The liquid film and pressure drop	189
7.2	Drop size, velocity and liquid entrainment	190
7.3	CFD drop simulations	191
7.4	Recommendations for further work	193
REFERENCES		
APPENDICES		

1 Introduction

In contrast to single phase flow, multiphase flow is a complex simultaneous process of multiple fluids in the same geometry. In industrial applications, gas-liquid, gas-solid and liquid-liquid flow or any other combinations are encountered. Multiphase flows are encountered in the petroleum, power generation and chemical and process, industries. For instance, two phase flow occurs when single phase water flows through a pipe and is subject to a heat flux, water vapour (steam) then starts to form along the pipe and a two phase flow system is created. In the petroleum industry a two phase system is found in wells, risers and pipelines.

The global energy demand is gradually increasing, partly due to the fast economical growth of developing countries. However, recently discovered hydrocarbon reserves are more often than not situated in geographical areas where aspects as production and processing get more challenging from an economical and engineering point of view. Modification of existing facilities on the other hand, to enhance production due to field depletion, comes with similar challenges. Hence, research in the field of multiphase flow is important from the latter perspectives in order to improve safety, reliability, sustainability, efficiency and a significant decreasing maintenance frequency of industrial processes.

1.1 Two-phase gas liquid flow risers

A hydrocarbon well can produce several fluids, i.e., oil, gas condensate, gas, water and sand. The design of the well, pipelines and risers systems must be carried out with caution because of the presence of

asphaltenes, waxes and hydrates which could cause blockage. These might demand the application of appropriate inhibitors. Fluid extraction from a reservoir implies that the natural pressure in the field drops in time, i.e. depletion. The dominant phase in gas-liquid flow has a great influence in well performance and consequently, may affect the entire production process, e.g., a too high liquid hold-up can shut down a well. This could be due to the gas pressure being insufficient to overcome the liquid static head.

Apart from slug flow, another problem encountered in some cases is severe slugging where a high quantity of accumulated liquid occupies the riser, usually associated with an inclined horizontal subsea pipeline. Eventually, when pressure behind the liquid slug builds up due to gas accumulation, the liquid slug will be pushed out at high momentum which may damage the process equipment. In addition large, expensive and space demanding slug catchers are thus required. Slugging in general is thus to be avoided if possible.

Erosion is also a limiting factor for the design of process equipment. Liquid drops, containing a solid such as sand, can be abrasive when travelling at high velocities. Corrosion by water and dissolved carbon dioxide can also be encountered and will require injection of corrosion inhibitors.

Apart from steel jacket production facilities, semi-submersible and fully submersible facilities are designed and constructed to allow oil and gas production in greater water depths, e.g., drilling ships and production facilities, also known as Floating Production Storage and Offloading facilities, and subsea well-templates. Rather than a fixed configuration, large diameter

risers with idem lengths can adopt catenary shapes. Therefore, the orientation of one riser can go through various stages, i.e., from horizontal to vertical.

All these challenges have to be addressed by the industry concerned with flow assurance and integrity. An additional problem is that there is evidence that gas-liquid flows in large diameter vertical risers behave differently compared to relative small diameter tubes. For example; there is consensus in vertical orientation on the non- existence of conventional slug flows in tube diameters >100mm. These differences can manifest themselves through different relationships between the phase flow rates and gas void-fraction/liquid hold-up, liquid-film characteristics, the dispersed phase. pressure gradient and wall-shear stress.

1.2 Aims

Omebere-Iyari (2006) successfully carried out the first experiments on a new 127 mm diameter closed flow loop test facility at the University of Nottingham. Omebere-Iyari's research campaign led to fundamental quantitative understanding of phase hold-up of both the gas and liquid phases in large diameter risers.

The present study is part of the fourth cycle of Transient Multiphase Flows (TMF4). Carried out in the Department of Chemical and Environmental Engineering at the University of Nottingham, it aims to provide (i) more detailed information on the transition from the churn to annular flow regime in vertical gas-liquid flow in a 127 mm diameter riser. More specifically, this project aims to provide information on the cross-section averaged and local phase fractions, film thickness and the dispersed phase, i.e., drops. (ii)

Especially drop behaviour and deposition is considered key in the current study and investigated. Although the nature of gas-liquid flow may be different in larger than smaller diameter pipes, it will be analysed using generic statistical methods.

There is yet no published material on the simultaneous measurements of the dispersed phase and liquid film thickness in the churn flow regime for pipe diameters >100 mm. For the first time, this study aims to perform measurements in this challenging flow environment.

1.3 Objectives

The objectives of this thesis are to concentrate on: (i) Vertical churn-annular air-water flows at moderate pressures (1 to 3 bara). (ii) gas and liquid superficial velocities varied between 3 and 20 and 0.004 and 0.7 m/s respectively. (iii) void fraction/film thickness measurements performed with calibrated conductance ring probes and a Wire Mesh Sensor. (WMS). (iv) drop size and velocities measured using Phase Doppler Anemometry. (v) statistical analysis methods applied in order to extract more in depth information from the data gathered. (vi) Star-CD simulations on drop behaviour carried out to accompany the experimental data. Figure 1.1 illustrates the area investigated in the present study.

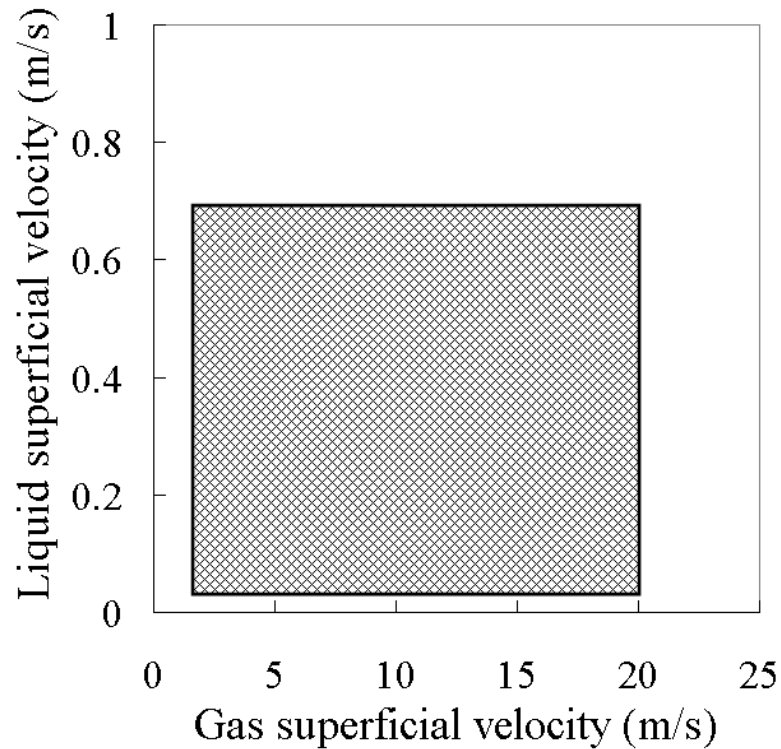


Figure 1.1 Investigated area of flow conditions

1.4 Scope of thesis

With the gaps in the research history and literature identified, and in line with the current trends towards the use of larger pipe diameters in process installations, the scope of this thesis is outlined as follows. The first Chapter introduces the practical applications of multiphase and gas-liquid flows and the challenges faced in the industries. Moreover it provides the aim and objectives of this thesis. The second Chapter highlights the main efforts carried out in the past in the field of vertical gas-liquid flows and the existing gap of knowledge for large diameter pipes and particularly the churn-annular transition. The third Chapter presents the experimental facility. It also provides sections devoted to the instrumentation and measurement equipment

employed and the governing theoretical fundamentals. Chapter four is the first out of three results chapters and presents data on void fraction and film thickness measurements at 2 barg in the 127 mm riser at Nottingham. Subsequently an improved fraction factor relationship along with a new churn-annular flow transition boundary are proposed. Chapter five introduces visual observations made on the creation of drops and disturbance waves. It also presents drop sizes and velocity results, accompanied with film thickness measurements at atmospheric pressure. In Chapter six, the results obtained with Star-CD simulations on drops are described, concentrating on drop deposition. Chapter seven provides conclusions of this thesis and recommendation for future research.

2 Literature Survey

For many years, multidisciplinary engineering research teams attempted to characterise and understand the behaviour of these types of fluid flows at a wide range of physical conditions, through various flow domains and geometries. A wealth of information is therefore available already. Consequently, a wide range of measurement techniques has been utilised to examine the characteristics and derive empirical models (the empirical approach). More recently, computer codes such as Computational Fluid Dynamics (CFD), originally developed for e.g. aerospace and aeronautical applications, are successfully further developed and applied in the simulation and prediction of multiphase flows (the modelling approach).

Two phase gas-liquid flows are studied to a greater extent compared to any other multiphase flow. The nature of gas-liquid flow compared to single phase flow of either a gas or liquid is significantly different. This difference can be found in interfacial interaction between the two phases while subject to forces due to gravitation, friction and acceleration.

This literature survey presents a brief overview of flow patterns occurring in vertical gas-liquid flows, including flow pattern maps. It will then highlight the past efforts made for derivation of those void fraction prediction performing reasonably in large diameter pipes. This is followed by flow pattern specific models for the transition from churn to annular flow in vertical pipes. More applied literature survey is provided in the concerning Chapters of this Thesis.

2.1 Vertical gas-liquid flow

Vertical gas-liquid flows commonly adopt four main patterns or regimes (Figure 2.1). These regimes occur when the flow conditions are varied. A good example is starting with single phase liquid flow. When the liquid is pumped into a vertical pipe and gas is simultaneously injected into the base of the pipe bubble flow occurs. By increasing the gas flow rate and keeping the liquid flow rate constant, the pattern in the pipe changes from bubble to slug (or plug). This can be associated with the coalescence of small bubbles. By increasing the gas flow rate further, the patterns change to churn and finally annular flow. The characteristics of these regimes are as follows (i) Bubbly flow: dispersed gas bubbles travel with a complex motion through a dominating liquid flow. (ii) Plug flow, or slug flow where the gas bubbles size tends towards that of the channel and bullet shaped bubbles are formed. The bubble (also called a Taylor bubble) is surrounded by a thin film of liquid. Recent studies have shown that in larger diameter pipes this pattern does not occur but instead a direct transition from bubble to churn flow takes place. (Cheng et al (1998)) (iii) Churn flow is the case when the Taylor bubbles have an unstable motion. This regime is very chaotic and is a process of continuous break up and dispersion of liquid into gas and gas into liquid. For large diameter pipes, Prasser (2003) provided a good example of an unstable “slug” flow. Several definitions have also been proposed by Ohnuki and Akimoto (2000) for large diameter pipes (iv) Annular flow is characterised by a relatively thin liquid film travelling on the pipe walls. The interface between the phases is often rough due to formation of waves. More details on waves are provided in Chapter 4. The core is formed by the continuous gas phase and

liquid drops are dispersed in the core. At very high gas flow rates, the dispersed phase can carry the majority of the liquid.

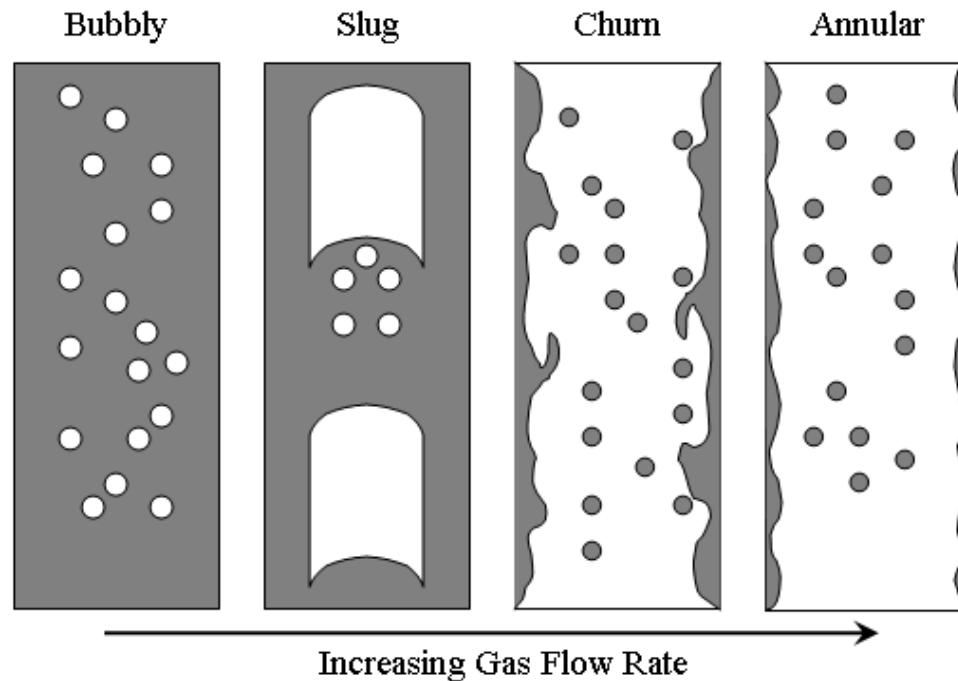


Figure 2.1 Vertical gas-liquid flow patterns (gas in white, liquid in grey)

2.2 Structuring flow patterns

In the previous section, commonly encountered flow patterns in vertical gas liquid flow were described. Structuring these often chaotic processes is a challenging task in itself. Flow patterns, observed by analyses of trends occurring in quantitative and qualitative data are usually organised in a systematic manner. A much employed method is “mapping” of these patterns. For a range of flow conditions the boundaries, in between which a particular pattern dominates the flow, can be drawn. Flow pattern maps can be graphically categorised both for vertical and horizontal multiphase phase flows. Once all pattern boundaries observed are mapped, a clear overview of behaviour can be observed as a function of flow conditions. Figure 2.2

illustrates the well reported flow pattern map for upward vertical gas-liquid flow from Hewitt and Roberts (1969).

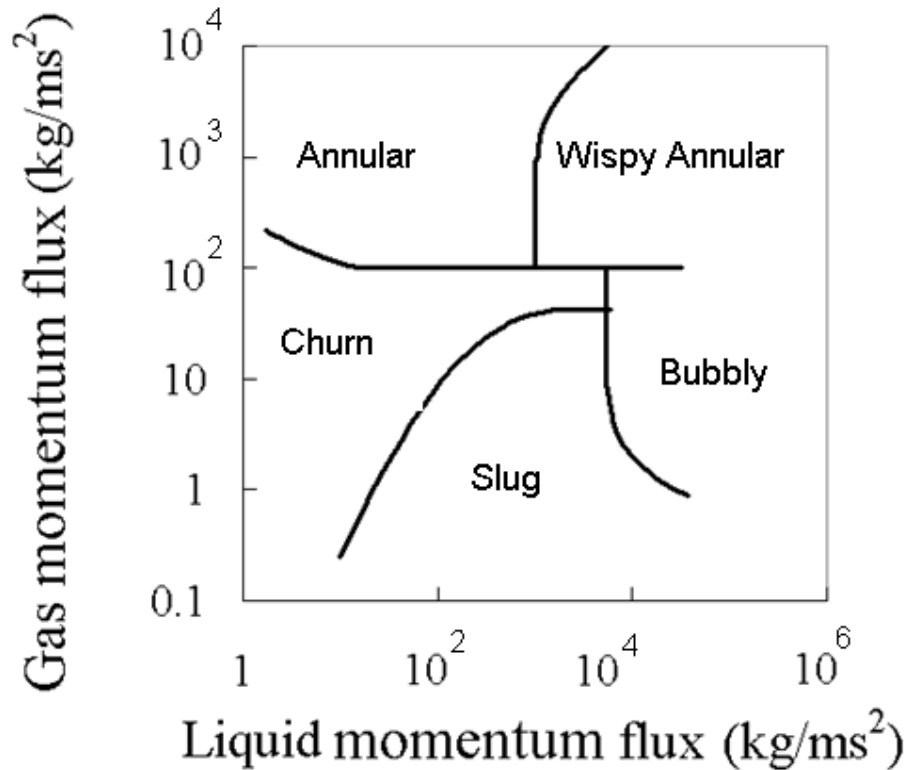


Figure 2.2 Reproduced gas-liquid flow pattern map for vertical upward flow (Hewitt and Roberts, 1969)

Sekoguchi and Mori (1997) performed a systematic study and re-examined flow pattern occurrence in a 26 mm vertical tube by using advanced local measuring probes. For annular flow they proposed an alternative approach. By measuring the frequency of slugs, waves and their velocity behaviour, they found that there are two types of waves occurring simultaneously: disturbance and huge waves, in the annular flow area. The boundary between the area in which the simultaneous occurrence of these two wave types was observed and the where there only appeared to be disturbance waves is taken as the transition from churn to annular flow. Figure 2.3 below illustrates the churn to annular flow boundary proposed by Sekoguchi and

Mori (1997) plotted in a dimensional version of the flow pattern map from Hewitt and Roberts (1969)

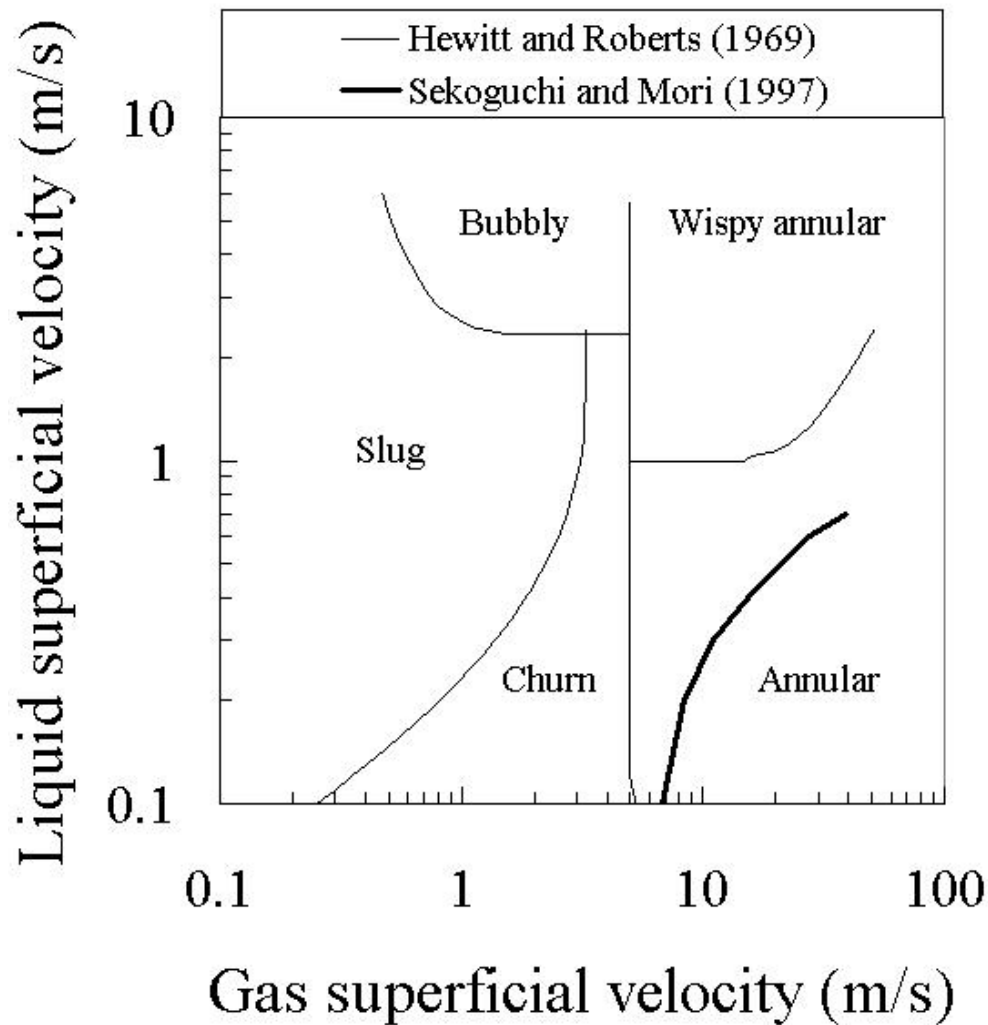


Figure 2.3 Different flow pattern transitions to annular flow.

It can be observed that the boundaries do not agree very well. This may imply that there is a difference between results obtained due to different variables and scales, i.e., fluid properties and or pipe diameters. Note that the annular flow boundary from Hewitt and Roberts could be not entirely represented by experimental data but are due extrapolation, introducing possible biases. Especially the importance of vertical churn flow is sometimes

underestimated and is perhaps still the least understood flow pattern of all. Azzopardi and Wren (2004) investigated the mechanism of liquid entrainment and some interesting conclusions are drawn. Churn flow occupies a relatively large area in flow pattern maps. Especially since the typical slug flow Taylor bubble has not been observed till present in larger diameter vertical pipes, the churn flow pattern area actually became a lot larger than typically seen in small pipe flows. Experimental data and empirical models have however been crucial in the development for 1D and multi-dimensional CFD software packages such as SPT's OLGA and CD-Adapco's Star-CD etc. The occurrence of the flow pattern is however encountered numerously in the oil and gas industry. Accurate prediction from CFD for churn flow therefore remains a challenge leaves room for improvements.

2.3 Dimensional analysis

By dimensional analysis, many workers have attempted merging of experimental data originating from different set-ups. Some more successful than others but until present the search for a good solution is still in progress. This next section provides an introduction in how dimensional analysis is applied in multiphase flows.

Dimensionless numbers are extensively employed in the area of fluid flows as they can be used in comparative analysis at different scales and properties, i.e., pipe diameter, density, surface tension, viscosity etc. Not only for flow pattern maps in general they can be used, but also for flow pattern specific analysis they are proven to be very useful. For instance, as it is a key motive for the present study, in the investigation of the transition from churn

to annular flows. In some cases, also the value of a dimensionless number can be a measure of the state of the flow.

As for the original flow pattern map shown in Figure 2.2, it can be seen that the axes do not represent the superficial velocities directly but instead a momentum flux ρU^2 is suggested. This flow pattern map was constructed based on three data sets taken in vertical gas-liquid flow. The data originated from air-water experiments in a 32 mm pipe and steam-water in a 12.7 mm pipe. The latter at pressures of 35 and 70 bar. Looking more closely at ρU^2 results in the dimensionless Weber number (Eq 1.1) which is commonly employed in fluid flows in which an interface between the fluids is encountered.

$$We = \frac{\rho U^2 D}{\sigma} \quad 1.1$$

In which ρ , U , D and σ are the density, velocity difference over the drop, pipe diameter and the surface tension respectively. Note that the physical properties of the respective phases can be employed for dimensional analysis.

Scaling the Weber numbers for the case of Hewitt and Roberts, based on similarity between the different data sets, shows that the ratio D/σ for the cases of 32 and 12.7 mm pipe at 35 bar are very similar. For the 12.7 mm data at 70 bar D/σ is a factor 1.7 greater than the former. Yet it brought the data sets together in the flow pattern map. Also for horizontal flow, the flow pattern maps suggested by Baker (1954) and Taitel and Dukler (1976) suggest the use of dimensionless numbers and groups thereof.

Another, very well known, example is the Reynolds number, a ratio between inertial and viscosity forces. Transition between laminar and turbulent flows can be determined by

$$\text{Re} = \frac{\rho U D}{\mu} \quad 1.2$$

Where η is the fluid viscosity. An additional dimensionless number used in scaling of fluid flows is a densimetric Froude number which relates the velocity to the gravitational behaviour of the gas-liquid interface. A modified version is better known for the analysis of multiphase flows and defined as

$$\text{Fr} = \frac{\rho U^2}{(\Delta\rho g D)} \quad 1.3$$

The Ohnesorge number is a dimensionless number which is a ratio of the viscosity, the density and surface tension forces.

$$\text{Oh} = \frac{\eta^2}{\rho\sigma D} \quad 1.4$$

A scaling rule in the form of a Kutateladze number groups the Weber and modified Froude number

$$\text{Ku} = \left(\text{Fr}^2 \text{We} \right)^{1/4} \quad 1.5$$

Apart from the abovementioned dimensionless numbers, more groups of these numbers have been examined on their scaling ability of flooding data by Zapke and Kröger (2000).

2.4 Void fraction correlations: Examples of dimensionless numbers

The previous section briefly covered the use and some examples of dimensionless numbers applied in the analysis and correlation of multiphase flows. This section outlines some of the well known correlations to predict the void fraction. In two-phase gas-liquid flows, void fraction is defined as the fraction of the cross-sectional area occupied by the gas. Void fraction is however not merely depending on the sum of input mass flow rates. A brief summary of empirically derived void fraction models, which give a fundamental understanding of the basics, is presented here. Except the correlations from Duns and Ros (1963), all correlations are comprehensively explained in Bertola (2003). In the practical field of flow assurance and integrity, the correlations from Duns and Ros (1963) are still used today. This is not surprising since the data is extracted from production wells and provide reasonable predictions. One of the correlations used for void fraction prediction is the homogeneous flow model. This one-dimensional equation does not allow for the slip between the gas and liquid phase.

Chisholm (1972) proposed a correlation to allow for the slip ratio in the homogeneous model. Another slip ratio correlation from Smith (1971) seems slightly more complex, yet it does often not give more accurate predictions than the former.

Premoli *et al.* (1970) at CISE, demonstrates a more complex approach to predict void fraction in vertical gas-liquid flow. Linking the previous sections with the current; they based correlation coefficients on Weber and Reynolds numbers.

Beggs and Brill (1973) provided correlations for the liquid hold up in oil and gas wells, based on correction factors for the homogeneous model as described above including a Froude number.

Azzopardi and Hills provide a performance comparison of various flow pattern specific models in their lectures provided in Bertola (2003). Omebere-Iyari (2006) tested the models against data obtained in a 127 mm diameter pipe. This shows that the annular flow model (described below) provides the best predictions for experimentally obtained data, especially at low liquid flow rates and high void fractions. The Beggs and Brill model performs best at higher liquid flow rates. This is not surprising, considered the origin of the model. It is worth noting that the models derived by Chisholm (1972) and Premoli *et al.* (1970) were empirically developed for heat exchange and nuclear applications respectively

2.5 Annular flow specific models

Flooding, a phenomenon in churn/annular flow where the liquid film becomes gravity dominated, is associated with the transition where the film starts to move upwards. Some workers, e.g. Zabaras *et al.* (1986) define flooding as the point from which the liquid starts to show upward motion with increasing gas flow rate. Owen (1986) and Govan *et al.* (1990) describe this phenomenon following Wallis (1961) in a similar manner and also provide detailed results on flooding. The correlation by Wallis (1961) is very popular in which two dimensionless groups for gas and liquid superficial velocities are suggested.

$$\sqrt{U_g^*} + \sqrt{U_L^*} = C \quad 1.6$$

$$U^* = \frac{\rho U^2}{g D \Delta \rho} \quad 1.7$$

Eq. 1.7 is equal to Eq. 1.3, the Froude number, and the transition from churn to annular flow in smaller tubes can be expected to take place when C is around unity. Similar to the boundary suggested by Hewitt and Roberts, also here applies that the boundary is a straight line.

For larger diameter pipes, the correlation from Pushkina and Sorokin (1969) has proven to be popular. For the inception of flooding, the gas phase Kutateladze number equals 3.2. This is similar to the value of 3.1 as suggested by Turner *et al.* (1969)

$$Ku = 3.2 = \left(Fr^2 We \right)^{1/4} \quad 1.8$$

Dukler and Smith (1979) developed the Wallis parameter further for curve fitting to their experimental data.

Taitel (1980) followed Turner *et al.* (1969) with a hydrodynamic state for transition in which the gas flow rate is just sufficient to suspend a drop, including a drag coefficient. The maximum stable drop size is found by the Hinze (1955) equation. However, this does not account for the liquid flow rate and thus is a straight line.

$$0.5 C_d \pi \frac{D_d^2}{4} \rho U^2 = \pi \frac{D_d^3}{6} g \Delta \rho \quad 1.9$$

Where D_d is the drop diameter defined by Hinze (1955) including a critical Weber number.

$$D_d = \frac{We_c \sigma}{\rho U^2} \quad 1.10$$

Barnea and Taitel (1985) extended the former model for inclined pipes and the effect of liquid flow rate was taken into account. The transition from churn to annular therefore perhaps became more applicable by curving to the right.

Jayanti and Hewitt (1992) followed Dukler and Smith (1979) and extended the Wallis (1969) parameter by using their experiments on flooding. They found that there is a great influence due to the film length on the flooding point.

$$\sqrt{U_g^*} + c_1 \sqrt{U_L^*} = c_2 \quad 1.11$$

$$c_1 = 0.1928 + 0.01089 \left(\frac{L}{D} \right) - 3.754 \times 10^{-5} \left(\frac{L}{D} \right)^2 \quad L/D < 120 \quad 1.12$$

Where L is the pipe length.

Zabaras et al (1986) followed the ideas of Moalem-Maron and Dukler in (1984). In a 50.8 mm pipe, they tested a theoretical film flow model proposed by the latter authors against experimental pressure drop, film thickness and wall shear stress. The model suggests that the film thickness varies between two processes at the transition from churn to annular flow, i.e, “switches”. From fully flowing upward to a sort of recirculation mechanism where the film can flow up and downward. The pressure drop goes through a minimum state with increase of gas flow rate. The latter was found earlier, amongst others, experimentally by Hewitt *et al.* (1965). Hewitt *et al.* proposed that this is a situation where the wall shear stress is zero and thus the film is theoretically static. Since the film thickness is the main contributor to pressure

drop and wall and interfacial shear stress, Zabaras et al, proved that all three parameters as a function of film thickness showed a minimum value. The ideas of Zabaras et al (1986) are taken further in Chapter 4.

More recently, Sawai et al (2004) performed experimental studies in a 25.8 mm pipe in which the pressure drop was related to the liquid film thickness and in particular to the wave magnitude and motion. To examine the contribution of waves to the frictional component of pressure drop, which is thought to be dominant in annular type flows, they proposed a method to extract information on the difference in liquid fraction contained in waves to that in the liquid base film. By plotting the probability density function (PDF) of the time varying liquid holdup, they assumed that the base film distribution would be Gaussian. If the PDF tails towards higher liquid fractions, the fraction occupied by the tail was taken as wave holdup. A version of the widely used equation for the frictional component of pressure drop was then adjusted for waves only can be written in the form

$$F_{wL} = P_w \left[\frac{4}{D} f_w \frac{\rho_l u_w^2}{2} \right] \quad 1.12$$

where

$$f_w = 0.0791 \left(\frac{D u_w}{\mu_l} \right)^{-0.25}$$

is the liquid phase friction factor, u_w is the wave velocity, commonly obtained by cross correlating film thickness signals and μ_l is the liquid viscosity. With increasing mixture velocity, they found that the contribution of waves to the pressure drop increased in the slug flow region, then a decrease in the churn flow region. After the churn flow region, a minimum was observed after which the significance of the wave pressure drop increased again. Though the

method of analysis is very useful in order to examine the ratios of interfacial wave to the frictional pressure drop, the trends are not surprising since they follow the overall pressure drop as reported above. The method of Sawai *et al.* (2004) is further investigated in Chapter 4.

Perhaps one of the most detailed models to predict annular flow in pipes is that first suggested by Whalley *et al.* (1974). In this model, mass balances are derived for three components of the flow: vapour, the liquid film and dispersed drops in the gas core, i.e., entrainment (Figure 2.4). The mass transfer coefficient between liquid and gas, film flow rate and interfacial friction are included in this model to be able to predict void fraction, drop entrainment, film thickness, and pressure drop.

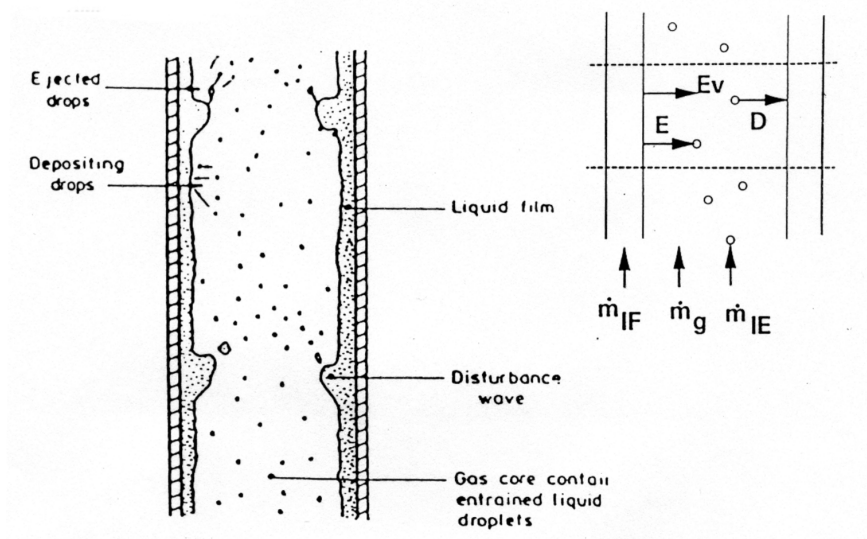


Figure 2.4 Concept of Whalley *et al.* (1974)

For the dispersed phase and liquid film they proposed the following correlations

$$\frac{d \cdot m_{le}}{dz} = \frac{4}{D_t} (E - D) \quad 1.13$$

$$\frac{d \cdot m_{lf}}{dz} = \frac{4}{D_t} (D - E) \quad 1.14$$

Where E and D are the entrainment and deposition flux of drops respectively.

Deposition can be described by

$$D = kc \quad 1.15$$

Where k is a mass transfer, or deposition coefficient, and c is the concentration of drops. Hewitt and Govan (1990) determined k from experiments and suggest the following correlations

And
$$k \sqrt{\frac{\rho_g D_t}{\sigma}} = 0.18 \quad \text{For } \frac{c}{\rho_g} < 0.3 \quad 1.16$$

$$k \sqrt{\frac{\rho_g D_t}{\sigma}} = 0.083 \left(\frac{c}{\rho_g} \right)^{-0.65} \quad \text{For } \frac{c}{\rho_g} > 0.3 \quad 1.17$$

As can be seen this is in the form of a Weber number.

In predicting the entrainment of drops, a maximum film flow rate was considered above which no entrainment would occur. This can be expressed by

$$m_{lfc} = \frac{\eta_l}{D_t} \exp(5.8504 + 0.4249 \frac{\eta_g}{\eta_l} \sqrt{\frac{\rho_l}{\rho_g}}) \quad 1.18$$

For values exceeding this maximum the entrainment is described by

$$E = 5.75 \cdot 10^{-5} m_g \left([m_{lf} - m_{lfc}]^2 \frac{D_t \rho_l}{\sigma \rho_g} \right)^{0.316} \quad 1.19$$

The interfacial friction factor plays an important role for the entrainment of drops. The equations for this proposed by Ambrosini *et al.* (1990) or Holt *et al.* (1999) prove to be popular

$$\frac{f_i}{f_s} = 1 + 13.8 We_D^{0.2} Re_g^{-0.6} \left(\delta_g^+ - 200 \sqrt{\frac{\rho_g}{\rho_l}} \right) \quad 1.20$$

Holt et al (1999)

$$\frac{f_i}{f_s} = 1 + \frac{13.8 We^{0.175} m_g^+}{Re_g^{0.7}} \quad 1.21$$

Where

$$\delta_g^+ = \frac{\delta U_g^*}{\eta_g} \quad 1.21$$

and

$$Re_g = \frac{U_{gs} \rho_g D_t}{\eta_g} \quad 1.22$$

and

$$We_D = \frac{\rho_g U_{gs}^2 D_t}{\sigma} \quad 1.23$$

The film thickness can then be calculated

$$\delta_l^+ = 0.0512 Re_{lf}^{0.875} \quad Re_{lf} > 1000 \quad 1.24$$

$$\delta_l^+ = 0.34 Re_{lf}^{0.6} \quad Re_{lf} < 1000 \quad 1.25$$

and the gravitational and friction pressure drop components can be obtained

$$\left(\frac{dp}{dz} \right)_g = [\rho_g \varepsilon_g + \rho_l (1 - \varepsilon_g)] g \quad 1.26$$

$$\left(\frac{dp}{dz} \right)_f = \frac{4 f_i \rho_g U_{gs}^2}{2 D_t} \quad 1.27$$

Due to the transition identification methods applied and findings, a number of publications are considered of key interest in Chapters 4 and 5. (i) Azzopardi and Wren (2004) (ii) Sekoguchi and Mori (1997). (iii) Zabarás *et al.* (1986). (iv) Sawai *et al.* (2001), (v) Omerbere-Iyari *et al.* (2007) and (vi) Zapke and Kröger (2000).

3 The Experimental Facility, Equipment and Instrumentation

This chapter describes the experimental facility. It also covers the measurement equipment and instrumentation employed in this study, i.e. pressure transducers, thermocouples, flush mount conductance probes and a new proposed calibration method, and the data acquisition system. Moreover, it also describes the Phase Doppler Anemometry employed for drop size and velocity measurements.

3.1 The experimental facility

The experiments conducted in the present study were carried out on a large closed loop facility within the Department of Chemical and Environmental Engineering. Most of the piping is made of polyvinyl chloride (PVC), with some polymethyl methacrylate (acrylic resin or PMMA) sections included for visualisation purposes.

Figure 3.1 shows a schematic flow sheet which also shows instrumentation. Liquid, stored in the stainless steel main separator, is pumped through 76mm piping into the riser base by a liquid pump (maximum capacity - 68m³/hr). Before being directed into the riser base, the liquid flows through a metering section containing two liquid flow turbine meters, and temperature and pressure transducers. Depending on the liquid flow rate required, by operating valves, either a 76mm (3 inch) or 38 mm (1.5 inch) pipe section is used to control and meter the flow.

Two liquid ring pumps (compressors), operated in parallel, are liquid cooled and two-phase gas and cooling water flows through a cooling water tank. The compressed gas is directed vertically into the metering section, whilst the cooling liquid flows back to the bottom of the tank. The same principle of control and metering is applied as in the liquid side of the system. The two phases meet in the two phase mixer, the gas flows through a 76 x 600 mm (dxh) internal pipe and the liquid through a 51 x 400mm (effective diameter, dxh) annulus. After that the fluids flow upwards in the 11 meter tall riser, the flow is directed horizontally (approximately 4 m) to the top of the downcomer and thence back into the separator. Here the phases are separated by gravity and returned to the compressors and pump respectively.

The riser is equipped with a PMMA section ~2 m long, starting at 6 m from the riser base. This section is fitted with multiple measurement stations, including; flush mount conductance probes, flush mount pin probes, wall shear stress probe and a differential pressure device. The transparent material allows for visual observations and the use of high speed photography. For the latter a water-box is provided to minimise refraction. The measurement techniques and instrumentation employed in the present study are covered in more detail in the next section.

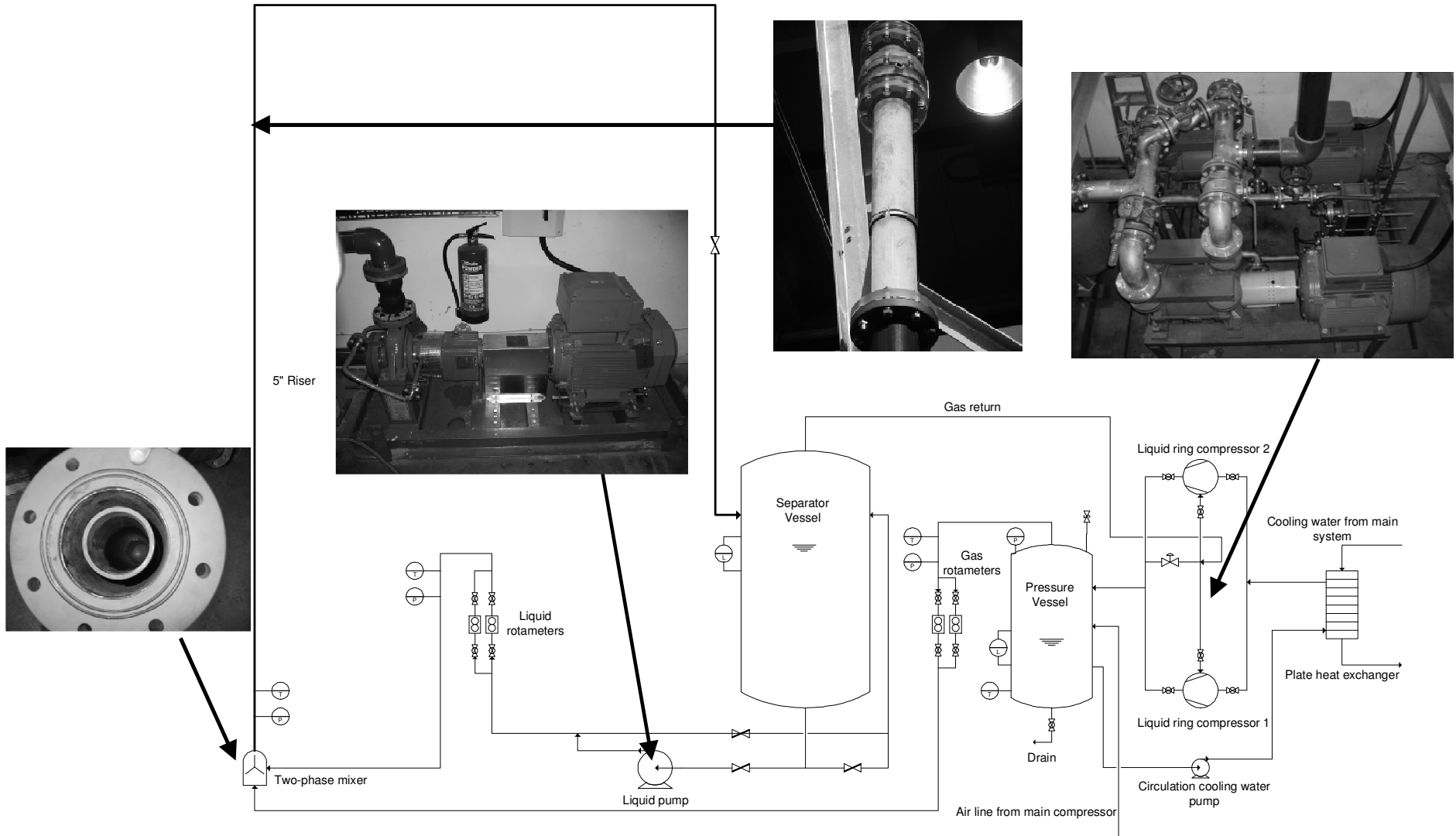


Figure 3.1 The 5 inch experimental facility.

3.2 Differential pressure cell

In a number of experiments, the total, time averaged, pressure drop was measured by an electronic differential pressure detector/transmitter (Rosemount 1151 smart model), with a range of 0- 37.4 kPa and an output voltage from 1 to 5 V, i.e. a resolution of 9.35 kPa per volt.

Two pressure tapings, separated by an axial distance of $12.9 z/D$, were provided on either side of the transparent viewing section, are connected to the differential pressure device via stainless steel lines. A known fluid density in the lines was established by purging to eliminate air bubbles. The latter procedure was repeated at the start of each set of the experiments. The calibration of the device was executed by Zangana (2011) and details provided in that thesis.

3.3 Flow meters

Four Küppers turbine flow meters were used to monitor the flow of liquid and gas, as described at the start of this chapter, one pair for the liquid side of the system and one pair for the gas side. The liquid flow meter for small rates has a range of 6-60 L/min and the flow meter for the higher rates 40-500 L/min. The gas side is, likewise, fitted with a small flow meter ranging from 2.5-11 m³/hr and a large flow meter 35-1030 m³/hr. The calibration of the devices was performed by Omebere-Iyari (2006) and details are provided in that thesis.

3.4 Pressure transducers

Two types of pressure transducers are employed here, one Messma type TD40 and two Gems Sensors type 1000, ranging from 0-16 bar and 0-11

bar respectively. Omebere-Iyari (2006) accurately calibrated the devices to return a 1-5V from the range supplied by the manufacturers of 4-20mA. Details on calibration can be found in that thesis.

3.5 Temperature

T-type thermocouples were employed at the same locations as the pressure transducers to measure the temperatures. Omeberi-Iyari (2006) performed the calibration, by using ice and boiling water to relate voltage output to temperature. Details on calibration can be found in that thesis.

3.6 Data Acquisition

Pressure, differential pressure, temperature, flow rate and void fraction measurements are acquired using a PC equipped with a National Instrument (NI) DAQ card in combination with a Labview programme. Guglielmini (2002) had developed a data acquisition scheme in Labview to convert the voltage output of the all instrumentation through the regression data as determined by several calibration procedures or by volumetric equations. The present study employs a modified version of that developed by Guglielmini (2002). A general layout of the system is illustrated in Figure 3.2.

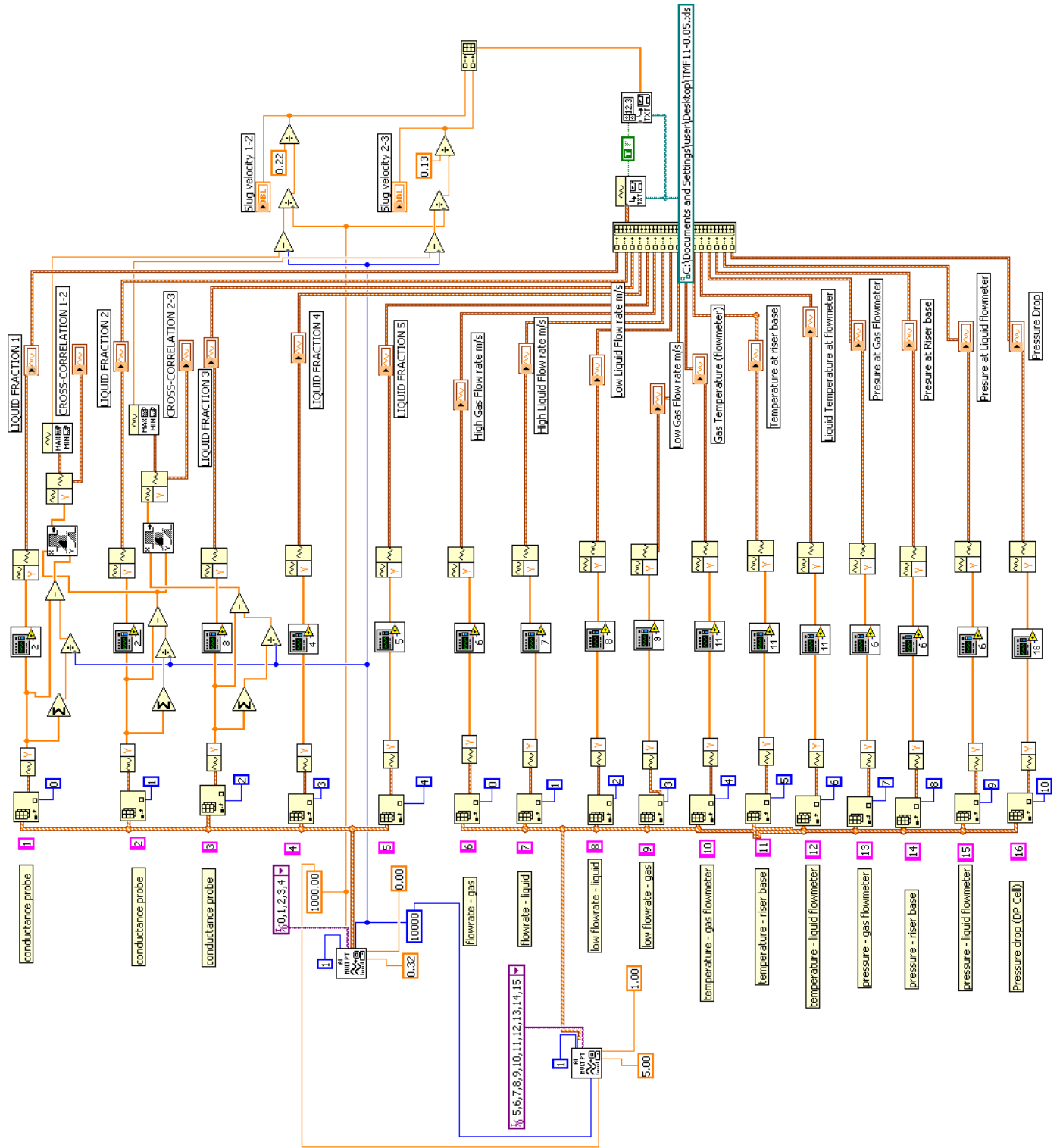


Figure 3.2 Labview data acquisition software user interface

3.7 Conductance Probes

In this study, an impedance technique to measure liquid hold-up was developed. This section describes the design and background of this technique, its basic theory and a new calibration method proposed.

The design of the probe rings as used in the present study was described comprehensively by Omebere-Iyari (2006). The six conductance probe rings, i.e. three probe pairs, are situated at 7963 mm, 8065 mm and 8319 mm from the riser base. This corresponds to 62.7, 63.5 and 65.5 pipe diameters respectively.

The probes are made of stainless steel and are mounted flush with the pipe wall. The latter is ensured by applying ¼ inch diameter dowels at either side of the centre of the individual parts. The thickness s of the rings is 3mm and the distance D_e between the probes is 25mm, insulated by non-conducting PMMA (Figure 3.3). This returns to a probe distance to pipe diameter ratio D_e/D of 0.20.

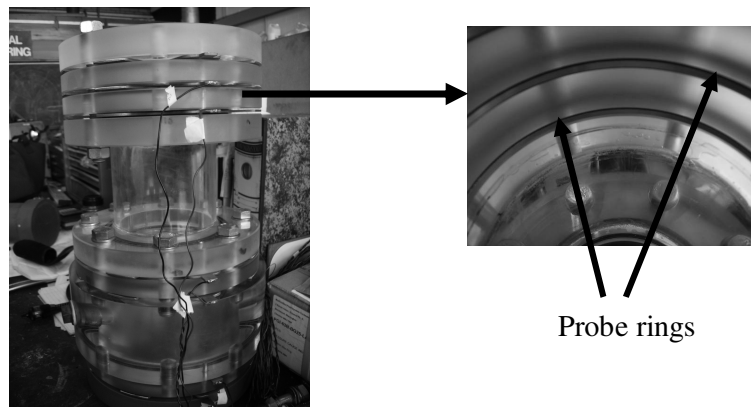


Figure 3.3 The conductance probe pipe section.

3.8 Probe Theory

The electrical properties of gas and liquid are such that, when subject to an electrical current, they can yield conductance in conducting fluids or the

capacitance in non-conducting fluids. From such measurements, the cross-section averaged, liquid-hold up ε_l can be determined. The gas void fraction is determined from $\varepsilon_g = 1 - \varepsilon_l$

In gas-liquid annular-type flow, the instantaneous wall film thickness can be determined by measurements of the electrical conductance between two electrodes in contact with the liquid film. Different types of electrodes such as parallel wires, flush-wires, flush-mounted pins and flush-mounted rings have been adopted (Miya *et al.* (1971), Brown *et al.* (1978), Asali and Hanratty (1985), Andreussi *et al.* (1988), Koskie *et al.* (1989), Kang and Kim (1992), Tsochatzidis *et al.* (1992), Fossa (1998), Conte and Azzopardi (2003). Amongst these probes, the flush-mounted parallel ring probe is attractive to researchers because, (i) it provides non-intrusive measurements, (ii) can pick up small impedance and (iii) allows the electric field to be efficiently confined. Coney (1973) proposed that the apparent conductance K_{app} for two parallel strips embedded flush onto a flat surface can be defined as;

$$K_{app} = K_{app}^* L \gamma \quad 3.1$$

With

$$K_{app}^* = \frac{k(m)}{k(1-m)} \quad 3.2$$

and

$$m = \frac{\sinh^2(\pi s/2h)}{\sinh^2[\pi(s + De)/2h]} \quad 3.3$$

Where, K_{app}^* is the dimensionless apparent conductance, L electrode length, s electrode width, γ liquid conductivity h liquid film thickness and Function k the complete elliptic integral of the first kind,

$$k(m) = \int_0^{\pi/2} (1 - m \sin^2 \theta)^{-0.5} d\theta \quad 3.4$$

Furthermore Coney (1973) proposed that the conductance of annular liquid film can be quantified by above equations by replacing h to a liquid equivalent thickness h_E ;

$$h_E = -\frac{D}{D_E} \ln(1 - 2h/D) \quad 3.5$$

Andreussi *et al.* (1988) defined $h_E = A_L / P_L$ where A_L is the cross-sectional area occupied by liquid and P_L the wetted length of electrode for the application of the annular and stratified flow. The analytical solution to the apparent conductance of the ring probe has been developed by Tsochatzidis *et al.* (1992) as,

$$K_{app}^* = \frac{\pi^3}{32} \left(\frac{2s}{L} \right)^2 \left[\sum_{i=0}^{\infty} (2i+1)^{-3} b_i^2 f_i \right] \quad 3.6$$

with
$$b_i = \cos[(De + s)\theta] - \cos[(De - s)\theta]$$

and f_i the product of modified Bessel functions I_0, I_1, K_0, K_1 ,

$$f_i = \frac{I_0(D\theta)}{I_1(D\theta)} \left[\frac{1 + \frac{I_1[(D-2h)\theta]K_0(D\theta)}{K_1[(D-2h)\theta]I_0(D\theta)}}{1 - \frac{I_1[(D-2h)\theta]K_1(D\theta)}{K_1[(D-2h)\theta]I_1(D\theta)}} \right] \quad 3.7$$

where
$$\theta = \frac{(2i+1)\pi}{2L} \quad 3.8$$

A different expression for b_i was adopted by Fossa (1998);

$$b_i = \cos[(D_e - 2s)\theta] - \cos[(D_e)\theta] \quad 3.9$$

3.9 Conventional Probe Calibration

The conductance probes require calibration before they can be employed for measurements. Annular-type flows are usually simulated by placing a non-conductive cylinder inside the pipe. The annulus between the cylinder and pipe wall is then filled with the conductive liquid. (Figure 3.4)

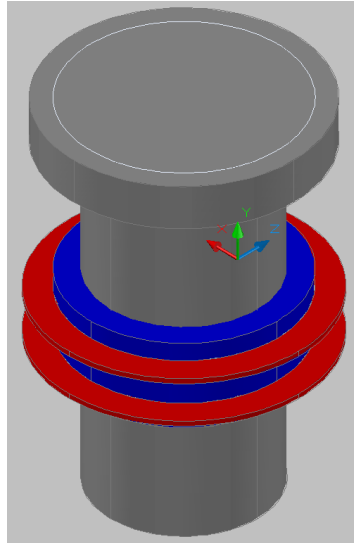


Figure 3.4 Impression of the calibration setup with the probe rings (in red), a water fragment (in blue) and the non-conducting cylinder (in grey).

The unique resistive characteristics of the individual conductance probes need to be quantified. When the probe pair is subject to an electrical current, the relationship between the dimensionless resistivity E (Eq. 3.12) of the probe ring and its voltage output V_{out} should be linear in the form of;

$$E = aV_{out} + b \quad 3.10$$

Constants a and b can be obtained from this relationship. The resistance R_x of the two phase flow is being simulated by a variable resistor in between each of the probe pairs. Hence, the probe resistance R_{probe} is the product of the applied

voltage V_{app} , the voltage measured subject to the applied variable resistor V_x and R_{ref} , the internal circuit variable resistance, by using;

$$R_{probe} = \frac{V_x}{(V_{app} - V_x)} R_{ref} \quad 3.11$$

By plotting the
expression;

$$E = \frac{(R_x / R_{ref} - 1)}{(R_x / R_{ref} + 1)} \quad 3.12$$

against V_{out} , values for equation 3.10 was obtained. The linear regression constants are $a = 3.21$ and $b = 0.042$. Equation 3.10 can then be substituted into the expression for the dimensionless conductance G_e^* of the two phase flow

$$G_e^* = \frac{(1 + E_{full}) / (1 - E_{full})}{(1 + E_{TP}) / (1 - E_{TP})} \quad 3.13$$

In which E_{full} is the dimensionless resistance for the flow domain fully occupied by liquid ($\varepsilon_l = 1$) and E_{TP} the dimensionless resistance for two-phase flow. Ultimately, by decreasing the diameter of the insert and a systematic repetition of calibration steps, the phase distribution can be related to the dimensionless conductance. The relationship of the calibration curve can be expressed in the form;

$$\varepsilon_l = c(G_e^*)^3 + b(G_e^*)^2 + a(G_e^*) + d \quad 3.14$$

Saturation of the system, i.e., too large liquid fractions, can cause erroneous results. The distance between the probes is technically a driver for the accuracy of the film thickness due to averaging over distance in time. Large distances

allow thicker films but the saturation error increases. An optimum has thus to be found. Figure 3.5 below shows the error expectancy of the current set-up.

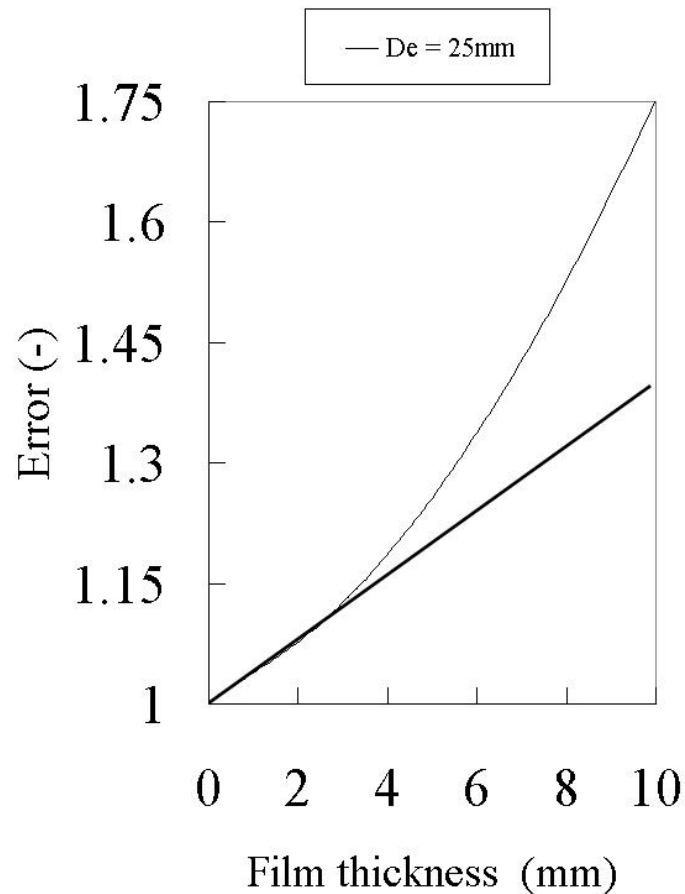


Figure 3.5 Typical error for present study

In general it is advised to operate within the quasi-linear area of the error curve as illustrated. For instance, at 3 mm of film thickness, the error is approximately 7 percent.

3.10 Sources of discrepancy and improvements

The conventional probe calibration method is an ‘ideal’ scenario in which it is assumed that the liquid film is totally liquid. In reality, in gas-liquid annular-type flows, the continuous trapping and folding actions of the disturbance waves at the interface transport gas bubbles into the liquid film. The presence of a considerable amount of bubbles in the liquid film was reported in both air-water horizontal and vertical annular-type flows ((Jacowitz and

Brodkey (1964), Hewitt *et al.* (1990), Omebere-Iyari (2006)). Rodriguez and Shedd (2004) quantified the bubble size distribution, bubble mean diameter and bubble number concentration in the wall film of a horizontal annular flow in a pipe of 15.1 mm diameter. Bubbles had an exponential distribution of sizes with average diameters between 15% and 45% of the film thickness at gas superficial velocities ranging from 28 to 65 m/s and liquid superficial velocities from 0.019 m/s to 0.14 m/s. Around 100 bubbles/cm² exist in the wall film at the gas superficial velocity 28 m/s. A typical bubble size distribution obtained from the present flow facility was obtained from image analysis for a range a gas superficial velocities and a liquid superficial velocity of 0.04 m/s. The results are shown in Figure 3.5.

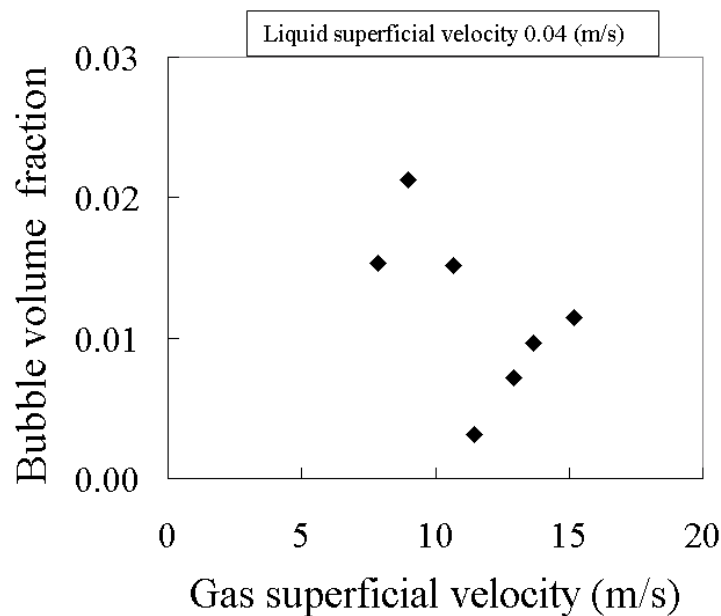


Figure 3.6 Typical bubble distribution

To account for this uncertainty, a new approach to probe calibration was devised. In order to simulate gas bubbles in the liquid film during annular-type flows, spherical glass beads were used (Figure 3.6)

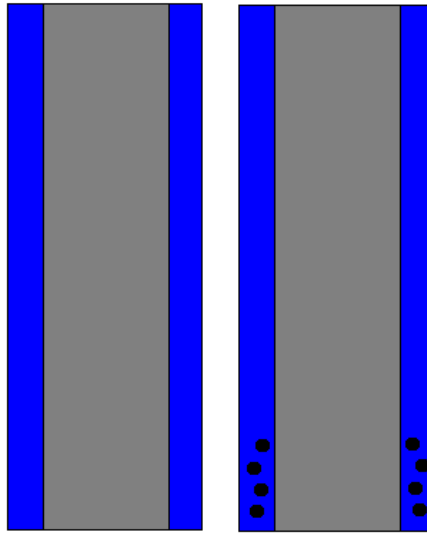


Figure 3.7 Illustration of a pipe with insert only (lhs) and with insert and beads (rhs).

The diameter of the insert was decreased in steps and spherical glass beads were used to occupy a fraction of the annulus between the insert and pipe wall. The diameters of beads used were 3, 4 and 6mm. The calibration procedure, carried out off-line, was performed according the following steps;

1. A conventional void fraction measurement was first made with the single insert only;
2. The test section was then emptied, dried and the insert re-installed;
3. A known volumetric amount of beads were added to the annulus;
4. The annulus was filled with water until the level of water was equal to the level of beads. The water left was then weighted and the in situ bead voidage calculated;
5. A void fraction measurement was performed;

6. The difference between the void fraction measured with the single insert and the single insert-beads was verified by repeating the calibration with an additional cylindrical insert. The latter representing the volumetric fraction equal to the sum initial insert and beads.

3.11 Results

In order to use the probes for the full range of flow patterns it is intended that a single calibration curve be produced, i.e. for bubbly to an annular flow regime. This might increase the risk of discrepancies in the data obtained. Figure 3.7 shows a conventional calibration curve for one of the probes with data for bubbly flow included. The scatter was obtained using uniformly stringed spherical beads (19.5 mm diameter). The number of beads was increased from 7 to 24.

The resistive characteristics of the probes were determined first (Figure 3.8). Not surprisingly, the data shows similar results to those obtained by Omerbere-Iyari (2006). Annular flow calibration data obtained from the 127mm pipe was plotted and compared to results by Tsochatzidis *et al.* (1992) and Coney (1973) (Figure 3.9). To obtain a well fitted polynomial, the liquid fraction was not increased greater than 0.26, according Costigan and Whalley (1997).

The differences between the initial calibration points by using the single insert for ideal annular-type flows and the new approach were not that apparent. Therefore, the error was determined using Equation 3.14. These results were plotted against the experimental G_e^* obtained during calibration with single insert-bead combination. Figure 3.10 shows this absolute error. It should be

noted that this not directly explains the relative effect of bead diameter. Therefore the relative error between the bead diameters was determined, shown by Table 3.1.

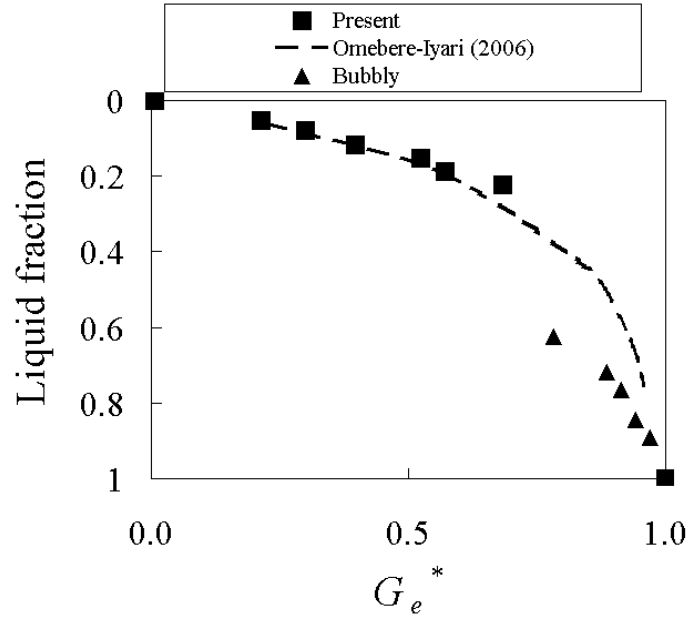


Figure 3.8 Conventional and bubbly flow probe calibration.

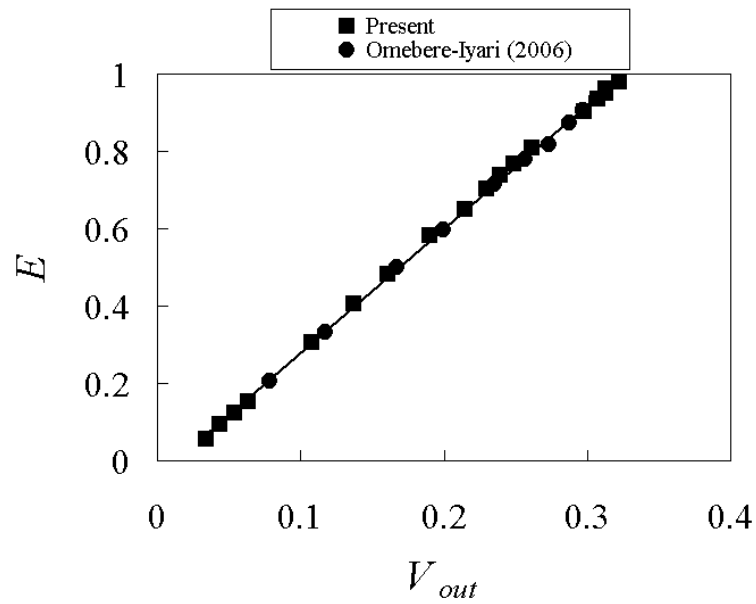


Figure 3.9 The resistive character of the probes

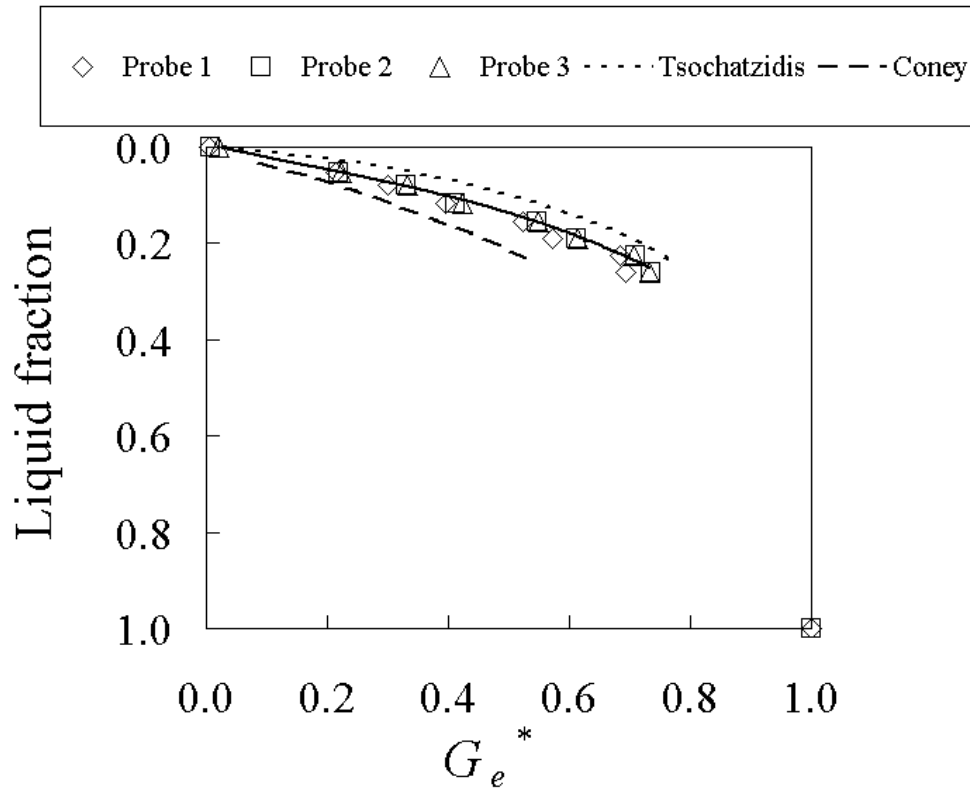


Figure 3.10 Annular flow calibration curve.

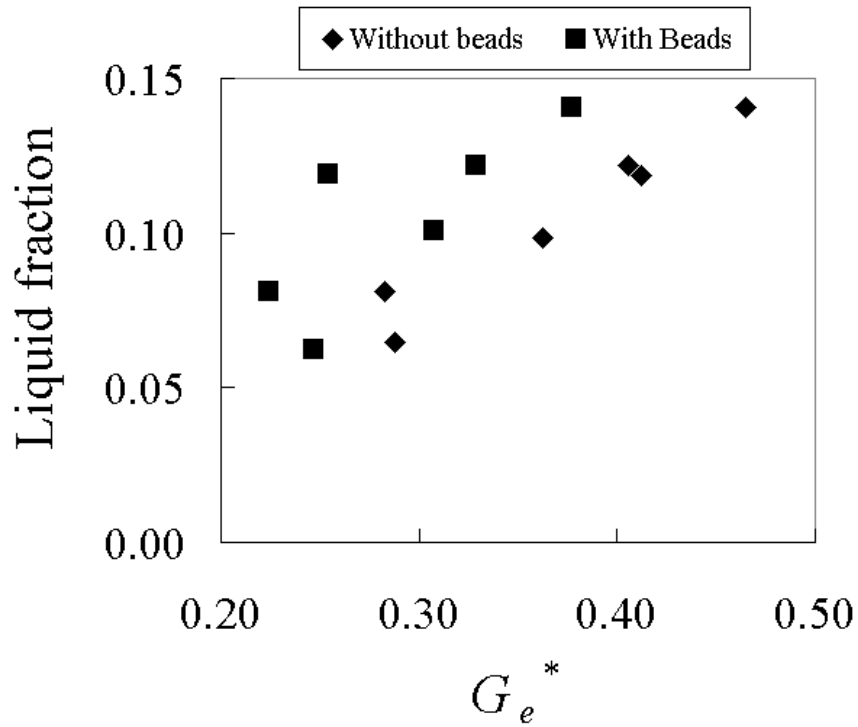


Figure 3.11 Error between calibration procedures (note expanded axis)

Table 3.1 Relative error between bead diameters

Bead diameter (mm)	Change in bead voidage (%)	Change in Error (%)
3	20	624.9
4	23.2	48.8
6	12.9	3.5

The results of the present study show that the calibration of conductance ring probes needs to be approached carefully. The performance and accuracy of these probe types is strongly dependant on the calibration procedures. In churn and annular-type gas-liquid flows one may encounter gas bubbles entrained in the liquid film, particularly in the waves on the liquid film.

The comparison between the new approach for the calibration of conductance probes in annular-type flows to the conventional method, shows that the gas bubbles entrained in the liquid film can cause erroneous results. Therefore, an inappropriate calibration of the conductance probes can lead to an unrealistic view of the phase distributions in annular-type flow and the transition to churn flow. Furthermore it may be deduced that not only bead diameter affects the probe response but also the number of beads and consequently a higher bead voidage returns a different probe response. Simultaneous phase distribution measurements and visual observation (e.g. high speed photography) may therefore reduce the risk of experimental errors. However, in general, it may be concluded that conductance probes, calibrated for a specific flow regime, are producing invalid results when used otherwise. It should be noted however that the impact of gas bubbles still depends strongly on the bubble concentration between two probe rings.

3.12 Laser Doppler Velocimetry and Phase Doppler Anemometry

The Dantec LDA/PDA system (Figure 3.2) was made available for the present study by the CAMERA centre at the University of Nottingham.

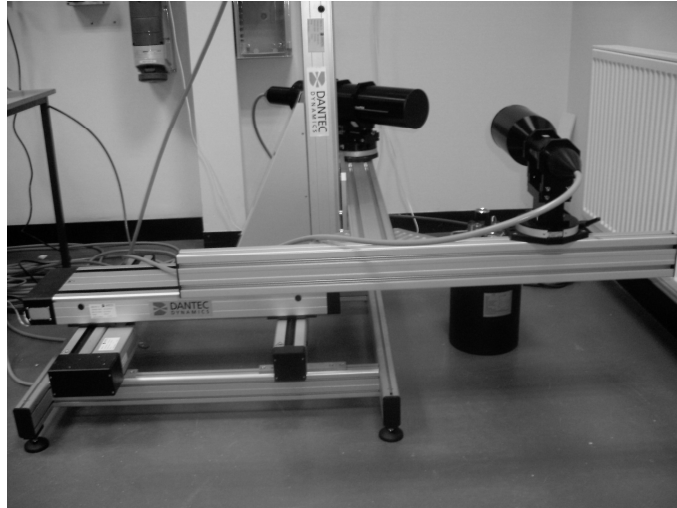


Figure 3.12 The LDA/PDA and traverse setup

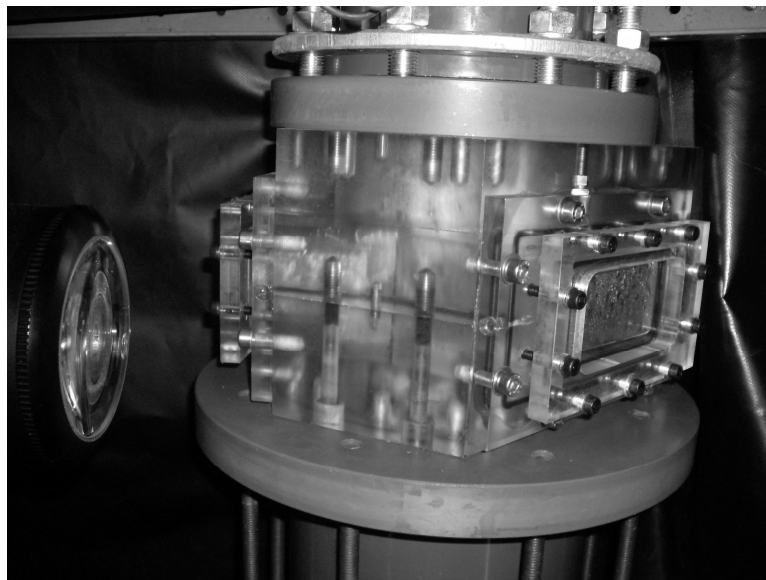


Figure 3.13 The optical access section. On the left hand side the laser beam transmitter.

In the application of laser methods for drop size and velocity measurements to annular gas-liquid flows in pipes, two problems need to be overcome. The first is the elimination of the curvature of the pipe by replacing pipe wall by flat windows. The second is diverting the wavy liquid film travelling on the pipe wall upstream of these windows so that it does not affect the visibility through the windows. These two problems were dealt with by using a specially designed optical access test section.

An existing test section, designed by Conte (2000), for measurements in T-junctions was modified and used here. The test section is depicted in Figure 3.13. It was installed at 10.5 m ($z/D = 83$) from the riser base. The LDA/PDA system was installed around the test section, such that there was sufficient space to traverse the system along the pipe cross section. Upstream of the viewing section, a film withdrawal section was installed to extract the liquid film travelling about the pipe periphery. A perforated, 127 mm i.d. pipe was inserted into a 200 mm i.d. pipe to create an annulus to capture the liquid flowing through the porous section. The film was then drained to the main separator of the system. The measurements stopped in case the liquid fraction would be too high and heavy deposition on the viewing windows would occur.

3.13 Fundamentals of Laser Doppler Anemometry

Laser Anemometry was initially invented for the purpose of measuring velocities by tracking drops in a gas stream which crossed a measurement area of a given size, formed by a fringe pattern of crossing laser beams. The fringe pattern is discussed later in this section. A typical two component LDA/PDA setup is shown in Figure 3.14.

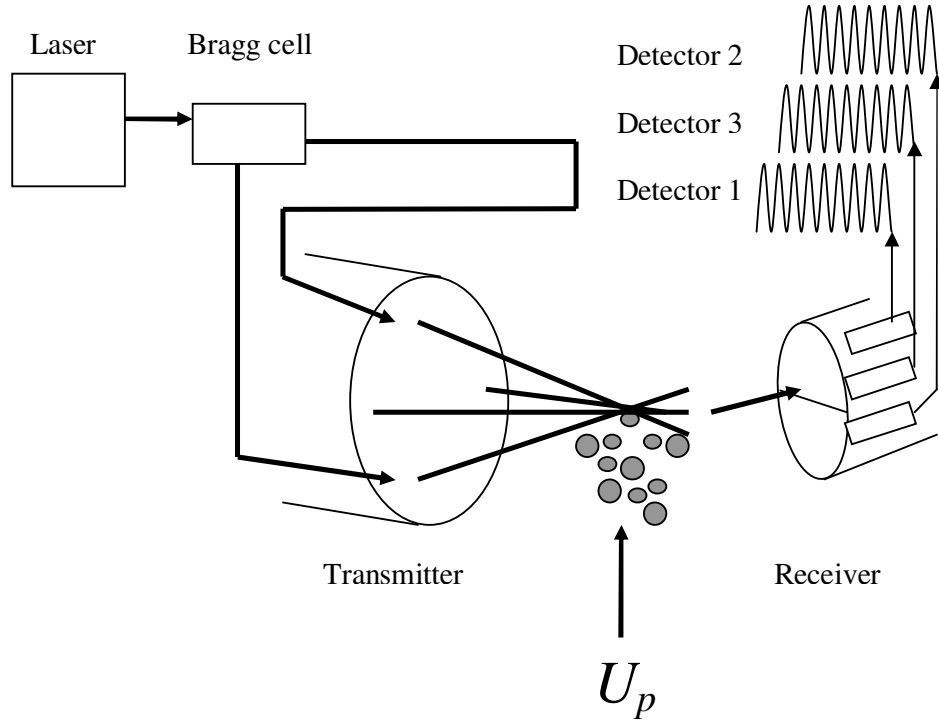


Figure 3.14 Schematic of a typical two component LDA/PDA setup with three photo detectors.

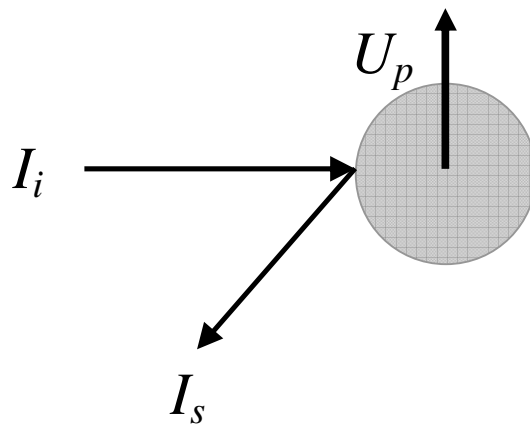


Figure 3.15 Single beam scattering principle

A drop scatters light when subjected to incident light (Figure 3.15). The incident light I_i onto the drop has a speed v_i and frequency f_i . If the drop is moving it changes the frequency f_s of light I_s transmitted to the receiving optics. This change in frequency is the Doppler beat received by the optics and is proportional to the velocity of the drop. The probability that a drop measured by a LDA system travels near the speed of light in multiphase systems, such as the present study, is very small. Obviously, the ratio of the velocity of the drop and the speed of light U_p/v_i is therefore rather large and expression for the frequency f_s as received by the photo detector then approximates;

$$f_s = f_i \left[1 + \frac{U_p}{v_i} (I_s - I_i) \right] = f_i \frac{f_i}{v_i} U_p (I_s - I_i) = f_i + \Delta f_i \quad 3.15$$

It is more common though, that a LDA system consists of two intersecting laser beams (Figure 3.16), i.e., the laser beam being split by a beam-splitter. Since the angle of the two beams is different, consequently the frequency of the beams is not equal at the time the drop interferes and therefore the frequency shift is being distinguishable by the photo detector.

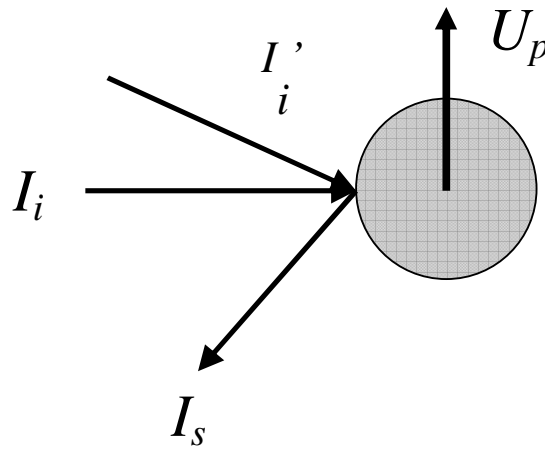


Figure 3.16 Multiple beam scattering principle

Eq. 3.16 then doubles since it is also valid for the second beam of incident light and the two can be combined to give the laser Doppler beat frequency which is caused by the continuous interference of the beam intersection;

$$\begin{aligned}
 f_d &= f_i' \left[1 + \frac{U_p}{v_i} (I_s - I_i') \right] - f_i \left[1 + \frac{U_p}{v_i} (I_s - I_i) \right] = f_i' \frac{U_p}{v_i} (I_i - I_i') \\
 &= \frac{f_i}{v_i} \left[I_i - I_i' \right] U_p \cos(\varphi) = \frac{1}{\lambda} 2 \sin(\theta/2) U_p \\
 &= \frac{2 \sin(\theta/2)}{\lambda} U_p
 \end{aligned}
 \tag{3.16}$$

From Eq. 3.16, it can be seen that the Doppler frequency is proportional to the velocity of a drop travelling normal to the fringe direction (Figure 3.17)

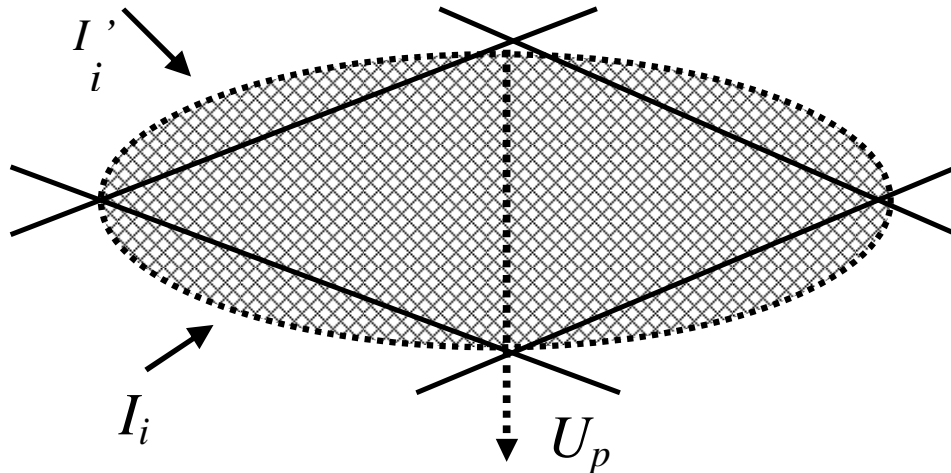


Figure 3.17 Laser beam intersection, measuring volume and fringes.

It is important to note however that this principle holds for multiple intersecting laser beams. In the present study a two component system was

employed which is normally able to measure drop velocities in axial and radial directions relative to the measuring volume.

Argon-ion laser beams, as employed in the present study have a Gaussian intensity distribution (Figure 3.18).

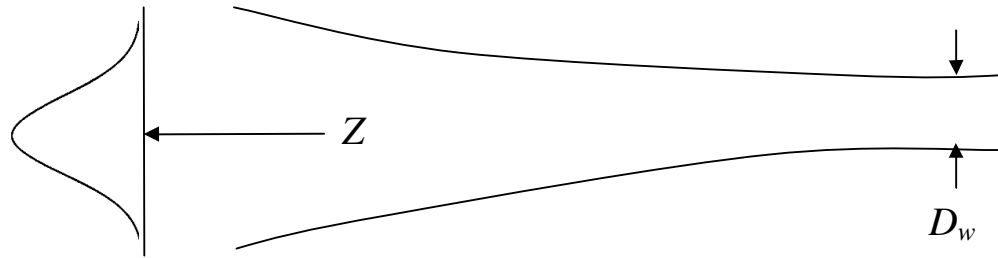


Figure 3.18 Gaussian beam character

When the curvature of the waves approach infinity at point D_w , the wave front adopts a straight line as indicated by the fringe pattern in Figure 3.17. Only in this case, when the beam waists intersect and adopt the smallest measuring volume possible, the fringe model (Eq. 3.16) holds. In case the beams do not intersect at D_w the problem gets more complicated due to the Gaussian distribution and the fringe spatial pattern will not be constant. In this case the Doppler beat will not be proportional to the velocity normal to the fringe direction.

3.14 Phase Doppler Anemometry

As the previous section covered the basics of LDA, in the present study the system was used in the conventional PDA mode with three photo detectors. This is an optional extension supplied by Dantec to the LDA system. The

principles of PDA are indissolubly linked with LDA as covered in the previous section. Therefore, a brief description of the mechanisms is described here.

The main difference between LDA and PDA normally is the number of photo detectors used. In this study, a setup with three detectors was used in combination with Mask C (Figure 3.19) for both LDA and PDA setups, again the LDA measures velocity in two components from a Doppler frequency returned by any of the photo detectors.

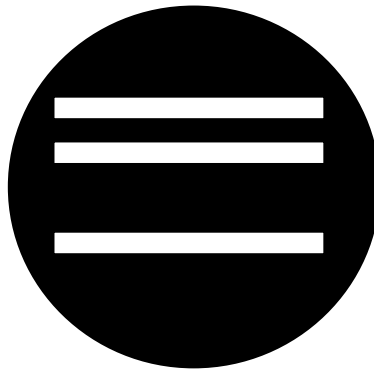


Figure 3.19 Sketch of mask C with small apertures for larger drop diameters.

The Doppler phase shift as a function of the detector angles is illustrated in Figure 3.20 and returns the drop diameter.

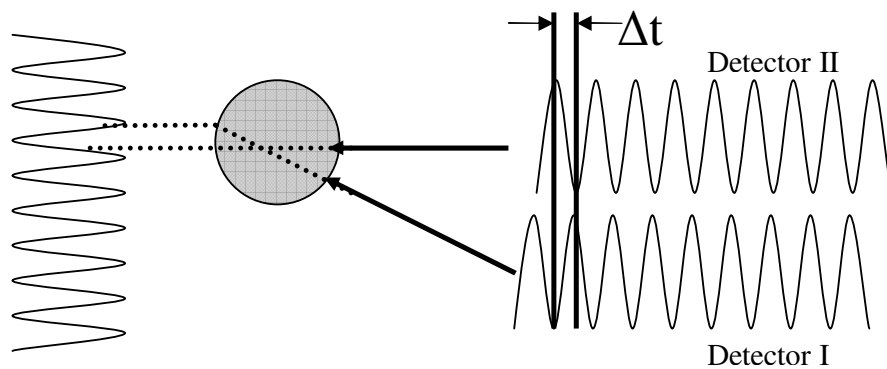


Figure 3.20 Doppler frequency shift due to the detector angular difference.

The Doppler burst received at any detector can be expressed as;

$$\Phi_i = \alpha\beta_i \quad 3.17$$

where

$$\alpha = \frac{\pi}{\lambda} D \quad 3.18$$

Where D is the drop diameter and β_i is a geometrical factor. When using two photo detectors with an angular difference, the phase difference can then be expressed by;

$$\Phi_{1,2} = \frac{\pi}{\lambda} D(\beta_1 - \beta_2) \quad 3.19$$

3.15 Sources of discrepancy

There are four predominant sources of discrepancy associated with LDA/PDA measurements. The cause, effect and solutions to these problems will be briefly outlined here.

1. 2π ambiguity effect
2. Sphericity determination
3. Trajectory effect
4. Slit effect

The 2π ambiguity effect is associated with the curvature of the drop measured. Small drops are most likely to cause a frequency phase shift of within 2π (360°). Large drops on the other hand can cause a larger phase shift and therefore it is hard to deduce whether the phase shift was greater than 2π and if so, to what extent. Therefore, the Dantec system employs a third sensor. As in the previous section shown by Figure 3.14 the detectors 1 and 2 have the largest separation distance, thus giving the greater slope in the linear diameter-phase shift relationship. Another instantaneous measurement is done by detectors 1

and 3 to give the smaller slope. The two shifts are then compared to find the matching intersecting values for the correct drop diameter.

The sphericity determination works according similar principles as the 2π ambiguity effect. As it is able to determine the correct drop size by comparing the frequency shift of two pairs of detectors, likewise it can determine the sphericity by comparing, and thereby closing, the curvature of a drop. This implies that if a drop is not spherical, it can be disregarded in the data and is unable to contribute to experimental error. In order to keep the experimental error low, a 15% threshold for spherical validation was set in the present study.

The trajectory effect (Figure 3.21) is a well reported problem. Teixeira (1988), Azzopardi (1988), Azzopardi and Teixeira (1988), Ziadi *et al.* (1998) all report comprehensively on the problem occurring when a drop is large relatively to the to the measuring volume. The problem is often related to the Gaussian distribution of the wave fronts of the laser beam, thus the intensity distribution is stronger affected by large drops compared to small drops since they tend to scatter and, more importantly for biased results, reflect more light.

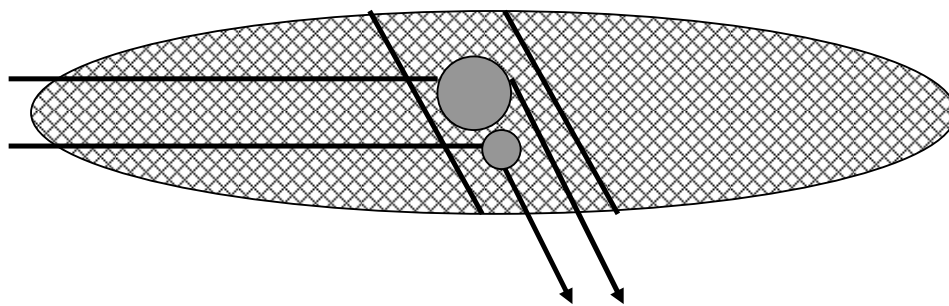


Figure 3.21 The Trajectory effect

A PDA system works on the basis of a threshold of received light through the slit aperture in order to detect drops and thus the larger drops have a

greater probability to be detected first when entering the probe volume boundaries. In fact, a large drop does not necessarily need be in the probe volume but, instead, very near the edge to already being detected by reflection. Teixeira (1988), compared laser diffraction and PDA techniques and found a large bias in the PDA data. The method postulated to overcome this problem is based on a distribution cut-off (Figure 3.22). When the “tail” of the distribution showed zero value, values for larger drops were disregarded from the data.

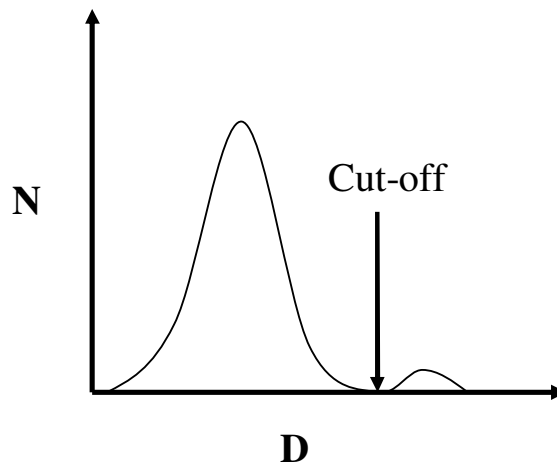


Figure 3.22 Sketch of the principle suggested by Teixeira (1988)

However, it is worth to note that when the laser beams intersect at the beam waist, the Gaussian effect tends towards infinity as discussed in the previous section. It is therefore perhaps more appropriate to separate the problem from being solely Gaussian-affected. Nevertheless, the Dantec BSA Flow Software can correct the data based on the principle as postulated by Saffman (1987). This principle is based on an automated on-line measurement of burst length and an appropriate measuring volume determination. Figure 3.23 illustrates the problem graphically and relates the drop counts to burst length

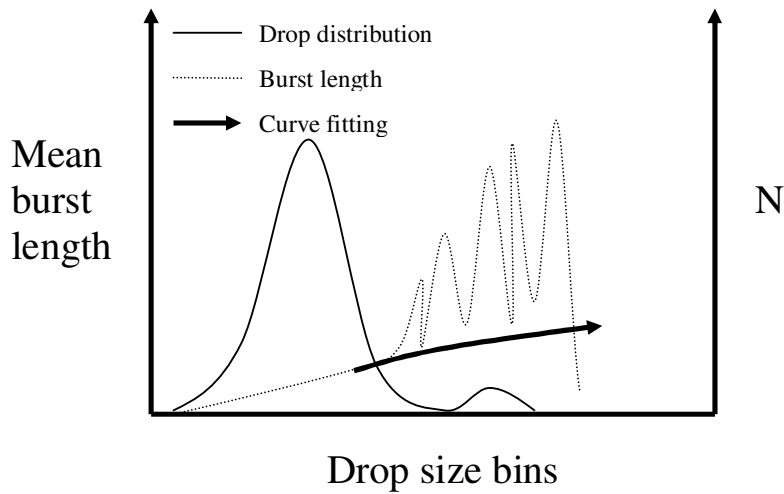


Figure 3.23 Sketch of the principle from Saffman (1987)

As can be seen from Figure 3.23 the burst length varies dramatically with increasing drop diameter, this is an unreliable measure and can thus not be processed. The Saffman (1987) method allows applying a curve fitting for the area to be smoothed in the form of;

$$L = \Delta t \sqrt{u^2 + v^2} \quad 3.20$$

For size classes containing significant counts of droplets, and

$$\overline{L^2} = A \ln D + B \quad 3.21$$

For size classes above the classes used for the curve fitting. Regression constants A and B are to be determined from the measured data.

The Slit effect is similar to the trajectory effect as discussed in the previous section. Due to the projected slit aperture, refracted light is somewhat suppressed for the photo detectors (Figure 3.24) if the drop is not fully in focus of the aperture.

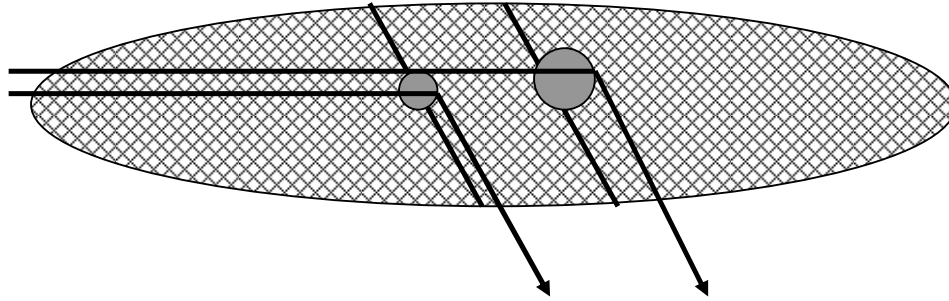


Figure 3.24 The slit effect

Durst *et al.* (1994) performed experiments to quantify the slit effect and proposed solutions to overcome the problem, such as the use of three or more photo detectors.

3.16 Wire Mesh Sensor

The Wire Mesh Sensor design (WMS), as employed in the present study, was proposed by Prasser *et al.* (1998) for local two-phase fraction measurements (Figure 3.25). The Department of Chemical and Environmental Engineering collaborates closely with Forschungszentrum Rossendorf, Germany, where it was developed. The sensor is extensively used by Sharaf (2011).



Figure 3.25 Illustration of the WMS

The WMS works according similar principles as flush mount impedance probes as described previously, but more specifically as local impedance measurement methods such as needle probes. By using different electrical circuitry, the probe itself can be used in both resistive as well as capacitive modes.

The WMS used here consists of 32x32 wires, i.e. transmitter and receiver wires in two planes. Figure 3.26 illustrates the principle in more detail.

The axial spacing between the wires is 2 mm and each cross point of the wires represents a measurement point. This way an equally spaced mesh, with 1024 cross points, occupies the cross section of the 127 mm pipe. This returns to a spatial resolution of approximately 4 mm (x, y) across the majority of the pipe, which is a great advancement compared to more traditional phase fraction measurement techniques.

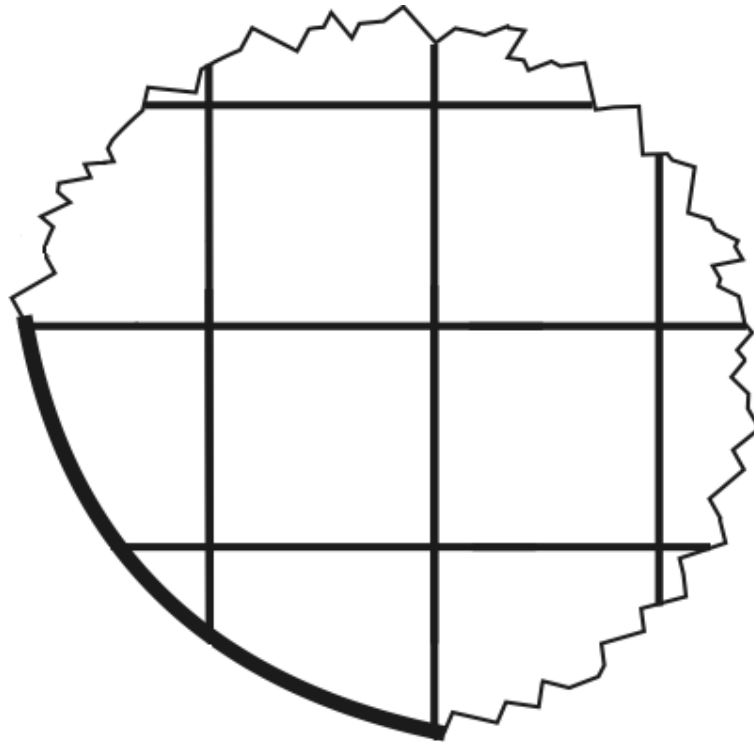


Figure 3.26 Section of the total cross sectional area of the pipe, with receiver wires horizontally and transmitter wires vertically.

3.17 Sources of Discrepancy

As mentioned before, the spatial resolution is uniform across the majority of pipe cross section. However, near the periphery, the resolution drops as can be seen in Figure 3.26. This problem could be solved by using local film thickness measurement probes, such as that used by Belt (2007).

Cross talk between the transmitter wires can occur. Since the wires are positioned very close together, i.e., D_t/N_w , where D_t and N_w are the pipe diameter and number of wires respectively, the driving current can travel between an activated wire and a (not yet) non-activated wire. This is dealt with in the electronics by keeping the transmitter drivers and receiving output

impedances lower than the working fluid impedance. This can be arranged during the calibration (full pipe of liquid and empty pipe).

The intrusiveness of the probe has been a subject for many discussions. The wires are exposed to the flow and, partly depending on the area occupied by the wires in relation to the total area of the pipe, do indeed disturb the flow in small extent. However, one important thing to note is that the flow, after passing the wires, is indeed disturbed. Therefore other measurements can not be performed just downstream of the WMS, of course this on the other hand depends on the development length available downstream. Tests have been performed at Nottingham in a 127 mm bubble column and high speed photography was employed to visualise the mechanisms of break-up of bubbles through the WMS. As expected, smaller bubbles were sliced up into smaller pockets but surprisingly, a Taylor bubble fully recovered after hitting the wires. Yet, still the principles of up and –downstream effects hold for accurate measurements.

4 Liquid Film Characteristics

This Chapter presents the results on the void fraction (or liquid fraction) measured with conductance ring probes. To some extent, it reports measurements made simultaneously with these probes and a Wire Mesh Sensor (WMS). The first section introduces the background and motivation for this Chapter. The experimental matrix is then presented. The third section presents some of the general results. The last section focuses on the liquid film including more detailed and statistical analysis of the behaviour of the liquid film and pressure drop in churn and annular flow. A relationship for the interfacial friction factor is presented along with a relationship describing some of the churn annular transitions from different experimental setups and workers within reasonable accuracy.

4.1 Background and motivation

In vertical gas-liquid flow, annular and churn flow regimes are quite different when examining the cross sectional phase distribution. Both flow regimes show different hydrodynamic phenomena. However, re-occurring patterns can be observed for each of the regimes individually. Annular flow is characterised by a liquid film travelling at the pipe periphery and an entrained liquid fraction, in the form of drops, of the film is carried upward by the gas core (drop size experiments are presented in Chapter 5). When the liquid film is relatively thin, and the flow is friction dominated, the total film tends to move upward. When the liquid mass flux is increased, an increase in liquid film thickness is generally observed. The effect of gravity on the film becomes more dominant. In the latter case, one may encounter simultaneous upward and

downward film flow. This switching mechanism is known as the flooding point reported by, e.g., Govan *et al.* (1990) amongst others. As a result, the entrained fraction of liquid in the gas core increases since the roughness of the gas-liquid interface increases as well as the interfacial shear stress ((Azzopardi (1997)). Also a phenomenon known as wispy flow can occur around this point of transition from churn to annular flow. The gas core in wispy annular flow contains relative larger liquid structures compared to the smaller droplets in annular flow.

Churn flow typically occurs at higher liquid mass fluxes. It is characterised by a thicker liquid film relative to annular flow and a larger proportion of the liquid is entrained. The flow is gravity dominated and can have a strong pulsating nature. Another characteristic of churn flow is the mechanism of liquid bridging. Liquid bridging occurs when huge waves occupy a large fraction of the pipe cross sectional area, the liquid film collapses due to gravitation and the liquid structures in the gas core coalesce with the collapsing film (Sekoguchi and Mori (1997)). Due to these liquid bridges, often referred to as liquid plugs, gas accumulates and in smaller pipe diameters this is the onset of slug flow. In larger diameter pipes with air-water flow, slug flow with a classical Taylor bubble has hitherto not been reported. Due to the diameter of the pipe and the physical properties of the fluids, the large gas bubble is unable to stabilise and where a Taylor bubble is expected, instead, there are collapsing and break up mechanisms active. Figure 4.1 shows a typical spatial averaged film thickness time-trace.

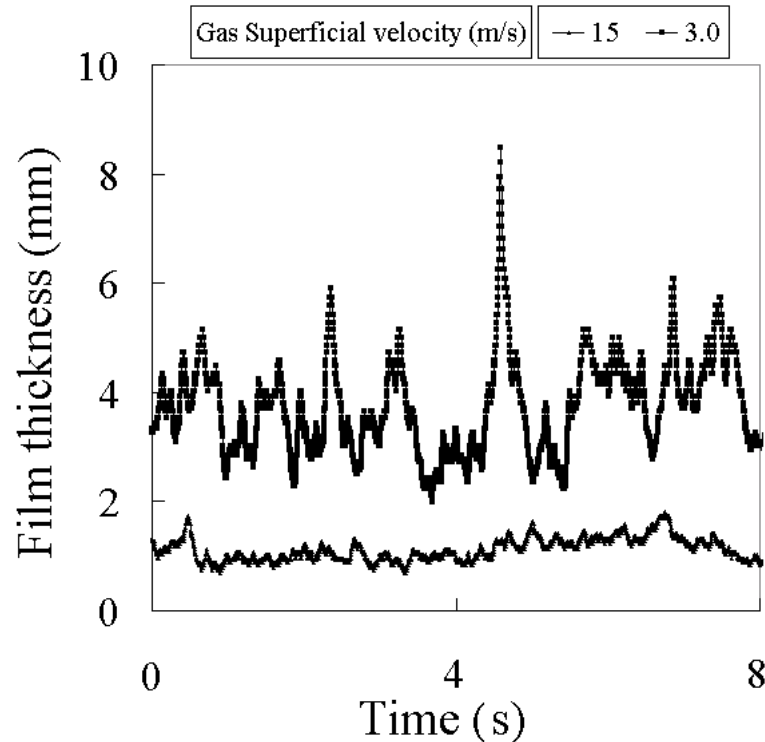


Figure 4.1 Typical film thickness time series for a liquid superficial velocity of 0.2 m/s. Interesting is the very large peak for gas superficial velocity of 3 m/s.

The rough wavy surface is caused by interfacial shear. There have been different types of waves reported: (i) ripple waves are small in magnitude, wavelength and velocity and travel on the liquid film in high gas and low liquid velocity flows; (ii) disturbance waves are characterised by a height greater than the mean film thickness. In addition, the wavelength is greater than that of ripples and the velocity is greater than that of the liquid base film; (iii) Sekoguchi and Takeishi (1989) and Sekoguchi and Mori (1997) reported waves larger in amplitude, wavelength and velocity than disturbance waves; they defined these as huge waves. These waves, in combination with wisps were found later by Hawkes and Hewitt (1995) in wispy annular flow which is evidence that might explain the hydrodynamic mechanisms of the transition area

between churn and annular flow. However, still little is known about this type of waves.

The present study tries to address this question and strives to find a relationship between disturbance waves and drop creation and huge waves and wisp creation. However, at some conditions ripples, disturbance and huge waves co-exist and interact. Because the velocities of disturbance waves and huge waves are considerably higher than ripples, they tend to increase in magnitude with ripples superimposed.

The physical occurrence of disturbance waves is some function of pipe diameter. In smaller diameter tubes the disturbance waves are uniformly distributed about the pipe circumference and are observed as liquid rings on the inner pipe wall. In large diameter pipes however, as reported by Azzopardi (1983) and confirmed by Omebere-Iyari (2006), the disturbance waves appear non-uniformly distributed about the pipe circumference and adopt a parabolic shape.

The inception of disturbance waves is linked to a wave inception velocity. Azzopardi (1997) reviewed several empirical correlations that are able to predict the inception velocity of disturbance waves. However, pipe diameter, liquid viscosity and surface tension can be accounted for deviation of data. Data on pipe diameter shows that disturbance wave inception decreases with increasing pipe diameter. Azzopardi *et al.* (1983) correlated three groups using dimensionless numbers in the form a liquid film Reynolds number $Re_l = m_l D_t / \eta_l$, an Ohnesorge number $On = \eta_l / \sqrt{(\sigma \rho_l D_t)}$ and a Weber/Reynolds number ratio $We/Re_g = \eta_g u_{gs} / \sigma$. They suggested that $Re_l \sqrt{On}$ should be combined. They showed that data from 50 and 125 mm

pipes did not correlate as good as that for smaller diameter pipes.

The velocity of disturbance waves can be obtained experimentally from cross correlation of the two liquid fraction signals from consecutive measuring instruments. Furthermore, the approximate velocity of disturbance waves can be deduced from high speed photography as employed by for instance Barbosa *et al.* (2001) whom also proposed a model to give more insight into wave behaviour in vertical gas liquid flow and the physical mechanisms that are accountable. Some high speed photography data will be presented for the present study in this section. Since available data is still very limited for larger pipe diameters, it is useful to examine the effects of pipe diameter on the characteristics described above and compare results obtained in the past in smaller diameter pipes.

4.2 Experimental outline

The experimental matrix is illustrated by Table A1 in the appendices of this thesis. Including 10 repeatability experiments, a total of 700 experiments at 2 barg were carried out on the facility and with the instrumentation defined in Chapter 3. The data acquisition rate of all instruments was 1 kHz. Higher sampling rates were assessed and no difference in data was obtained. Assuming that a wave would travel at 6 m/s, the wave would be sensed 4 times at a sampling rate of 1 kHz over the probe distance of 25 mm. The liquid superficial velocity was varied from approximately 0.005 to 0.7 m/s and the gas superficial velocity from 1.4 to 16.5 m/s. The experiments were carried out by varying the gas flow rate systematically from high to low values, keeping the liquid flow rate constant. The maximum gas flow rates achieved depended on the liquid flow rates. The gas flow rates were decreased until liquid blockage

was encountered i.e., the gas flow was unable to overcome the oscillating flow of liquid, well into the churn flow region. This is usually referred to as flooding. Moreover, high speed photography was employed to examine the flow visually.

In addition, another but smaller set of experiments on the liquid film was carried out as part of the drop size measurements. This film data at atmospheric pressure is presented together with drop size data in the Chapter 5.

4.3 Results

In order to test the results against prior data, and to get an indication of the flow regimes, 5 sets of void fraction measurements have been plotted on the flow pattern maps from Hewitt and Roberts (1969). The results are shown in Figure 4.2

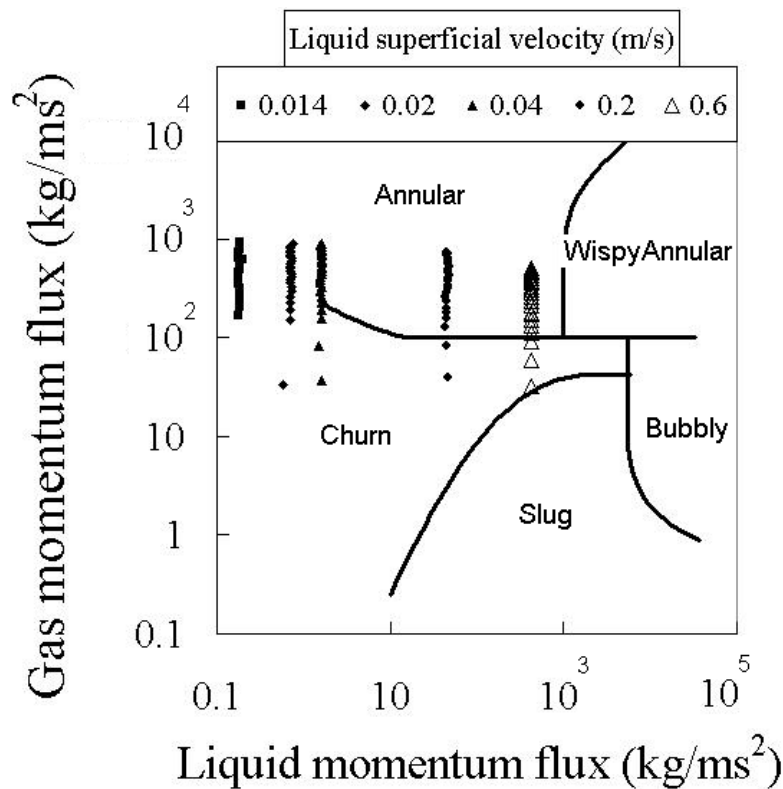


Figure 4.2 Data for 2 barg plotted on flow pattern map from Hewitt and Roberts (1969)

As can be seen, the flow pattern map suggests that the majority of data are situated in the annular flow region. Visual observation is still a powerful technique to identify flow patterns. The next Figures 4.3 and 4.4 show high speed photographs of the flow at a frame rate of 1000 frames per second. Pictures were taken by using a flat-faced viewing section around the pipe to compensate for the pipe curvature.

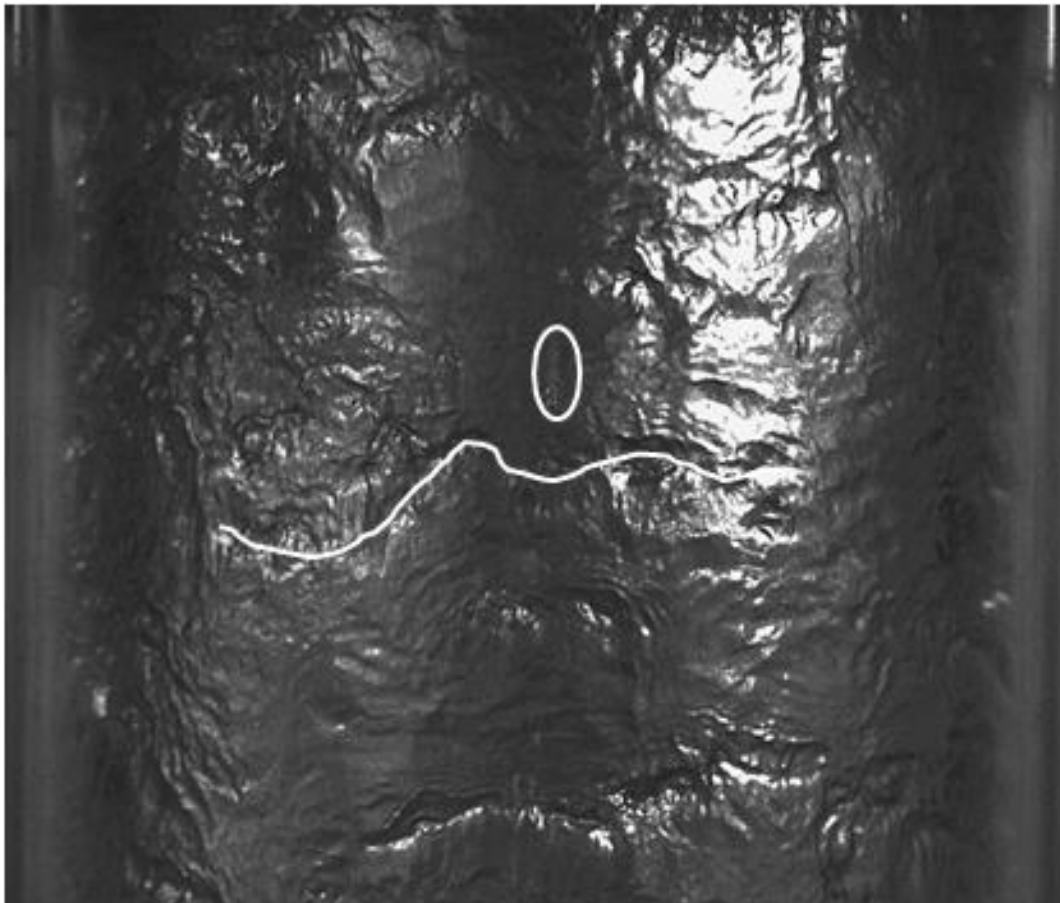


Figure 4.3 Annular flow. Gas superficial velocity 16 m/s, liquid superficial velocity 0.014 m/s. The non-coherence of the waves is clearly visible. The white ellipse marks a string of newly entrained drops from the marked wave.



Figure 4.4 Churn-annular flow. Gas superficial velocity 10 m/s, liquid superficial velocity 0.04 m/s. Waves are very irregular, moving “sideways” on the pipe wall. Also gas bubbles in the liquid film can be observed.

It can be observed that the film at the wall is relative smoother in Figure 4.3, showing non uniform disturbance and ripple type waves. The film in Figure 4.4 is much rougher. Moreover, here air entrainment into the liquid film can be seen. This is possibly due to folding and trapping of the larger waves at these conditions. The waves are not moving merely perfectly in the axial direction but move around the periphery of the pipe, i.e., “sideways”. This may be an indication of the onset of a gravity dominated film flow. It is also observed that the quantity of liquid entrained in the gas core is higher than for Figure 4.3.

4.4 The liquid Film

Here, a number of methods are applied in order to extract detailed information from the 700 time series obtained and to get an indication of the actual flow regimes during the experiments.

The film thickness for all experiments is shown in Figure 4.5. Similar to Kaji and Azzopardi (2010), the spatially and temporally averaged thickness is calculated from the time series using

$$\delta = \frac{D_t}{2} (1 - \sqrt{\epsilon_g}) \quad 4.1$$

where D_t is the pipe diameter and ϵ_g the average void fraction.

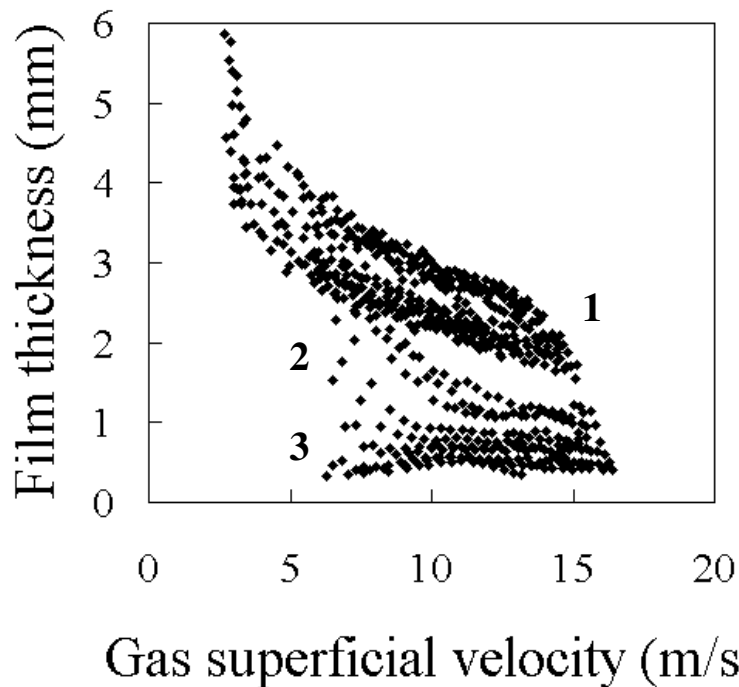


Figure 4.5 Film thicknesses for all experiments in the experimental matrix (conductance probes).

Three main regions can be observed in Figure 4.5; (1) the higher region of film thickness represent the higher liquid low rates (2) The intermediate region represent medium liquid flow rates (3) the lower region represents the lowest liquid flow rates. The slopes of the graphs indicate a systematic effect of the gas flow rate on the film thickness. In order to examine this more in detail, a selection of flow rates and regions, including the pressure drop, are described below.

A selection of results for the film thickness and the frictional pressure drop are shown by Figures 4.6, 4.7 and 4.8 respectively.

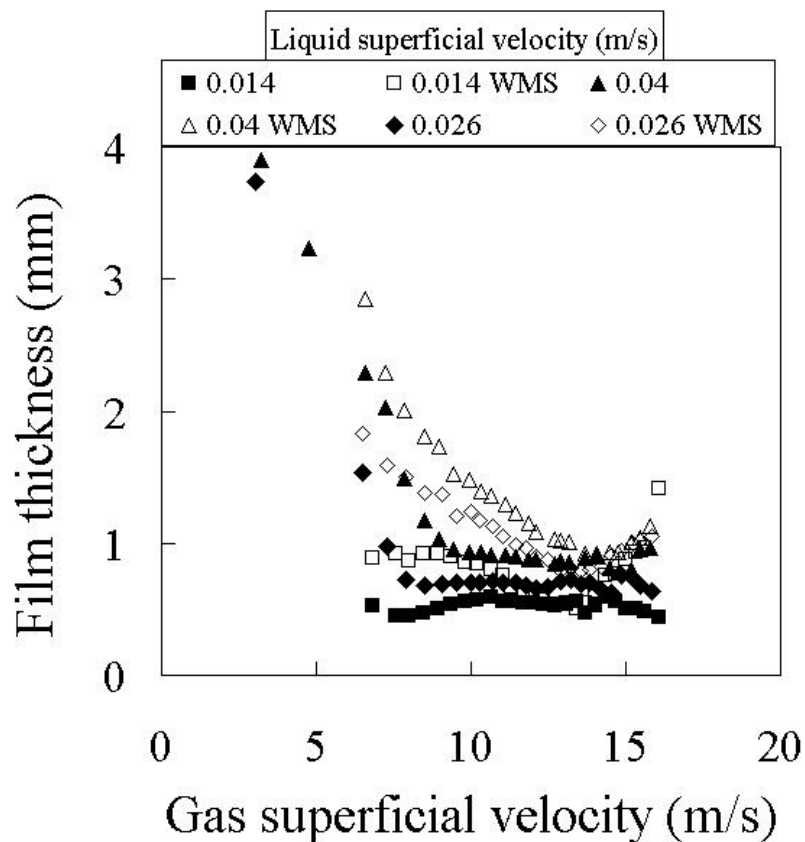


Figure 4.6 Film thickness for selected experiments. WMS denotes data obtained with the wire mesh sensor.

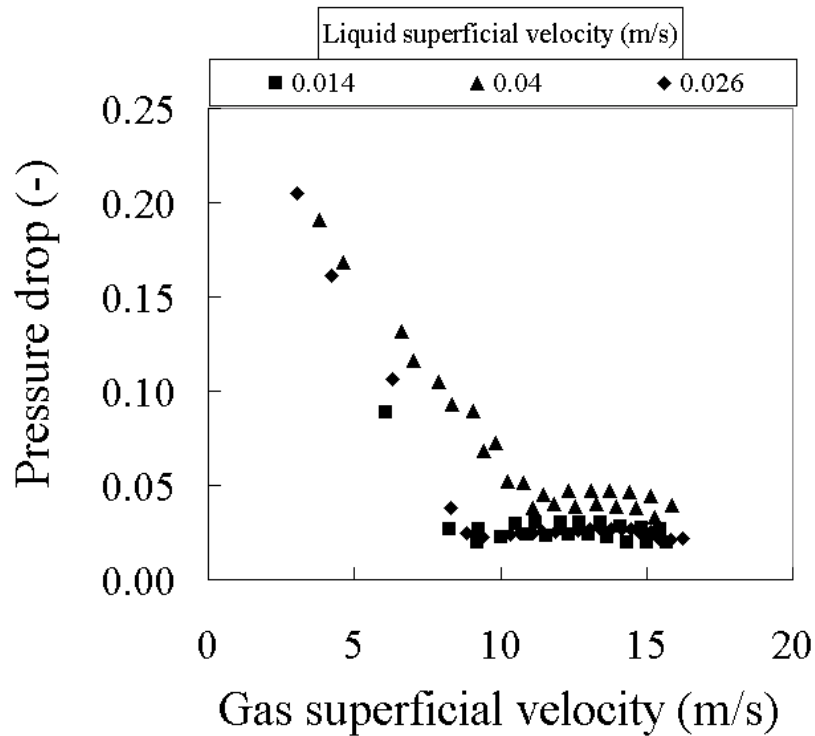


Figure 4.7 Frictional pressure drop for selected experiments.

For much higher liquid flow rates, the curves for both film thickness and pressure drop show trends different to those for lower liquid flow rates as illustrated by Figure 4.8 (a) and (b). These Figures are shown separately and rescaled. The change with gas velocity is of a more gradual nature than that for the lower liquid flow rates. However, a clear systematic effect of the superficial gas velocity on the film thickness and the pressure drop can be observed. There is a steep decrease of both film thickness and pressure drop at lower gas and liquid superficial velocities. For the conductance probe data, at higher gas superficial velocities there is a gradual increase and for the conductance probe data, minima can be observed around a gas superficial velocity of 13 m/s. The WMS data shows a much stronger increase.

Nevertheless, this increase exhibited by the output of both measurements, might be an indication of a transition of flow pattern from perhaps churn to annular flow. In contrast to the smaller diameter cases (Hewitt *et al.* (1965)), the pressure gradient in annular flow for this larger pipe increases only slowly with gas velocity. This is not surprising as frictional pressure gradient is inversely proportional to the pipe diameter. Therefore the expected minimum is not very clear. However, the trends do show similarities with those found by Govan *et al.* (1990) who studied the onset of flooding between the churn and annular flow regime. The pressure drop they reported also showed a steeper decrease for a liquid superficial velocity of 0.03 m/s and gas velocities ranging from 12 to 34 m/s.

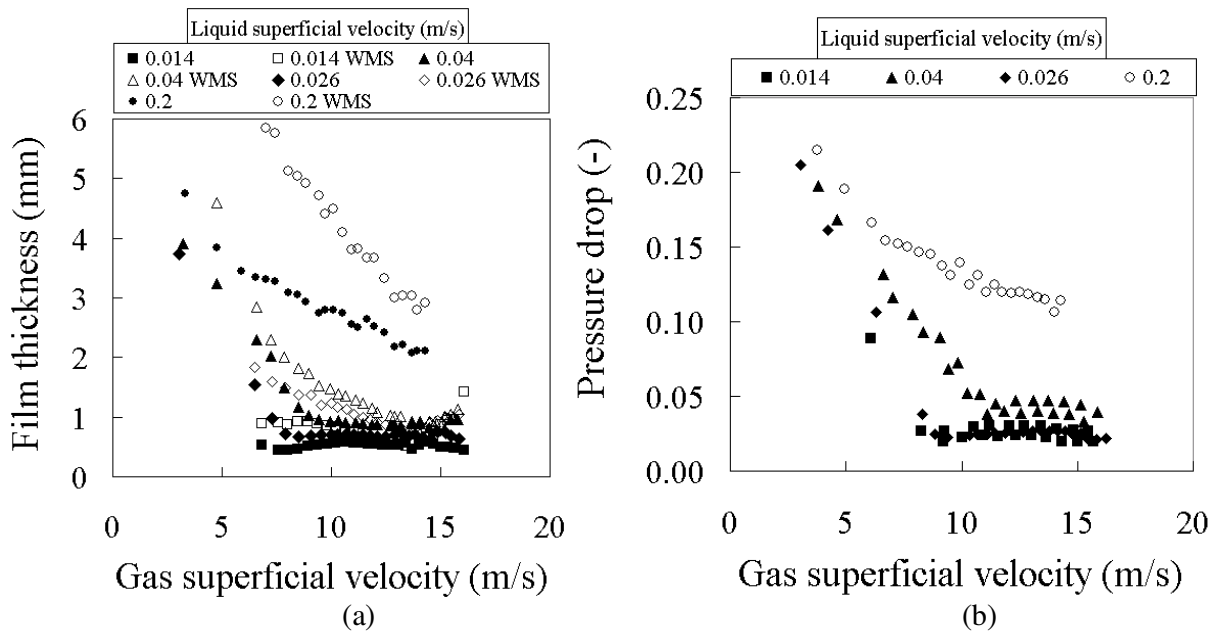


Figure 4.8 Film thickness (a) and pressure drop (b), including higher liquid flow rates

An explanation of why the WMS shows a more profound increase may be found in the fact that the WMS is much more localised than the conductance probes. Therefore, due to averaging of data over a larger distance between the rings, lower values are expected for the conductance probes. In order to compare the two instruments, the calculated film thicknesses were plotted as illustrated by Figure 4.9.

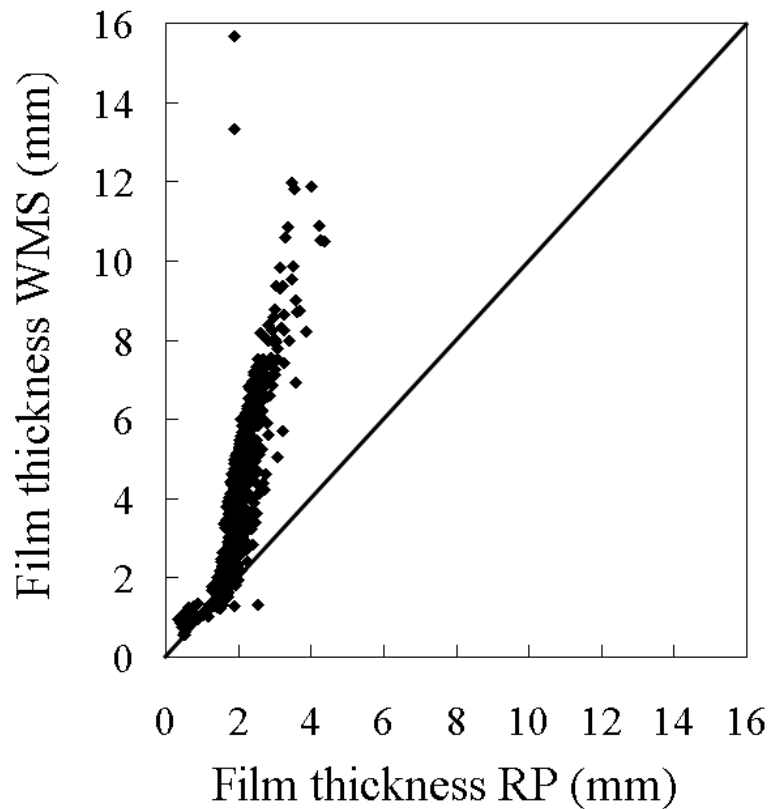


Figure 4.9 Comparison of film thickness measured experimentally by conductance probes and WMS (symbols) and best fit line (bold line)

From Figure 4.9 it can be observed that the WMS measures higher values, except for very thin films. This is however not surprising. The WMS sensor is able to sense the dispersed liquid phase in the gas core but the fraction is too small to be measured accurately due lack of spatial resolution. The drops at high gas flow rates, thus high void fraction, are smallest and the entrained

fraction is also relatively low. Further details on this are given in Chapter 6. Therefore, the liquid measured by the WMS in the gas core is being added to the liquid film, consequently returning a higher value for the film thickness. The conductance probes however can only measure the liquid at the pipe wall. In addition, error from the conductance probes would not be such to result in the difference between conductance and WMS probes.

From examination of the evolution of the film a preliminary conclusion can be made that for the very low liquid velocities, due to the sharp change in slope, a possible inception of flow pattern transition is taking place around a gas superficial velocity of 10 m/s. Since the film thickness shows this clear trend, a more detailed analysis was performed for the selected experiments on the time traces from the conductance probes and structure velocities were obtained. Another popular method to identify flow patterns is the probability density function of the void fraction as suggested by Costigan and Whalley (1997). The latter was employed in a 32 mm pipe. Omebere-Iyari (2006) found poor agreement with those experiments conducted in a 127 mm pipe. This indicates that perhaps the former method may not aid in identification of flow patterns accurately in large diameter pipes.

Though the analysis was performed in order to examine the interfacial structures, it is important to note that the circumferential non-coherency of waves in large diameter pipes, also reported by Azzopardi (1883) and Omerbere-Iyari (2006), introduces an additional complication since the conductance probes can only measure at one axial position. Zangana (2011) investigates this more elaborately.

Figure 4.10 shows the amplitude of the waves, i.e. the maximum base film thickness subtracted from the maximum wave height. The difference between the two is largest at low gas superficial velocities. It shows similar features to those observed in the overall film thickness.

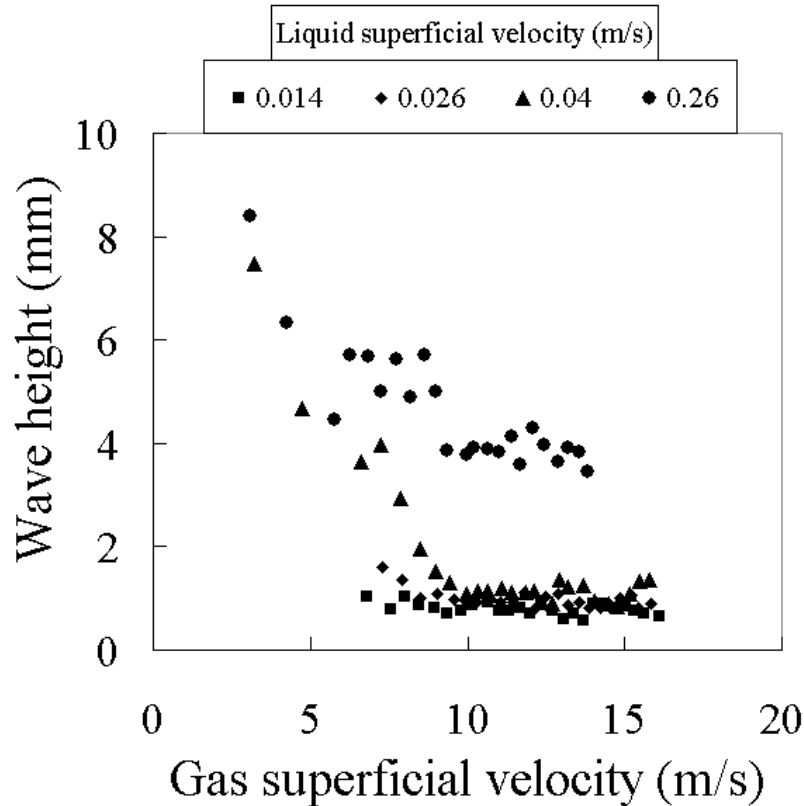


Figure 4.10 Wave heights for selected flow rates.

Azzopardi *et al.* (1979) carried out studies on the velocity and frequency of waves occurring in annular gas-liquid flows. There have been a number of subsequent papers. Structure velocity is obtained by cross correlating the signals from two conductance probes, positioned (axially) 0.203 m apart and dividing the physical distance between the probes by the time lag at the maximum correlation coefficient. From this, the average velocity over distance of the liquid film as an entity, including interfacial structures can be

determined. In previous work different trends of structure velocity with mixture velocity for different flow regimes have been found. For bubbly flow the structure velocity increases with mixture velocity, for slug and churn flow the structure velocity decreases with mixture velocity and finally for annular flow, the structure velocity tends show an increase with mixture velocity. From Figure 4.11 it can be seen that these trends are present in the data. However, the values are negative for lower liquid and gas flow rates and become positive around a mixture velocity of 13 m/s. This implies that there are possible features of counter and co-current flow. For a liquid superficial velocity of 0.04 m/s, a drastic drop and thereafter recovery can be observed.

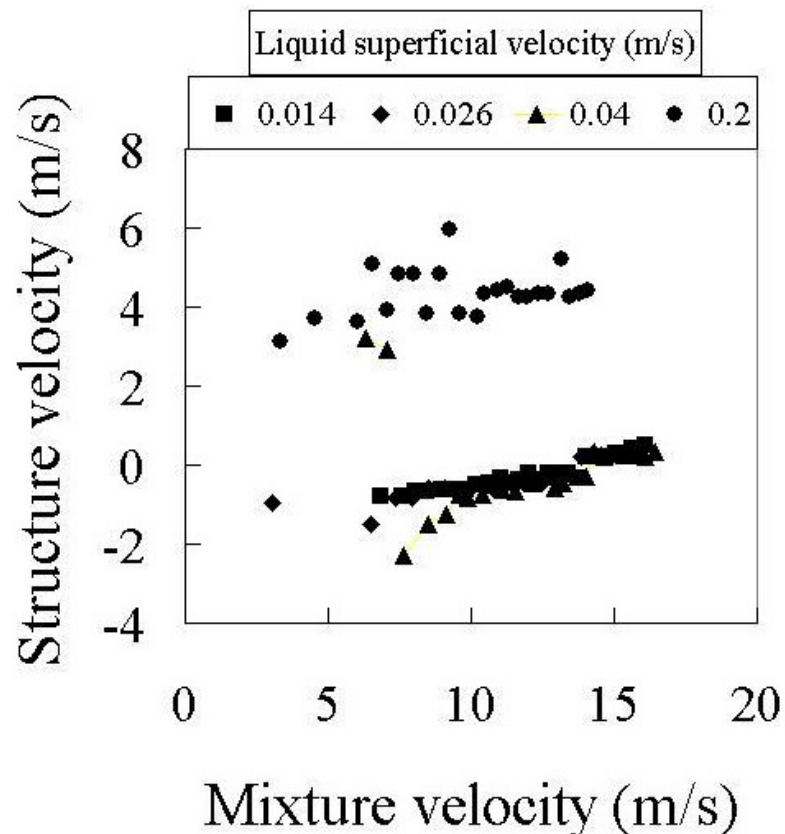


Figure 4.11 Structure velocities for selected experiments.

In order to examine these features in more detail, the correlograms obtained from these structure velocity calculations were examined. Figure 4.12 shows the maximum correlation coefficients obtained for the selected experiments. With gas flow rate, clear trends can be observed. The values decrease to a minimum, after which the slopes switch drastically to positive. From the correlograms it can be seen that dominant peaks with a positive time lag, indicating a co-current flow, can be seen for low gas flow rates. The correlograms show a more chaotic nature, both co-and counter-current flow, at medium gas flow rates. For higher gas flow rates the correlograms are higher in magnitude and gradually tend towards single peak positive values. For higher liquid flow rates the effect is less apparent but still marginally present.

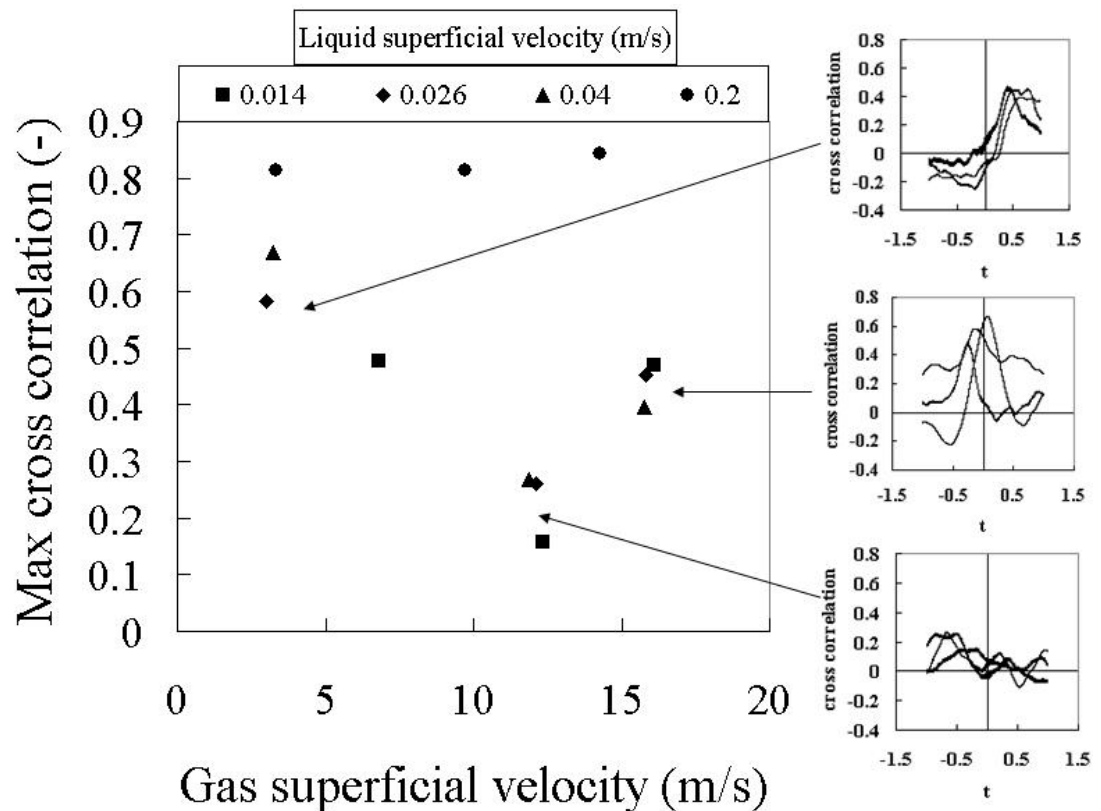


Figure 4.12 Effect of gas flow rate on correlation coefficient and correlograms.

Cross correlation results from Zabarar et al (1986) show very similar features. For low gas flow rates they report single peak correlation curves at positive time lag. At intermediate gas flow rates they report peaks at negative time lag. The present data shows good similarity of trends at the change of slopes, which they suggest to be a stationary process that switches between states of the system. The same applies to higher gas velocity where the peaks gradually shift from near-zero negative to positive time lags, suggesting transition from roll type waves to propagating disturbance waves. The latter is thought to be due to full suppression of the switching mechanism indicating annular flow. As mentioned before, Zabarar *et al.* (1986) also measured wall shear stress and pressure drop simultaneous to the film thickness. Taking the ideas of Moalem-Maron and Dukler (1984) further, they tested their data against the findings by the latter authors. They found that there is a critical point in the film thickness where the wall and interfacial shear stress equal zero. At this point, the pressure drop and film thickness shows a minimum and the liquid film is relatively stationary but can drastically switch sign with increasing or decreasing gas flow rate. Since the pressure drop and film thickness in the present study do not show a very clear minimum, possible detail may be found in the behaviour of the interfacial shear stress. The interfacial shear stress is a strongly dependent on the roughness of the film and therefore a driving factor in the pressure drop, especially the friction dominated proportion. The interfacial shear stress was calculated from the experimentally obtained pressure drop and film thickness according the relationship first suggested by Dukler *et al.* (1983)

$$\tau_i = -\frac{dP}{dz} \left(\frac{D_t - 2\delta}{4} \right) \quad 4.2$$

The results are shown in Figure 4.13. Unlike the trends in the film thickness as well as the pressure drop, the interfacial shear stress indicates a minimum. Yet not as strong as seen in smaller diameter pipes, also shown by Zabaras *et al.* (1986), but it may suggest a more conclusive level of detail. They defined the region at large film thickness (above minimum) as “up flow re-circulation” and at low film thickness (below minimum) as “up flow”. Figure 4.14 shows the minima as a function of liquid flow rate.

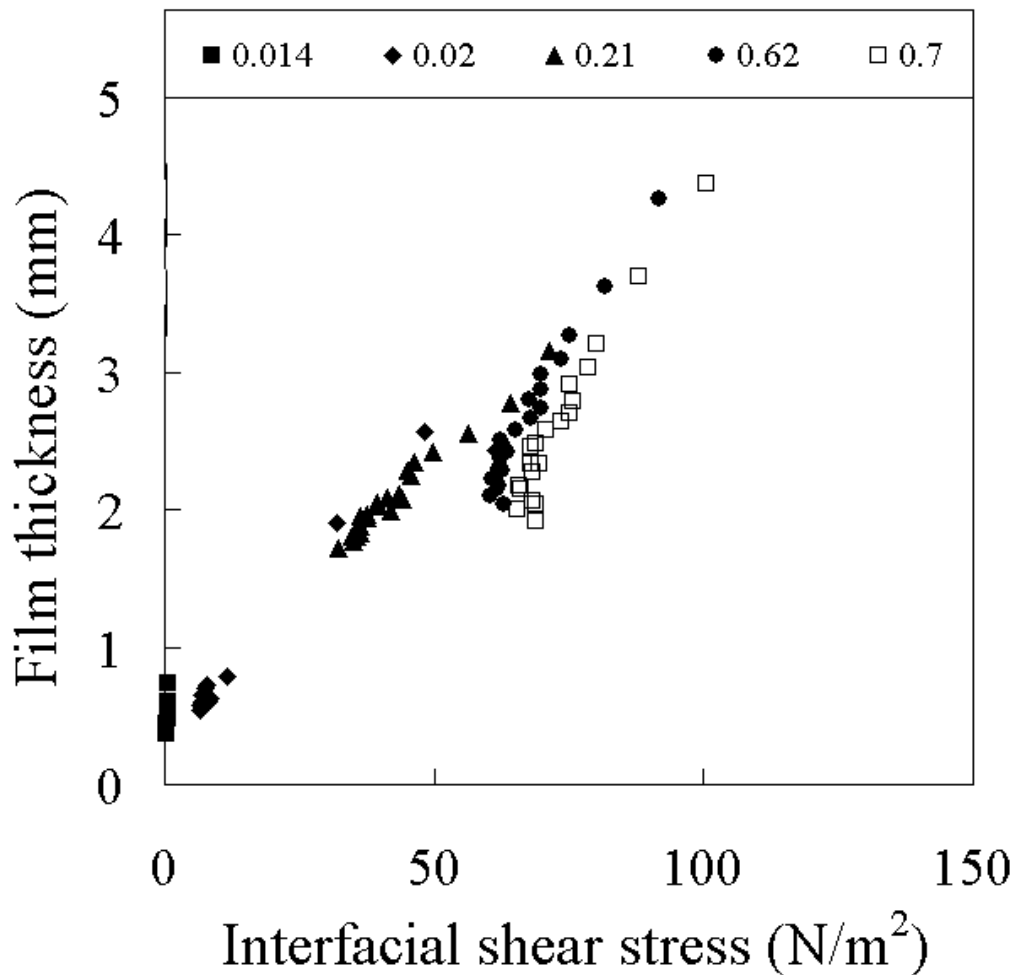


Figure 4.13 Interfacial shear stress vs. film thickness.

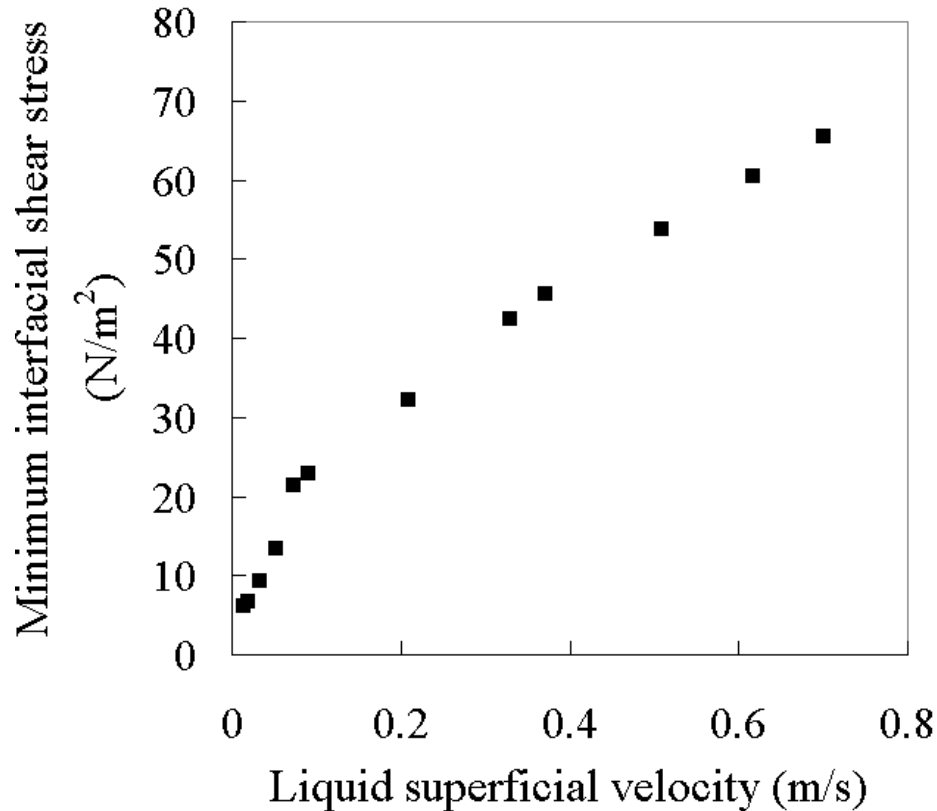


Figure 4.14 Interfacial shear stress vs liquid superficial velocity

It can be seen that the slope of the interfacial shear stress changes rather sharply around a liquid superficial velocity of 0.07 m/s. This may be due a change of wave type i.e., from relatively small disturbance to larger rolling type waves, causing a change in the interfacial interaction between the gas and liquid, as suggested by Zabaras *et al.* (1986). More importantly, linking this to Figure 4.4, in which a photograph is presented of the flow at liquid superficial velocity of 0.04 m/s, may well be evidence that between 0.04 and 0.07 m/s for the liquid, the liquid film is semi-stationary since it is apparent that waves start to move sideways on the pipe wall.

However, Eq. 4.2 is rather simplified and should actually include terms to account for the gas core density as well, since the pressure drop can significantly be influenced by the dispersed phase. Especially when considering that the entrained fraction for the present study for high liquid flow rates, as presented in Chapter 6, is relatively high and therefore the flow ‘resistance’ imposed on the gas core is significant due to drops. Therefore more elaborate equations are presented below for the interfacial and wall shear stress and the results compared with Eq. 4.2. In order to put this into the right context, firstly the different components of the total pressure drop are shown in Figure 4.15 and 4.16 for 0.02 and 0.7 m/s of liquid superficial velocity respectively. The entrained fraction used to estimate the gas core density is adopted from Azzopardi and Wren (2006) and is valid if $u_{gs} > 5$ m/s.

$$E_f = 0.47u_{gs}^{0.16}u_{ls}^{0.35} \quad 4.3$$

And the gas core density is calculated by using

$$\rho_c = \frac{(m_g + \rho_l u_{ls} E_f)}{(u_{gs} + E_f u_{ls})} \quad 4.4$$

Where m_g is the gas mass flux. The core, gravitational and frictional pressure drop components are respectively calculated by using

$$\Delta P_c = \frac{g \left[\frac{\rho_c (D_t - 2\delta)^2}{D_t} \right]}{D_t} \quad 4.5$$

$$\Delta P_g = \frac{g \left[\frac{\rho_l (\delta - 2\delta^2)}{D_t} \right]}{D_t} \quad 4.6$$

$$\Delta P_f = \Delta P - \Delta P_c - \Delta P_g \quad 4.7$$

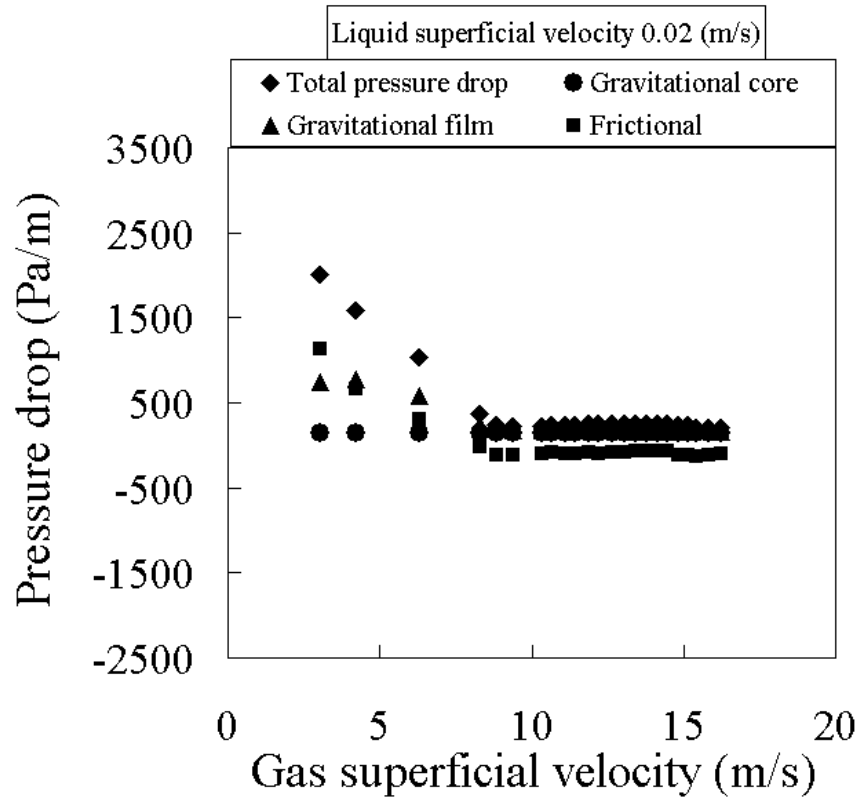


Figure 4.15 Components of the pressure drop for annular type flow

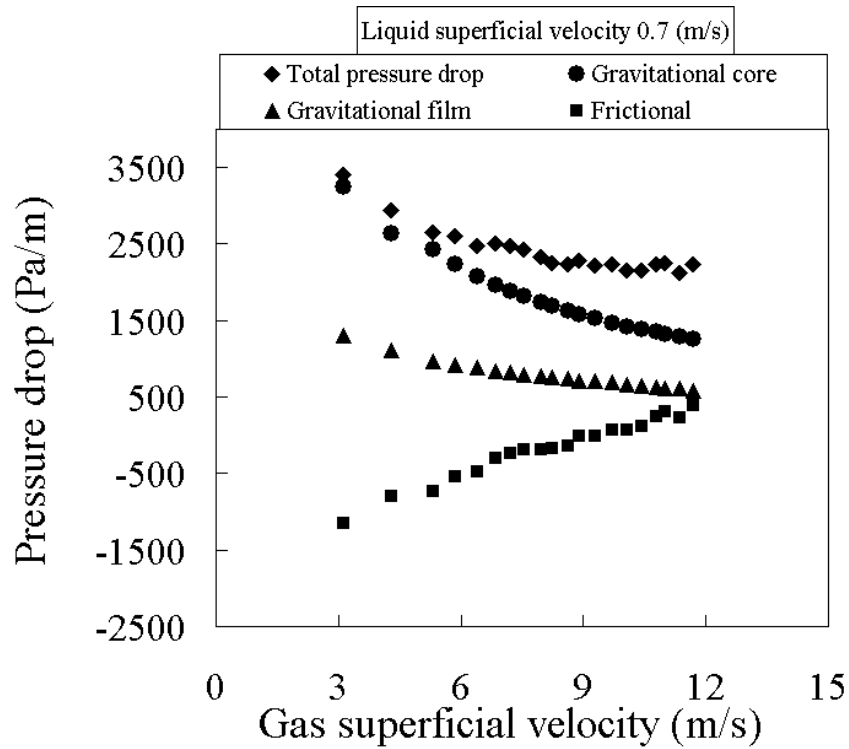


Figure 4.16 Components of the pressure drop for churn type flow

From Figure 4.15 it can be observed that the components of pressure drop more or less converge at the higher gas flow rates. Only at the lower end, the frictional pressure drop due to the liquid film tends to dominate. As can be observed in Figure 4.16, this switch is not profoundly present as such. Extending the trends would imply a convergence around 32 m/s for the gas. In addition, it can be seen that the ratios between the components and total measured pressure drop are much greater than Figure 4.15. An interesting feature is that the gravitational core contribution is dominating the other components. The maximum core density obtained is 95 kg/m³. This indeed may be evidence of the major contribution of the core density to the overall pressure drop. Another is the negative frictional component due to the liquid film for the lower end of gas flow rates. This switches sign at approximately a gas superficial velocity of 10 m/s and may be due to what Zabaras *et al.* (1986) defined as the switch between up flow and up flow with “re-circulation”. As stated above, the more elaborate equations for wall and interfacial shear stress are derived in the following manner

$$P_0 \frac{\pi D_c^2}{4} = P_1 \frac{\pi D_c^2}{4} + \tau_i \pi D_c \Delta Z + \rho_c g \frac{\pi D_c^2}{4} \Delta Z \quad 4.8$$

Where P_0 , P_1 , D_c , ρ_c and Z are the pressures at a given axial location Z , the average gas core diameter and density respectively.

Rearranging in terms of the interfacial shear stress τ_i then yields:

$$\tau_i = \frac{dP}{dZ} \left(\frac{D_t - 2\delta}{4} \right) - \rho_c g \left(\frac{D_t - 2\delta}{4} \right) \quad 4.9$$

And for the derivation of the wall shear stress τ_w :

$$P_0 A_f - \tau_i \pi D_c \Delta Z = P_1 A_f + \tau_w \pi D_t \Delta Z + \rho_l g D_t \Delta Z \quad 4.10$$

Rearranging in terms of the wall shear stress τ_w then yields:

$$\tau_w = \frac{dP}{dZ} \frac{A_f}{\pi D_t} + \tau_i \frac{\pi D_c}{\pi D_t} - \rho_l g \frac{A_f}{\pi D_t} \quad 4.11$$

Where D_t is the pipe diameter and A_f is the cross section of the pipe occupied by the liquid film with thickness δ :

$$\frac{A_f}{\pi D_t} = \delta - \frac{\delta^2}{D_t} \quad 4.12$$

Figure 4.17 below presents the performance of Eq. 4.2 and 4.9. It can be observed that for the lower end of liquid flow rate, i.e., annular flow, the results from both equations show reasonable agreement. Moving to higher liquid flow rates shows a gradual increasing deviation up to 30 percent of Eq. 4.2 to 4.9. This implies that indeed the inclusion of the gas core density has a great effect on the interfacial shear stress in non-annular flows and the validity of Eq. 4.2 is limited to annular flow.

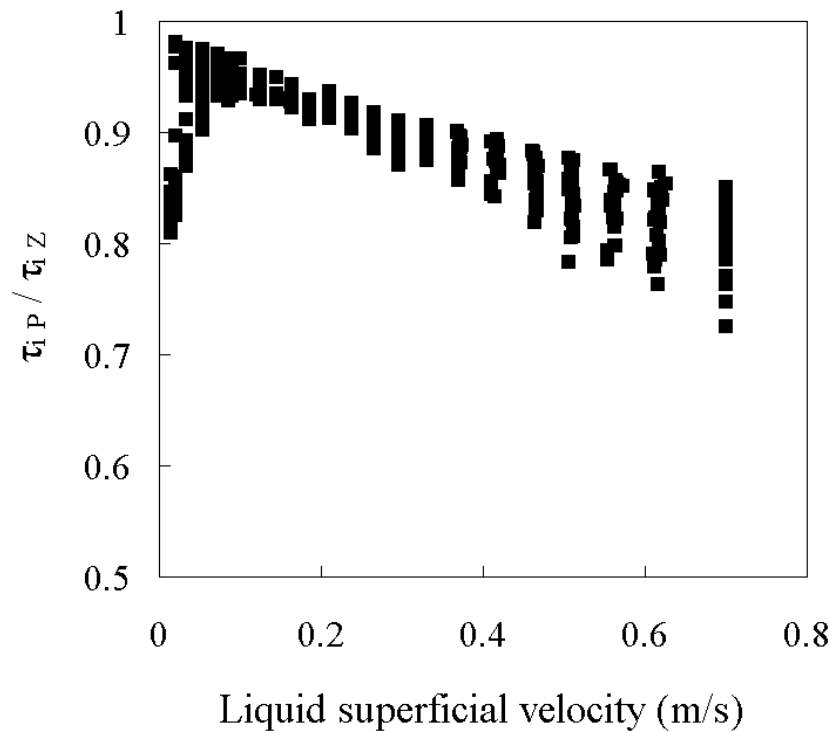


Figure 4.17 Comparison of interfacial shear stress equations

Re-computing Figure 4.14 above then shows the deviation of interfacial shear stress minima.

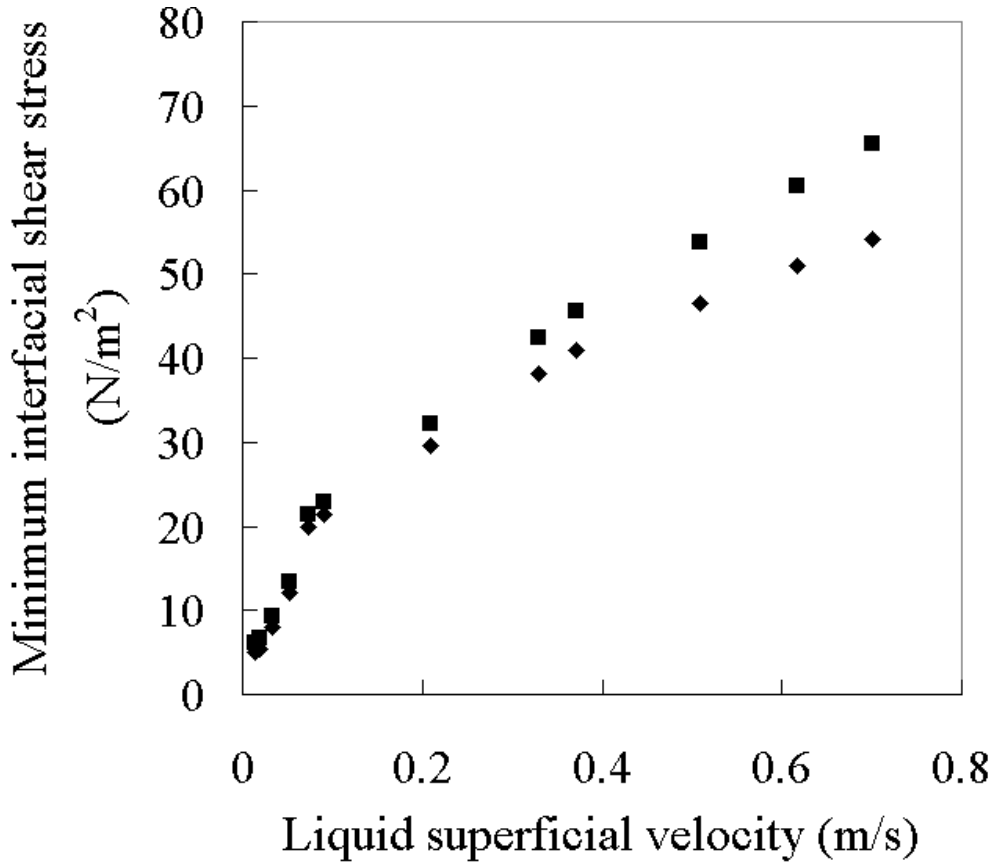


Figure 4.18 Comparison of interfacial shear stress minima (squares are data by Zabaras et al, diamonds are data from the present study)

Also the interfacial friction factor (Figure 4.19) was also examined by

$$\frac{f_i}{f_s} = \frac{2\tau_{iP}}{f_s \rho_g U_{gs}^2} \quad 4.13$$

Where f_s is the Blasius friction factor and compared with that of Wallis

(1969)

$$\frac{f_i}{f_s} = 0.005(1 + 300 \frac{\delta}{D_t}) \quad 4.14$$

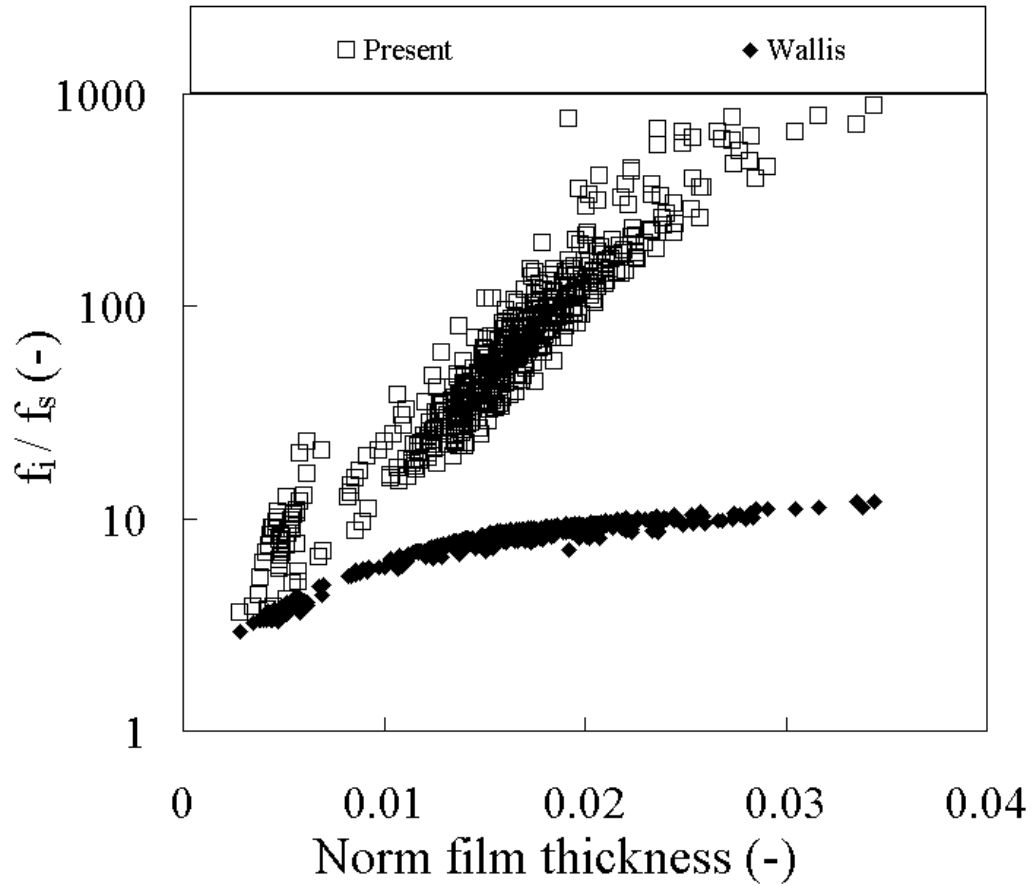


Figure 4.19 Comparison of interfacial friction factor equations

It can be observed that Eq. 4.14 predicts reasonably well at very thin liquid films. With increasing film thickness, the data shows a large deviation. Regression analysis of the present data was performed in order to predict the interfacial friction factor more accurately for these larger diameter pipes. By curve fitting, the following friction factor relationship is suggested

$$\frac{f_i}{f_s} = 2.6334\Gamma^{193.72} \left(\frac{\delta}{D_i} \right) \quad 4.15$$

Where Γ is equal to the mathematical constant e .

The wall shear stress as calculated from the conductance probes and WMS as function of superficial liquid velocity were also compared, this is illustrated in Figure 4.20 below. It is not surprising that the two devices deviate due to the difference in film thickness initially calculated. Details are provided above. Therefore the results from the conductance ring probes are considered.

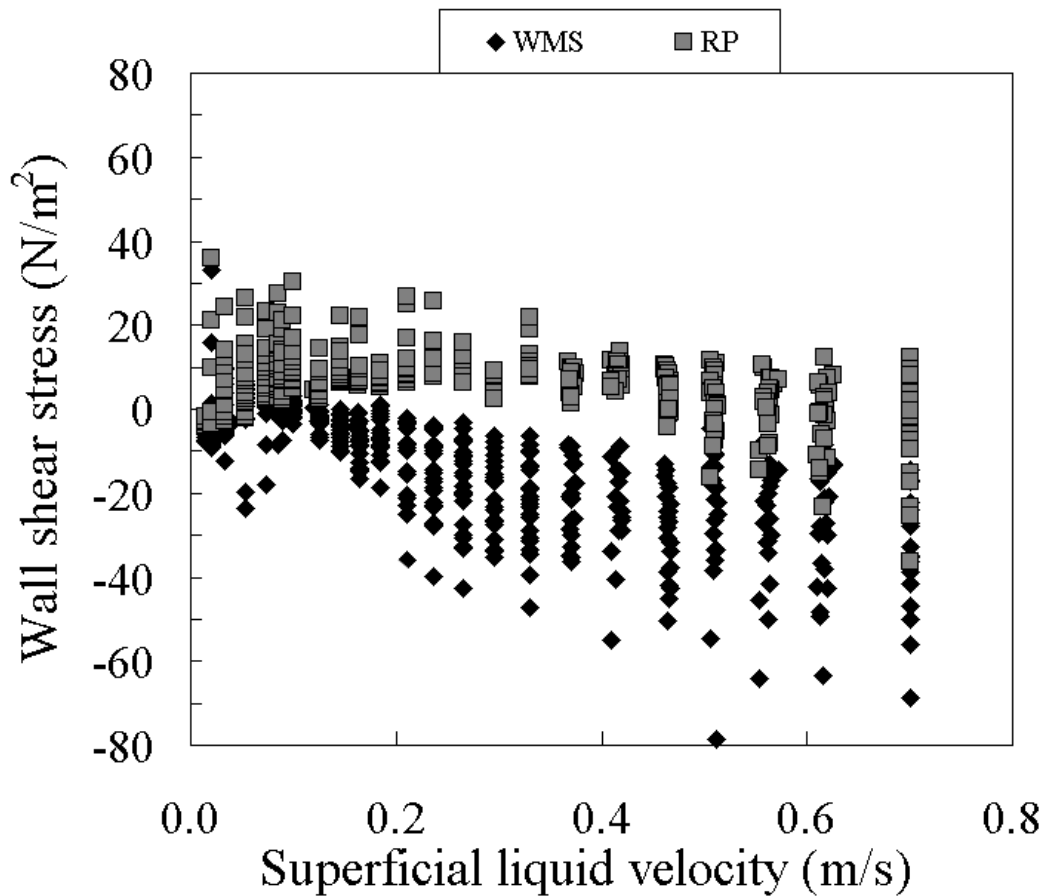


Figure 4.20 Comparison of calculated wall shear stress of ring probes and WMS

It can be observed that the ring probe wall shear stress first varies with gas flow rate at low liquid flow rates. Positive wall shear stress is for high gas velocities, negative wall shear stress is for low gas velocities. At around 0.4

m/s for the liquid this effect appears to be less, i.e., the data groups together disregarding the variation of gas flow rate. After this point, the data seems to show again a larger spread in terms of wall shear stress. This may indicate a point of switch for wave type and up flow and up flow with re circulation as identified by Zabaras *et al.* (1986). The interfacial and wall shear stress are also plotted. Figure 4.21 illustrates the results along with the some results from Zabaras *et al.* (1986)

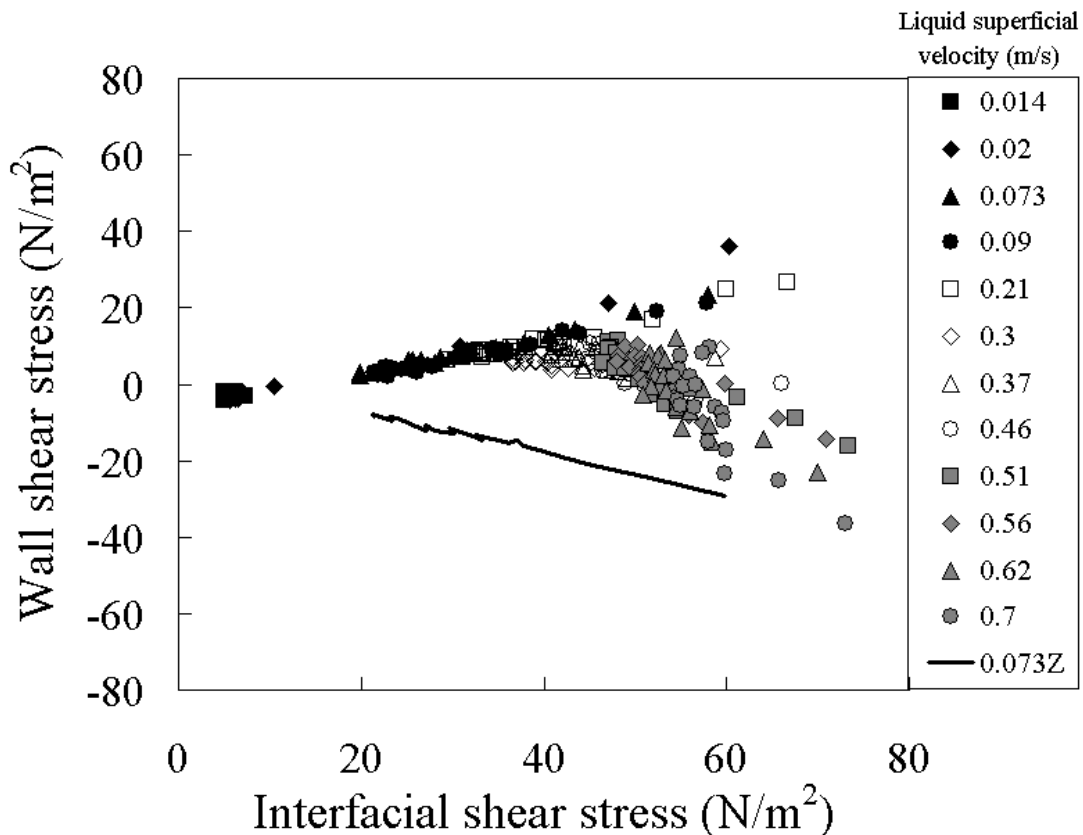


Figure 4.21 Ring probe comparison of calculated wall vs. interfacial shear stress for different superficial liquid velocities along with selected data from Zabaras *et al.* (1986)

It can be seen that the relationship between the two parameters shows profound trends but are different to the data calculated by the methods from Zabaras *et al.* (1986). For the lowest liquid flow rate (black squares), the data groups together and barely shows dependency. For the other lower liquid flow

rates (closed black symbols), the relationship is linear, i.e., with a decrease of gas flow rate, increase in interfacial shear stress, and the wall shear stress increases as well. For the intermediate liquid flow rates (open symbols), the wall shear stress remains semi-constant with an increase in interfacial shear stress. For higher liquid flow rates (closed grey symbols), the relationship shows the interfacial shear stress with a weak minimum around zero for wall shear stress as found by Zabarar *et al.* (1986). It should be noted however that the inlet geometry for the present study is not specially tailored in order to examine specific phenomena like Zabarar *et al.* (1986) with a sinter. This is also expected to be one of the important reasons of the differences observed in the present study.

Sawai *et al.* (2004) suggest a method in order to predict the average contribution of waves to the pressure drop. Their suggested method is based on division of the liquid hold-up, i.e, film thickness, into two categories: the base film and the wavy surface. They suggested the following relationship for the total average contribution of the liquid to the frictional pressure drop:

$$-\frac{dP}{dz} = \frac{4}{D_t} f_s \frac{\rho_l}{2} u_l^2 \quad 4.16$$

where D_t , f_s , ρ_l and u_l are the pipe diameter, Blasius friction factor, liquid density and liquid velocity respectively. They suggested a correction factor P_w to account for the contribution of the waves only.

$$F_{wL} = P_w \left(\frac{4}{D_t} f_{wave} \frac{\rho_l u_w^2}{2} \right) \quad 4.17$$

Where f_{wave} is the wave friction factor $f_{wave} = 0.0791 \left(\frac{D_t u_w}{\eta_l} \right)$ and u_w is the wave velocity as predicted through cross-correlation above. For

estimation of the liquid fraction contained in waves (P_w), they assumed that the base film probability is of Gaussian nature. Hence, if a given distribution tails off towards larger film thickness, the area outside the Gaussian base film distribution is assumed to be the fraction of film contained in waves. For the present study, a different approach is applied, quite similar to that of the de Jong and Gabriel (2003). By examination of the average liquid holdup time series, the average wave height was set at twice the standard deviation added to the time averaged liquid holdup. Likewise for the height of the base film, but subtracted from the time averaged liquid holdup. The ratio of difference and the maximum holdup obtained was assumed to be the liquid contained by waves. Figures 4.22 and 4.23 show the results.

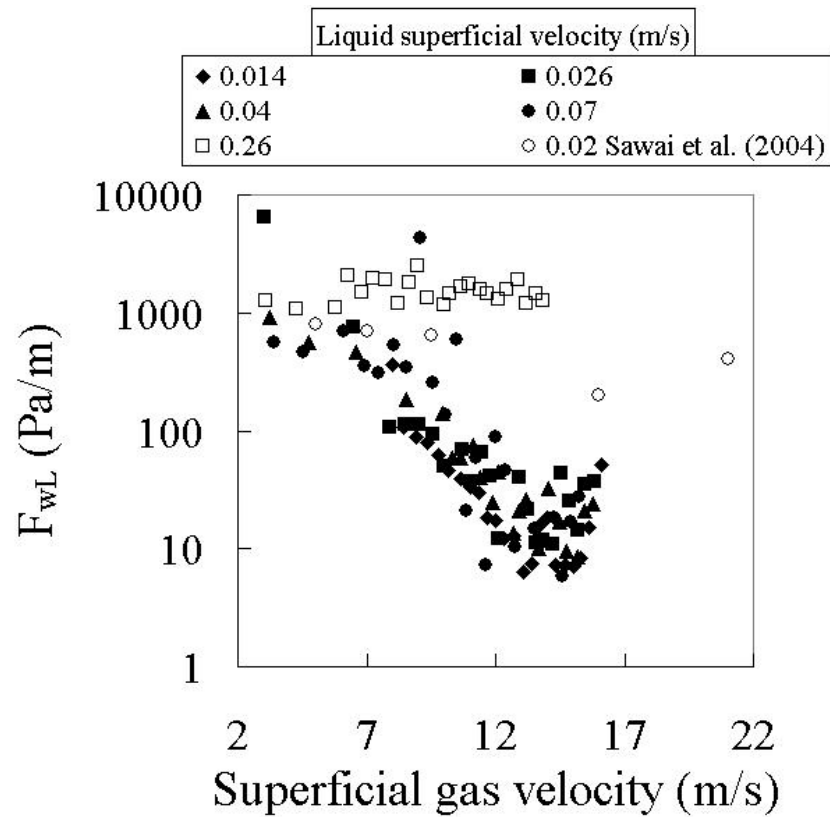


Figure 4.22 Calculated wave pressure drop vs superficial gas velocity.

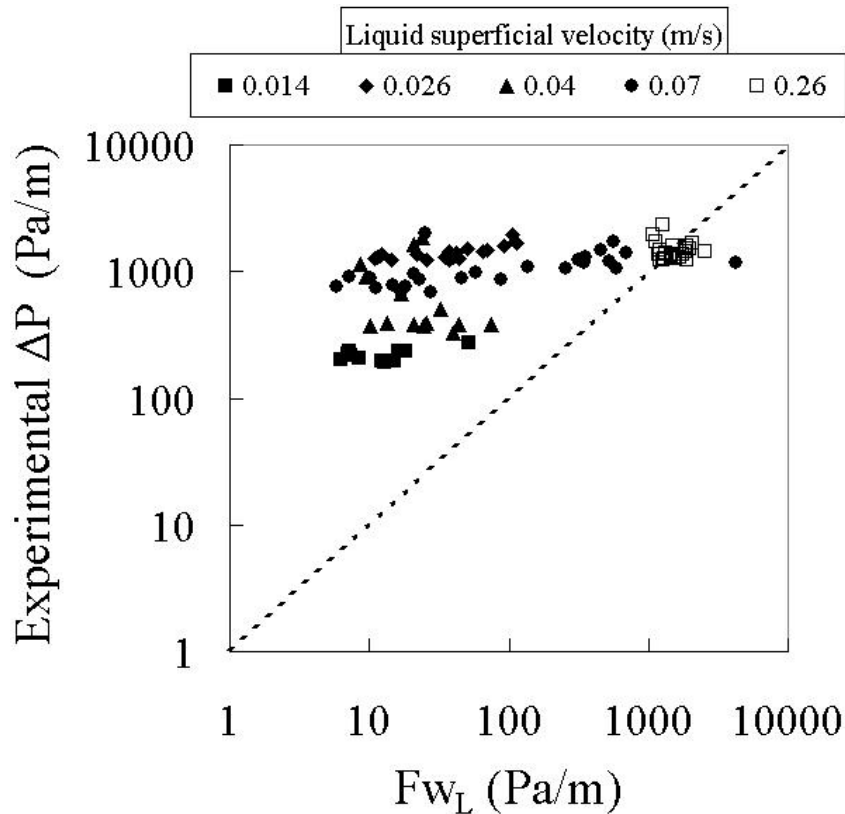


Figure 4.23 Calculated pressure drop vs. measured pressure drop.

Figure 4.22 presents a clearer view on the physical phenomena caused by the superimposed waves on the base film. The data tends to converge at low gas flow rates, hence high pressure drop. This is not surprising since at low gas velocities, larger roll type waves tend to form and perhaps owe a higher contribution to pressure drop. With increasing gas flow rate, a decrease in pressure drop can be observed. This trend is similar to the pressure drop as reported above in, e.g., Figure 4.8b. The difference however can be seen in the switch to positive slope from about a gas superficial gas velocity of 13 m/s in Figure 4.22. For high liquid flow rates this switch does not appear as such. Comparing the data with an example extracted from Sawai *et al.* (2004) shows that the switch for the present data occurs at a generally lower gas flow rate

and the magnitude of the pressure drop is lower as well. The former may be due to effect of gravity on the liquid. The latter is not surprising since pipe diameter plays an important role as denominator in pressure drop calculations. Figure 4.23 presents a comparison between calculated wave and measured pressure drop. Clearly the measured overall pressure drop is higher, but with decreasing gas flow rate, hence larger waves, the data shifts towards the 45 degree line, suggesting a better agreement. Figure 4.23 may therefore suggest, also since a high liquid superficial velocity of 0.26 m/s shows a reasonable fit, that Eq. 4.17 from Sawai *et al.* (2004) predicts the pressure drop in churn flow reasonably well, also for the present study.

In order to explore the aforementioned particular conditions in more detail, the results from the WMS were examined. Figure 4.24 (a), (b) illustrate the findings. The binary obtained data was converted using the accompanied software and the spatial and temporal data plotted.

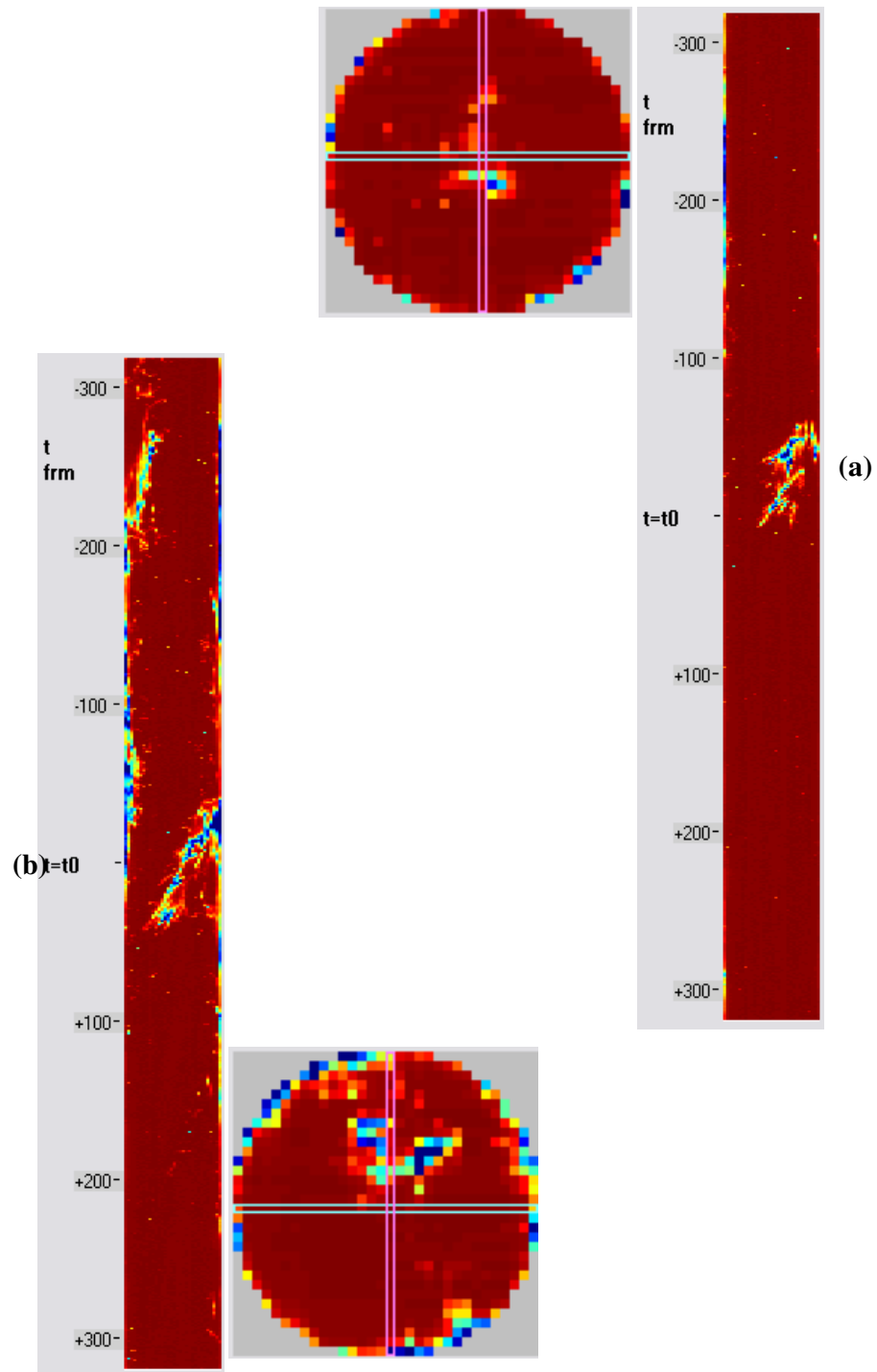


Figure 4.24 Wire mesh spatial results. Superficial gas velocity 10 m/s and liquid superficial velocity 0.04 m/s (a) and superficial gas velocity 7.85 and liquid superficial velocity 0.04 m/s (b)
Red is gas, blue is liquid

Both results for the cross sectional as well as the axial phase distribution in time, in milliseconds, are displayed. The axial distribution is displayed as sliced in half. Red indicates gas and blue liquid. A large liquid structure in the gas core can be observed for (a) and a larger structure for (b). In addition, for (b), huge waves as reported by Sekoguchi and Mori (1997) can be observed. The huge waves give rise to the probability that large quantities of liquid are being torn from the waves and entrain the gas core. At higher gas velocities, no such large structures were observed, indicating a drastic and sudden change in flow phenomena around this particular liquid flow rate. It is not an unreasonable assumption that this condition also corresponds to the flooding point reported by Zabaras *et al.* (1986) and Govan *et al.* (1990) for the present experiments. This also correlates positively with the high speed photography analysis for the current experiments and the change in pattern observed for a gas superficial velocity from 10 m/s and a liquid superficial velocity of around 0.04-0.07 m/s. This is at much lower gas flow rates than reported in smaller diameter pipes.

In order to put the above information into context systematically, the data (including high speed photographs) were re-examined to identify a probable churn to annular flow pattern transition boundary for the present experiments. Figure 4.25 illustrates this flow pattern map. Data from Sekoguchi and Mori (1997) was modified to compensate for the difference in gas and liquid flow rate, gas density and pipe diameter to obtain an estimate of the huge/disturbance wave transition for the present conditions. In addition, the conditions at which liquid structures in the gas core were observed are plotted.

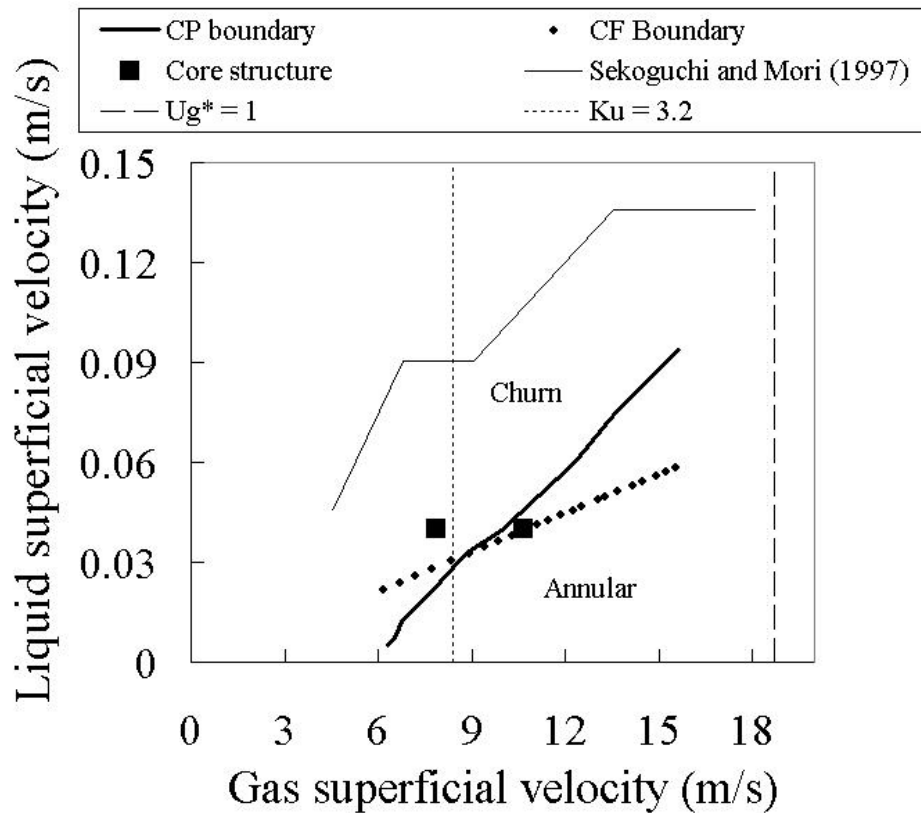


Figure 4.25 Flow pattern map for the churn-annular transition in a 127 mm pipe. CP boundary is obtained from conductance probes, CF boundary is estimated from cine film.

From the flow pattern map a difference between conductance probes and high speed photography data can be observed. The difference is most probably due to the fact that the high speed photography data is based on visual observations for a smaller range of flow rates and extended by linear extrapolation. The new proposed boundary from the conductance probe data is based on the features observed in the detailed analysis described above. The transition from churn to annular flow in the present study starts at gas superficial velocities of 10 m/s i.e, the end of a negative slope representing the churn flow regime. The flow goes through a minimum for both film thickness

and pressure drop up to 15 m/s. From structure velocity and the interfacial shear stress results, possible changes in interfacial wave types occur around a gas superficial velocity of 13 m/s. It then adopts a positive slope, i.e., annular flow.

The compensated data from Sekoguchi and Mori (1997) shows a deviation from the new proposed boundary. It is obtained through the assumption of equality of Weber number, similar to Hewitt and Roberts (1969), and obtained by $U_{sm}^2 0.026 = U^2 0.127$, for both liquid and gas superficial velocity. Where U_{sm} represents the velocities from Sekoguchi and Mori (1997) and U the velocities from the present data. The deviation between the present boundary and Sekoguchi and Mori (1997) may be explained by the ratio between the different pipe diameters of 0.3 and the system pressure, hence gas density, in the two data sets. The data does however show a similar trend. The annular flow models by Taitel (1980) and Barnea and Taitel (1985) do show a good agreement for the gas, but not for the liquid dependencies. The Wallis (1969) parameter, $ug^* = 1$ yields a vertical line on Fig 4.25 at a constant gas superficial velocity of 18.7 m/s for the transition from churn to annular. This does not agree with the observed transition. Although closer, the same applies to the widely used criterion of the Kutateladze number = 3.2, which yields a gas superficial velocity of 8.4 m/s for the present data.

As reported in Chapter 2, Zapke and Kröger (2000) successfully converged flooding data obtained by different experimental setups from Clift *et al.* (1966) and Chung *et al.* (1980) by using dimensionless gas and liquid Froude numbers and a liquid Ohnesorge number. They found that the gas Froude number is some function of the liquid Froude and Ohnesorge number.

Differences between the data sets were based on different viscosity and surface tension as outlined in their paper. Pipe diameter was the same in the two experimental setups. They based their dimensional analysis on the following equations:

$$Fr_G = \frac{\rho_g U_{gs}^2}{g D_t (\rho_l - \rho_g)} \quad 4.18$$

The gas Froude number

$$Fr_L = \left(\frac{\rho_l U_{ls}^2}{g D_t (\rho_l - \rho_g)} \right)^{0.2} \quad 4.19$$

The liquid Froude Number

$$Oh_L = \left(\sqrt{\frac{\eta_l^2}{\rho_l D_t \sigma}} \right)^{0.3} \quad 4.20$$

The Ohnesorge number.

By multiplying the two terms for liquid, i.e, the liquid Froude and Ohnesorge number they created a dimensionless group as a function of the gas Froude number. A similar approach was applied to the churn/annular transition data of the present study. However, since different pipe diameters were used for comparison, accounting for the pipe diameter can only be achieved by division. Reasonably good convergence of the present and Sekoguchi and Mori (1997) data was obtained and in addition, data from other workers also came closer together as presented in Figure 4.26.

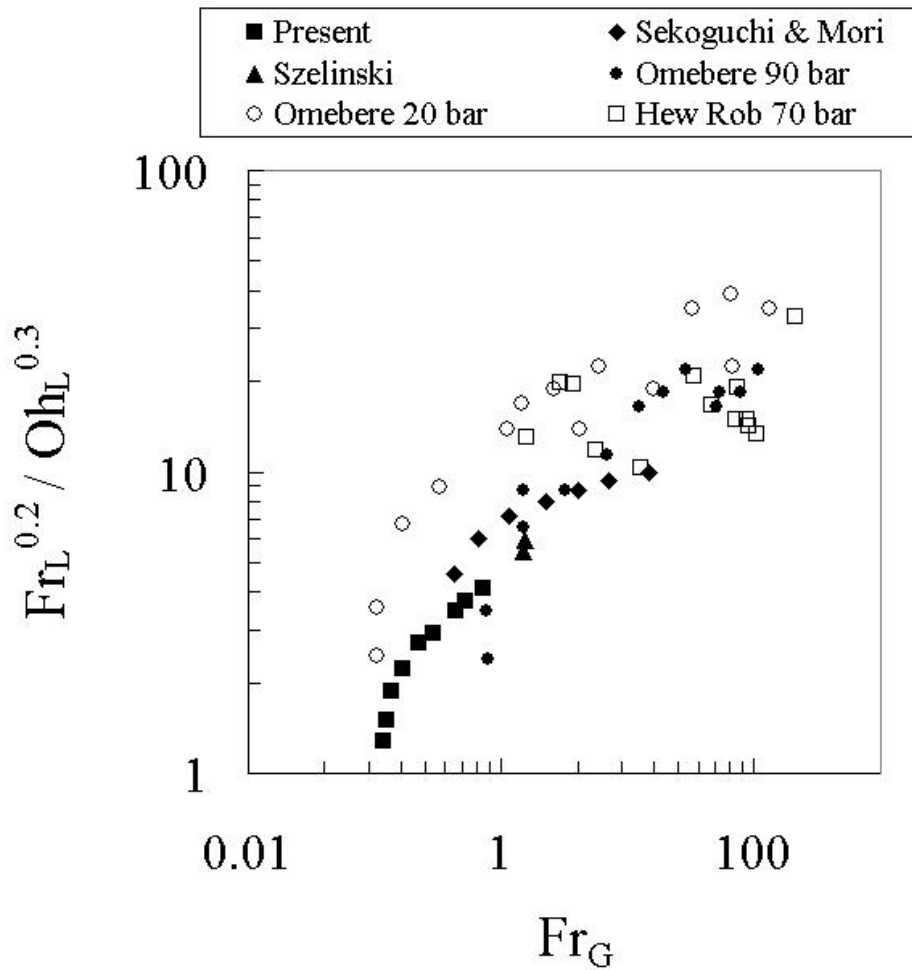


Figure 4.26 Dimensional analysis of churn/annular transition data.

Since the data shows close similarity, a combined curve fit was applied to the present and Sekoguchi and Mori (1997) data. A new relationship was then derived and the model tested against other churn to annular transition data for a large range of liquid superficial velocities. In unrefined form, the relationship obtained can be expressed as

$$\frac{Fr_L^{0.2}}{Oh_L^{0.3}} = 1.47 \ln(Fr_G) + 4.7 \quad 4.21$$

Substituting the properties and the gas superficial velocities from the various sets of data then allows prediction of the churn to annular boundaries, the results are shown in Figure 4.27

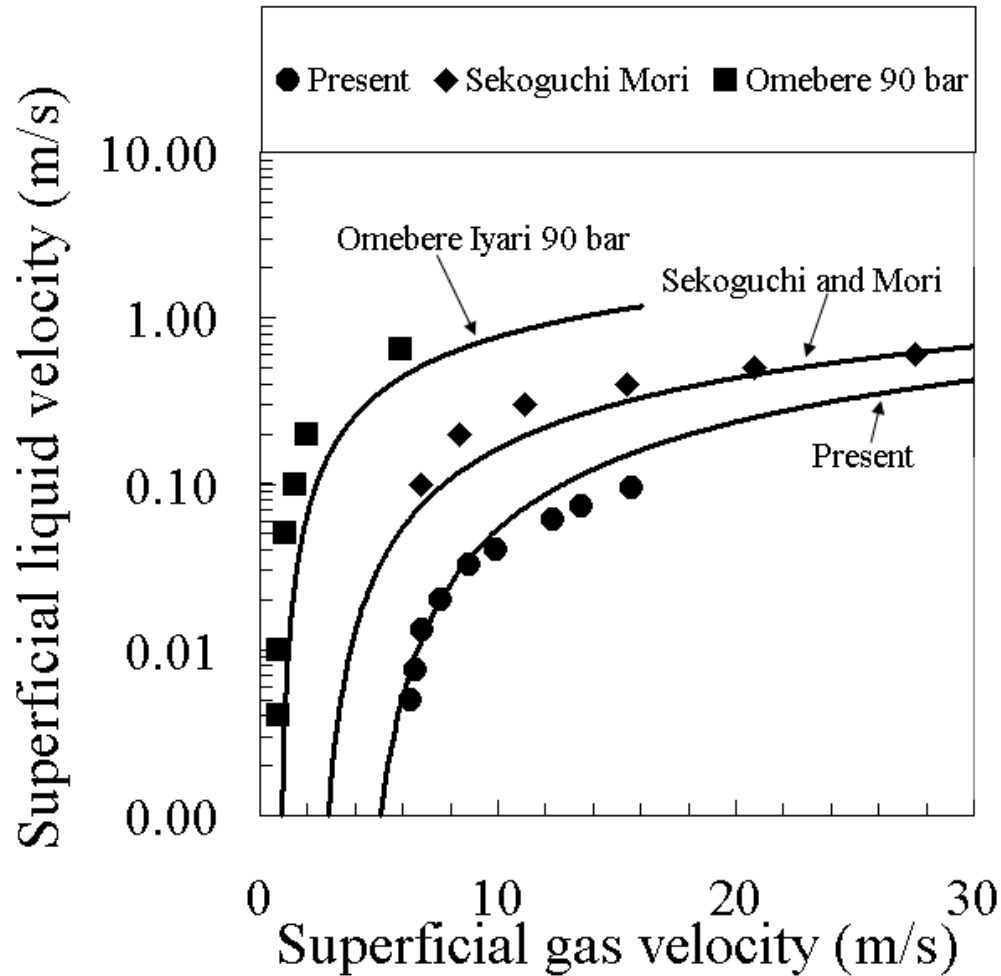


Figure 4.27 Performance of Eq. 4.21 (solid lines) versus experimental churn to annular transition data from different authors (symbols).

It can be seen that the relationship shows a good agreement for most of the experimental data. Although most empirical correlations are tested against data they were derived from it predicts the transition curve from Omebere Iyari (2006) for naphta/nitrogen in the 189 mm SINTEF-riser reasonably within 36 percent error. The data from the present study and

Sekoguchi and Mori (1997) (air/water in a 26 mm pipe at 2 bara) data is predicted within 12 and 16 percent error respectively. In first instance, the model shows however less good agreement with data from Hewitt and Roberts (1969) (steam/water in a 12.7 mm pipe at 70 bar), Omebere-Iyari (2006) (naphta/nitrogen in a 189 mm pipe at 20 bar) and Szalinski *et al.* (2010) (silicon oil/air in a 67 mm pipe at ambient conditions). Evaluation of the variables shows that the correlation depends strongly on gas density, i.e., system pressure. Figure 4.28 illustrates this by two curves on the graph; one for original Omebere-Iyari (2006) data, and one for the present study with an adjusted gas density to that from Omebere-Iyari (2006).

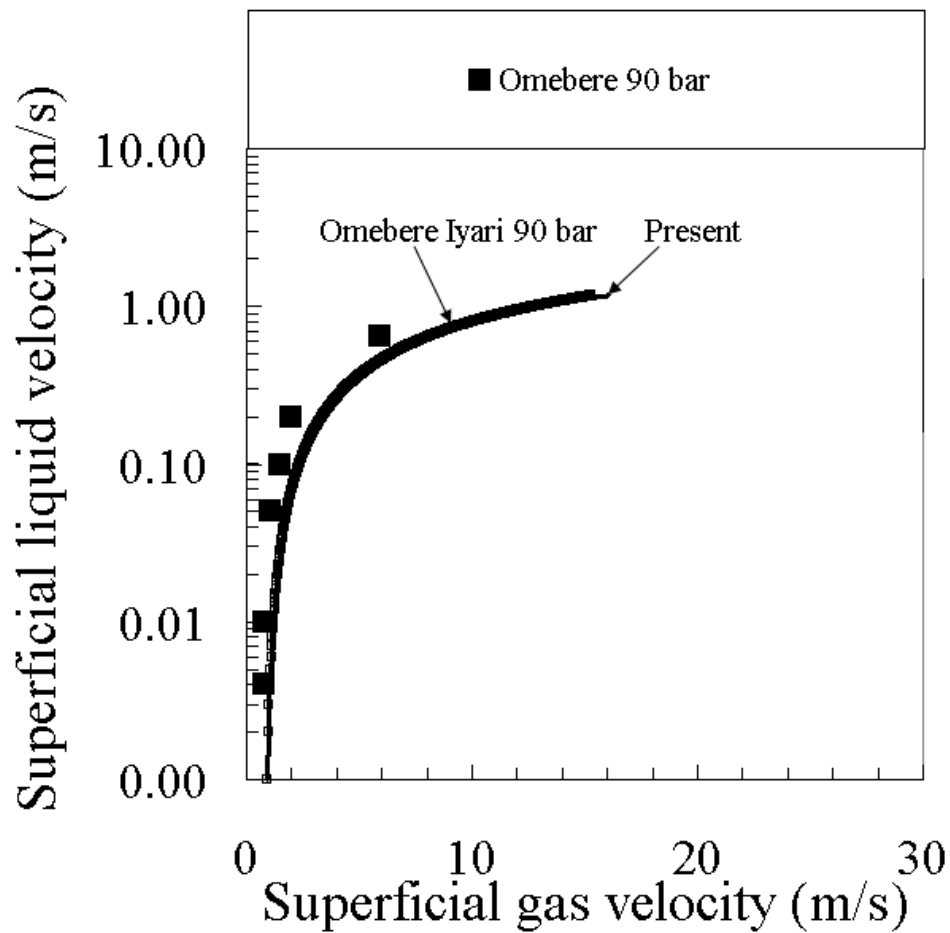


Figure 4.28 Effect of gas density.

Taking the curve for the data from present study from Figure 4.27 and increasing the gas density with a factor 28 to match the gas density of the Omebere Iyari (2006) 90 bar experiments shows that the curves match very well. Thus suggesting that pipe diameter, liquid density, viscosity and surface tension differences are not significant. This is also the case when using the Sekoguchi and Mori (1997) data with adjusted gas density. By using the data from Szalenski *et al.* (2010) and increasing their gas density with a factor 3 to match the present properties shows a that the correlation curve tends to converge at the conditions where few data points are available as shown in Figure 4.29.

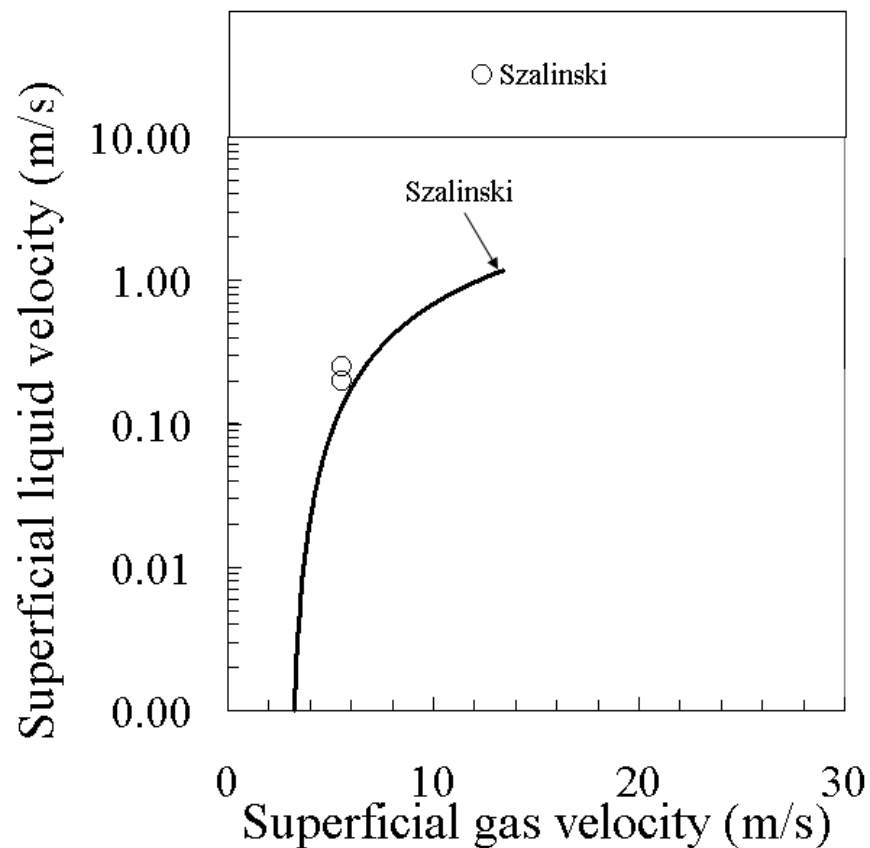


Figure 4.29 Effect of gas density on data from Szalenski *et al.* (2010)

The model therefore suggests that the accuracy of the churn to annular flow boundary prediction is reasonable rather independent of pipe diameter, liquid density, viscosity and surface tension. Gas density plays the most important role and the lower threshold for application should be 3.6 kg/m^3 . For the case of Szalinski *et al.* (2010), the boundary does show a good agreement but only when the gas density is increased to the lower threshold set by the present study. The deviation of the model with regard to the data from Hewitt and Roberts (1969) may be due to that what has been pointed out in Chapter 2, i.e., they annular flow area is not entirely described by experimental data per se.

By summarising the results in this Chapter it may be concluded that the liquid film and pressure drop show that a possible transition from churn to annular flow takes place around a gas superficial velocity of 10 m/s in a 127 mm diameter pipe.

From film thickness, structure velocity and the associated correlograms there is evidence that at a gas superficial velocity of 13 m/s a change takes place between (part of) the liquid film flowing countercurrent to co-current; the sudden “jump”.

At high liquid superficial velocities this phenomenon is not observed due to possible huge waves, hence churn flow.

The latter is confirmed by computations of the interfacial shear stress calculated in relation with the pressure drop. This shows a minimum as a function of the film thickness and this is associated with “up flow” and “up flow re-circulation”, the latter is when the film re-circulates, i.e., simultaneous up and downward motion.

Relating the interfacial shear stress with liquid superficial velocity shows a change in slope, suggesting a switch between the main source of interfacial shear stress, i.e., different wave types in annular and churn flow.

Calculation of the fraction of pressure drop due to waves also shows a switch at a gas superficial velocity of ~13 m/s. At higher liquid velocities this switch is fully suppressed by possibly huge type waves, typically associated with churn flow, similar to the trends of the structure velocity.

A new interfacial friction factor relationship is suggested for the present data.

From the work presented above it is suggested that the one-dimensional smooth interface models commonly employed to describe these flows are inadequate. A second dimension must be considered so that the effect of the simultaneous upwards and down wards motion of waves on the interface can be taken into account

The computations of the results and comparison of previous results obtained in smaller diameter pipes, shows similar trends, but different values in terms of the proposed churn annular transition boundaries.

Dimensional analysis by relating the gas Froude number with the ratio between the liquid Froude and Ohnesorge numbers, brings data originating from different pipe diameters and with different physical properties closer together.

Correlation of the relationship between these dimensionless numbers based on the present and Sekoguchi and Mori (1997) data shows a reasonable agreement with the present and other churn to annular flow regime boundaries originating from different pipe diameters, physical conditions and properties.

Although the relationship seems to produce promising results, it should be noted that there is still room for future improvements.

5 The Creation, Behaviour and Sizes of Drops

This Chapter describes the results obtained in the 127 mm pipe on drop creation, size/velocity and the effect of gas and liquid flow rates on these parameters. The first section presents the background of the experiments. The second section covers the experimental outline. The third shows the results from pre-PDA experiments obtained by high speed photography on the creation of drops and disturbance waves. The fourth section focuses on the results obtained by simultaneous film thickness and (PDA) drop size measurements. The fore last section presents post PDA experiments with high speed photography. This is followed by the conclusion.

5.1 Background on drops in gas-liquid flows

Drops play an important role in annular flow since they contribute to various hydrodynamic parameters. In boiling, cooling and other applications where a liquid film on the pipe periphery is preferred, annular flow can cause difficulties when the film thickness reaches a state where full evaporation of the film occurs. This phenomena is referred to as “dry-out” and results in poor heat exchange characteristics and possible failure of equipment. Also erosion is associated with drops and particles. Fore and Dukler (1995) found that drop acceleration can have quite a significant contribution to the total pressure drop, up to about 20 percent. Azzopardi (1997) noted that rough films at the pipe wall, which occur in annular and churn flow, promote drop entrainment. More specifically, drops entrain from disturbance waves as discussed in the previous Chapter. The crests of disturbance waves are subject to shear from the gas phase flowing over it. Parts of the crests are then torn off to form drops which are then

dispersed in the gas core. Two major types of break up have been reported, namely ligament and bag break up as illustrated by Figure 5.1 (a) and (b)

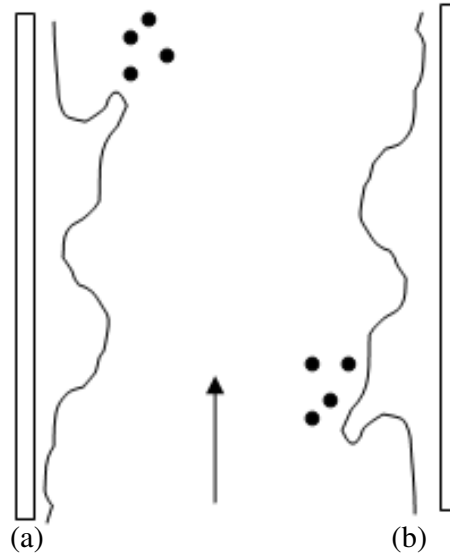


Figure 5.1 Simplified break up mechanisms in vertical annular flow. Ligament break up (a) and bag break up (b)

Ligament break up occurs when the crest of the wave breaks in the direction of the gas flow. Part of a wave crest is stretched to form a ligament, a filament of liquid. This then breaks into drops. Bag break up occurs when the gas undercuts the wave crest. Gravity helps this take the shape of a bag with a thin body and a thicker rim. It resembles a blown bubble gum. The body bursts first to produce fine drops. The rim then breaks down to form coarser drops. Krezysowski (1980) showed that large drops introduced into gas flows break up by similar mechanisms. He identified that which of these mechanisms occurs depends on the values of a Weber number that employs the original drop diameter as its length scale. Azzopardi (1997), seeing the analogy to this drop break up, suggested that the boundary between bag and ligament break up in annular flow can be described by a Weber number

$$We = \frac{\rho U_{gs}^2 h_w}{\sigma} \quad 5.1$$

U_{gs} is the gas superficial velocity, h_w is the wave height, ρ is the gas density and σ is the surface tension.

The rates of entrainment and deposition can be determined by a technique proposed by Leman *et al.* (1980). By injecting a tracer into the liquid film they found that the concentration of tracer in the film decreased with axial distance relative to the initial value because of entrainment and secondly, decreased more due to drops which contained no tracer. They found that both the rate of entrainment and deposition increased sharply with axial distance to a maximum and hereafter it decreases gradually to a semi-constant value. Azzopardi (1983) employed an experimental entrained fraction measurement technique first proposed by Cousins and Hewitt (1968) and further developed by Whalley *et al.* (1974). By extracting the liquid film from the pipe wall through a porous wall section, and measuring the fraction of liquid and gas taken off, a mass balance between inlet and measurement section can be made.

The size of drops have been measured using a number of techniques, e.g. high speed photography, direct contact probes, Laser Diffraction and Phase Doppler Anemometry (PDA) techniques. The latter two became increasingly popular over the last two decades due to continuous improvements on the accuracy and ease of operation of the instruments. PDA and high speed photography has been employed in the present study. Azzopardi (1997) states that, in general, laser light techniques are perhaps most suitable for annular gas-liquid flows.

5.2 Experimental outline

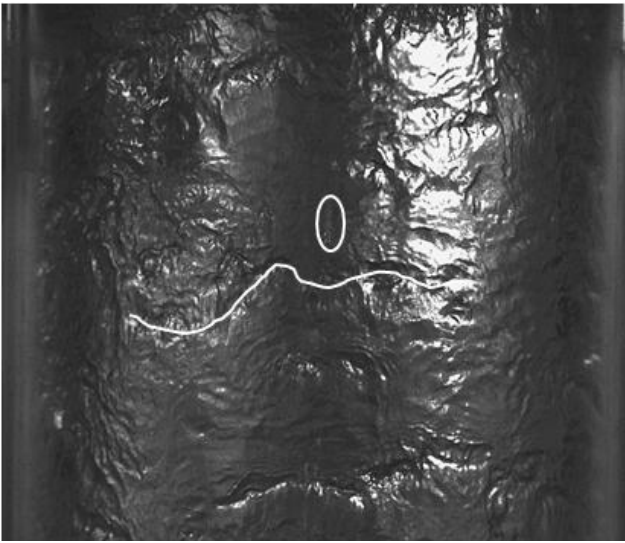
A set of 80 experiments were carried out in which drop size/velocity and void fraction/film thickness experiments were measured simultaneously on the 127 mm flow loop at atmospheric pressure. The experimental matrix is shown in Table A2 in the appendices of this thesis. The experiments for the PDA were taken for durations of 10 seconds or 10^4 data points. The conductance probes were set at a sampling rate of 1 kHz. The experiments were carried out at atmospheric pressure since the viewing section for the PDA was equipped with relatively thin windows. Therefore it was not considered sensible to pressurise the facility.

5.3 Scoping experiments

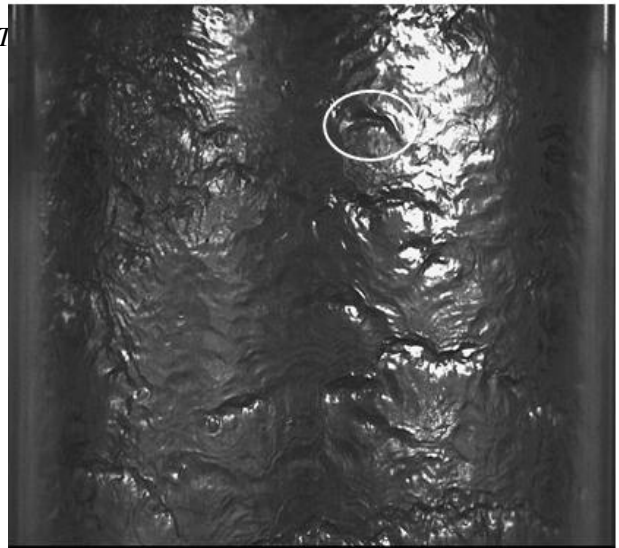
High speed photography experiments were carried out for annular flow with liquid superficial velocities of 0.014 and 0.04 m/s and gas superficial velocities of approximately 13 and 16 m/s. The camera was set up just upstream of the test section containing the conductance probes. A square –box shaped-viewing section filled with water mounted around the transparent section of the pipe was used to minimise refraction.

High speed videos are analysed frame by frame. This is most productive at higher gas velocity than at lower ones. For the former films are thinner and less wavy. For the latter the thick films on the wall diminish visibility in to the pipe core. Drops, mainly near the film interface were tracked. From the position time data their size and velocity were calculated. In addition the wave behaviour, its direction and velocity, was determined. The impact of drops onto the film and the consequent creation of disturbance waves were also studied.

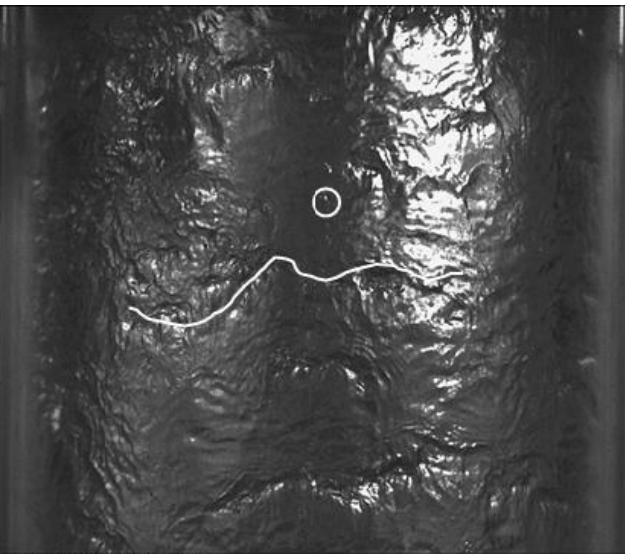
Figure 5.2 show a sequence of photographs taken at a liquid superficial velocity 0.014 and gas superficial velocity 16 m/s. From the results presented in Chapter 4, this is considered to be annular flow. White lines and circles are used to mark disturbance waves to mark drops or impaction.



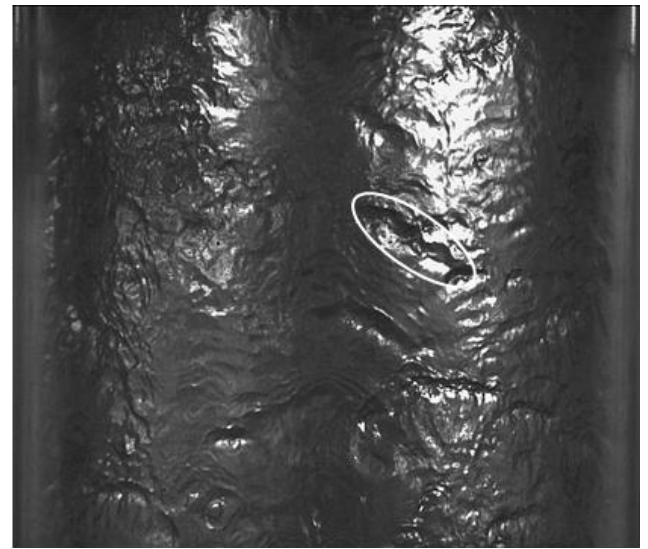
(a)



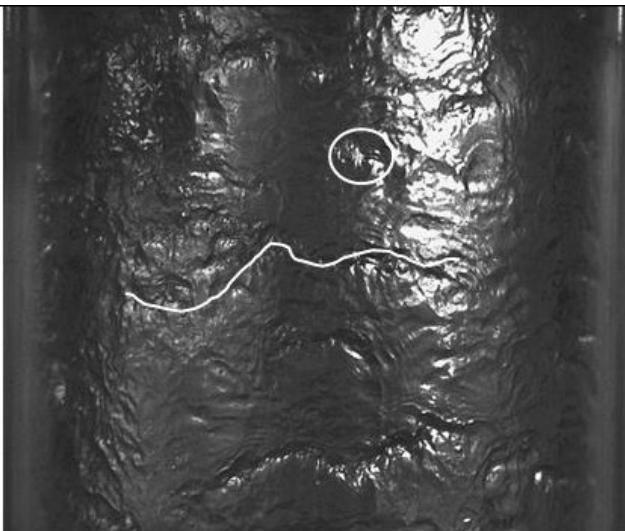
(d)



(b)



(e)



(c)

Figure 5.2 Gas superficial velocity 16 m/s,
Liquid superficial velocity 0.014 m/s

- (a) $t = 0$ ms, a disturbance wave and entrained string of drops
- (b) $t = 2$ ms, entrained string of drops coalescence and forming one drop
- (c) $t = 4$ ms, drop impaction and indentation in liquid film.
- (d) $t = 29$ ms, Disturbance wave creation.
- (e) $t = 40$ ms, Disturbance wave developed

From the sequence of photographs it can be observed that the impact of a drop of significant size (about 800 μm) can act as an inception of a new disturbance wave. In the sequence mentioned above, both a drop near the wall and nearer the pipe centre were followed. The velocities of the two drops and the disturbance wave plotted as a function of axial distance travelled. The results are illustrated in Figure 5.3.

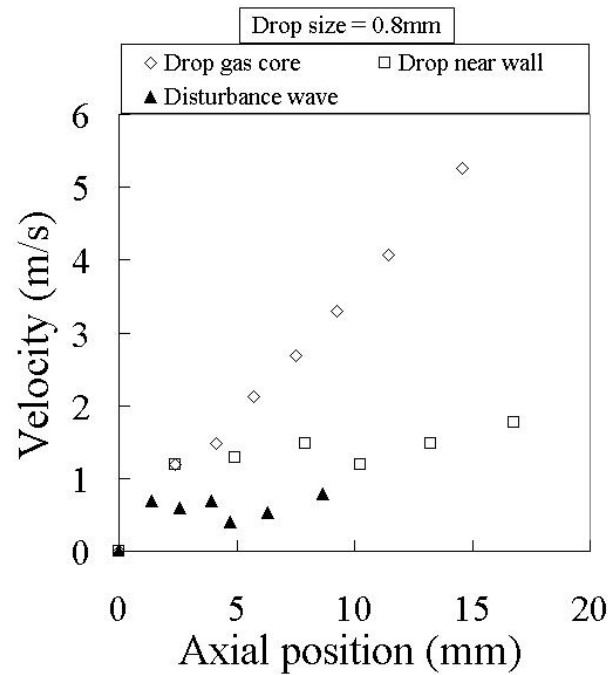


Figure 5.3 The velocity of a drop near the wall, a drop in the gas core and a disturbance wave.

The drops have contrasting trends in velocity. The drop near the interface is subject to gas of a lower velocity (because of the radial velocity profile of the gas). Therefore it accelerates less than the drop deeper in to the gas core. Therefore the velocity can adopt an almost constant value. A plausible explanation for the difference in behaviour between these two drops is that they were ejected at different angles in combination with a gas velocity profile. This will be developed further when discussing the work on drop simulations

(Chapter 6). The velocity of the disturbance wave shows a value similar to those obtained from the correlation of the ring probe signal which were reported and discussed in Chapter 4 of this thesis.

Another set of stills is given in Figure 5.4. Here the gas superficial velocity was 13 m/s and the liquid superficial velocity was 0.014 m/s

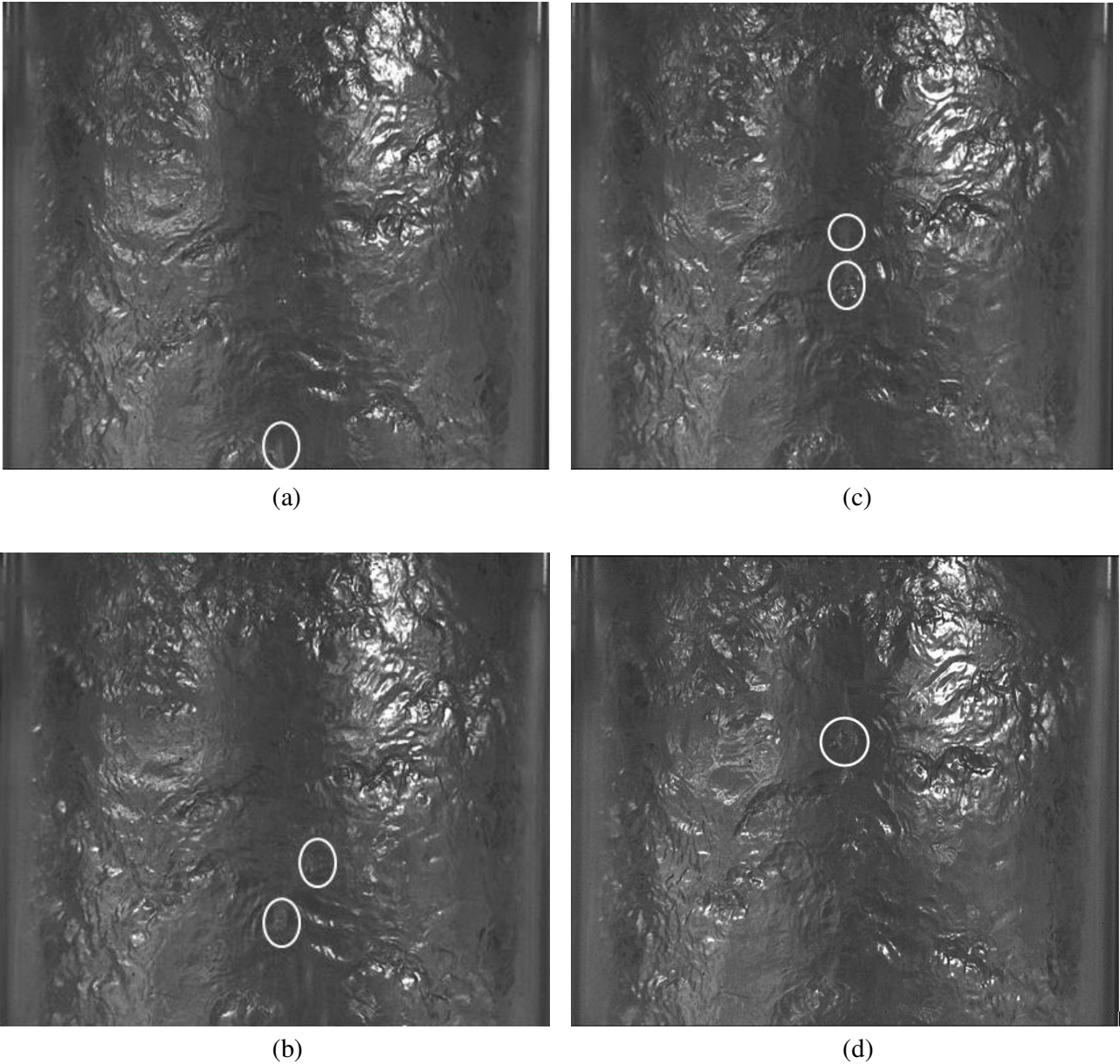


Figure 5.4 Gas superficial velocity 13 m/s, liquid superficial velocity 0.014 m/s

- (a) $t = 0$ ms, Sting of drops near wall
- (b) $t = 3$ ms, Impaction onto liquid and structure breakup.
- (c) $t = 7$ ms, Bouncing off, second impaction and spray formation
- (d) $t = 10$ ms, Bouncing off and third impaction

In contrast to the results from a gas superficial velocity of 16 m/s it is evident that the large entrained drop featured is very unstable. It can be seen to break up. Only a part of the drop continues to travel upwards, the rest of the drop bounces several times before it is deposited back onto the film. The total time for the process to complete does not exceed one hundredth of a second. The velocities of the objects observed in this sequence of stills are shown in Figure 5.5.

As can be observed the events show reasonable constant velocities. This is different to what is reported in the previous sequence of photographs since the gas flow rate is lower and break up and bouncing of the drop contributes to lower drop velocities. It can be seen however that, from the increase in acceleration, the fraction of the drop that continues to travel upwards is being picked up by the gas phase at a later stage. Also here, the disturbance wave velocity shows similar velocities to what is reported in Chapter 4.

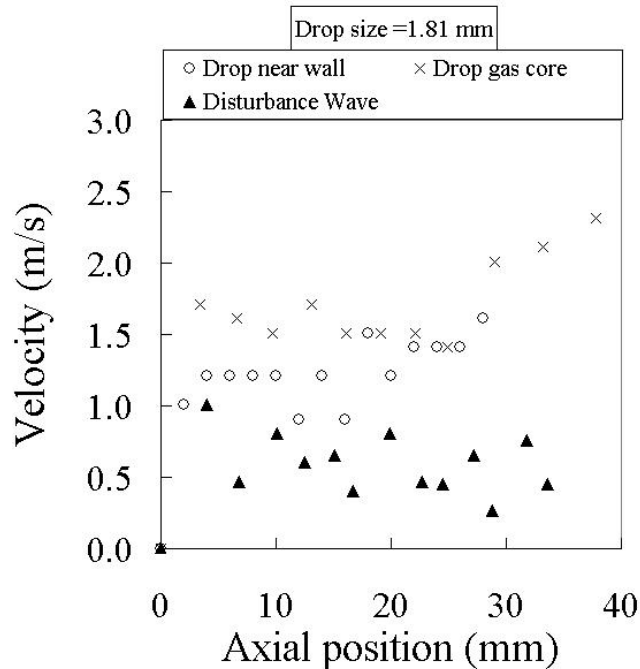


Figure 5.5 The velocity of a drop breaking up near the wall, a drop reaching the gas core and a disturbance wave.

A third photograph is reported. The case presented in Figure 5.6 is also annular flow but at a higher liquid rate. One drop followed travelled near the interface whereas another drop was observed further into the gas core. At a gas superficial velocity of 16 m/s and a liquid superficial velocity of 0.04 m/s, the drops followed here showed no other features rather than moving upwards.

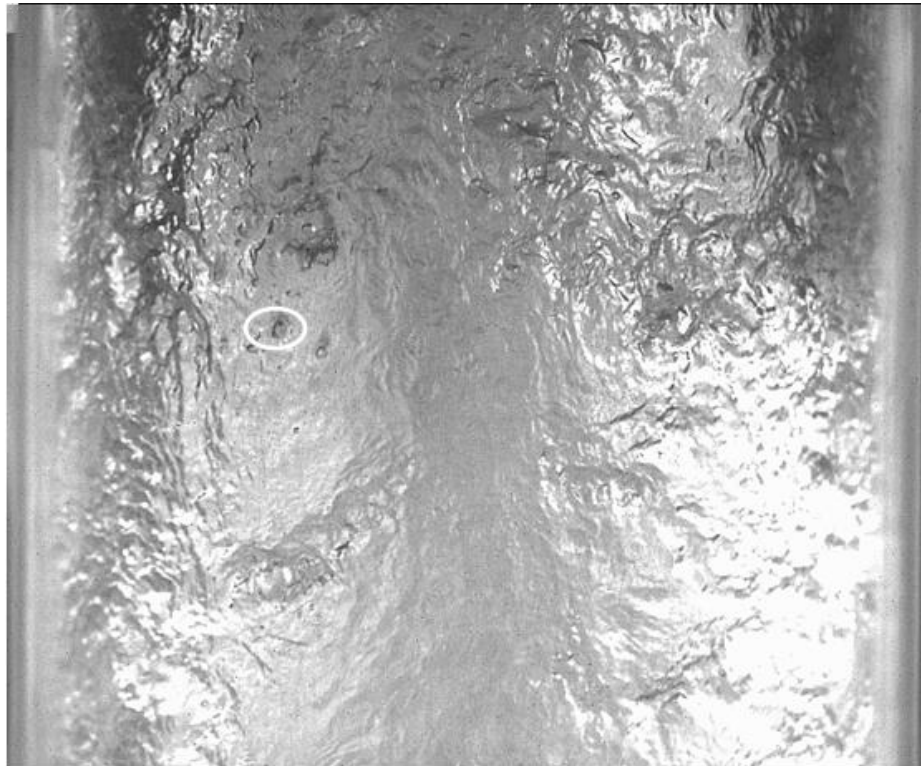


Figure 5.6 $t = 0$ ms, drop travelling upwards near the wall. Liquid superficial velocity 0.04, gas superficial velocity 16 m/s.

This condition has a gas superficial velocity of ~ 3 m/s greater than that for the transition condition point, reported in Chapter 4. In addition to the drops, also small gas bubbles entrained into the liquid film were observed. These bubbles were employed as flow followers for the base film, i.e., the fraction of the film below the wave troughs. It is appreciated that they will not necessarily be good film flow followers. The results are presented in Figure 5.7.

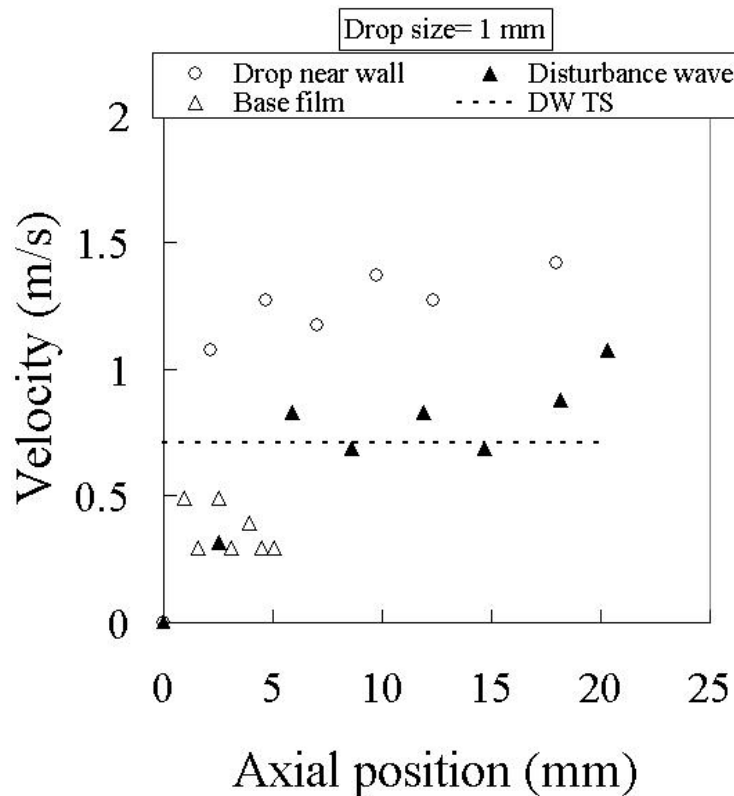


Figure 5.7 The velocity of a drop breaking up near the wall, a drop reaching the gas core, a disturbance wave, bubble in the film and the average disturbance wave velocity obtained from the conductance probes (dashed line).

It can be observed that the drop does not accelerate as fast than that observed in Figure 5.3, this is perhaps size related. As expected the base film is slower than the disturbance waves. The values of the disturbance wave velocity obtained here agree well with that calculated from the cross-correlation of the time series of the conductance probes.

From the photographs analysed there was evidence that the creation of disturbance waves does not only occur due to the interaction between the liquid and gas phase but also when a drop impacts on the liquid film. From Figure 5.2 it can be seen that the drop causes an indentation in the film, resulting in a new rough surface on the liquid film. Possibly this rough surface is susceptible to the gas shear and so a new wave is created. Figure 5.8 presents a proposed cycle of drop and wave creation. One might ask; which came first, the drop or the wave?

Most probably, since the flow is continuously developing, the waves are present due to the interaction of the phases at the riser entrance.

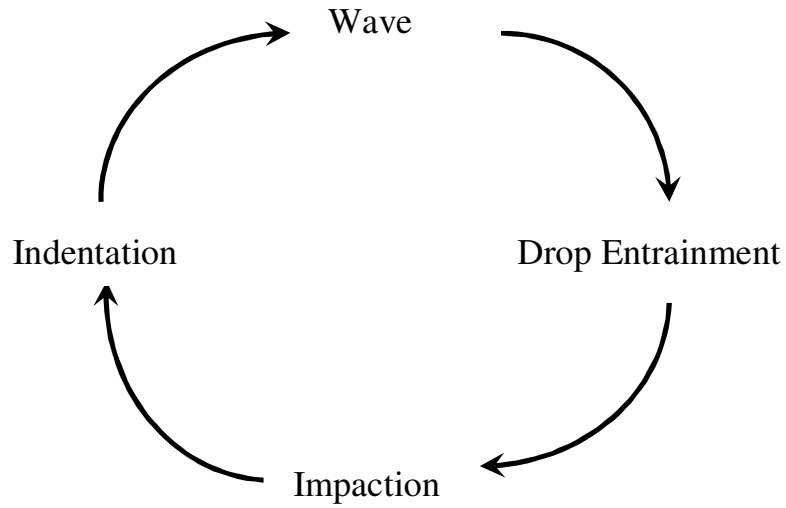
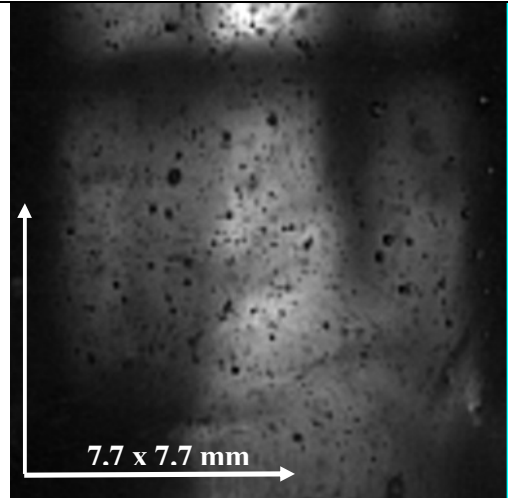
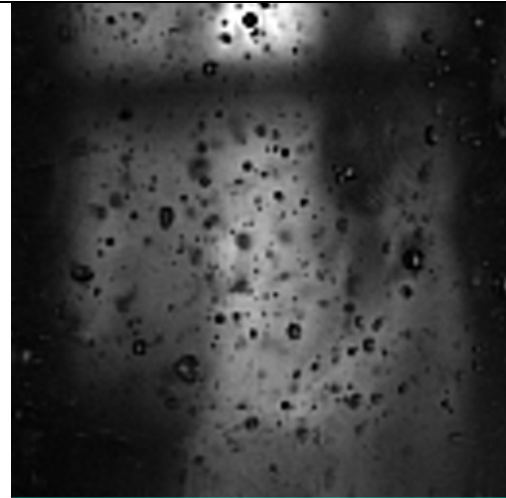
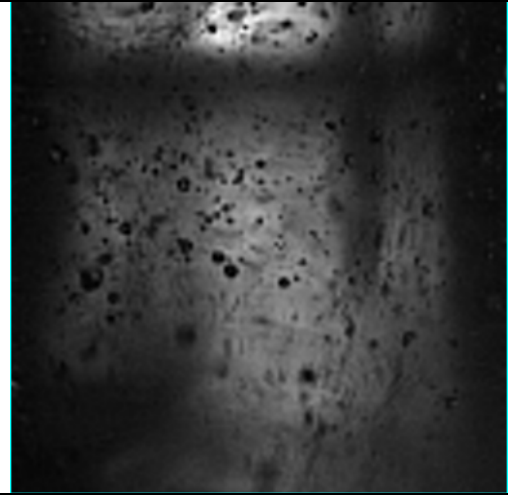
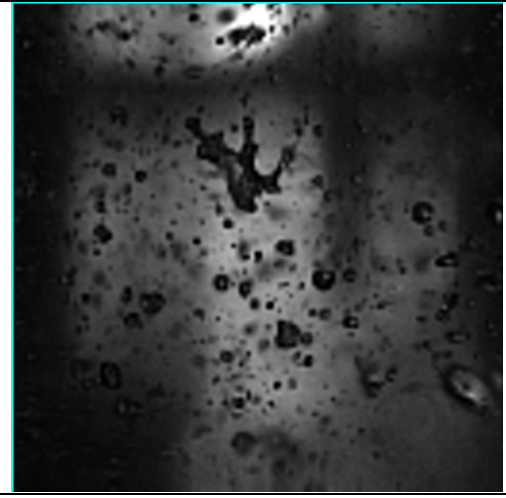
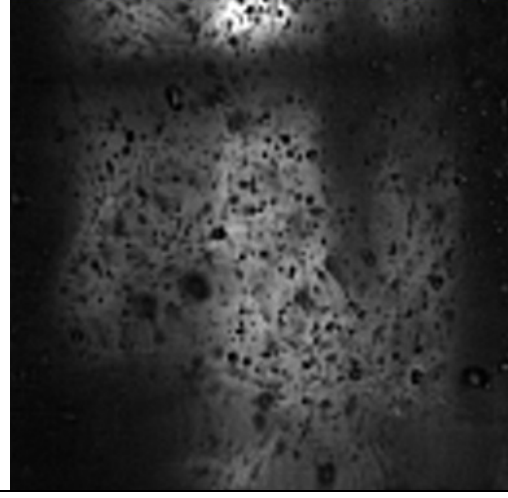
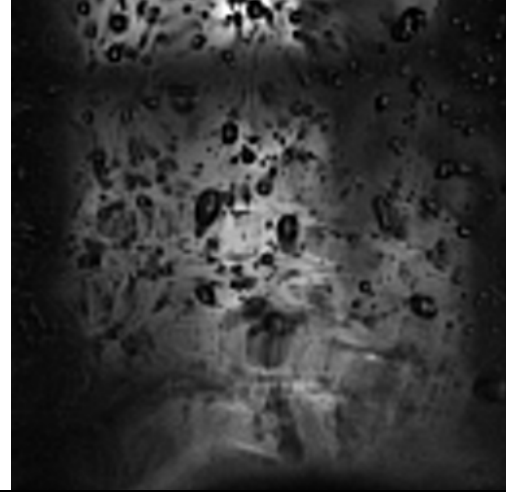


Figure 5.8 Cycle of disturbance wave and drop creation

5.4 Photography without the liquid film present

A number of high speed videos were taken through the windows of the test section used for PDA measurements. The camera was set at 10^5 fps at a resolution of 128×128 ($\sim 60 \mu\text{m/p}$) in order to be able to capture the high velocity drops in the gas core. Table 5.1 illustrates the results. The photographs were taken in order to quantitatively examine the effect of gas and liquid flow rates on the entrainment and to get an indication of drop size, i.e., no time interval between photos was taken into account.

Table 5.1 Drop size and entrainment behaviour

	
<p>Gas superficial velocity 20.19 m/s Liquid superficial velocity 0.0045 m/s</p>	<p>Gas superficial velocity 14.12 m/s Liquid superficial velocity 0.0045 m/s</p>
	
<p>Gas superficial velocity 19.12 m/s Liquid superficial velocity 0.03 m/s</p>	<p>Gas superficial velocity 11.92 m/s Liquid superficial velocity 0.03 m/s</p>
	
<p>Gas superficial velocity 18.28 m/s Liquid superficial velocity 0.05 m/s</p>	<p>Gas superficial velocity 12.73 m/s Liquid superficial velocity 0.05 m/s</p>

As can be seen from Table 5.1 the drop concentration and size changes quite profoundly for different conditions. For high gas flow rates, the number of drops per unit area is high and the size is small. With an increasing liquid flow rate it can be observed that the drop size increases. Note at a superficial velocity of 11.9 m/s for the gas and 0.03 m/s for the liquid a drop breaks up via the ligament break up mechanism (Azzopardi (1997))

5.5 Phase Doppler Anemometry Results

Here drop size and velocity results obtained in the 127 mm pipe with PDA are presented. Measurements were taken at 50 points distributed about the cross section of the pipe. The centreline of the pipe was found by estimating the position of the measuring volume. With the facility running at maximum gas velocity, the approximate centre line was found by the maximum drop velocity in the pipe cross section. The maxima, in terms of outer boundaries, in the x and y directions were then found by traversing along the cross section and monitoring the data rate the instrument was measuring. The maxima in terms of coordinates were then saved in the traverse memory. The positions at which data were taken are shown in Figure 5.9.

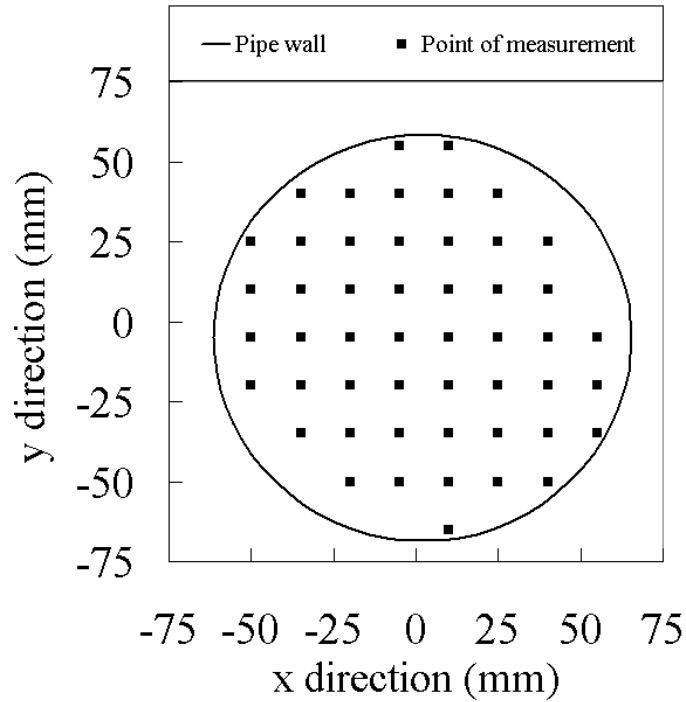


Figure 5.9 Cartesian coordinates of measuring points across the pipe cross-section.

Drop velocity and diameter profiles were taken over x -50 to 55 mm, keeping y constant at -5 mm. There are two areas where no data could be acquired due to the shape of the windows used (see Chapter 3). The parameters of the PDA setup are outlined in Table 5.2.

Table 5.2 Setup parameters of the Dantec PDA

Property	Green	Yellow
Wavelength (nm)	532	561
Beam diameter (mm)	1.35	
Beam spacing (mm)	38	
Expander ratio (-)	1.95	
Scattering angle (deg)	50	
Focal length receiving optics (mm)	500	
Focal length transmitting optics (mm)	310	
Refraction	Yes	
Aperture mask	C	
Fringe direction	Negative	
Spherical validation band (-)	0.15	
Maximum drop diameter (μm)	437.1	

The data was acquired and then analysed using methods similar to those applied by van 't Westende (2008). Initially, the correction for drop diameter bias as described by Saffman (1987) and reviewed in Chapter 3 of this thesis, was applied. In addition, the distribution cut-off method proposed by Teixeira (1988) and described in Chapter 3 was tested. The drop size distributions obtained however did not show the latter bias.

Zhang and Zaida (1999) used a Dantec system to measure mass fluxes of a water jet. They concluded that the diameter bias is not merely dependant on the diameter of a drop, as reported by Saffman (1987), but also on its direction

within the measuring volume. It is possible that a drop travels diagonally through the measuring volume. For a multi component velocity mechanism they suggested an expression for the projected cross sectional area of the measuring volume as used by van 't Westende *et al.* (2005). Since in the present study it is assumed that axial velocities are dominant and thus perpendicular relative to the measuring volume, the more complex expression to calculate the measuring volume cross sectional area reduces to

$$A_m = D_m L_m \quad 5.2$$

where, A_m , D_m and L_m are the cross sectional area, the diameter and the length of the measuring volume respectively. There are two unknowns in the rhs term in Eq 5.2 for the present study. However, van 't Westende *et al.* (2005) suggested that the diameter of the measuring volume in relation to a given drop diameter could be measured from the instantaneous drop size and velocity data obtained by the PDA. Assuming that the direction of velocity of the drop is parallel to the pipe axis, then the distance that the drop travelled through the measuring volume can be calculated by the transit time and its velocity

$$l_d = t_t U_d \quad 5.3$$

Where l_d , t_t and U_d are the length that the drop travelled, the transit time in the measuring volume and the drop velocity respectively. Similarly, for the length travelled by the drop, the expression

$$l_d = D_m \frac{\pi}{4} \quad 5.4$$

holds. One remaining unknown in Eq 5.2, L_m is taken from the properties of the PDA directly and has a value of 672 μm for the present study. It has to be noted that according Eq 5.4 the diameter of the measuring volume has been

made variable with drop size, the length has a negligible influence on the cross sectional area. Accordingly, the corrected Sauter mean diameters were calculated according aforementioned procedure from van 't Westende (2008). The volume and the area of the drops were calculated using d^3 and d^2 , where d is the arithmetic drop diameter. The corrected volume and area of the drops was then calculated by using

and
$$d^3_{cor} = \frac{d^3}{\left(\frac{A_m}{U_d T}\right)} \quad 5.5$$

$$d^2_{cor} = \frac{d^2}{\left(\frac{A_m}{U_d T}\right)} \quad 5.6$$

In which d and T are the corrected drop diameter and the total duration of an experiment.

The uncorrected and corrected Sauter mean diameter then follows from

and
$$d_{32} = \frac{\sum d^3}{\sum d^2} \quad 5.7$$

$$d_{32cor} = \frac{\sum d^3_{cor}}{\sum d^2_{cor}} \quad 5.8$$

An example of the difference between the uncorrected and corrected Sauter mean diameters at the centreline is shown in Figure 5.10. This shows that there is only a small difference.

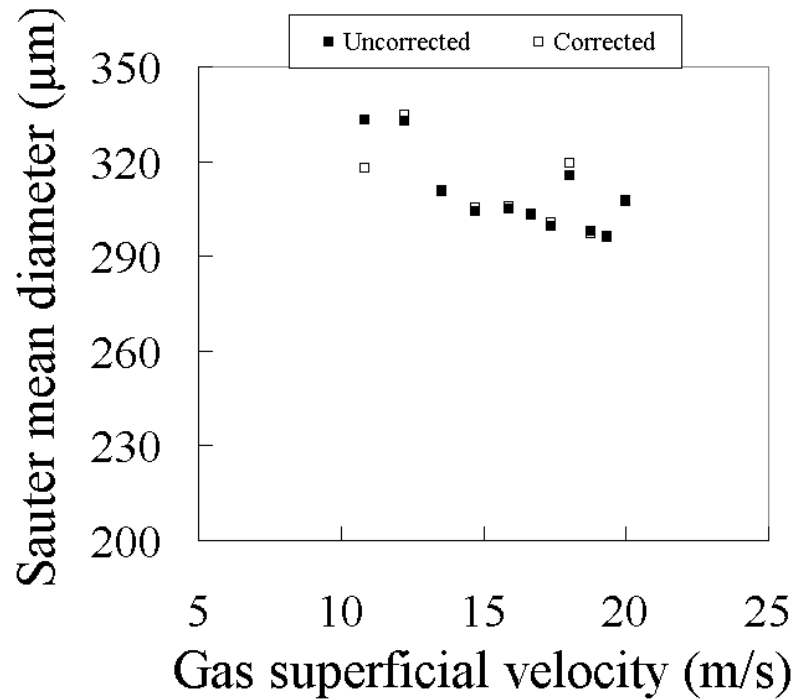


Figure 5.10 Example of corrected and uncorrected Sauter mean diameter at the pipe centreline.

It should be noted that the corrected Sauter mean diameter is referred to as the d_{32} for the remainder of this Chapter.

The entrained fraction is calculated using the dispersed phase holdup at the centreline of the pipe. This has been expressed by van 't Westende *et al.* (2005) in the following manner

$$\alpha_d = \frac{d^3 \frac{\pi}{6}}{\left(\frac{A_m}{U_d T} \right)} \quad 5.9$$

$$\alpha = \sum \alpha_d \quad 5.10$$

The dispersed phase only holds at the centreline, where it is assumed that the drop axial velocity is dominant.

The entrained fraction is an area fraction balance over the total cross section of the pipe. The film flow was not collected for the present data.

Therefore the film thickness, obtained from the conductance probes is included to calculate the fractions of the pipe obtained by each of the phases. The entrained fraction then follows from

$$\beta_f = 1 - \frac{A_f}{A_p} \quad 5.11$$

and

$$E_f = \frac{\alpha}{(\alpha + \beta_f)} \quad 5.12$$

where β_f , A_f , A_p and E_f are the fraction of liquid film, area of the pipe occupied by the liquid film, the total area of the pipe and the entrained fraction.

The Sauter mean diameter at the centreline is shown for all liquid superficial velocities in Figure 5.11.

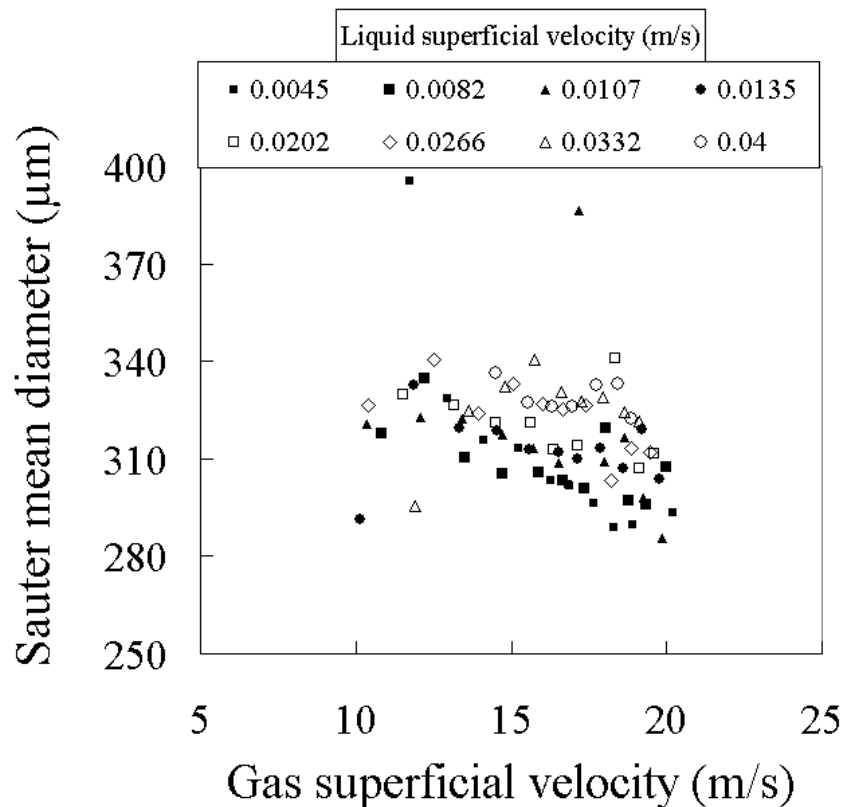


Figure 5.11 Sauter mean diameters for all liquid velocities. Note expanded axis

The Sauter mean diameter (Figure 5.11) decreases, though to a smaller extent compared to smaller pipes, with increasing gas flow rate as expected, the higher gas velocity and therefore momentum, the smaller the drops. There is evidence of a change of slope a gas superficial velocity of 10 m/s and a slight increase in diameter can then be observed from around 15 m/s for the gas. The liquid superficial velocity appears to have an influence on the condition of the latter changes as well. Another interesting feature observed is the increase, or “jump”, in size for the majority of graphs at around a gas superficial velocity of 18 m/s. In fact, the trends show quite similar features to that observed in the film thicknesses in Chapter 4 but it appears that the drop diameter reacts at slightly higher gas superficial velocities. In general it can be observed that the Sauter mean diameter increases slightly with liquid flow rate. For the purpose of closer examination, four cases were selected and re-plotted as shown in Figure 5.12. The explanation of Figure 5.11 then becomes clearer.

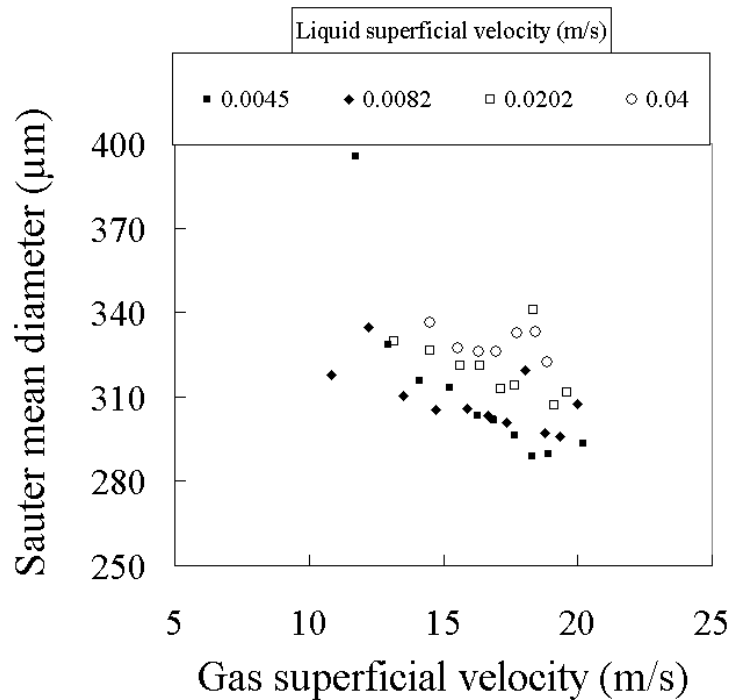


Figure 5.12 Selected cases for the evolution of the Sauter mean diameter

As aforementioned, the decrease in size is perhaps not as systematic as generally observed in smaller diameter pipes. This may be due to other, not yet identified mechanisms. The variation of the Sauter mean diameter about the pipe cross section has also been examined. Figure 5.13 illustrates this for gas superficial velocities of 18.3 and 14.5 m/s and the same liquid superficial velocity group as illustrated in the previous Figure. Radial positions are normalised with the pipe radius. As can be seen the profile is rather flat and there is little effect of gas and liquid flow rate. This agrees with the results obtained by Gibbons *et al.* (1983). Note that this is an expanded scale. It is interesting to observe that both the gas and liquid superficial velocities do not have a great effect on the Sauter mean diameter in cross-sectional terms. What can be argued is the fact that for a higher gas superficial velocity the diameter can vary significantly. This may be due to the fact that for higher gas flow rates, the turbulence intensity increases and hence an increase of the randomness probability. Some of the data show a very weak effect in the pipe centre by showing slightly smaller values. This has also been reported by van 't Westende (2008). This may be due to higher gas velocities, hence a higher atomisation rate of drops, at the pipe centre.

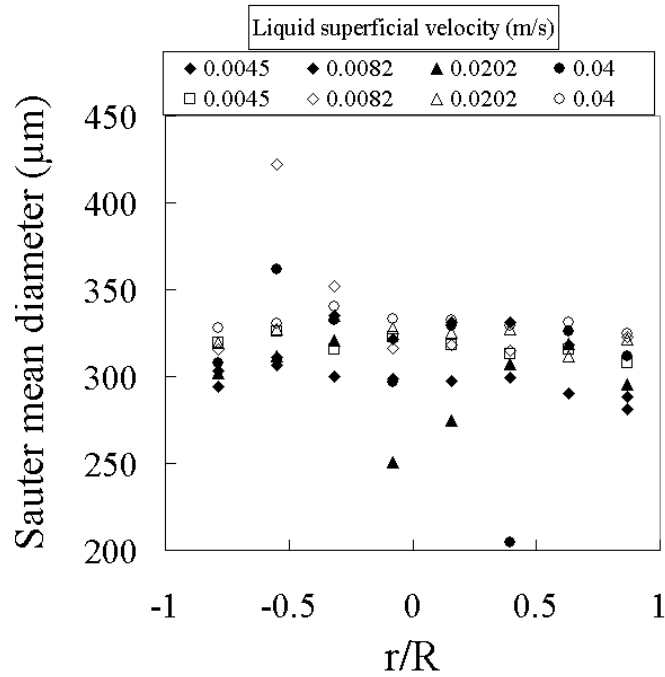


Figure 5.13 Sauter mean diameter in relation to the pipe cross section. Closed symbols represent a gas superficial velocity of 18.3 m/s, open symbols those for 14.5 m/s.

The velocity profiles of the selected liquid flow rates are shown in Figure 5.14. Also shown are the mean velocities of drops with small diameter to act as faithful followers of the gas. The tracer drops were defined as $\leq 20 \mu\text{m}$. In addition a gas velocity profile obtained through Computational Fluid Dynamics (CFD) as described in Chapter 6 is plotted for comparison.

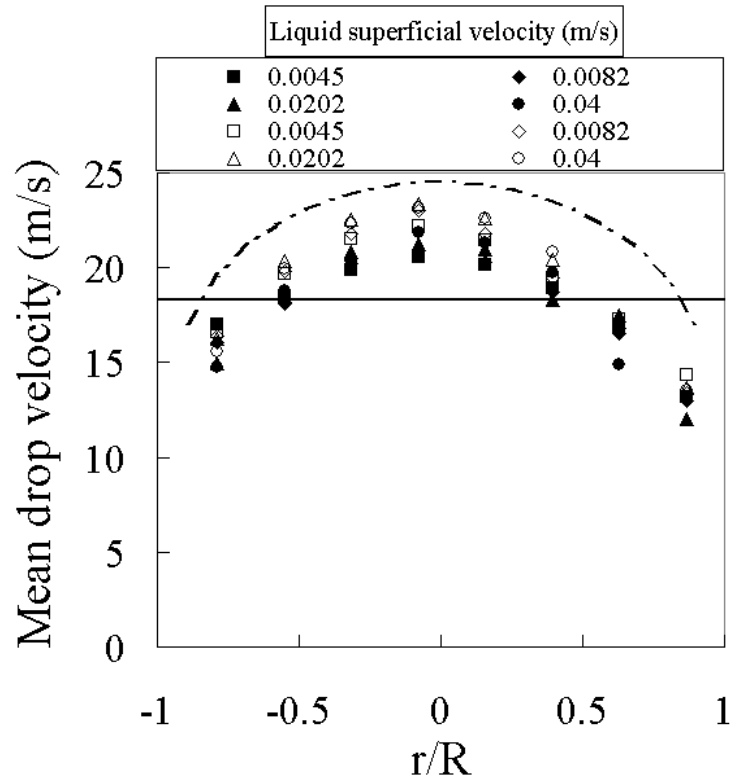


Figure 5.14 Mean drop velocity for an average gas superficial velocity of 18 m/s. Open symbols represent the overall mean velocity, closed symbols represent tracer drops. The straight line is the overall averaged gas superficial velocity. Dashed line is gas velocity profile from simulations for a gas superficial velocity of 20 m/s.

In order to examine the performance of CFD simulations in more detail, PDA experiments in which a gas superficial velocity of 20 m/s was obtained, are illustrated by Figure 5.15 together with the gas velocity profile obtained with the CFD calculations. As can be seen, there is good agreement.

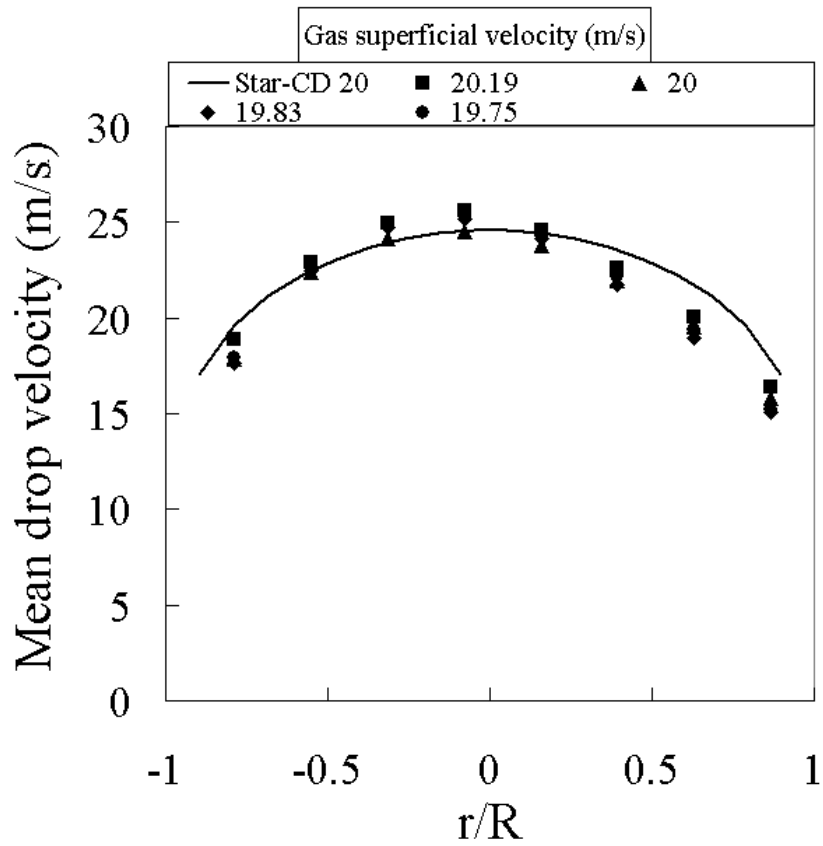


Figure 5.15 Experimental mean drop velocities for various superficial gas velocities. Solid line represents the Star-CD data obtained for a gas superficial velocity of 20 m/s.

A second example for a gas superficial velocity of ~ 14.5 m/s is shown in Figure 5.16

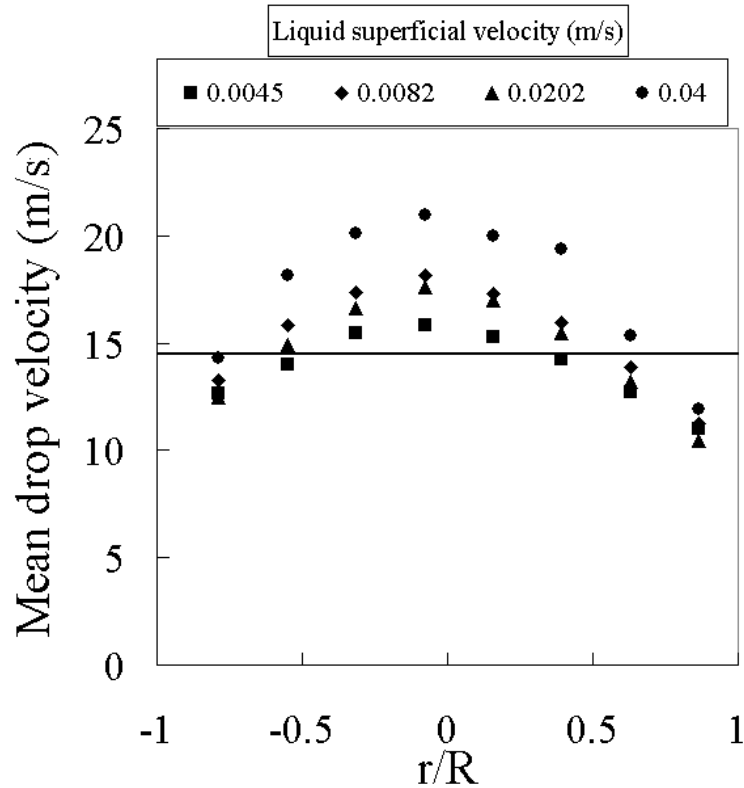


Figure 5.16 Mean drop velocity for an average gas superficial velocity of 14.5 m/s. Closed symbols represent the overall mean velocity. The straight line is the overall averaged gas superficial velocity.

The mean drop velocities show a similar radial profile to the gas velocity profiles observed in these types of flows. The gas velocities as measured using tracer drops show a slightly smaller mean velocities than those of the rest of the drops. This could be due to the small size of the tracer sample sets. However, looking at the overall drop velocity profiles, it can be concluded that for higher liquid velocities, also a slightly higher drop velocity is measured. This could be due to a larger spread in the velocity probability as described later in this Chapter. It is in agreement with Teixeira (1988) and Altunbas (1999). In addition, Altunbas (1999) reported that the overall mean drop velocities measured over the cross-section were lower than the gas superficial velocity. As

can be observed, this is not the case for the current data. In fact, the drops from about r/R -0.5 to 0.5 actually show a much higher mean velocity.

Figures 5.14-5.16 show that the mean drop velocity predominantly changes with gas velocity and a small effect of liquid velocity can be observed. As for Figure 5.16, the deviation of data between different liquid velocities becomes larger, indicating less dependence on gas velocity. An odd feature is observed for a liquid superficial velocity of 0.04 m/s. The mean drop velocity is much higher than the other data. As described in Chapter 4, this condition may be in the churn-annular transition area. Therefore it could be that the difference is caused by change of drop breakup mechanism. The standard deviation of the tracer drops was plotted and shown in Figure 5.17. It can be seen that for the tracer drops, the standard deviations show similar trends and as reported by Altunbas (1999) and Teixeira (1988). Note that the number of tracer drops measured is relatively low compared to van 't Westende (2008). A general increase with liquid superficial velocity. The effect of gas superficial velocity is seen to be secondary. However, for the highest liquid superficial velocity, the data would logically be expected to adopt higher values. This is however not the case and also this indicates that this particular liquid condition shows different features than the others.

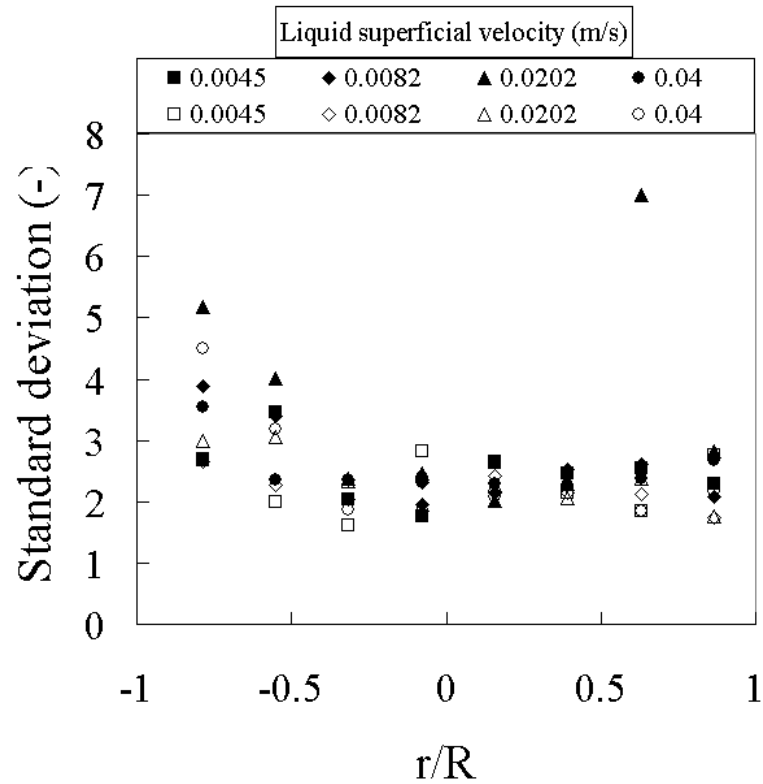


Figure 5.17 Standard deviation for gas superficial velocities of 18.3 m/s (closed symbols) and 14.5 m/s (open symbols).

The velocity results are compared with those from Altunbas (1999), Teixeira (1988) and Fore and Dukler (1995) in the form of values normalised by the maximum obtained. Figure 5.18 shows the results and Table 5.3 shows the comparison data.

Table 5.3 Experimental conditions comparison

	Gas superficial velocity (m/s)	Liquid superficial velocity (m/s)	Pipe diameter (mm)	Fluids
Altunbas (1999)	30	0.02	38	A/W
Teixeira (1988)	24.3	0.015	32	A/W
Fore and Dukler (1995)	23.3	0.014	50.8	A/W
Present	18.3	0.0045/0.0082 0.0202/0.04	127	A/W

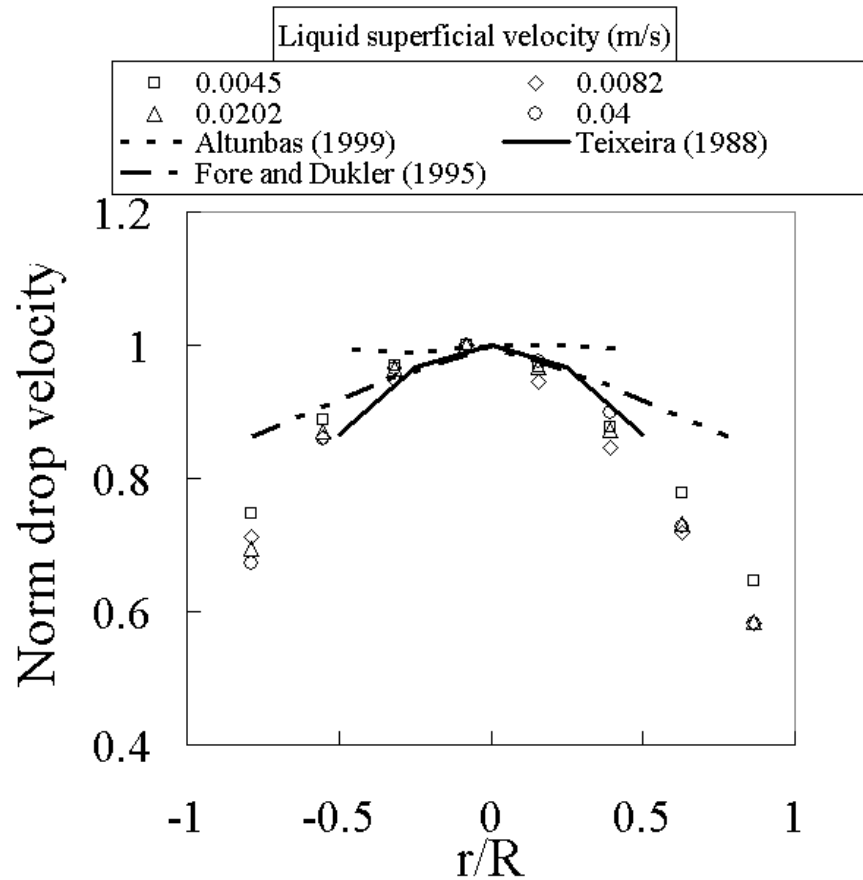


Figure 5.18 Comparison with previous work.

Note that the data from Fore and Dukler (1995) and Teixeira (1988) is extended to negative r/R .

From Figure 5.18 it can be seen that the data from Teixeira (1988) shows good agreement with the present data. Note that the present gas Reynolds numbers are a factor 2.5 times higher than those of Teixeira (1988) and 2 times higher than Fore and Dukler (1995). The data from Altunbas (1999) shows a much flatter profile over the cross-section. Perhaps the gas Reynolds number plays an important role on the drop velocity behaviour.

Drop velocities at the centreline and near the pipe wall are plotted against gas superficial velocity (Figure 5.19), both for the drops travelling at the centreline and pipe wall. This covers all superficial liquid velocities studied. Centreline drop velocities are seen to be 0 to 30 percent greater than the gas superficial velocities. The drops travelling near the wall, are 60 to 80 percent lower. The liquid superficial velocity has almost no effect on the drop velocity. For the centreline data, it can be seen that it actually starts to deviate from a gas superficial velocity of 13 m/s. This also applies to the data at the wall but in a less obvious manner. The group of points actually on the 45 degree line at low gas flow rates are interesting. Linking this with the Sauter mean diameter it can be observed that this is the point where a drastic change of slope occurs. Since van 't Westende (2008) observed counter-current features around these flow condition, it is therefore perhaps not an unreasonable assumption that this may indicate an inception point for the transition from churn to annular flow.

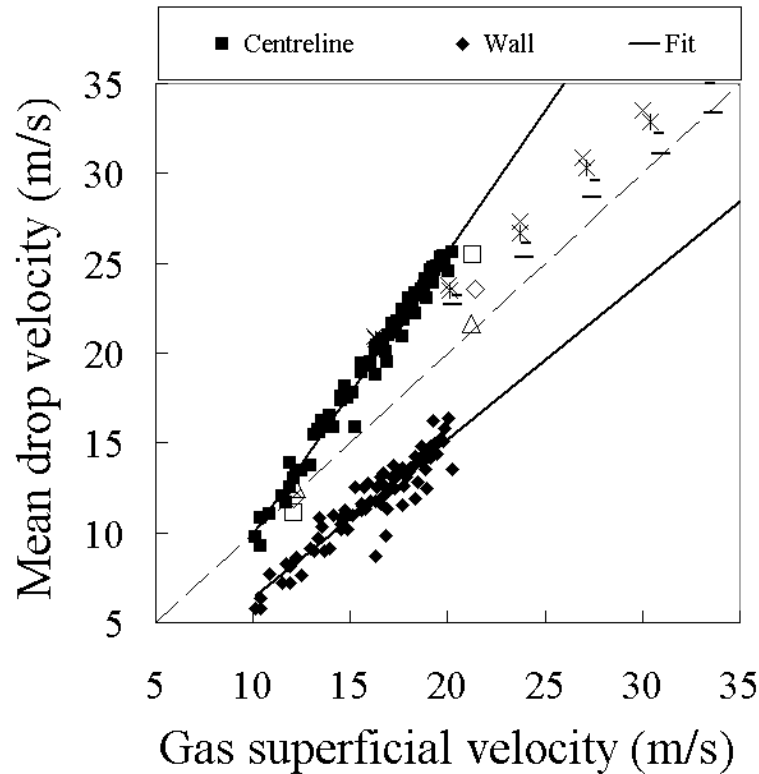


Figure 5.19 Overall mean drop velocity at the centreline and pipe wall. Marks represent data from Fore and Dukler (1995) for liquid superficial velocities from 0.015 to 0.045 m/s. Open symbols represent data from van 't Westende (2008) for liquid superficial velocities from 0.01 to 0.04 m/s

The equivalent data from Fore and Dukler (1995) and van 't Westende (2008) are also plotted on this figure. It can be seen that the data at the centreline in general shows quite a different pattern compared to Fore and Dukler (1995). The data of van 't Westende (2008) shows good agreement with the present data at the lower gas superficial velocity end. It is interesting to observe that the present data does not show as much liquid flow rate dependence as the other data. This might be due to a pipe diameter effect.

Normalised probability distributions of diameter and velocity over the entire cross section are illustrated in Table 5.4. For high gas flow rates, the diameter distribution has a longer tail towards larger sizes. The distribution is less wide than for the lower gas velocity. The effect of longer tails can be quantified via the skewness of the distribution. This is the third moment of the distribution (the first being the mean and standard deviation). The above can be restated as: there is a positive skewness. The standard deviation is rather large for low gas flow rates and higher liquid flow rates, where the distribution shifts to negative skewness. Still being statistically representative, the data rate at low gas and high liquid flow rate are lower due to partial obstruction of vision through the viewing windows. The drop velocity peaks are negatively skewed. Most interesting is the observation that the drop velocities for the lower gas flow rates show a symmetrical probability distribution. To examine this further, the skewness was normalised with its maximum for each set of liquid flow rates. Hence, a symmetrical skewness of 0 becomes 1. This is depicted in Figure 5.20 and shows that the normalised skewness tends to form a plateau around 1 and starts to deviate at a gas superficial velocity of approximately 13 m/s. By comparing this with for instance the overall mean drop velocity at the centreline (Figure 5.18) it can be seen that the group of data points at low gas and mean drop velocities are in the velocity ranges of this criterion. After this point, the data starts to deviate from the gas superficial velocity. Linking the skewness with the gas superficial velocity gives the following correlation: If the maximum normalised skewness for the drop velocity is equal or close to 1, then the ratio between gas superficial velocity and drop velocity is also 1. This can be expressed as

$$\frac{\gamma}{\gamma_{max}} \approx \frac{U_d}{U_{gs}} \approx 1 \quad 5.13$$

Where γ is the skewness for each drop velocity distribution, γ_{max} is the maximum skewness, U_d is the drop velocity and U_{gs} is the gas superficial velocity. It is interesting that this is the skewness condition where the slip velocity ratio, as commonly employed to calculate the drag force acting on a single drop, equals 1. This might be linked with the transition from churn to annular for the present study. In fact, the condition at which this change occurs is similar that as identified in Chapter 4, i.e., a change as defined by Zabaras *et al.* (1986) from “upward” to “upward re-circulation” and change of wave type, probably concerning huge waves. Similarly, with an increase of liquid flow rate, the skewness tends to react in positive terms as well.

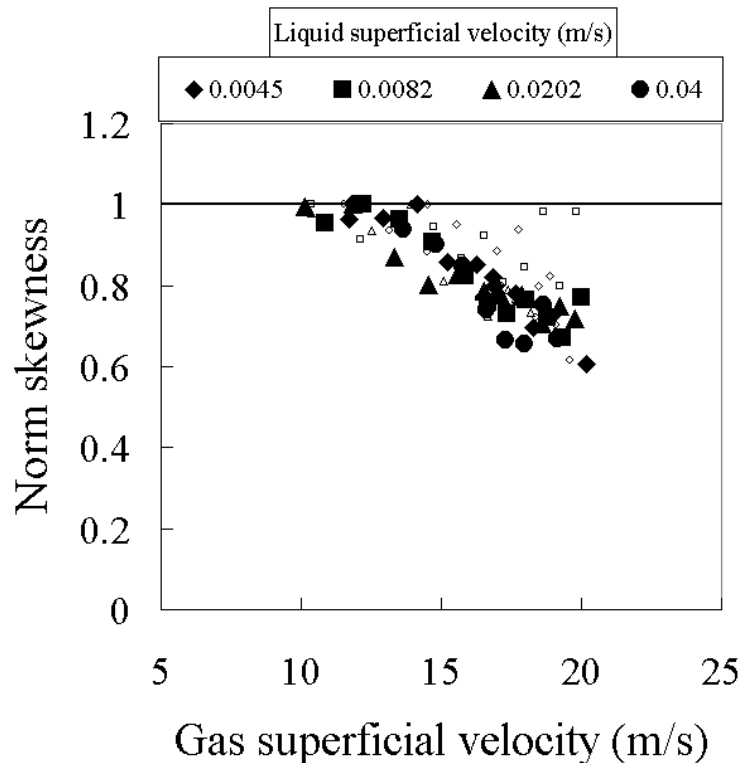
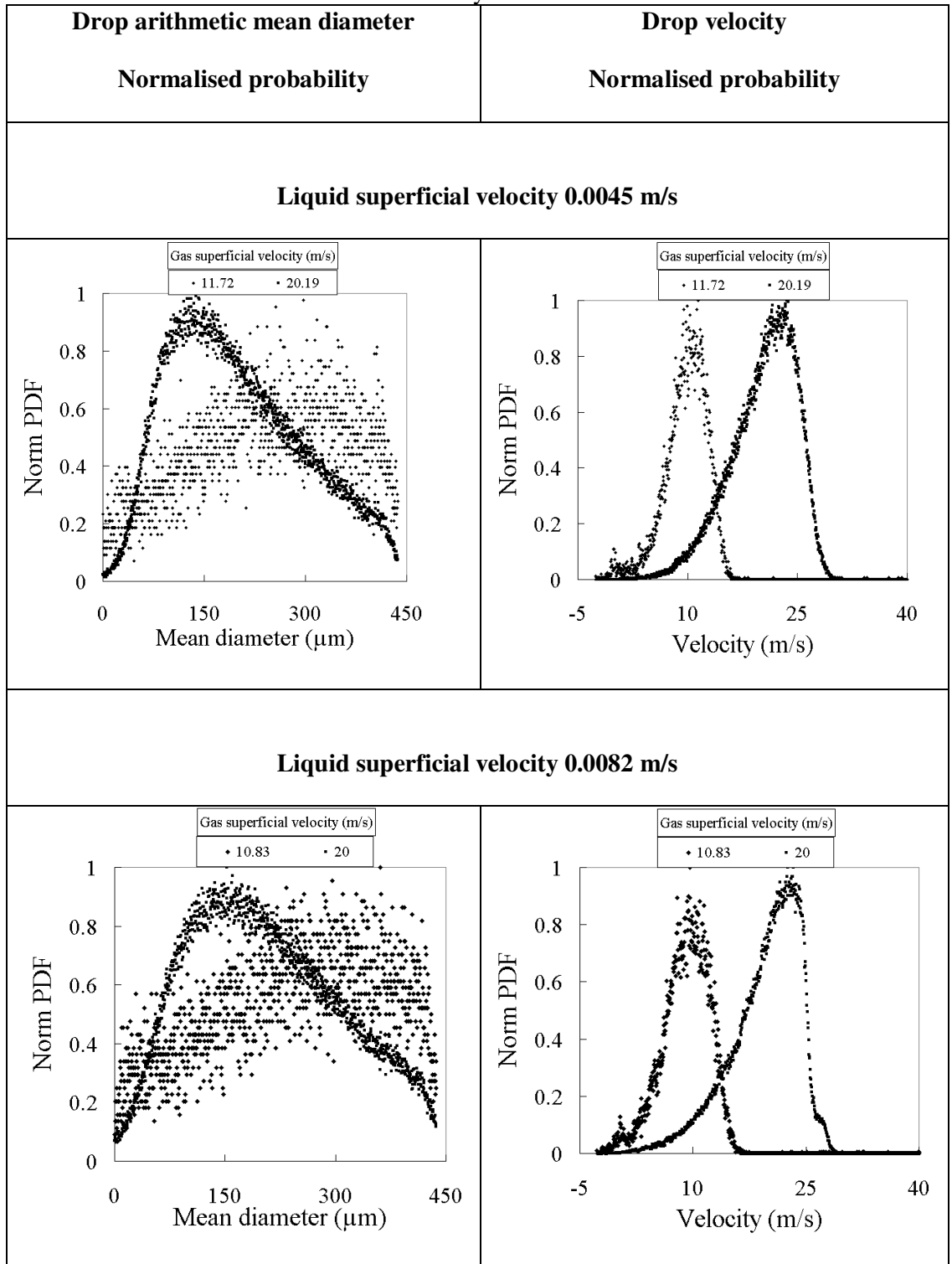
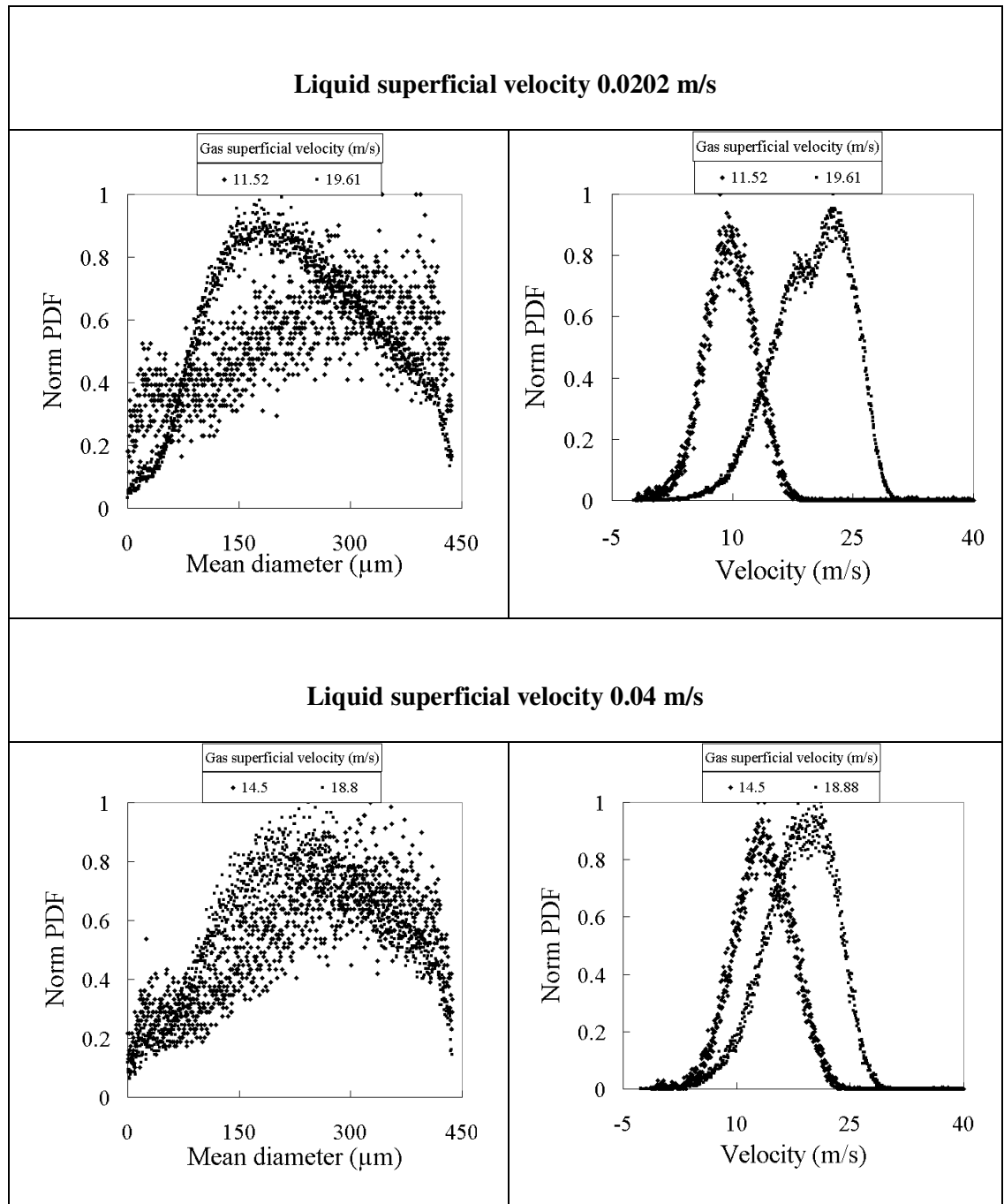


Figure 5.20 Normalised skewness of drop velocity distributions. Closed symbols represent the selected experiments; open symbols represent all other experiments.

Table 5.4 Probability distributions





Note that some negative, i.e., downwards drop velocities were measured. There are only few of these falling drops which are probably associated with those travelling near the wall where there is less upwards drag. Furthermore, drop size measurement limitations and, to some extent, extrapolation methods are described in the appendices of this thesis.

5.6 The liquid film and entrained fraction

The drop size and velocity data can be linked with the liquid film measurements taken simultaneously with the conductance ring probes. The analysis performed for this data set is similar to that carried out in Chapter 4. Figure 5.21 shows the cross section and time averaged results for the film thickness in relation to the gas superficial velocity.

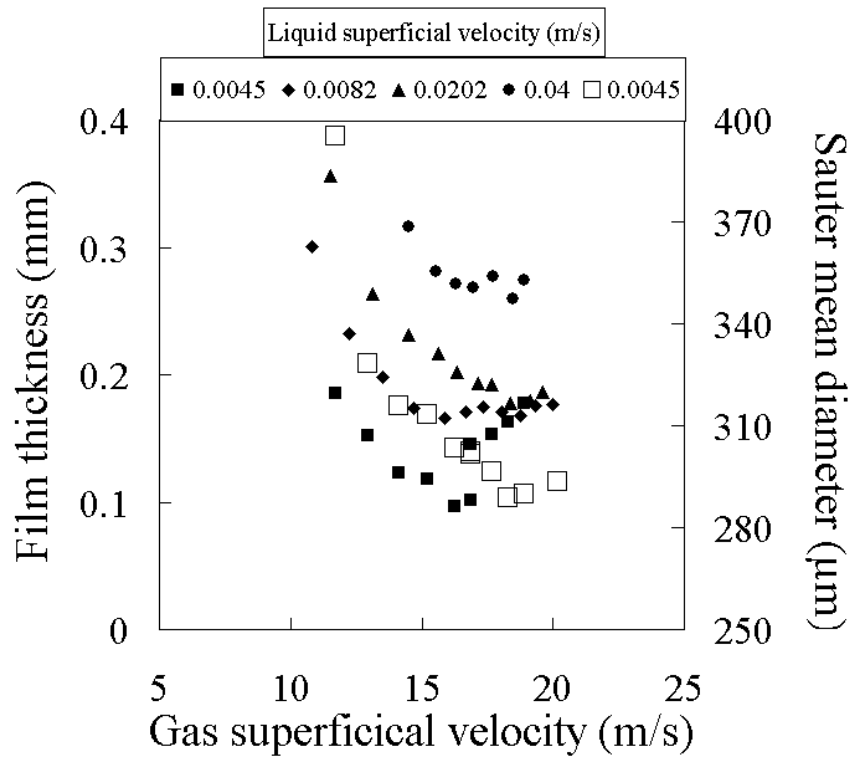


Figure 5.21 The liquid film thickness for selected experiments. The Sauter mean diameter for liquid superficial velocity 0.0045 m/s is illustrated to examine the trends (open symbols).

As can be seen from the film thickness plots, the film thickness shows similar trends to those observed in Chapter 4. However, film thicknesses from these atmospheric measurements are lower than those reported from 3 bara. Comparing the Sauter mean diameter behaviour with the liquid film behaviour shows a good agreement. It is evident that the Sauter mean diameter decreases with decreasing film thickness and increases with increasing film thickness.

Similar features have been reported by Alamu *et al.* (2010) in a 19 mm diameter pipe. As discussed in the beginning of this Chapter, the film thickness was also applied in order to calculate the entrained fraction for the selected experiments.

Figure 5.22 illustrates the entrained fraction for the selected experiments.

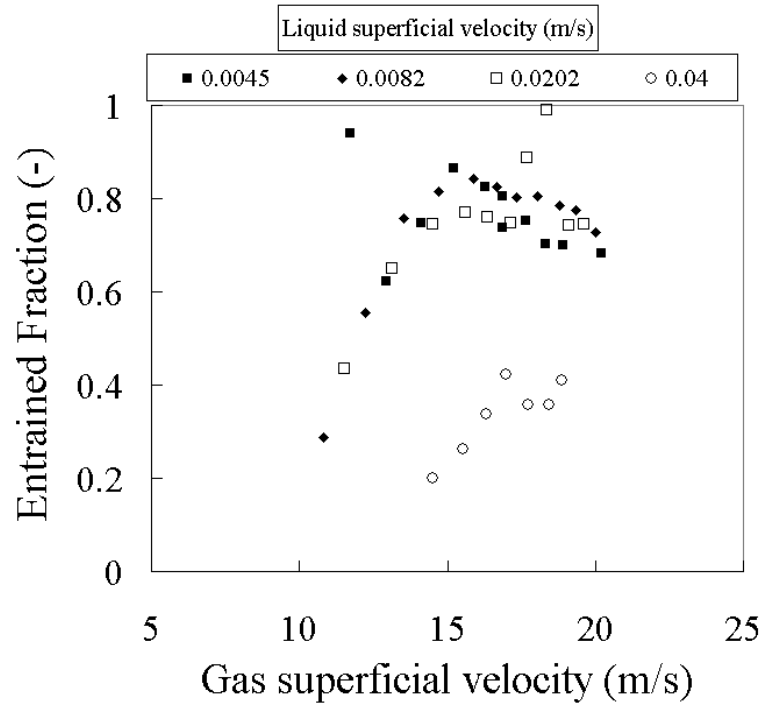


Figure 5.22 Entrained fraction for selected experiments.

Although the entrained fraction is related to the film thickness and the dispersed phase holdup, it can be observed that the entrained fraction increases when the film thickness decreases. This is possibly due to exchange of mass between the two phases due to interfacial shear stress. It is worth noting that the entrained fraction is higher overall than has been reported in annular flow.

However, at 0.04 m/s for the liquid a much different behaviour is observed. This may be because it is in the transitional area as found in Chapter 4. At about a gas superficial velocity of 15 m/s, the slopes switch from positive to negative. This can be observed for all liquid flow rates, except for the highest

liquid flow rate where this switch seems to occur at a higher gas flow rate. As can be observed in the film thickness and drop size, this change of slope occurs at higher gas velocities since the gas to liquid ratio is lower. The change in slope count indicate a change from co-current to counter-current flow, i.e., the transition between churn and annular flow as also observed in the drop velocity section of this Chapter and Chapter 4. A comparison was made between data from Azzopardi (1983) and Verbeek (1992) and shown in Figure 5.23.

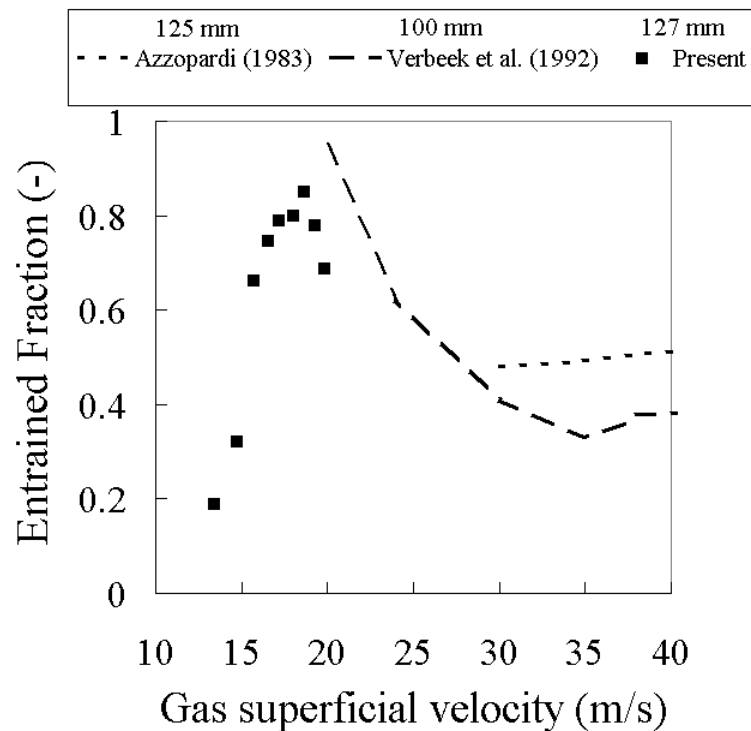


Figure 5.23 Comparison with the entrained fraction obtained by Azzopardi (1983) and Verbeek *et al.* (1992). Liquid superficial velocities are all 0.01 m/s.

Figure 5.23 shows that the data obtained for the present study does show a trend that may aid to the understanding of entrainment in the churn flow

region in these larger diameter pipes. The trend of the entrained fraction could complete the gap between the data sets. This has been verified by adopting the method from Ahmad *et al.* (2010). They propose a method to estimate the entrained fraction in churn flow, taking the ideas of Hewitt and Govan (1990) further. The latter model is evaluated in more detail in Chapter 6. By means of a correction factor to account for the higher entrained fraction in churn flow compared to annular flow they proposed the following relationship

$$\frac{E_{Annular}}{E_{Churn}} = -8.73u_g^* + 9.73 \quad 5.14$$

Where U_g^* is the Wallis (1969) parameter as described in Chapter 4. Similarly, the entrained fraction at higher gas velocities, i.e., $u_g^* > 1$ has been calculated by employing the method from Hewitt and Govan (1990). A comparison between the entrained fraction calculated from the PDA measurements and the method from Ahmad *et al.* (2010) for a liquid superficial velocity of 0.01 m/s is presented in Figure 5.24.

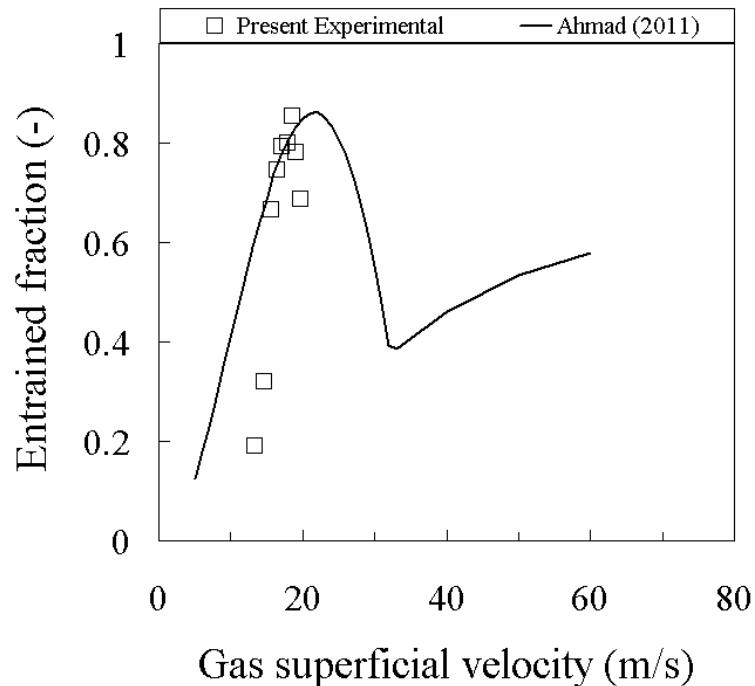


Figure 5.24 Comparison of entrainment in churn flow

As can be observed from Figure 5.28, the Ahmad *et al.* (2011) method shows a reasonable resemblance of the present data. Therefore, also liquid superficial velocities of 0.01, 0.02 and 0.04 along with data from Azzopardi *et al.* (1983) and Verbeek *et al.* (1992) are computed as illustrated in Figure 5.29 below. The results show a good agreement with the experimental data. Similar to the values calculated from the present experimental results, it shows a decreasing trend for the entrained fraction with increasing liquid flow rate in the churn flow area. This is a particularly interesting feature that is perhaps due to a higher rate of coalescence and deposition in churn flow. For values i.e., $u_g^* > 1$ it can be observed that the entrained fraction increases with increase in gas flow rate. This is generally accepted and is due to the increase of interfacial stress as described in Chapter 4.

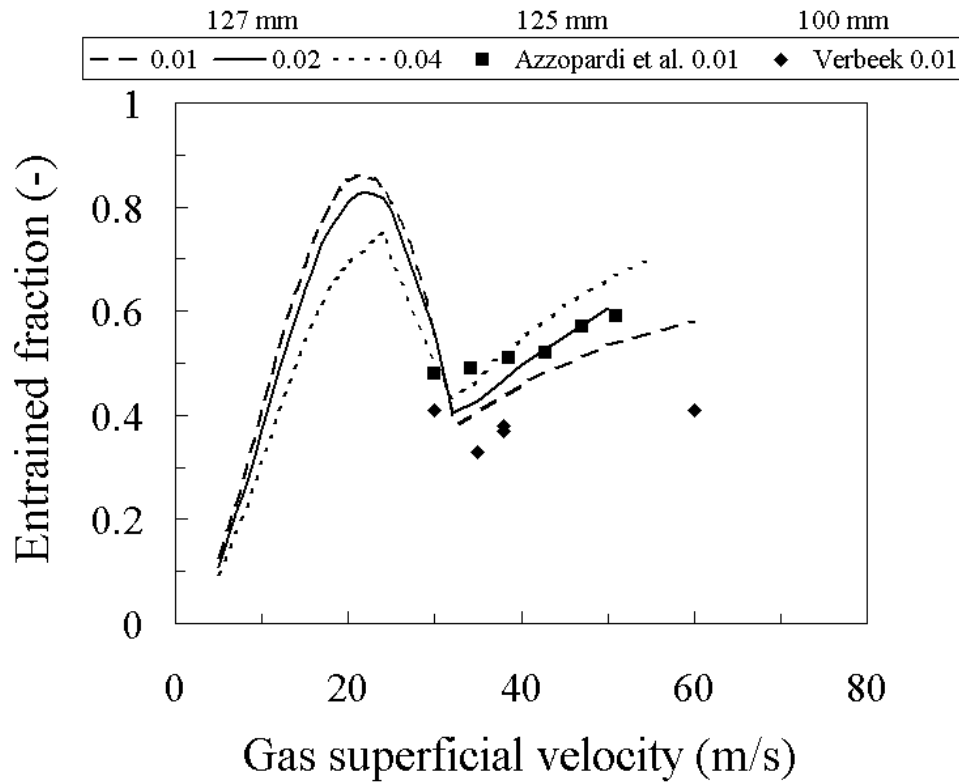


Figure 5.25 Comparison of entrainment in churn flow including others.

Recalling Chapter 4, it is reported that the gravitational gas core pressure drop plays a dominant role at higher liquid flow rates (churn flow). Thus a high entrained fraction contributes more significantly to the total pressure drop relative to the liquid film. Fore and Dukler (1995) report a maximum figure of 20 percent, whereas in the present study for the highest liquid flow rate (0.7 m/s) the average contribution is 75 percent, being a large difference. In Figure 4.16, Chapter 4, the pressure drop components are reported. At the point where the pressure drop due to the dense core would be zero, the gas superficial velocity would be 32 m/s. In Figure 5.25 above, this is switching point of slopes. The gas core density is at its minimum at this point. This may indicate that the onset of the transition from churn to annular flow is visible “earlier” in the liquid film and pressure drop characteristics from about 10 to 15 m/s for the gas. This ties in with the skewness analysis of the drop velocity described above. From Figure 5.25, this seems to trigger a mechanism from about 15 to 30 m/s, causing drastic decrease in entrained fraction, hence the relative gravitational gas core pressure drop contribution. This mechanism may be evidence that indeed the flow does not simply switch between churn and annular flow, but a transitional region is present where entrainment still plays a dominant role. It seems plausible that the entrainment is carried in the form of huge waves or wisps, as described by Azzopardi and Wren (2004). In Chapter 4, huge wave are reported from the WMS results in churn conditions around and below 10 m/s for the gas superficial velocity.

Similar to Chapter 4, also here the liquid film is investigated in more detail. The mean film velocity was calculated by using

$$U_f = U_{ls} D_t \frac{(1 - E_f)}{4\delta} \quad 5.15$$

where U_f is the mean film velocity, D_t the pipe diameter, E_f the entrained fraction and δ the mean film thickness. Figure 5.26 illustrates the results for the selected experiments.

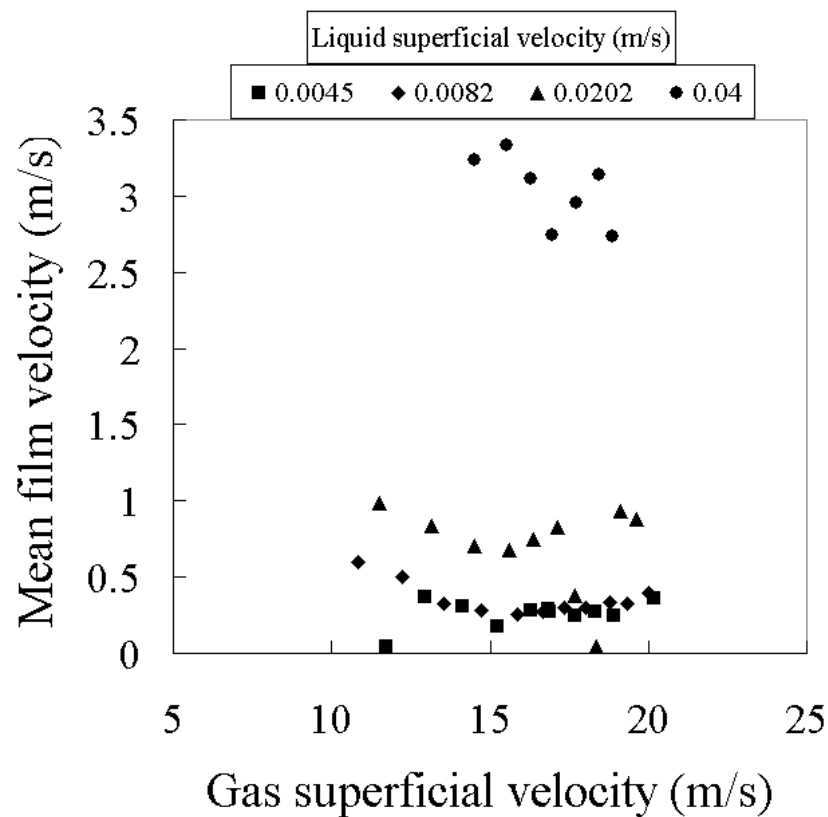


Figure 5.26 Mean liquid film velocity

Apart from the more obvious increase of the mean film velocity from about 15 m/s for the gas, a profound effect on the mean film velocity can be observed. For the three lower liquid flow rates, the trends show a minimum, after which it increases at a gas superficial velocity of 15 m/s. The magnitude is

similar for the two lowest liquid flow rates but then starts to increase for the two higher liquid flow rates. For a liquid superficial velocity of 0.02 m/s, the mean film velocity still shows a uniform trend but shows a factor 3 higher values, whereas this is not the case for 0.04 m/s which shows a larger scatter and a factor 12 higher values. The structure velocity was also examined and an example illustrated by Figure 5.27.

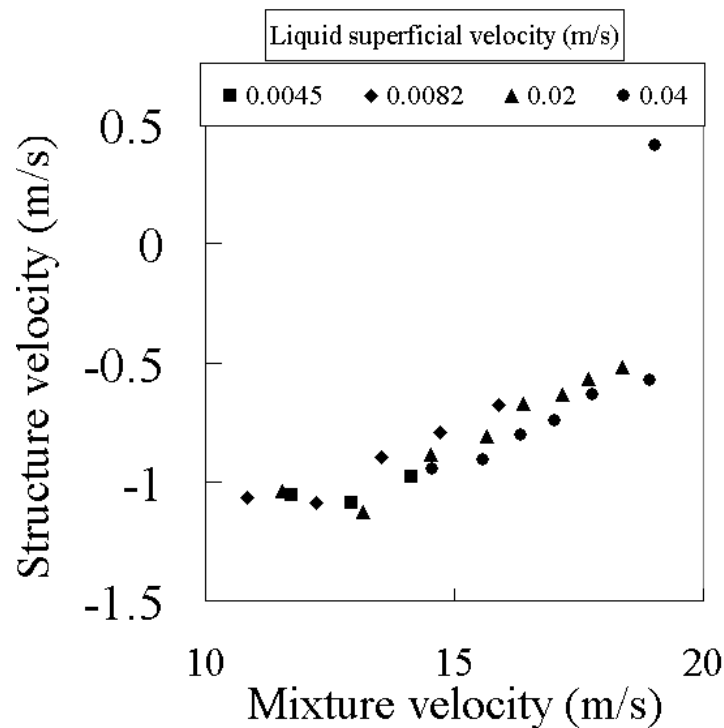


Figure 5.27 The structure velocity (closed symbols). The mean liquid film velocity for 0.0045 m/s is also plotted for illustration.

As in Chapter 4, also here negative structure velocities can be observed and a similar explanation may apply. In addition, for larger diameter pipes it can not be assumed that the waves travel uniformly about the periphery of the pipe wall. As mentioned, waves travelling sideways on the pipe wall have also been observed. This non-uniformity has an influence on the film thickness in general but also on the wave velocity, frequency, amplitude and spacing. Zangana

(2011) addresses this problem in more detail by employing local conductance probes in combination with wall shear stress probes.

From the above, i.e., drop size, drop velocity and drop entrainment, a few main conclusions can be drawn.

The drop size shows a weak but gradual decrease with gas flow rate, it then increases after which it again decreases. This may be linked inversely with the entrainment which seems to increase, then decreases and then again increases

There is evidence in this Chapter along with Chapter 4 and 6. The possible inception point of the transition from churn to annular flow was observed by examination of the diameter and velocity distributions taken over the entire cross-section of the pipe. There is evidence that when the skewness of the drop velocity distribution is symmetrical, the ratio between drop velocity and gas superficial velocity is around unity.

The latter occurs when the liquid film thickness, pressure drop and entrained fractions show their minima and maxima respectively. The gravitational pressure drop due to the dense core shows its maximum.

This mechanism may be evidence that indeed the flow does not simply switch between churn and annular flow, but a transitional region is present where entrainment still plays a dominant role. This is described in Chapter 6.

For this range, it seems plausible that the entrainment is carried in the form of huge waves or wisps, as described by Azzopardi and Wren (2004). For the present study, huge wave are reported from the WMS results in churn conditions around 10 m/s for the gas superficial velocity.

6 Drop Simulations

This chapter presents the results of flow simulations performed using Star-CD. The first section introduces the motivation of the study followed by the outline. The third section describes the background of the predictions including the numerical method by James *et al.* (1980) and the current method. The next section covers the results of the simulations. The last section describes the lateral and axial development of drop trajectories and analysis of deposition mechanisms more detailed.

6.1 Previous work

The present simulation study follows from work carried out at AERE Harwell in the period 1970-1988. Those started with the study of liquid or solid dispersions in turbulent gas streams by Hutchinson *et al.* (1970) which developed a stochastic model to predict the interaction between the continuous and dispersed phase. This is based on the random walk process which a drop undergoes, random trajectories in a pipe when subject to forces such as turbulence. The model was tested and shown to perform satisfactory against experimental data obtained in pipe of 9.5 to 63.5 mm ((Alexander and Coldren (1951), Cousins *et al.* (1965) and Cousins and Hewitt (1968)).

James and Hutchinson (1978) extended the model by simulating trajectories of individual drops. James *et al.* (1980), Andreussi and Azzopardi (1982) (Figure 6.1) and Wilkes *et al.* (1982) applied and further refined this method. James *et al.* (1980) particularly focussed on the mechanisms referred to as “direct impaction” and “diffusion” where drops deposit back onto the pipe wall by a linear trajectory and by a more random (walk) trajectory respectively.

Star-CD incorporates such a random walk process. It is essentially a Lagrangian/Eulerian approach. The conservation of mass, momentum and energy equations are written for each single element in the dispersed phase. For the continuous phase, i.e. the gas phase, the Navier-Stokes equations are employed, taking into account several different terms associated with the dispersed/continuous phase interactions. Examples of the earlier simulations are given in Figure 6.1. Those results were replicated using Star-CD and then extended to the present pipe size.

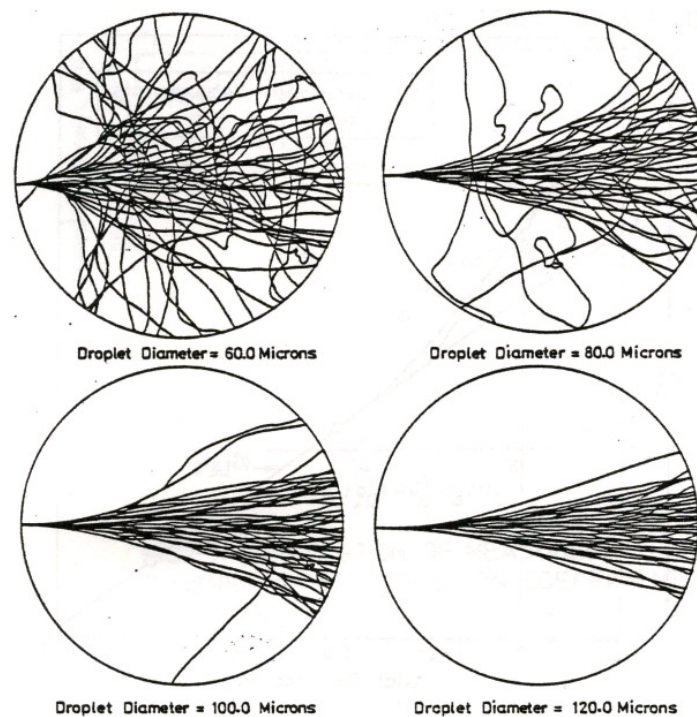


Figure 6.1 Example simulation of drop motion ((Andreussi and Azzopardi (1981)) ($D_t = 32$ mm, $U_l = 0.9$ m/s, $U_{gs} = 29$ m/s)

6.2 Outline

The objectives of the present work were:

1. To reproduce the results of James and Hutchinson (1978) using Star-CD;
2. To simulate drop behaviour under conditions similar to those of James and Hutchinson (1978) by equivalent simulations for a 127 mm pipe;
3. The performance of the dispersed multiphase flow model and comparing results with a Reynolds Stress Model (RSM);
4. To study the effect of multiple angle drop ejection;
5. Comparing the effect of mesh design;
6. Quantification of drops likely to deposit on the pipe wall by the diffusion or direct impaction mechanisms.

Table 6.1 shows the different conditions at which simulations were performed. A gas superficial velocity of 29 m/s was simulated for comparison with the work of James *et al.* (1980) and Andreussi and Azzopardi (1981), further simulations were carried out at a gas superficial velocity of 20 m/s which represent the maximum achieved experimentally in the 127 mm pipe. In addition, a RSM (see next section for definition) simulation was performed for the case of $D_t = 32$ mm and $D_d = 450$ μm in order to determine whether eddy viscosity would affect the results compared to the k- ϵ model used in the rest of the simulations. Since it is important to gain understanding in the fundamentals of drop trajectories, performing all simulations with the RSM model is perhaps appropriate for future work. Moreover, another case, for $D_t = 127$ mm and $D_d =$

150, 450 and 750 μm , in which drops were injected at multiple angles of 33, 66, 90, 123 and 156 degrees was carried out. That is, each angle being a separate injection point, injecting drops with an interval of 1 s. Most calculations were carried out with an injection velocity of 0.7 m/s. To examine the effect of ejection velocity one case with an ejection velocity of 0.2 m/s was simulated for the 127 mm pipe. Also, a simulation was performed to quantify the effect of gas superficial velocity using a value of 15 m/s instead of 29 or 20 m/s.

Table 6.1 Simulation conditions

Drop diameter D_d μm	Pipe diameter D_t mm	Superficial gas velocity U_{gs} m/s	Drop ejection velocity U_I m/s	Simulation #
150	32	29	0.7	1
150	127	29	0.7	5
150	127	20	0.7	8
150	127	20	0.7	17
450	32	29	0.7	2
450	32	29	0.7	3
450	127	29	0.7	6
450	127	20	0.7	9
450	127	20	0.2	10
450	127	15	0.7	11
450	127	20	0.7	18
650	127	20	0.7	12
750	32	29	0.7	4
750	127	29	0.7	7
750	127	20	0.7	13
750	127	20	0.7	19
850	127	20	0.7	14
1000	127	20	0.7	15
1500	127	20	0.7	16

The drop ejection velocity of 0.7 m/s was selected from analysis of cine film as discussed in chapter 5. This was based on liquid superficial velocities ranging from 0.014 to 0.04 m/s and gas superficial velocities from 13.14 to 16

m/s. Drop ejection velocities were found to be in the in the range of 0.6 to 0.8 m/s, the average being about 0.7 m/s. The drop ejection velocity ties in with the value of 0.9 m/s reported by Andreussi and Azzopardi (1981). It is perhaps not an unreasonable assumption that the latter drop ejection velocity value is slightly higher as the flow rates from which they were obtained were higher.

6.3 Numerical drop trajectory experiments

The one equation method used by James *et al.* (1980) is described by the turbulence method of Hutchinson *et al.* (1970) with constants in the form of an eddy length scale L_e , an eddy velocity scale U_e and an eddy/drop lifetime T_e

$$L_e = 0.22R \quad 6.1$$

and

$$U_e = \sqrt{\frac{\tau}{\rho_g}} \quad 6.2$$

and

$$T_e = 1.6 \frac{L_e}{U_e} \quad 6.3$$

$$\tau = 0.5 \rho_g U_{gs}^2 f$$

where

$$f = 0.079 R_{e_g}^{-0.25} \quad 6.4$$

6.5

Where R is the pipe radius, τ is the shear stress at the gas-liquid interface, ρ_g the gas density, U_{gs} the gas superficial velocity, f the (Blasius) friction factor and R_{e_g} the gas Reynolds number. The drag force acting over the drop is expressed by

$$F_d = 0.5 \rho_d c_d (V_e - U_d)^2 \frac{\pi}{4} d^2 c \quad 6.6$$

where c_d is the drag coefficient of the drop,

$$c_d = 0.44 + \frac{24}{Re_d} c \quad 6.7$$

where the drop Reynolds number includes the drag velocity of the drop.

By following aforementioned steps, they suggested the change of motion u, v relative to non-dimensional time θ , normal and tangential to a ejection point of a drop to be:

$$\frac{du}{d\theta} = a(S_1 - u)|S_1 - u| + b(S_1 - u)c \quad 6.8$$

and

$$\frac{dv}{d\theta} = a(S_2 - v)|S_2 - v| + b(S_2 - v) \quad 6.9$$

Here, S is the position of a droplet relative to an imaginary straight line from the ejection point to the tube axis and a and b are constants described by:

$$a = \frac{0.33L_e \rho_g}{d\rho_l} \quad 6.10$$

and

$$b = \frac{18L_e \mu_g}{d^2 \mu_l U_e} \quad 6.11$$

They proposed the following solutions for the interaction between drop and eddy. It is important to note that (i) these equations solve for the lateral direction in a pipe, (ii) they hold when assumed that the droplet passes through the eddy in a straight line and (iii) that the drag coefficient is constant over an o -th iteration. The velocity of the drop in radial and circumferential directions u , v respectively then becomes;

$$u = S_1 - \frac{b(S_1 - u_o)e^{-b\zeta}}{b + a(1 - e^{-b\zeta})|S_1 - u_o|} \quad 6.12$$

and

$$v = S_2 - \frac{b(S_2 - v_o)e^{-b\zeta}}{b + a(1 - e^{-b\zeta})|S_2 - v_o|} \quad 6.13$$

and the displacements becomes:

$$h_1 = S_1 \zeta - \frac{1}{(a) \operatorname{sgn}|S_1 - u_o|} \ln \left\{ 1 + \frac{a(1 - e^{-b})S_1 - u_o}{b} \right\} \quad 6.14$$

and

$$h_2 = S_2 \zeta - \frac{1}{(a) \operatorname{sgn}|S_2 - v_o|} \ln \left\{ 1 + \frac{a(1 - e^{-b})S_2 - v_o}{b} \right\} \quad 6.15$$

Hutchinson *et al.* (1970) suggested that the contact time between eddy and drop is t_d . Logically, it is assumed that the drop/eddy contact time can not exceed the eddy lifetime:

$$\zeta = 1.6 = \frac{T_e}{L_e/U_e} \geq t_d \quad 6.16$$

Star-CD employs a similar simulation. However, there are several differences between the Hutchinson *et al.* (1970) and the present study. First is that here a two-equation high Reynolds $k-\varepsilon$ (turbulent kinetic energy and dissipation respectively) model is employed, which is contrary to the model by Hutchinson (1970). The latter being a single or “zero-equation” model since it finds its basis in the mixing length model. Second, the flow mechanisms are two-way coupled, i.e., the gas phase interacts with drops and vice versa. Third, the momentum energy and mass evolution is solved for lateral and axial directions. Fourth is that the number of droplets injected into the system is 100 to 200 times greater compared to the studies carried out at Harwell. However, to keep the time required to complete a sufficient amount of iterations reasonable, neither coalescence nor deposition was included, i.e., droplets were unable to coalesce and disappeared from the domain outlet or hit the wall or evaporated from the system. The latter ties in with the work of James *et al.* (1980)

Verification of the performance of the $k-\varepsilon$ model was achieved by running one case with the more complex Reynolds Stress Model. This model employs a more advanced turbulence model. The computational power required is however much higher, resulting in longer iteration times. The results are shown in the next section.

The mesh is designed by Tkaczyk (2011). Pipe lengths of 5 m (32 mm pipe) and 10 m (127 mm pipe) were used. Injection points were at 3 and 3.5 m from the pipe inlet respectively. This allows for development of the continuous phase flow prior to drop injection at with a time interval of 1 s. The lack of sensitivity of the calculation to mesh size was confirmed by using meshes with increasing numbers of cells. It is verified here by considering cases where the number of cells was increased by a factor 2 for both 32 and 127 mm diameter pipes; meshes used are shown in Figure 6.2 and 6.3. The gas velocity profiles obtained using both cases showed no significant differences (Figure 6.4 and 6.5)

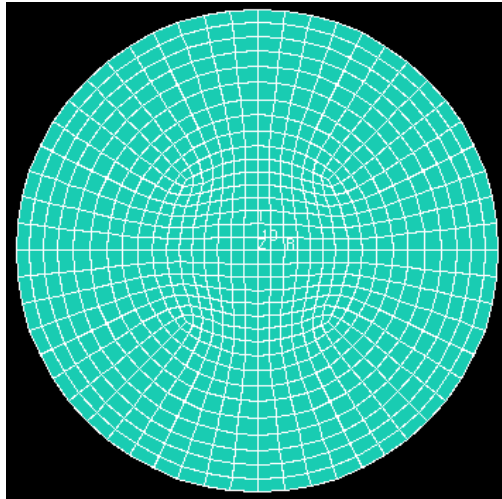


Figure 6.2 Initial Mesh 1

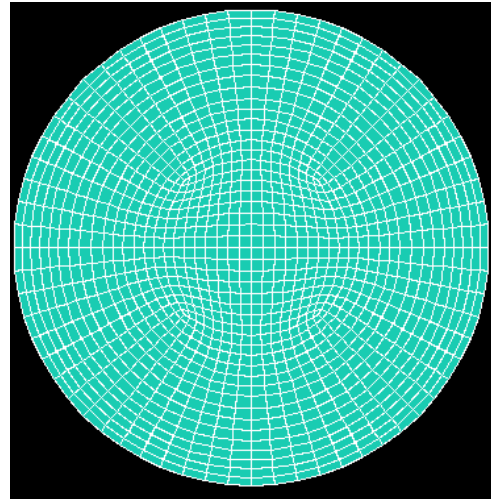


Figure 6.3 Refined mesh 2

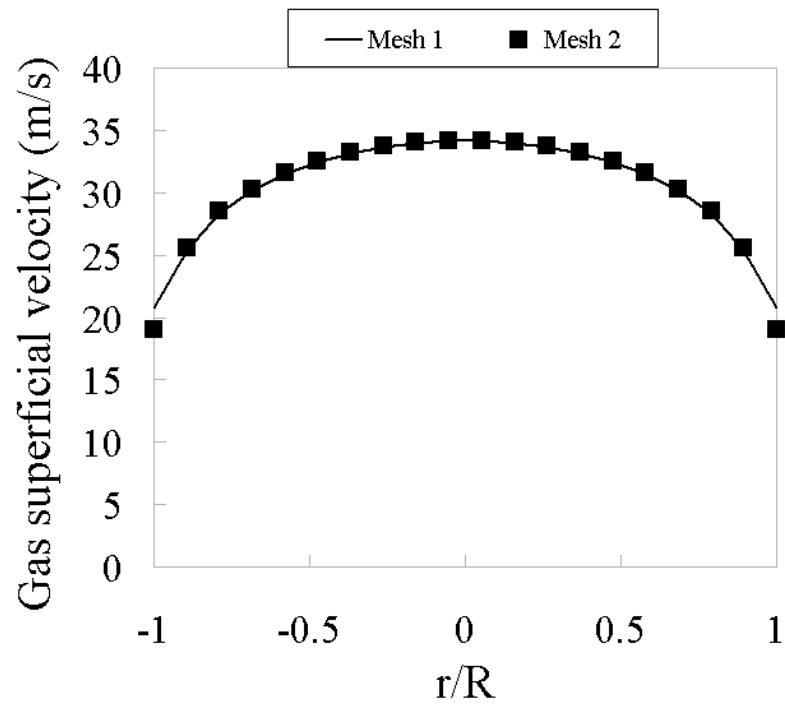


Figure 6.4 Gas velocity profile in the 32 mm pipe.

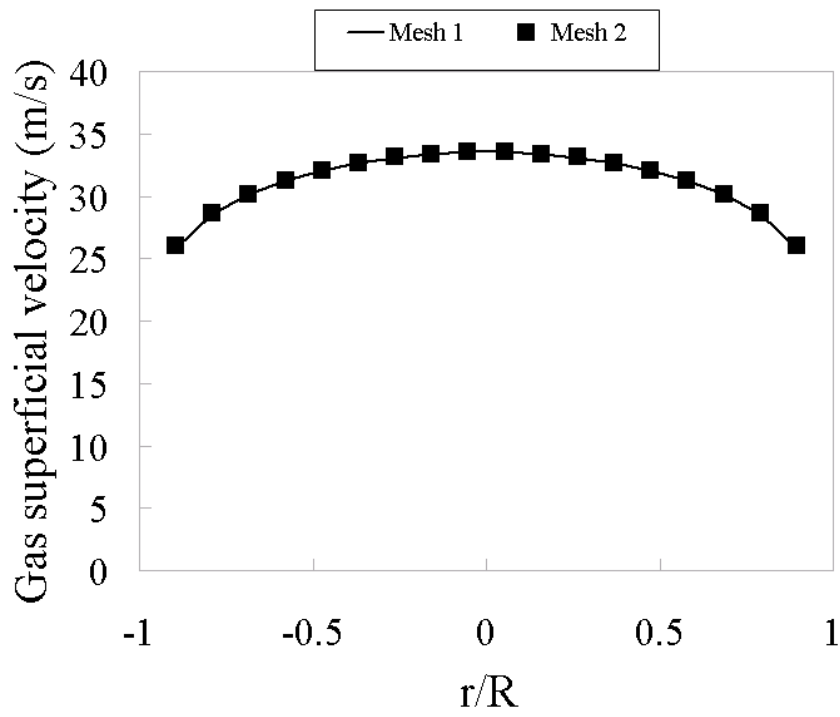


Figure 6.5 Gas velocity profile in the 127 mm pipe.

6.4 Results

The results are presented as drop trajectories in Table 6.2. The results show trends similar to the earlier Harwell work. Differences might well be due to the fact that large numbers of drops are used in the present work than previously rather than be due to the employment of a different turbulence model. In addition, also here drops can move in a direction opposite to that in which the drops were injected. However, because of higher number of drops, this is not always clearly visible.

Runs 1 to 4 are for the 32 mm diameter pipe. Run 1 shows different features when compared to James *et al.* (1980) for the same flow conditions. The lateral plot shows a significant scatter of droplets. The drops penetrate towards the centre of the pipe, but not to a great extent. After injection, they move both in the direction of the opposite semi circle as well as in negative direction relative to the injection direction. In contrast, the results by James *et al.* (1980) show a direct impaction mechanism. This is perhaps the first evidence that the performance of a “zero-equation” model gives a cruder estimate of the droplet trajectory. The results however show a better agreement with those from Andreussi and Azzopardi (1981). The differences could be due to difference in ejection velocity. This is supported by the fact that in Run 3, despite the much larger droplet size, the drops are not yet travelling in a perfectly straight line, indicating that there is still an effect of turbulence at this larger drop size. Run 2 shows the results obtained with the RSM model. From this, it can be observed that the more complex turbulence model does not produce a significant difference from run 3. The results obtained with run 4 are in good agreement with the data by James *et al.* (1980).

In order to compare those from the present work and earlier ones from Harwell, with those for the 127 mm diameter pipe, runs 5 to 7 were carried out. There are differences between runs 5 to 7 and runs 1 to 4; the turbulence intensity and residence time play a more dominant role in the 127 mm pipe. This can be linked to the Reynolds number being proportional to the pipe diameter, i.e. the Reynolds number increases with increasing pipe diameter, provided a constant gas flow rate. Run 5 also shows a more random motion compared to that in the 32 mm pipe. Not many droplets tend to travel beyond one radius centred on the injection point. Note, here all drops are injected radially inwards. Run 6 for medium sized drops is quite different from the equivalent case (run 3) in the 32 mm pipe. Here drops travel back towards the origin in the cross-sectional sense. A similar feature may also occur in run 5 but is less clearly visible. However, the large mass and hence momentum of a larger droplet causes the droplets to penetrate further laterally. Another interesting feature of both runs 6 and 7, compared to 3 and 4, is illustrated by Figure 6.6.

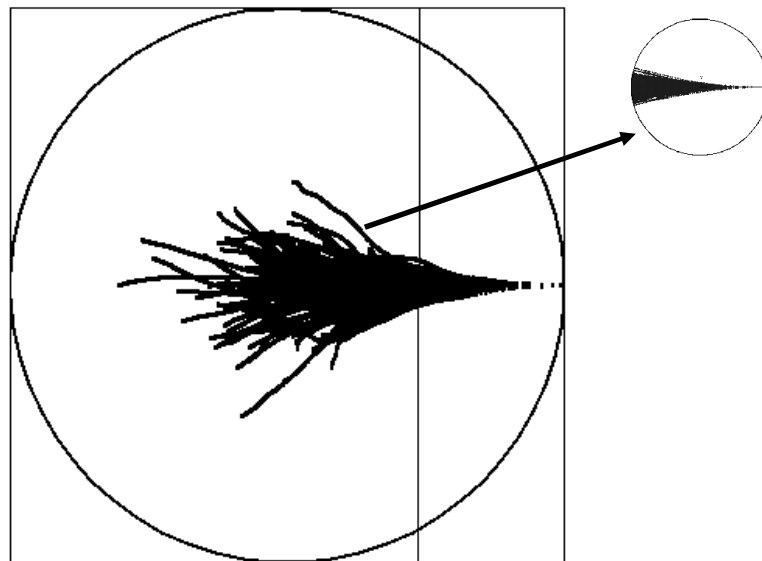


Figure 6.6 Cross sections presented in scaled manner run 7 and run 4

Figure 6.6 highlights a quarter of the 127 mm pipe and the insert shows run 4 with the 32 mm pipe. If one considers that 32 mm is about four times smaller than 127 mm, then the one quarter part of run 7, in which the inertia is greater than the diffusive effect of the continuous phase, it shows similarities with runs 2, 3 and 4. This is perhaps a crude comparison, but, as stated earlier, it suggests that the turbulence intensity and residence time increases with pipe diameter, i.e., turbulence becomes more influential in a large diameter pipe, and this may aid in the explanation for the difference between flow phenomena in small and larger diameter pipes.

Runs 8 to 16 show a different set of runs with gas superficial velocities of 20 m/s. This lower gas flow rate corresponds to the maximum value studied in the current experiments. Run 8 shows features similar to run 5. In run 8, however, majority of the drops reach about 40 percent into the cross-section, whereas in 1 this is about 70 percent. Run 9 can be analysed in the same manner as applied to runs 7 and 4. Figure 6.7 shows the interpretation.

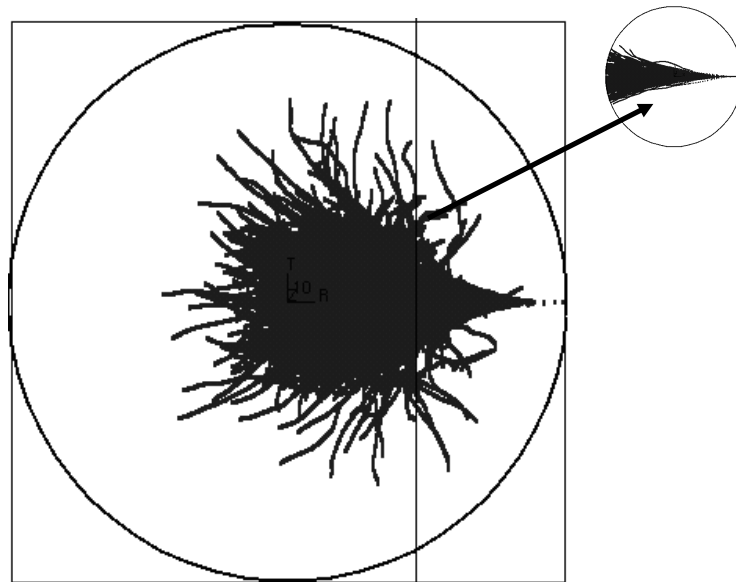


Figure 6.7 Cross sections presented in scaled manner run 9 and run 3

Figure 6.8 below shows a simple illustration of the estimated drop (velocity) response time (Clowe *et al.* 2012) and the time required for a drop to travel from the injection side to the opposite side of the pipe at a constant velocity of 0.7 m/s. This indicates that drops up to 150 μm could respond with a change in direction in a 32 mm pipe and drops up to 650 respond in a 127 mm pipe. This rough estimate ties in with the results presented in Table 6.2 further below.

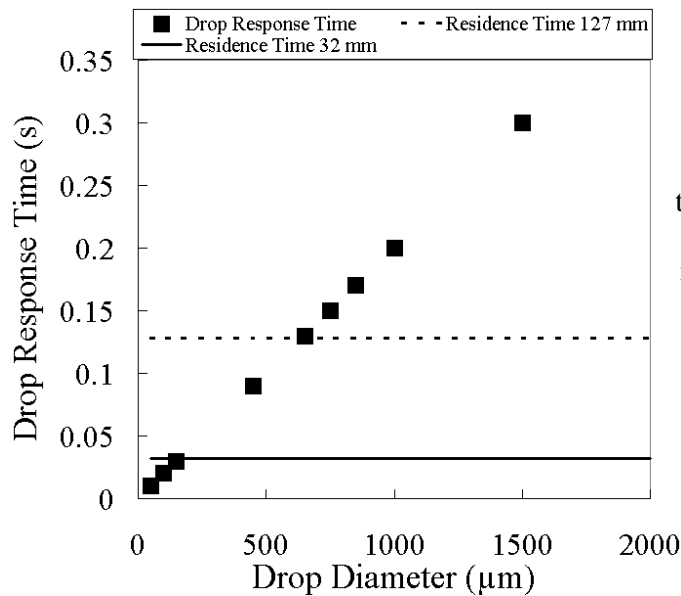


Figure 6.8 Drop response time and the time required for a drop to travel radially at 0.7 m/s in a 32 mm and 127 mm pipe

From run 3 it is evident that the relatively large 450 μm drops in the 32 mm pipe almost all show a direct impaction mechanism. In the 127 mm pipe there is more diffusion. The quarter highlighted in Figure 6.6 could be compared with the behaviour of drops in run 3. On the other hand, comparing run 9 with run 7, the gas superficial velocity and its effect on the turbulence intensity becomes obvious. The drops in run 9 do not have a high momentum compared to run 7 but experience less influence of the continuous phase, and therefore penetrate further into the pipe before diffusion commences. Runs 10 and 11 show the results keeping the drop size constant but changing the parameters of injection and gas superficial velocity respectively. The results are rather self-explanatory.

The results shown for runs 12 to 16 show the behaviour of the droplets with increasing drop size. The change in behaviour is very systematic from diffusion to direct impaction starting from run 13. It is worth noting that for longer pipes deposition would be noticed for smaller drop sizes. Run 12 could be a good example for the latter hypothesis. As mentioned, the drops start hitting the opposite semi-circle in run 13 and the band of droplets narrows to a smaller angle with increasing drop size through to run 16. Runs 17, 18 and 19 represent the results obtained by injecting the drops under various angles as outlined in the framework section of the study. The effect of the ejection angle does not appear to cause major differences in run 17 when compared to runs 1, 5 and 8. The 150 μm drops are very susceptible to the continuous phase turbulence and spread out by diffusion from the start. The function of the trajectory length however plays an important role in the difference between direct impaction and diffusion. This ties in with the results reported for the 32 mm pipe. The drops with a diameter of 450 and 750 μm show similar results to the simulation cases with equal drop sizes. However, the distances the drops travel decrease with increasing deviation from 90° . In order to quantify drops deposition the following relationship is proposed. If D_{diff} is greater than this value deposition is by diffusion.

$$D_{diff} \approx \frac{\delta}{L} = 0.4 \quad 6.17$$

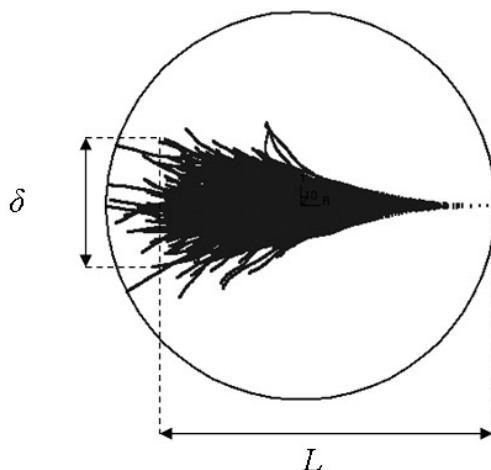
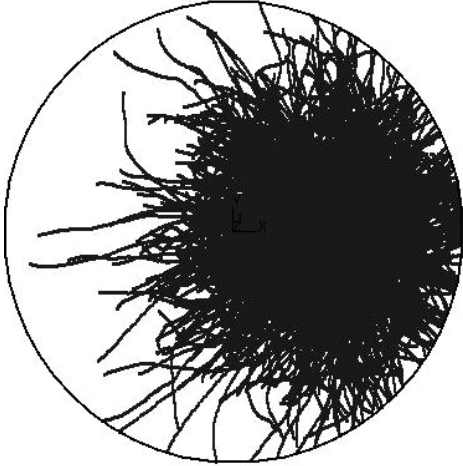
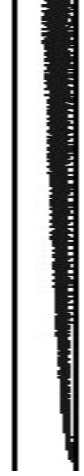
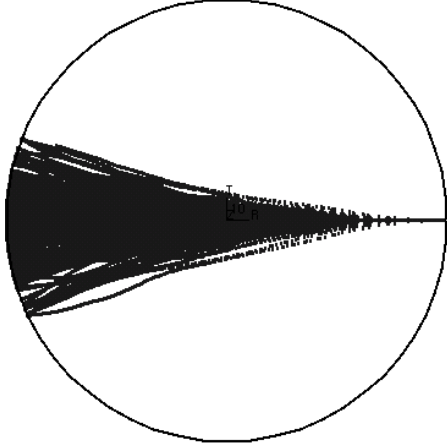

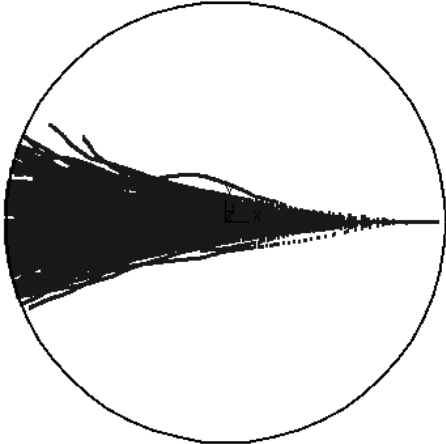
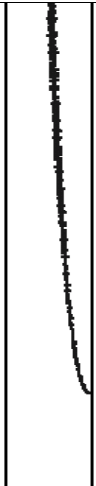
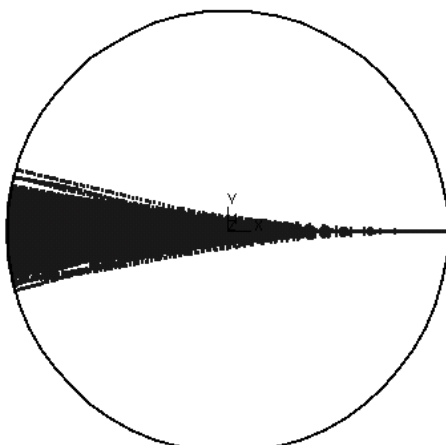
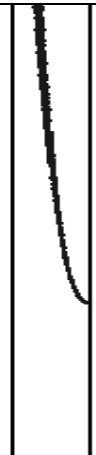
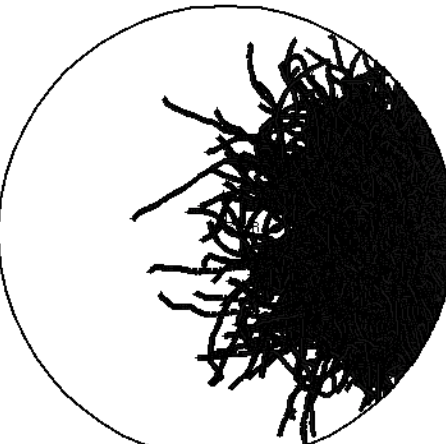

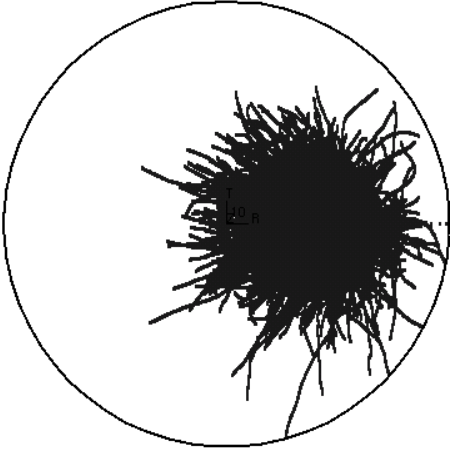

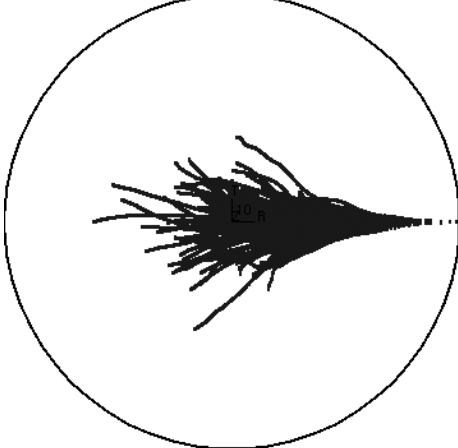

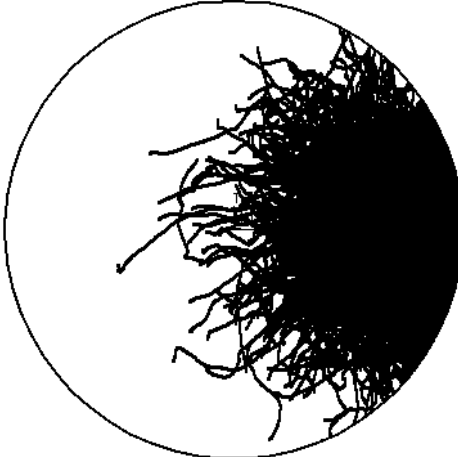



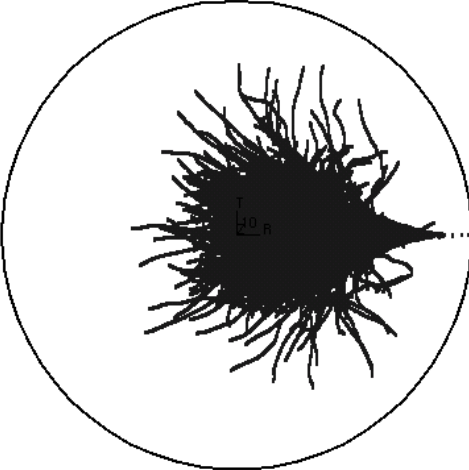
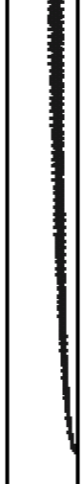
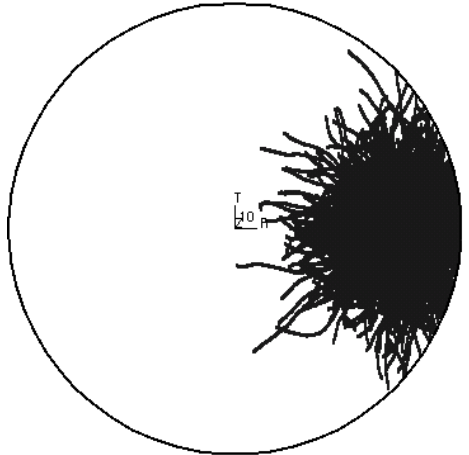

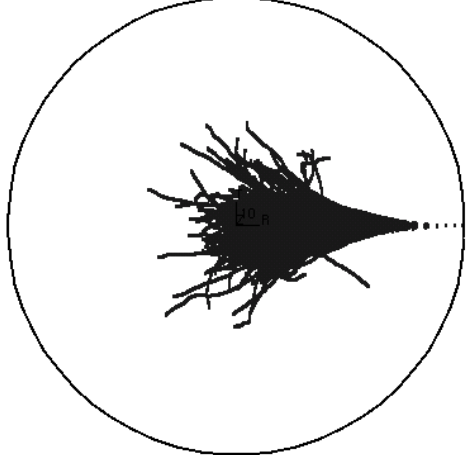
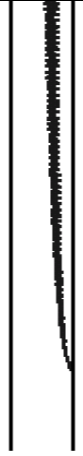
Figure 6.9 Quantification of diffusion, L and δ are the approximate length and width of the bulk of drops

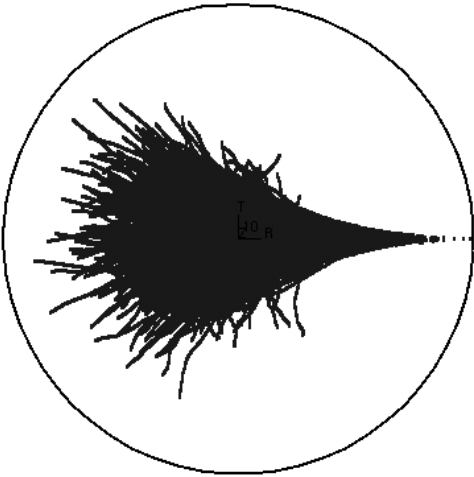

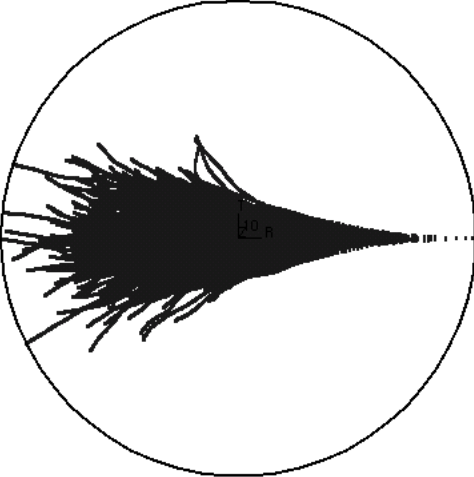

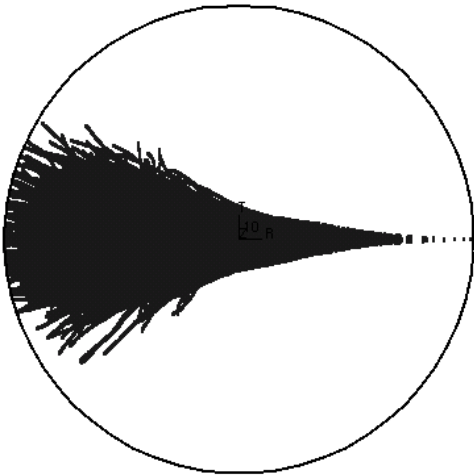

Table 6.2 Simulation results
 (Model, D_t , D_d , U_{gs} and U_I denote the turbulence model employed, pipe diameter, drop diameter, gas superficial velocity and drop ejection velocity respectively).

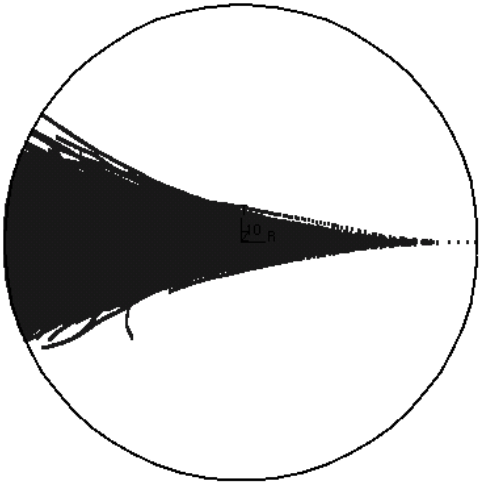

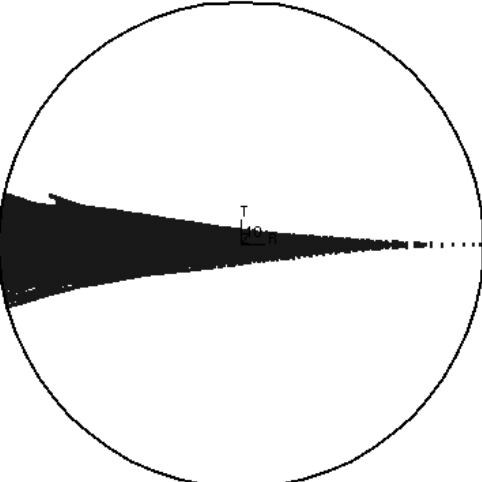

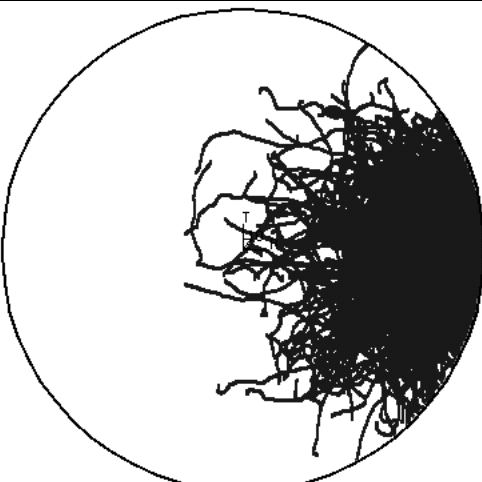

Run	Conditions	Lateral view	Axial view
1	model k- ϵ D_t 32 mm i.d. D_d 150 μm U_{gs} 29 m/s U_I 0.7 m/s		
2	model RSM D_t 32 mm i.d. D_d 450 μm U_{gs} 29 m/s U_I 0.7 m/s		

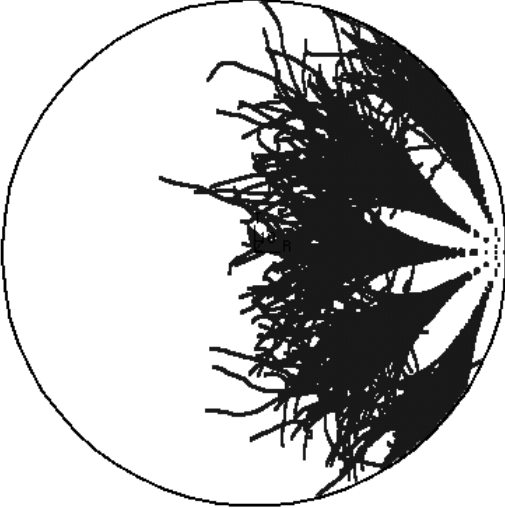

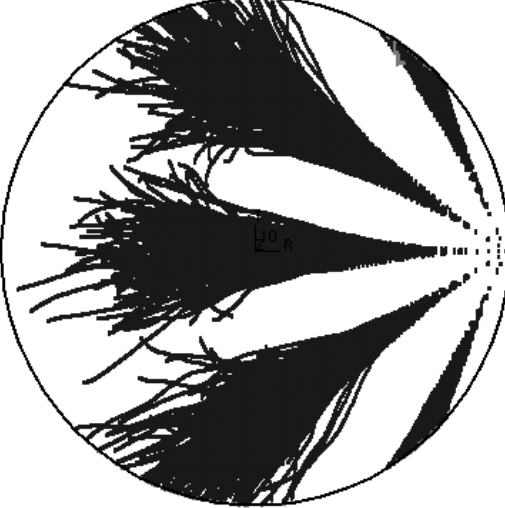

<p>3</p>	<p>model k-ϵ D_t 32 mm i.d. D_d 450 μm U_{gs} 29 m/s U_l 0.7 m/s</p>		
<p>4</p>	<p>model k-ϵ D_t 32 mm i.d. D_d 750 μm U_{gs} 29 m/s U_d 0.7 m/s</p>		
<p>5</p>	<p>model k-ϵ D_t 127 mm i.d. D_d 150 μm U_{gs} 29 m/s U_l 0.7 m/s</p>		

<p>6</p>	<p>model k-ε D_t 127 mm i.d. D_d 450 μm U_{gs} 29 m/s U_l 0.7 m/s</p>		
<p>7</p>	<p>model k-ε D_t 127 mm i.d. D_d 750 μm U_{gs} 29 m/s U_l 0.7 m/s</p>		
<p>8</p>	<p>model k-ε D_t 127 mm i.d. D_d 150 μm U_{gs} 20 m/s U_l 0.7 m/s</p>		

<p>9</p>	<p>model k-ε D_t 127 mm i.d. D_d 450 μm U_{gs} 20 m/s U_I 0.7 m/s</p>		
<p>10</p>	<p>model k-ε D_t 127 mm i.d. D_d 450 μm U_{gs} 20 m/s U_I 0.2 m/s</p>		
<p>11</p>	<p>model k-ε D_t 127 mm i.d. D_d 450 μm U_{gs} 15 m/s U_I 0.7 m/s</p>		

<p>12</p>	<p>model k-ε D_t 127 mm i.d. D_d 650 μm U_{gs} 20 m/s U_I 0.7 m/s</p>		
<p>13</p>	<p>model k-ε D_t 127 mm i.d. D_d 750 μm U_{gs} 20 m/s U_I 0.7 m/s</p>		
<p>14</p>	<p>model k-ε D_t 127 mm i.d. D_d 850 μm U_{gs} 20 m/s U_I 0.7 m/s</p>		

<p>15</p>	<p>model k-ϵ D_t 127 mm i.d. D_d 1000 μm U_{gs} 20 m/s U_l 0.7 m/s</p>		
<p>16</p>	<p>model k-ϵ D_t 127 mm i.d. D_d 1500 μm U_{gs} 20 m/s U_l 0.7 m/s</p>		
<p>17</p>	<p>Multiple injection model k-ϵ D_t 127 mm i.d. D_d 150 μm U_{gs} 20 m/s U_l 0.7 m/s</p>		

<p>18</p>	<p>Multiple injection model k-ϵ D_t 127 mm i.d. D_d 450 μm U_{gs} 20 m/s U_l 0.7 m/s</p>		
<p>19</p>	<p>Multiple injection model k-ϵ D_t 127 mm i.d. D_d 750 μm U_{gs} 20 m/s U_l 0.7 m/s</p>		

6.5 Quantitative information

In the material presented so far, the output of the simulations has been presented pictorially. However, Star-CD simulations provide a wealth of quantitative information. This data was analysed in order to attempt a more detailed quantification of droplets deposited by diffusion and direct impaction mechanisms. Star-CD is able to give a breakdown of drops active, stuck to the wall or otherwise disappeared through the outlet of the flow domain. This breakdown was analysed by means of quantifying the ratio of volume of drops which arrive at the wall and the total volume of drops present, referred to as fractional deposition. Figure 6.10 shows a comparison between runs 1, 3, 4 in the 32 mm pipe and runs 5, 6, 7 in the 127 mm pipe of this ratio. For given drop diameters the volume of drops deposited in the 32 mm pipe is larger than for the 127 mm pipe. In general, this ties in with the analysis presented in the previous section.

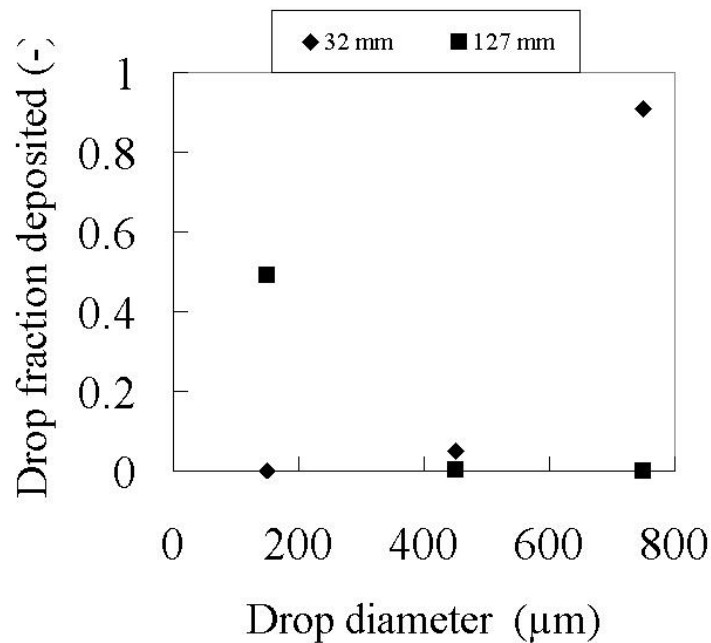


Figure 6.10 Volumetric fractional deposition rates in the 32 and 127 mm pipe. Superficial gas velocity, 29 m/s, drop ejection velocity, 0.7 m/s.

Figure 6.11 shows the data for gas velocity of 20 m/s for both pipe diameters. High levels of deposition are seen for the 150 mm diameter drops. This was not seen at higher gas flow rates in the 32 mm but it did appear in the 127 mm pipe. The latter is probably due to those drops being sent back to the side of the pipe from whence they came by the gas turbulence. For the larger drop diameters, it can be seen that the deposition rate increases with increasing drop diameter. There is a minimum in the deposition rate/drop size curve at 650-750 μm with diffusion dominating at the lower end and direct impaction at the higher.

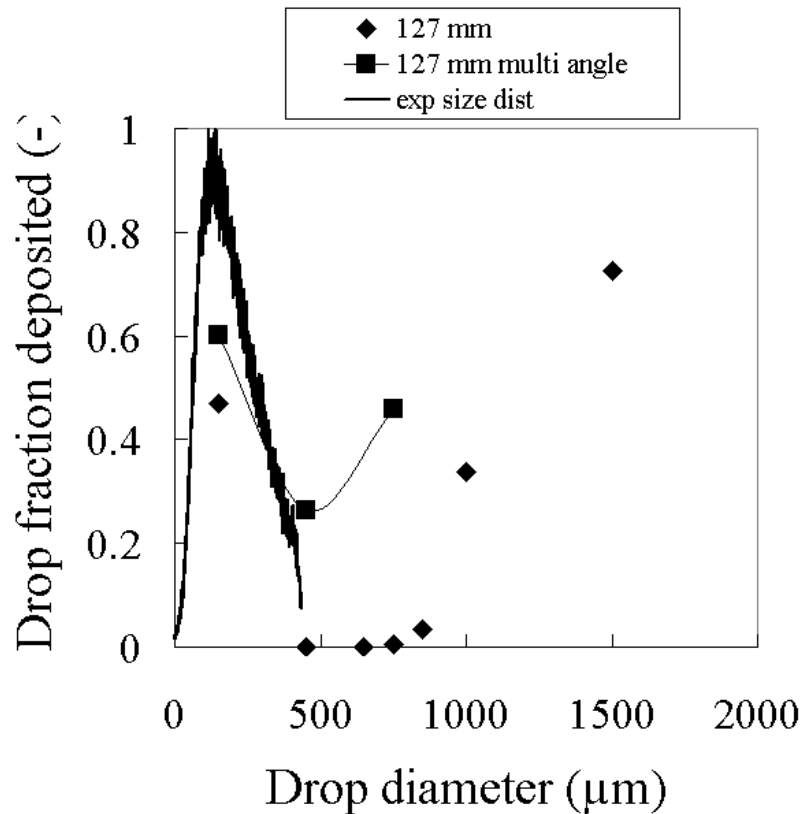


Figure 6.11 Volumetric fractional deposition rates in the 127 mm pipe including multiple angle drop injection. Gas superficial velocity is 20 m/s, drop ejection velocity is 0.7 m/s. Solid line is an experimental size distribution for gas and liquid superficial velocity 20.2 and 0.0045 m/s respectively.

For those simulations with injection at a number of angles there are slightly higher deposition rates than those injected radially. This is related to the distance a drop would have to travel for depositing. Radially injected should be the minimum and the data from the multiple angle injection (127 multi angle) should represent the maximum. All other data is then expected to fall in between. The solid line represents a typical drop size distribution found experimentally in this study, more details on this is presented in Chapter 5. The data suggests that about 60 percent of the small drops would be likely to deposit, whereas only a quarter of the medium diameter drops would deposit. As stated previously, in terms of reality, it should be noted that the multiple angle injection of the droplets can be interpreted as a more complex way of simulation, between one directional and Gaussian injection angles (Figure 6.12). It may be assumed that data for a Gaussian distribution of ejection would show slightly different values.

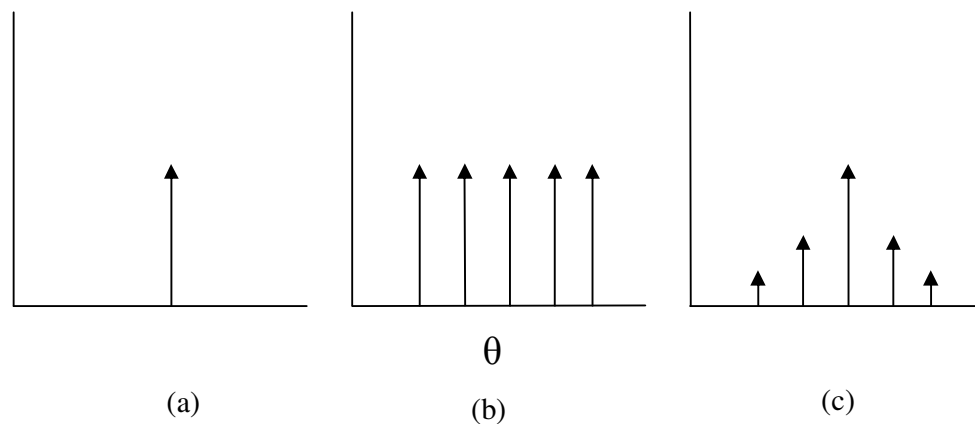


Figure 6.12 Simple approach (a), more complex (b) and Gaussian (c) angular distributions

From the simulations it is possible to extract directional velocity data. The lateral trajectories for runs 1 to 4 are shown in Figure 6.13. The velocity u into the pipe is positive when the drop motion is towards the injection side. As can be seen, the smallest drop diameter shows a strong diffusional pattern. With drop diameter, hence momentum, the evolution smoothens and tends towards direct impaction. Apart from the strong fluctuations, it can be observed that the drop is cumulatively moving in the direction of the opposite quadrant of the injection point but also shows large peaks due to motion towards the wall of injection point. In general it can be noted that some drops adapt a terminal lateral velocity before leaving the pipe outlet without depositing. These are possibly drops that stay closer to the wall and are less affected by the turbulent gas core.

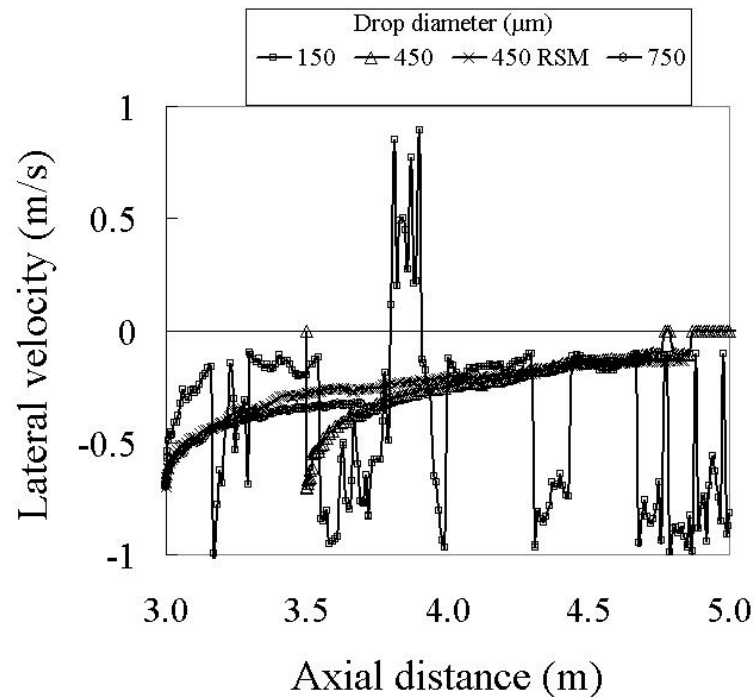


Figure 6.13 Lateral velocity, 32 mm pipe for one drop sample. Note for the 450 μm drop the injection point was set at 3.5 m.

Similarly, for the same conditions in the 127 mm pipe, runs 5, 6, and 7 were plotted as illustrated by Figure 6.14

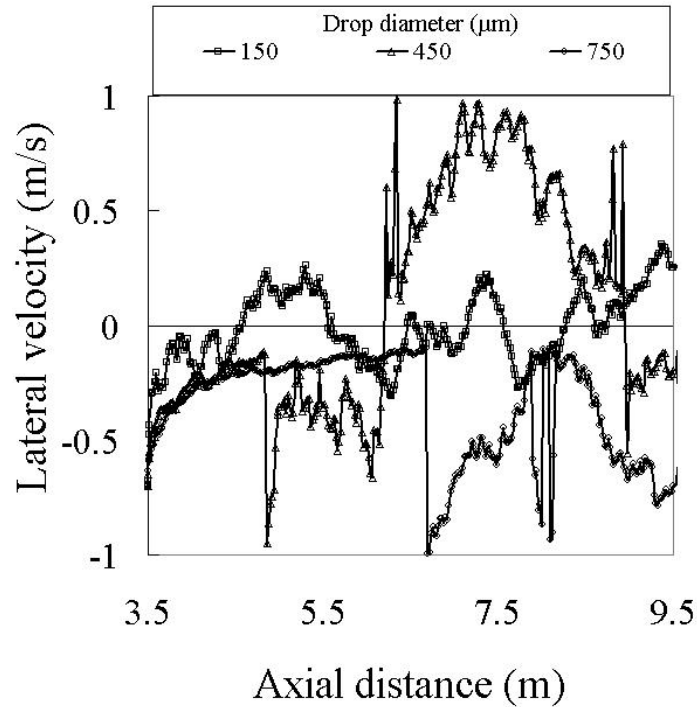


Figure 6.14 Lateral velocity, 127 mm pipe for one drop sample

It is rather obvious, compared to the nature in the 32 mm pipe that the drops in the 127 mm pipe behave more irregular and the magnitude of oscillation for all drop diameters is more intense. This ties in with the observations in the previous section. Interestingly the magnitude of oscillation of the smallest drop diameter in the 32 mm pipe is relatively lower. For the largest drop diameter, a similar direct impaction pattern up to about 7 m can be observed compared to the 32 mm pipe. After this point turbulence plays a dominant role.

The lateral velocities were also plotted for runs 8, 9, 13, 15 and 16, i.e. the 127 mm pipe with a superficial gas velocity of 20 m/s (Figure 6.15). This selection was made to present the data clearly. It can be observed that the lifetime of the 150 μm drop is rather short and impacts on the drop injection side of the pipe. The nature of the 450 μm is comparable with that of the 150 μm drop in run 1. For the remaining drop diameters, the plots start to smoothen and also show that they remain in the core until the outlet.

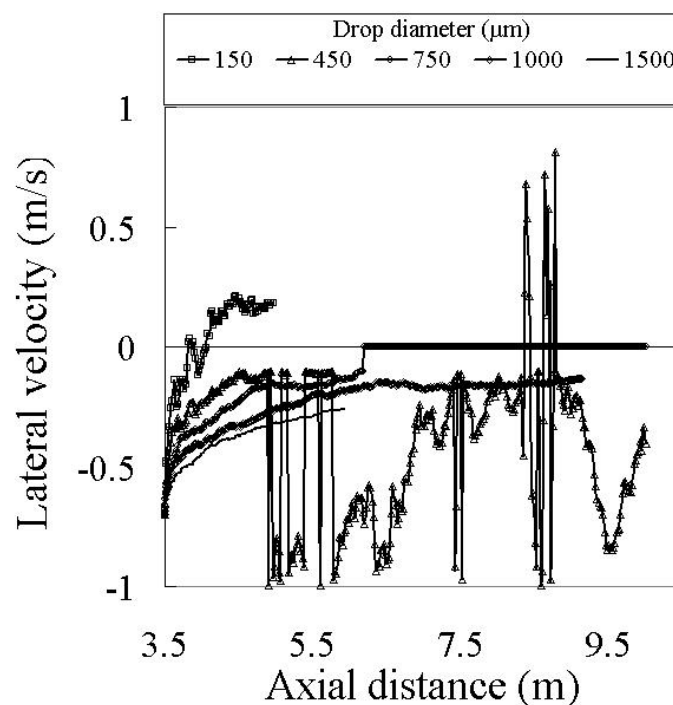


Figure 6.15 Lateral velocity, 127 mm pipe for one drop sample

Lateral velocities for the multiple angle case from runs 17, 18 and 19 are shown in Figure 6.16. Although the direction of the initial momentum is different for these cases, it does still show a similar trend with runs 8, 9 and 13. Except, here the 450 μm drop adapts a terminal velocity after being injected. It is not fully clear why this happens and not a chaotic pattern occurs, but perhaps,

the drop does not travel far enough into the core to be subjected to higher turbulence intensity.

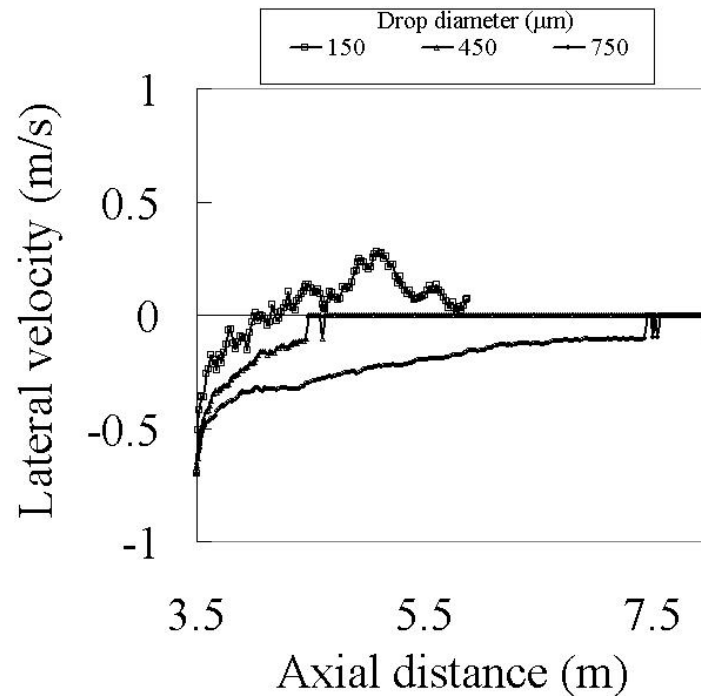


Figure 6.16 Lateral velocity, 127 mm pipe and multiple angle injection for one drop sample.

The axial velocities for the all simulations were also plotted as shown in Figure 6.17 - 6.20. Two features that stand out, (i) is the negative velocity gradient of the drops deposited just prior to impact. As can be seen, this deceleration feature is independent of drop diameter, gas velocity and ejection velocity. The magnitude of the deceleration seems however dependent on the drop size. The deceleration occurs most likely due to the gas velocity profile in the cross-section of the pipe. (ii) the maximum velocities do not deviate so much for drop sizes up to 750 μm . The deviation then increases relatively more with drop diameter.

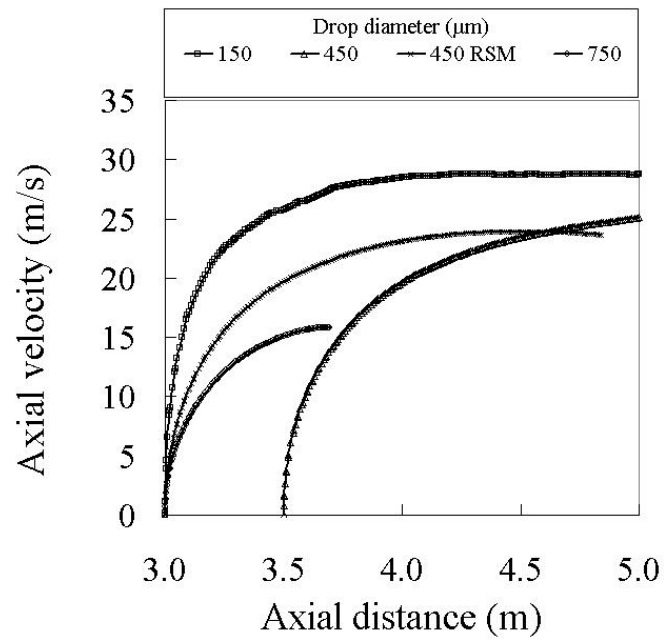


Figure 6.17 Axial velocity, 32 mm pipe for one drop sample. Note for the 450 μm drop the injection point was set at 3.5 m.

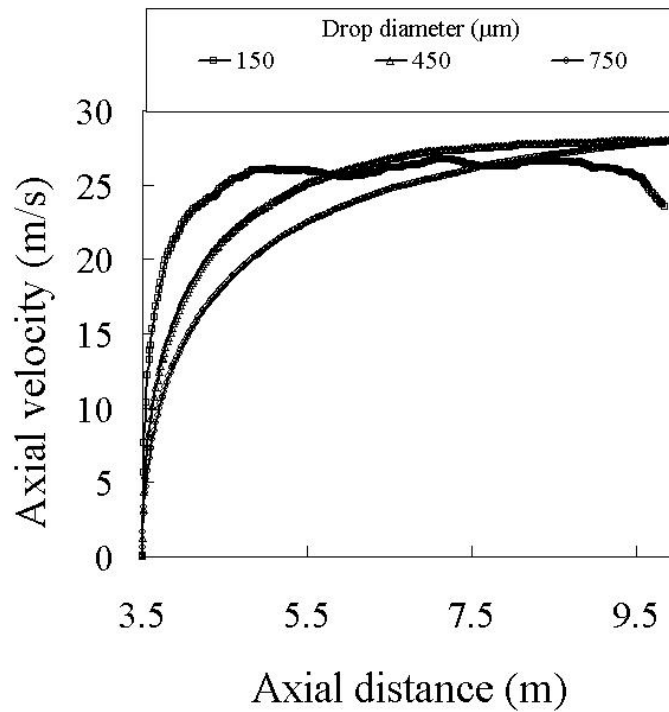


Figure 6.18 Axial velocity, 127 mm pipe for one drop sample

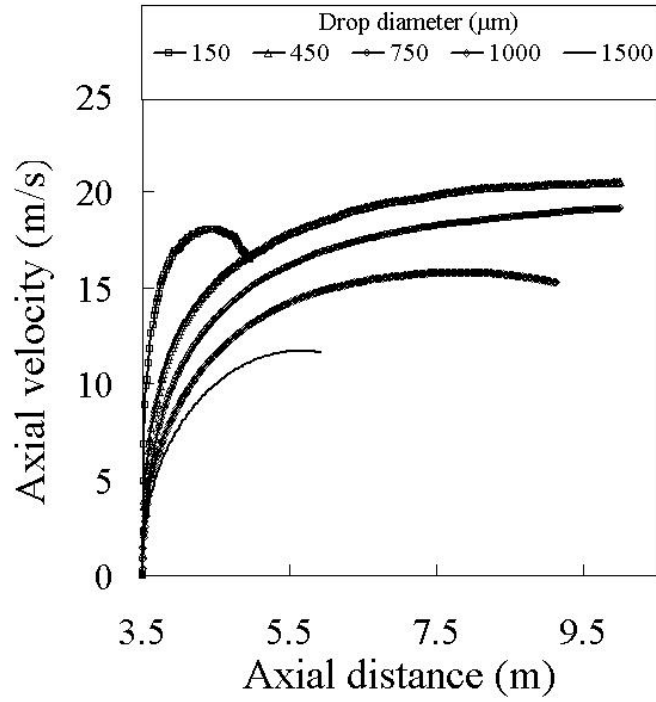


Figure 6.19 Axial velocity 127 mm pipe, for one drop sample.

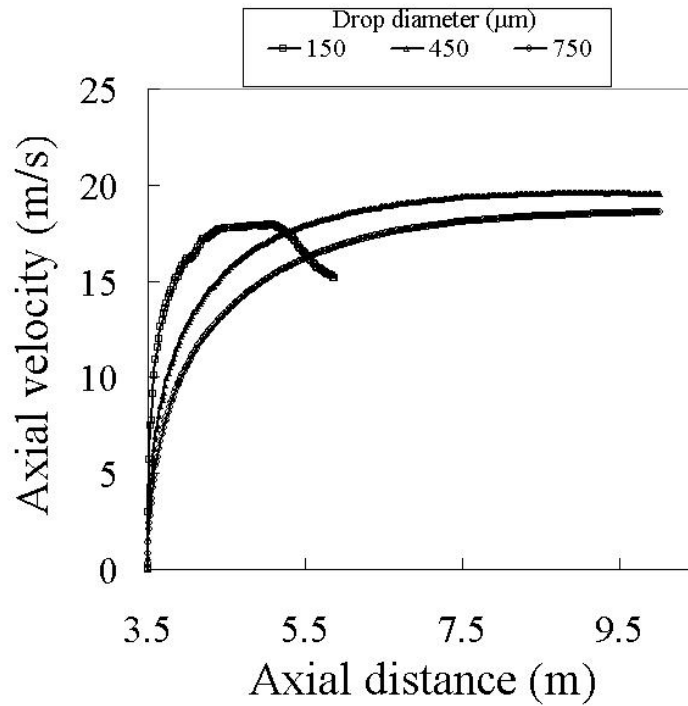


Figure 6.20 Axial velocity, 127 mm pipe and multiple angle injection for one drop sample.

More detailed analysis was done by quantifying the distance of deposition. Figure 6.21 shows the data from runs 1,3 and 4, Figure 6.22 shows the runs 8, 9, 13, 15 and 16 and Figure 6.23 illustrates runs 17 to 19. The cut-off in the Figures is due to drops that leave the computational domain without depositing.

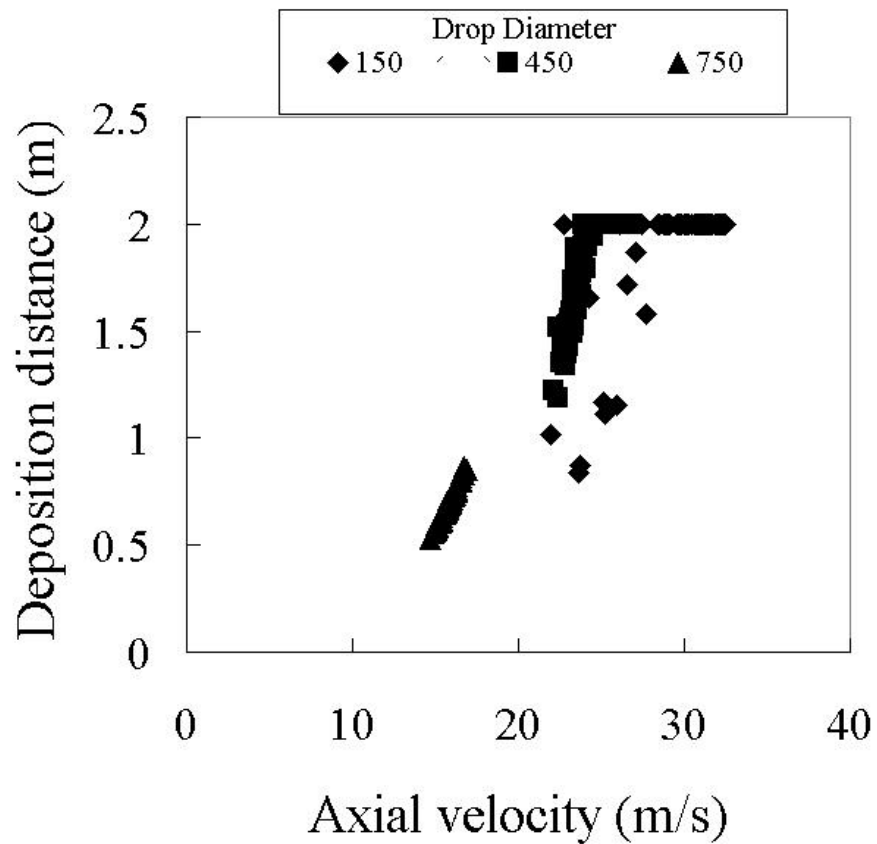


Figure 6.21 Axial distance and axial velocity for runs 1, 3 and 4

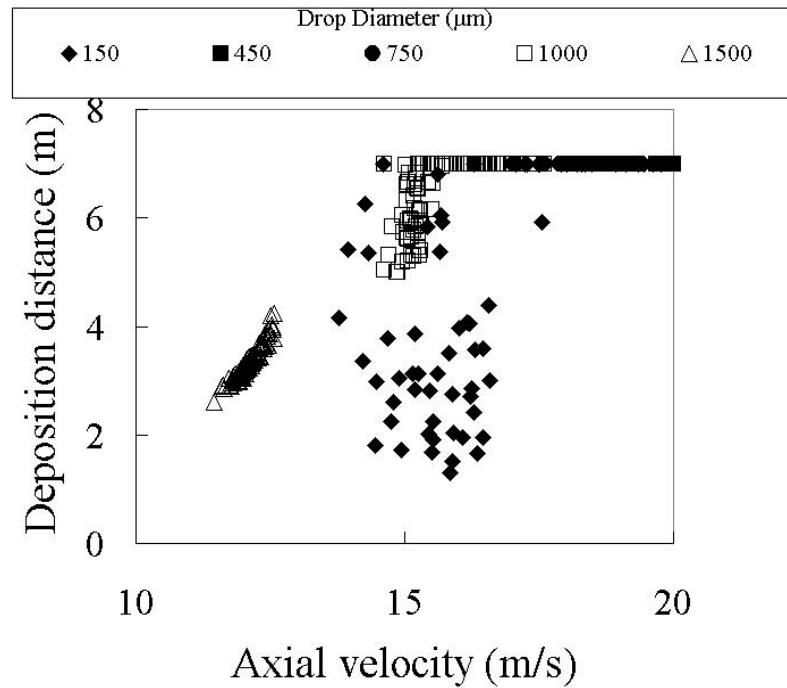


Figure 6.22 Axial distance and axial velocity for runs 8, 9, 13, 15 and 16

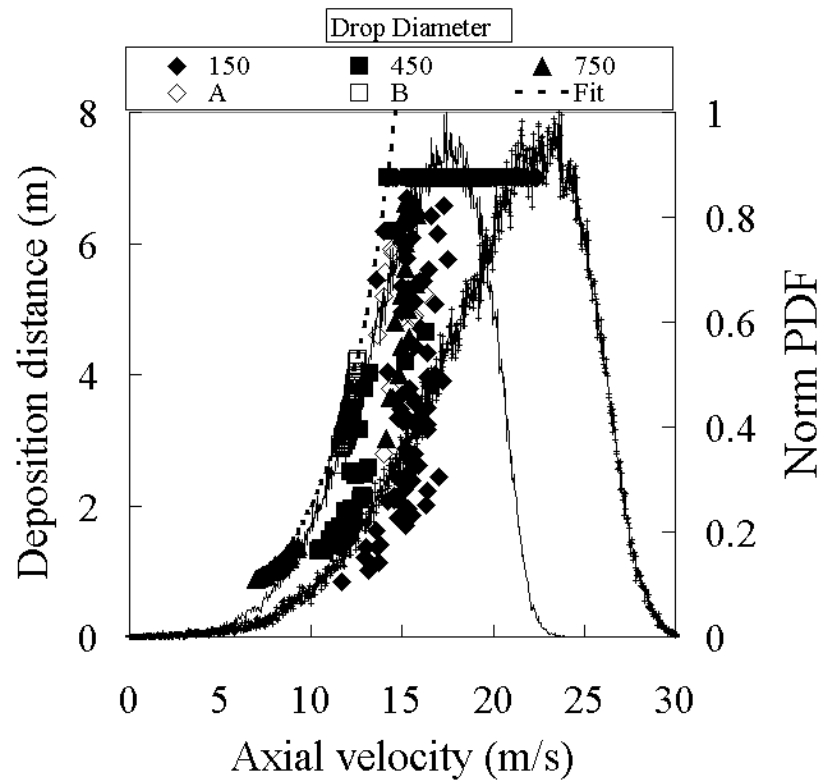


Figure 6.23 Axial distance and axial velocity for runs 17 to 19. For comparison “A” is run 10 and “B” is run 16. Solid line and solid line with marks denote experimentally obtained drop velocity distributions for gas superficial velocities of 16.86 and 20.19 m/s. Liquid superficial velocity 0.0045 m/s

Values of axial drop velocity against axial deposition distance for 100 drops were plotted for all drop diameters. The origin was chosen as the drop injection point. Some drop diameters show hardly any deposition. This is supported by the results in Table 6.2. Apart from the smallest drop size, which clearly shows a diffusional pattern, the former may indicate that some drop diameters have sufficient momentum to reach the core but are carried by the continuous phase until they leave the outlet. In first instance it can be observed that the smaller drop diameters show a considerable range of deposition distances. Also it can be seen that the deposited drops shows an exponential relationship between the two parameters, i.e. the distance travelled by the drop increases with axial drop velocity. The latter does not appear as strongly in the 127 mm pipe. Figure 6.21 has therefore a different x-axis range to magnify this effect. For 1000 μm more data was recorded and also this starts to show an exponential trend. With increasing drop diameter, in general, it can be observed that the deposition distance decreases and is more localised.

Figure 6.24 illustrates data simulations of injections at several angles. These show greater deposition. Obviously, this is a more realistic case. There is a limit below which data is not found. In addition to the aforementioned features, it can be clearly observed that apart from the exponential relationship, the data also shows a minimum boundary (Fit) after which drop deposition only appears to occur. The boundary is formed by the larger drop diameters. As a test two other sets of data, from runs 10 and 16, were plotted to see the effect. Also these appear after the boundary. Although the boundary adopts a very steep slope, it does suggest that all drops for each drop diameter will eventually deposit. Data from smaller drops would shift to the right in the plot, adopting a

higher drop velocity; this implies that the deposition distance increases in a great extent before it touches the boundary, that is, a larger scatter. Larger drops will shift more to the left in the plot, suggesting that both drop velocity and deposition distance decreases. The velocity distribution for two experimental conditions, further described in chapter 5, show that for high gas flow rates, the data indeed skews negatively. Evidence shows that high gas flow rates cause higher rates of drop atomisation, thus the drop diameter is smaller. This works the other way around for low gas flow rates, thus larger drop diameters are expected. For a lower gas low rate, the positive slope of the distribution shows a very similar regression compared to the exponential fit from the simulations. The relationship between axial deposition distance and drop velocity can be approximated using:

$$Z_{dep} \approx \Gamma^{0.3U_{dr}} \quad 6.18$$

In Chapter 5 it is described that the axial drop velocity is about a factor of 1.3 greater than the gas superficial velocity. This factor could be built into Eq. 6.18 for those cases where the axial drop velocity is unknown.

The lateral movement of drops are illustrated in Figures 6.23 and 6.24 for 32 and 127 mm respectively. Note the small drop by depositing rather soon after injection.

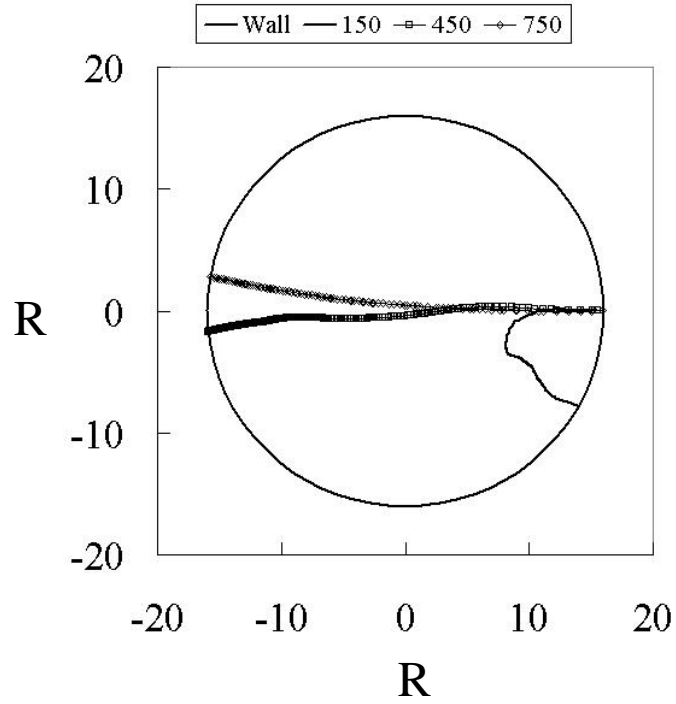


Figure 6.24 Typical drop trajectories in the 32 mm pipe for runs 1, 3 and 4

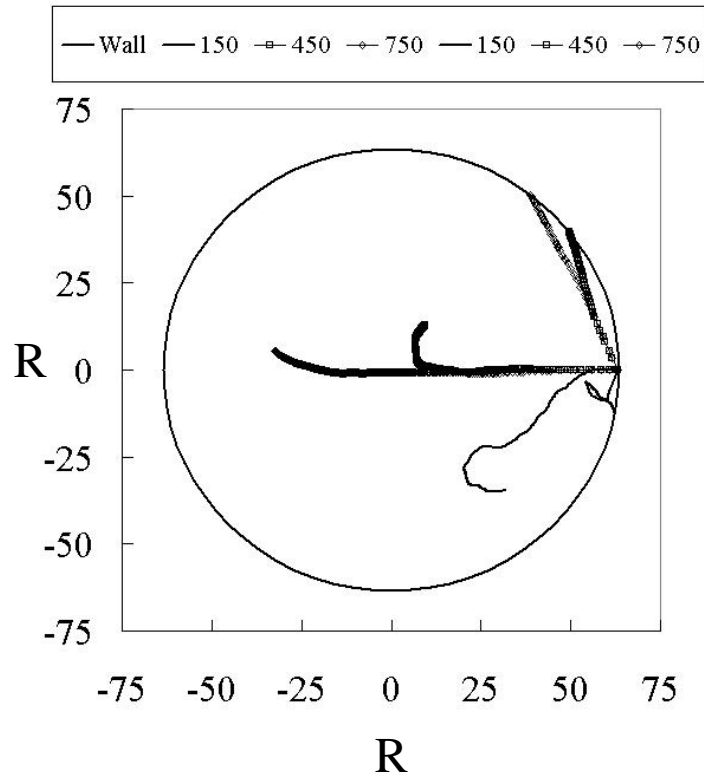


Figure 6.25 Typical drop trajectories in the 127 mm pipe for runs 17, 18, 19 and 8, 9 and 13

From Figures 6.24 and 6.25 it can be observed that there is a strong effect of injection angle on deposition distance. For runs 18 and 19 it can be seen that the some data are closely grouped at low deposition distances. It is not an unreasonable assumption that these data represent either angles of 33 or 66 degrees or the equivalent in the opposite direction. The data was analysed in more detail for run 13, Figure 6.26 shows a Gaussian approximation of the relationship between angle and deposition distance. The points represent the inception of deposition. Most probably, data for larger drops will show lower values and data for smaller drops will show higher values.

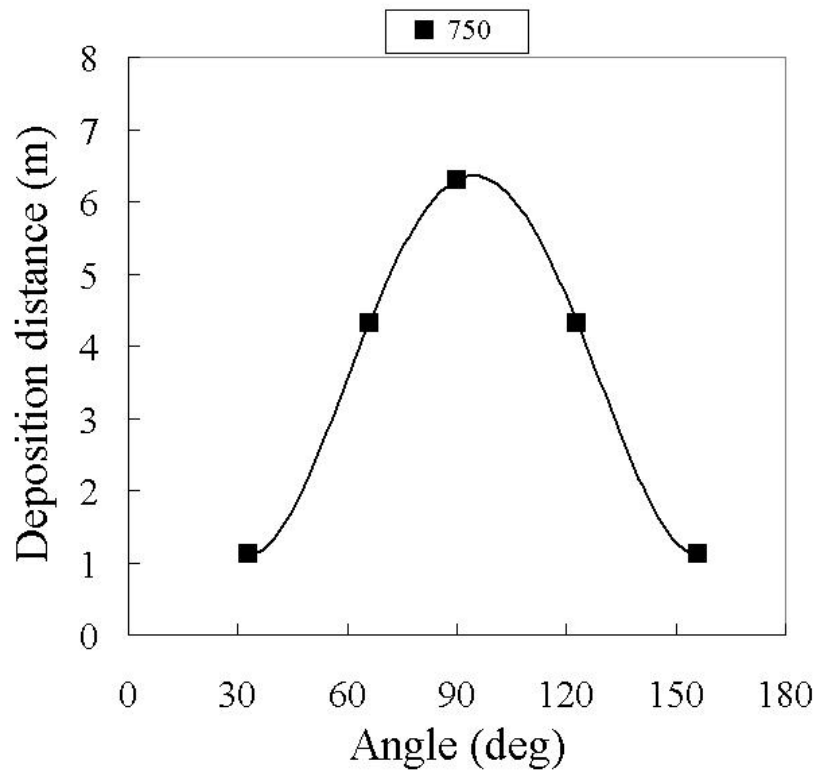


Figure 6.26 Effect of angle of injection on deposition distance.

In order to examine the exact injection angle effect, the data for runs 17, 18 and 19 was categorised in the respective angles under which they were injected. Figure 6.27 shows the deposition results for 200 drops at each angle.

As can be seen the effect of angle on the fraction of drops deposited is indeed of a Gaussian nature. At small angles, i.e, 33 and 156 degrees, large drops show the highest rate of deposition. This switches at angles of 66 and 123 degrees. This suggests that diffusion is dominant and small and medium drops deposit due to diffusive behaviour. For large drops it can be seen, also from Figure 6.26, that they tend to follow the flow to further downstream at 90 degrees. In addition, data from Figure 6.11 for multiple angles was included (open symbols). It could be possible that small drops have diffusive, medium drops transitional and large drops direct impaction characters. However, the angle and thus the interfacial area have a significant effect on the deposition mechanisms.

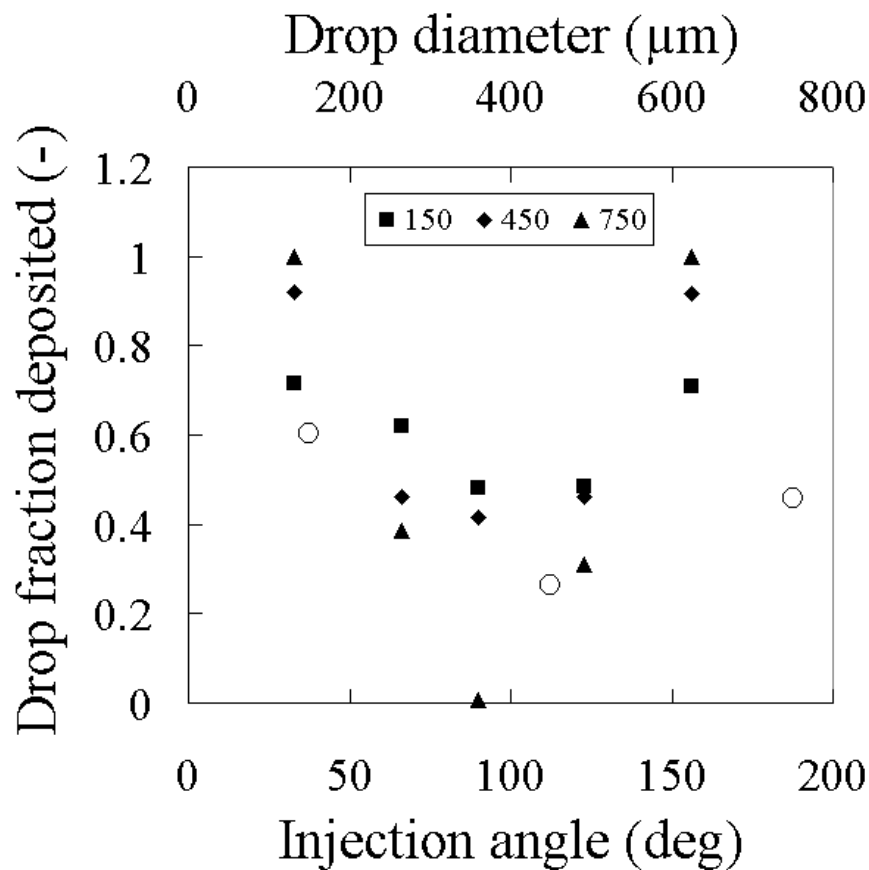


Figure 6.27 Drop deposition fractions for various ejection angles (closed symbols) and diameters (open symbols)

One of the key studies considered important in terms of drop deposition is that by Cousins and Hewitt (1968). Azzopardi (1997) reports that the rate of deposition D consists of two components, the deposition coefficient k and the drop concentration in the core c . Several forms of equations for the rate of depositions were proposed but here the version by Azzopardi (1997) is used:

$$D = kc \quad 6.19$$

As reported by Schadel *et al.* (1988) the equation can also be expressed in the form of

$$D = k_d \frac{4W_{le}}{\pi D^2 U_{gs} S} c \quad 6.20$$

where k_d is a deposition coefficient, W_{le} is the total liquid fraction entrained, D the pipe diameter, U_{gs} the gas superficial velocity and S the slip velocity acting over the droplet. The latter is expressed by

$$S = \frac{U_d}{U_{gs}} \quad 6.21$$

And k can be expressed by

$$k = \frac{k_d}{S} \quad 6.22$$

The deposition coefficients for runs 8, 9 and 12 to 19 were quantified by using the square root of the drop velocity in the x and y direction, expressed by

$$k = \sqrt{u^2 + v^2} \quad 6.23$$

Of all values in the data range, a probability analysis was performed in order to determine the dominant frequency for k . The deposition coefficient for different drop diameters is illustrated by Figure 6.28.

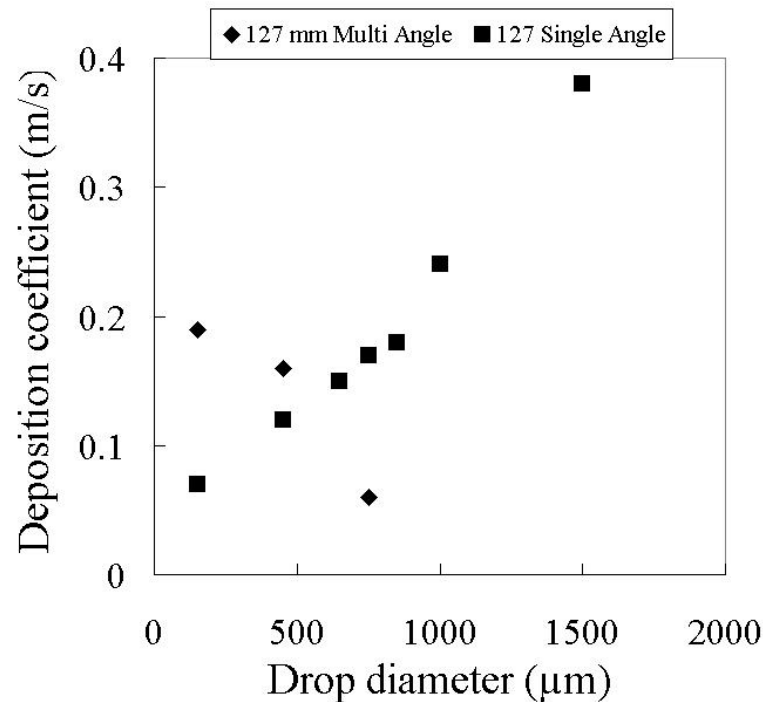


Figure 6.28 Deposition coefficients for runs 8, 9 and 12 to 19

From Figure 6.28 it can be observed that for runs 8, 9 and 12 to 16 there is a change of slope between 650 and 750 μm , indicating a possible transition between diffusion and direct impaction deposition mechanisms. For runs 17, 18 and 19, the results show, in first instance, a surprising downward trend. In combination with the results presented above, this may be due to that small drops show a higher deposition rate than larger drops.

However, considered the results presented above, one may ask the question: Would the two deposition mechanisms suggested at Harwell, diffusional and direct impaction, explain the results obtained in a 127 mm pipe entirely, or is there another mechanism involved in larger pipe diameters? To answer this question, the experimentally obtained data (Chapter 5) was analysed. Azzopardi (2006) suggested a relationship that brings together diffusional deposition data from different fluids and pipe diameters.

$$F_D = 1 - e^{-\left[2.217 \frac{We^{1.42}}{Re_g^{0.89}} + 0.27\right]} \quad 6.24$$

where

$$We = \frac{\rho_g u_{gs}^2 D_t}{\sigma} \quad 6.25$$

and

$$Re_g = \frac{\rho_g u_{gs} D_t}{\eta_g} \quad 6.26$$

Where F_D is the fraction of drops deposited by diffusion. To match the simulations, experiments in which a maximum gas superficial velocity of 20 m/s was obtained were selected. To determine the range of F_D the lowest and highest gas superficial velocities were used from each selected experiment. The results in terms of gas flow rate are presented in Figure 6.29.

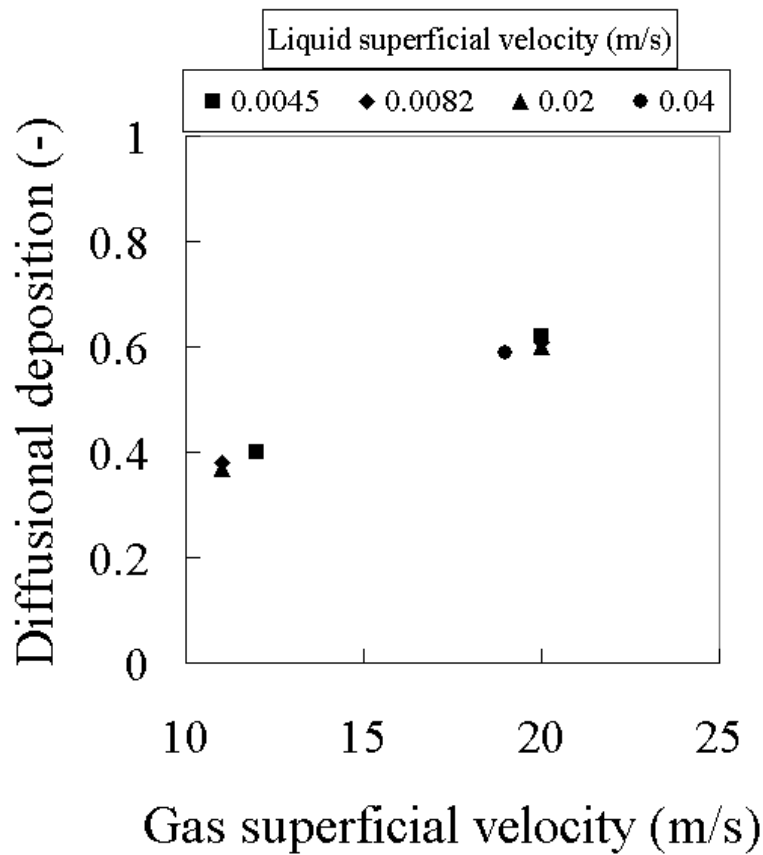


Figure 6.29 Drop fraction deposited by diffusion.

As can be observed, a linear relationship is obtained. This does however neither show a possible effect of drop diameter nor angle effect as observed previously in Figure 6.10 and 6.27. Therefore, the dominant arithmetic drop diameters were extracted from the processed data described in Chapter 5 and the calculated F_D plotted in terms of drop diameter. The results, along with the multiple angle simulation results from Figure 6.10, are shown in Figure 6.30.

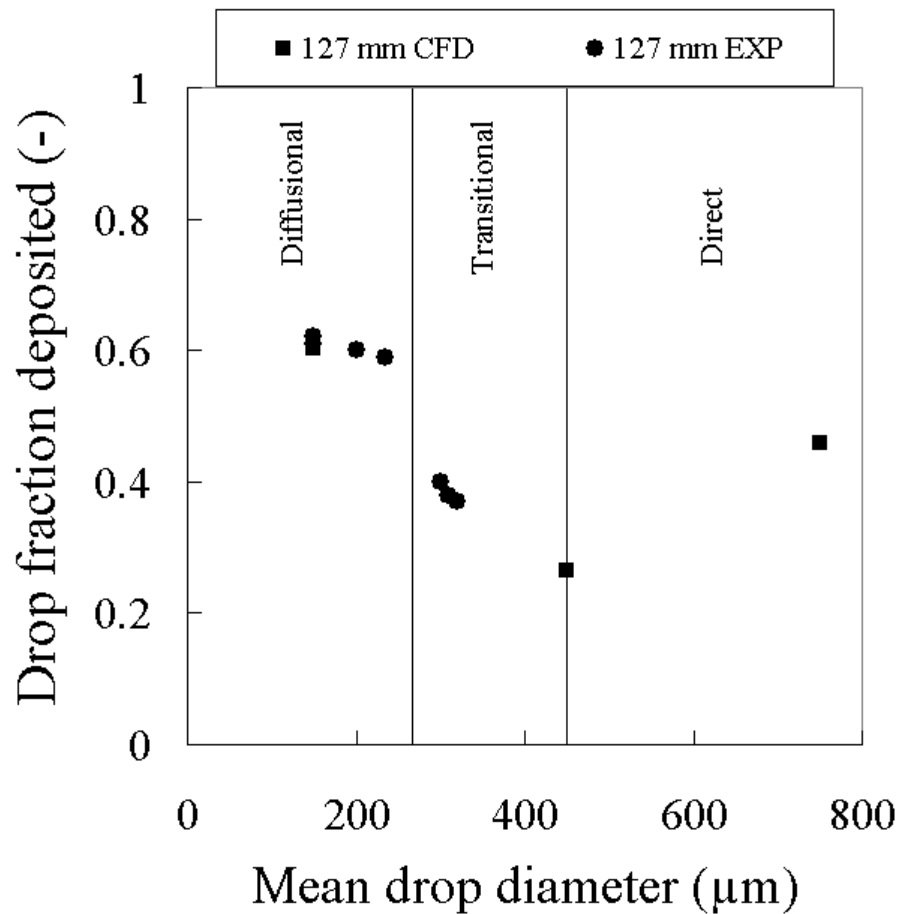


Figure 6.30 Simulation and predicted drop deposition fractions. Simulation results (squares), experimental results (circles) at gas superficial velocities of 20 and 11 m/s and boundaries between the expected deposition mechanisms (solid lines).

As can be observed, the predicted data from experiments agree well with the multiple angle simulations. The most important feature in Figure 6.30 is

that, apart from diffusional and direct impaction deposition mechanisms, another possible mechanism applies to larger diameter pipes, i.e., transitional deposition. In this region, the drops are hindered to travel further radially than half the pipe diameter but instead are carried by the gas core over a large axial distance as can be observed from run 18. They only show a direct impaction mechanism at small injection angles. The predictions by Eq. 6.24 from the experimental data show this feature around the transition from churn to annular flow as proposed in Chapter 4. It could also be argued that, although drops at an experimental gas superficial velocity of 11 m/s are shown, it is generally accepted that drop diameters depend on the gas flow rate. Diffusional deposition occurs at high gas flow rates (annular flow), the drop diameters are smaller and tend to stay more concentrated in the interfacial area from which they were entrained and then deposit due to random motion. Direct impaction seems to depend low gas flow rates (churn flow) on the drop diameter. If the drop is large enough it seems to be able to cross the gas core in a radially straight trajectory to the opposite quadrant. The possible answer to the question asked is therefore that there is strong evidence that indeed a third deposition mechanism is active in larger diameter pipes, perhaps in the transitional area between churn and annular flow. Pipe diameter and thus the trajectory length travelled by a drop plays an important role in these mechanism. Figure 6.31 illustrates the difference between a 32 mm and a 127 mm pipe.

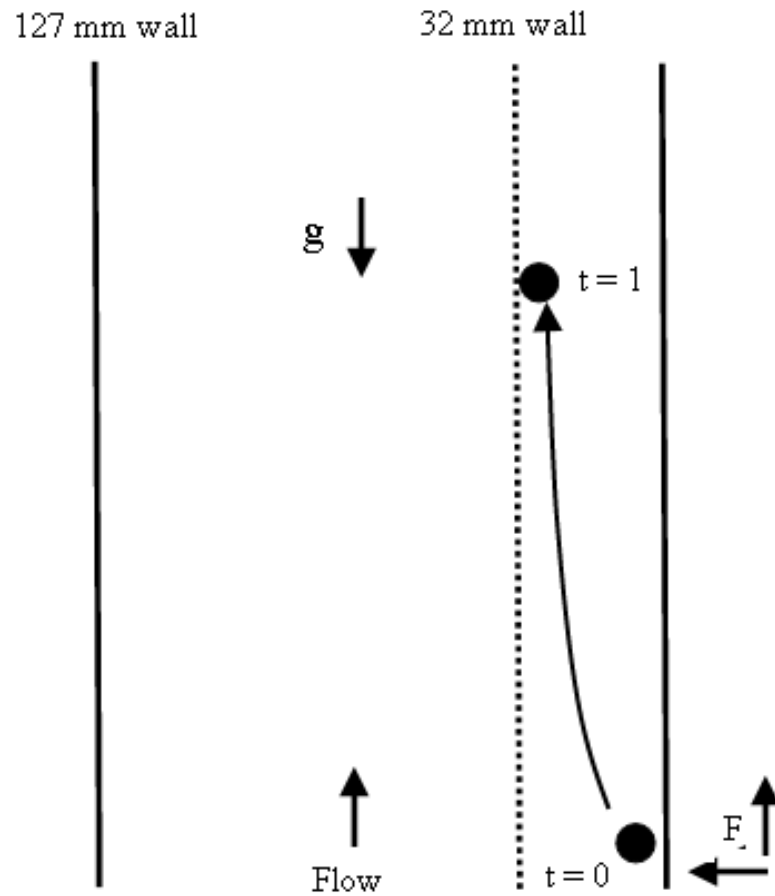


Figure 6.31 Pipe diameter effect

Figure 6.31 suggests that a drop must yield a substantial higher initial momentum in the present study in order to overcome the gas core (turbulence) and travel to the opposite quadrant of the pipe to that in a small diameter pipe.

The above results on deposition, drop diffusion and direct impaction show that all drops in annular type flows will eventually deposit. Though the trajectory can be considerably long.

This is linked to the drop and gas momentum and the angle of injection. In addition, values for the deposition coefficient are reported which show high values for small drop diameters and low values for large drop diameters.

Lateral velocities overall show a chaotic nature for small drop diameters, i.e. sometimes travelling both towards the opposite side of the pipe and back towards the ejection side of the pipe. This chaotic behaviour decreases as drop diameters increase.

Diffusion only occurs for a drop diameter of 150 μm in the 32 mm diameter pipe, beyond this it is direct impaction, i.e., two deposition mechanisms apply: diffusional and direct impaction. This agrees with the results in a 32 mm pipe from studies carried out at Harwell.

In addition to diffusional and direct impaction, in a 127 mm pipe, there is evidence that a third deposition mechanism applies, i.e., transitional deposition. In this region, the drops are hindered to travel further radially than half the pipe diameter but instead are carried by the gas core over a large axial distance as can be observed from run 18. They only show a direct impaction mechanism at small injection angles. The predictions from the experimental data show this feature around the transition from churn to annular flow. This may support the observations of transition from churn to annular flow in Chapters 4 and 5.

7 Conclusions and Recommendations

The main aim of this thesis is to quantify the churn to annular flow transition for vertical gas-liquid flows in a 127 mm diameter riser. The experimentally obtained results for cross-section averaged and local phase fractions, film thickness and the dispersed phase, i.e., drops, are used. This chapter presents the conclusions drawn from the results and interpretation of experimental data obtained in this study. In addition, recommendations are made for future research.

7.1 The liquid film and pressure drop

It is observed that churn flow covers a wide range of flow rates in the large diameter pipe studied.

Analysis and comparison of trends in the film thickness, structure velocity, pressure drop and its gravitational and frictional components show that the gravitational component of the gas core is dominant in churn flow. The density of the core increases significantly with increasing liquid flow rate. The interfacial shear stress is commonly calculated using a one-dimensional approach, i.e., the total pressure drop multiplied by some geometrical factor to account for the film thickness. This does hold in annular flow (at very high and low gas and liquid velocities) since the density of the gas core is insignificant. There is evidence that in churn flow this is not valid. The wall shear stress is calculated by including the interfacial shear stress.

Therefore refined interfacial and wall shear stress equations are proposed to be used for churn flow in these large diameter pipes.

Consequently the results for the interfacial friction factor, showed that for annular flow the results agreed with e.g., the Wallis (1969) friction factor. For churn flow however the results did not agree well.

Therefore, also a refined equation is proposed to be used for these large diameter pipes.

A churn-annular flow transition boundary has been derived based on trends in film thickness, pressure drop and structure velocity data. It is supported by observations made using high speed photography. Minima are found in plots of film thickness and pressure gradient against gas superficial velocity at low liquid flow rates. These minima are not clearly visible at higher liquid flow rates.

By extensive analysis of the boundary derived for the present study and comparison of boundaries proposed by other workers based on a range of different pipe diameter, physical properties of the fluids and experimental flow conditions, a more unified correlation is derived. The correlation is based on dimensional analysis by using dimensionless quantities.

The correlation predicts the boundaries observed reasonably well

7.2 Drop size, velocity and liquid entrainment

Evidence has been observed of new waves being created by large drops impacting on the film surface.

The profiles of the velocities of the drops as well as the gas (obtained using tracer drops $<20\mu\text{m}$) both show a maximum peak at the pipe centerline. This is typical for these types of turbulent flows.

From the analysis of the drop velocity probability distributions there is evidence that when the Gaussian shape of the probability is symmetrical, the ratio between the highest probable drop velocity obtained and the associated gas superficial velocity is around unity. This is evidence that the slip velocity is thus near-zero. This phenomenon occurs and finds support from and at the churn to annular flow boundary conditions identified above.

The entrained fraction in the gas phase shows an increasing trend in churn flow with increasing gas flow rate. This entrained fraction in churn flow is instead perhaps due to large waves and wisps and not necessarily droplets only. This is supported by the occurrence of huge waves and wisps observed from the WMS data at these conditions. At higher gas flow rates the entrainment shows a decrease. Following the ideas of Azzopardi and Wren (2004), this is perhaps due to a higher rate of break-up and atomisation of large waves and wisps. This is expected to be an onset of annular flow. At the very high end of gas flow rate the entrainment predictions again shows an increasing trend. This may occur since no longer are large waves present and liquid mass transfer between the phases is only from the relatively thin liquid film. This is expected to be annular flow with a fairly homogenously-dispersed entrained liquid fraction.

7.3 CFD drop simulations

There is evidence that the axial trajectory of drops can be considerably

long. Drops of a large size class deposit sooner than drops of middle size classes. Small size classes show more diffusive characteristics, and would therefore take a longer distance to deposit. This is linked to the drop and gas momentum and the angle of injection.

A relationship has been derived to estimate the deposition distance of drops of all sizes only depending on the drop velocity.

The drop ejection angle and size were successfully related to the volumetric fraction of drops deposited back onto the pipe wall. There is evidence that the drop fraction deposited is larger for small ejection angles. The fraction deposited also shows dependence on size in the sense that it shows a minimum with increasing drop size. Small drops have high deposition fractions, middle sized show a minimum and towards larger sizes the fraction deposited shows an increase.

From comparison between drop fractions deposited by diffusion and direct impaction in the CFD and experimental results, there is evidence that in large diameter pipes a third deposition mechanism applies: Transitional deposition. In the analysis the Reynolds and Weber number are the driving dimensionless numbers. These numbers are smaller for lower gas flow rates, implying that transitional impaction occurs at medium sized drops at medium gas flow rates. Around these conditions, large waves are present in the flow as described above. It may well be that the third deposition mechanism occurs since it is plausible that the majority of entrained liquid is carried in large waves and wisps as reported above. Therefore, at the transition from churn to annular flow in large

diameter vertical pipes, the behaviour of the flow is not typical to that observed in smaller diameter pipes.

7.4 Recommendations for further work

With the key areas of interest identified, the next recommendations can be made for further investigation. Apart from the fact that a 127 mm pipe diameter is considerably larger than in the majority of studies, even larger pipes could be investigated to examine the effect of pipe diameter on flow patterns and transitions. Especially drop size, velocity and the entrainment mechanisms in churn and the churn to annular flow transition could be further explored. A better understanding of the entrainment is of crucial importance for flow models. Studies in flexible risers could be undertaken to quantify differences between straight and pipe flow with different orientations simultaneously. Further and more detailed dimensional data analysis could bring datasets for small and large diameter pipes closer together.

References

Ahmad, M., Peng J.D., Hale, C.P., Walker, S., Hewitt, G.F., (2010) Droplet entrainment in churn flow. Presented at the International Conference on Multiphase Flow 2010 (ICMF-2010), May 30 - June 4 2010, Tampa, Florida.

Alexander, L.O., and Coldren, C.L., (1951). Droplet Transfer from Suspending Air to Duct Walls, Ind. Eng. Chem., Vol. 43 pp 1325-1331

Altunbas, A, PhD thesis, University of Nottingham, Private Communication.

Ambrosini, W., Andreussi, P., and Azzopardi, B.J. (1990). A physically based correlation for drop size in annular flow. Int. J. Multiphase Flow Vol. 17 pp 497-507

Andreussi, P., and Azzopardi, B.J., (1983) Droplet Deposition and Interchange in Annular Two Phase Flow. Int. J. Multiphase Flow Vol. 9 pp 681-695.

Andreussi, P., and Azzopardi, B.J., (1984). On the Entrainment of Drops by the Gas in Two Phase Annular Flow. Chem. Eng. Science. Vol. 39 pp 1426-1428

Andreussi, P., Di Donfrancesco, A. and Messia, M. (1988) An impedance method for the measurement of liquid hold-up in two-phase flow. Int. J. Multiphase Flow, Vol. 14 pp 777-785

Asali and Hanratty (1995). Ripples Generated on a Liquid Film at High Gas Velocities. Int. J. Multiphase Flow Vol. 19 pp 229-243

Azzopardi, B.J., (1979). Measurement of Drop Sizes. Int. J. Heat Mass Transfer. Vol 22, pp 1245-1279.

Azzopardi, B.J., (1983) Mechanisms of Entrainment in Annular Two-Phase Flow. UKAEA Report AERE-R11068

Azzopardi, B.J., Freeman, G., and Whalley, P.B., (1978) Drop Sizes in Annular Two-Phase Flow. UKAEA Report AERE-R8227

Azzopardi, B.J., Freeman G. and King, D.J., (1980) Drop sizes and deposition in annular two-phase flow. *UKAEA Report AERE R9634*

Azzopardi, B.J., Pearcey, A, and Jepson, D.M, (1991) Drop size measurements for annular two-phase flow in a 20 mm diameter vertical tube. *Exp. Fluids*, 11, pp. 191–197.

Azzopardi, B.J., Taylor S., and Gibbons, D.B. (1983). Annular two phase flow in a large diameter tube. *Int. Conf. Phys. Mod. of Multiphase Flow*, Coventry, UK.

Azzopardi, B.J., (1987) Observations of Drop Motion in Horizontal Annular Flow. *Chem. Eng. Science*. Vol. 42 pp 2059-2062.

Azzopardi, B.J., (1997). Drops in Annular Two-Phase Flow. *Int. J. Multiphase Flow* Vol. 23 Suppl. pp 1-53

Azzopardi, B.J., and Hills, J., (2001) Published in; Bertola, V, (2003) *Modelling and Experimentation in Two Phase Flow*, CISM Courses and Lectures No.450. International Centre for Mechanical Sciences, ISBN 3-211-20757-0. Springer-Verlag. Wien New York.

Azzopardi, B.J., Teixeira, J.C.F., and Jepson, D.M. (1989). Drop Sizes and Velocities in Vertical Annular Two-Phase Flow. *Proc. Int. Conf. on Mechanics of Two-phase Flow*. Taipei, Taiwan, pp 261-266.

Azzopardi, B.J., Teixeira, J.C.F. (1994) Gas Core Turbulence and Drop Velocities in Vertical Annular Two-Phase Flow. *Two Phase Flow and Heat Transfer, HTD*. Vol. 197 pp 37-46

Azzopardi, B.J., and Wren, E., (2004) What is entrainment in two-phase churn flow? *J. Multiphase Flow* Vol. 30 pp 89-103

Barbosa Jr, J.R., Govan, A.H. and Hewitt, G.F., (2001) Visualisation and modelling studies of churn flow in a vertical pipe. *Int. J. Multiphase Flow*, Vol 27. pp 2105-2127

Beggs, H.D., and Brill, J.P. (1973) A study of two-phase flow in inclined pipes. *Journal of Petroleum Technology*, Vol. 25. pp 607-617

Belt, R.J., (2007) *On the Liquid Film in Inclined Annular Flow*, PhD Thesis, TU Delft, The Netherlands.

Bertola, V, (2003) *Modelling and Experimentation in Two Phase Flow*, CISM Courses and Lectures No.450, International Centre for Mechanical Sciences, ISBN 3-211-20757-0, Springer-Verlag Wien New York.

Brown, D.J., Jensen, A. And Whalley, P.B. (1975) Non-equilibrium Effects in Heated and Unheated Annular Two-Phase Flow. ASME Paper 75-WA/HT/7

Cheng, H., Hills, J.H., and Azzopardi, B.J. (1998) A Study of the Bubble-to-Slug Transition in Vertical Gas-Liquid Flows in Columns of Different Diameter. *Int. J. Multiphase Flow*, Vol. 24. pp 431-452

Chisholm, D., (1972). Pressure gradients due to friction during the flow of evaporating two-phase mixtures in smooth tubes and channels. *Int. J. of Heat and Mass Transfer*. Vol. 16. pp 347-358

Crowe, C.T., Schwarzkopf, J.D., Sommerfelt, M, and Tsuji, Y. (2012) *Multiphase Flows with Droplets and Particles* 2nd Edition. CRC Press ISBN 978-1-4398-4050-4

Coney, M.W.E., (1973). The theory and application of conductance probes for the measurement of liquid film thickness in two-phase flow. *J. Phys. E: Scient. Instrum*; 6:903-10

Conte, G. (2000). Private communication

Conte, G. and Azzopardi, B.J., (2003) Film Thickness Variation about a T-junction. *Int. J. Multiphase Flow*, Vol. 29. pp 305-328

Costigan, G and Whalley, P.B., (1997) Slug Flow Regime Identification from Dynamic Void Fraction Measurements in Vertical Air-Water Flows. *Int. J. Multiphase Flow*, Vol. 23. pp 263-282

Cousins, L.B., Denton, W.H., and Hewitt, G.F., (1965) Liquid Mass Transfer in Annular Two-Phase Flow. *Proc. Symp. Two-phase Flow*, Vol 2, paper C4, Exeter, UK.

Cousins, L.B and Hewitt, G.F., (1968) Liquid Phase Mass Transfer in Annular Two-Phase Flow: Droplet Deposition and Liquid Entrainment. UKAEA Report AERE-R5657

Dantec PDA System detailed user manual

Dukler, A.E. and Smith, L. (1979) Two-Phase Interaction in Countercurrent Flow: Studies of the Flooding mechanism. Annual Report, Nov. 1985-Oct. 1987, NUREG/CR-0917, U.S. Nuclear Regulatory Commission, Washington, DC.

Durst, F., Tropea, C., and Xu, T.H., (1994) The Slit Effect in Phase Doppler Anemometry, Second Int. Conf. on Fluid Dynamics Measurement and its Applications, Beijing.

Fossa, M., (1998) Design and performance of a conductance probe for measuring the liquid fraction in two-phase gas-liquid flows. *Flow Meas. and Instr.* 9, pp 103-109.

Fore, L.B. and Dukler, A.E. (1995) The distribution of drop size and velocity in gas-liquid annular flow. *Int. J. Multiphase Flow*, Vol. 21. pp 27-44, pp. 137–149.

Fore, L.B. and Dukler, A.E. (1995), Droplet deposition and momentum transfer in annular flow. *AIChE J.*, 41 (1995), pp. 2040–2046

Govan, A.H., Hewitt, G.G., Richter, H.J., and Scott, A. (1990) Flooding and Churn Flow in Vertical Pipes. *Int. J. Multiphase Flow*, Vol. 17. pp 27-44

Guglielmini, G., (2002) Caratterizzazione sperimentale del moto bifase intermittente in presenza di singolarita mediante sonde ad impedenza, Laurea Thesis, Universita degli studi di Genova, Italia.

Hawkes, N.J., and Hewitt, G.F., Experimental studies of wispy-annular flow, Int. Conf. on Two Phase Flow Modelling and Experimentaion, Rome, 1995

Hewitt G.F., Lacey P.M.C., and Nicholls B. (1965) Transition in film flow in a vertical tube symposium on two phase flow, Exeter, 2 pp. B401-B429.

Hewitt, G.F., Jayanti, S., and Hope, C.B., (1990) Structure of Thin Films in Gas-Liquid Horizontal Flow. *Int. J. Multiphase Flow*, Vol. 16. pp 951-957

Hewitt G.F., and Roberts, (1969) Studies of Two Phase Patterns by Simultaneous X-Ray and Flash Photography, UKAEA Report, AERE M2159.

Holt, A.J., Azzopardi, B.J., and Biddulph, M.W., (1999) Calculation of Two-Phase Pressure Drop for Vertical Upflow in Narrow Passages by Means of a Flow Pattern Specific Model. *Transactions of the Institution of Chemical Engineers* 77A:7-15

Hutchinson, P., Hewitt, G.F., and Dukler, A.E., (1970) Deposition of Liquid or Solid Dispersions from Turbulent Gas Steams: a Stochastic Model. *Chem. Eng. Sci.* Vol. 26. pp 419-439.

Jacowitz, L.A., Brodkey R.S., (1964) An analysis of geometry and pressure drop for the horizontal, annular, two-phase flow of water and air in the entrance region of a pipe. *Chem. Eng. Sci.* Vol. 19. pp 261–274.

James, P.W., Hewitt, G.F., and Whalley, P.B., (1980) Droplet Motion in Two-Phase Flow. UKAEA Report AERE-R9711

James, P.W., Hutchinson, P., (1978) Droplet Deposition in an Annular Geometry. UKAEA Report AERE-R9008

Jayanti, S., and Hewitt, G.F., (1992) Predication of the Slug-to-Churn Flow Transition in Vertical Two-Phase Flow. *Int. J. Multiphase Flow*, Vol. 18. pp 847-860

Jepson, D.M., Azzopardi, B.J. and Whalley, P.B., (1989) The effect of gas properties on drops in annular flow. *Int. J. Multiphase Flow*, **15**), pp. 327–339.

de Jong, P., and Gabriel, K.S., (2003) A preliminary Study of Two-Phase Annular Flow at Microgravity: Experimental Data of Film Thickness. *Int. J. Multiphase Flow*, Vol. 29. pp 1203-1220.

Kang, H. C. and Kim, M. H. (1992) The Development of a Flush-Wire Probe and Calibration Method for Measuring Liquid Film Thickness. *Int. J. Multiphase Flow*, Vol. 18. pp 423-437.

Koskie, J.E., Mudawar, I. and Tiederman, W.G. (1989) Parallel Wire Probes for Measurements of Thick Liquid Films. *Int J. Multiphase Flow*. Vol 15. pp 521–530.

Martin, C.J., and Azzopardi, B.J., (1985) Waves in Vertical Annular Flow. *Physicochem. Hydrodyn.* Vol. 6. pp 257-265.

Miya, M., Woodmansee, D. E. and Hanratty, T. J. A (1971) Model for Roll Waves in Gas-Liquid Flows. *Chem. Eng. Sci.* Vol. 26. pp 1915-1931.

Ohnuki, A., Akimoto, H., (2000), “Experimental study on transition of flow pattern and phase distribution in upward air-water two-phase flow along a large vertical pipe”, *Int J. Multiphase Flow*. Vol 26. pp 267–286.

Omebere-Iyari NK., (2006) The Effect of Pipe Diameter and Pressure in Vertical Two-Phase Flow, PhD Thesis, University of Nottingham, UK

Prasser, H.M., Bottger, A., and Zschau, J., (1998) A New Electrode-Mesh Tomograph for Gas-Liquid Flows. *Flow Meas. And Instr.* Vol. 9. pp 111-119

Prasser, H.M., Beyer, M., Bottger, A., Carl, H., Lucas, D., Schaffrath, A., Schuttz, P., Weiß, F.P. and Zschau, J., (2003) Influence of the Pipe Diameter on the Structure of the Gas-Liquid Interface in a Vertical Two-Phase Pipe Flow. 10th Int. Mtg. Nuclear Reactor Thermal Hydraulics, Seoul, Korea.

Premoli, A., Francesco, D., and Prina, A. (1970). An Empirical Correlation for Evaluating Two-Phase Mixture Density Under Adiabatic Conditions. *Eur. Two-Phase Flow Group Mtg. Milan.* [cited in Bertola, 2003]

Rodriguez, D.J., and Shedd, T.A., (2004) Entrainment of Gas in the Liquid Film of Horizontal, Annular, Two-Phase Flow. *Int J. Multiphase Flow.* Vol 30. pp 565–583

Pushkina and Sorokin (1969) [Cited in Azzopardi and Hills (2001)]

Saffman, M., (1987) Automatic Calibration of LDA Measurement Volume Size. *Applied Opt.* 26: 2592-2597

Sawai, T., Kaji, M., Kasugai, T., Nakashima, H., Mori, T. (2004) Gas-liquid interface structure and pressure drop characteristics of churn flow. *Exp T and Fl. Sc.* Volume 28, 6, pp 597-606

Schadel, S.A., Leman, G.W., Binder, J.L., and Hanratty, T.J., (1988) Rates of Atomization and Deposition in Vertical Annular Flow. *Int J. Multiphase Flow.* Vol 16. pp 363–374

Sekoguchi, K, and Mori, K., New development of experimental study on interfacial structure in gas-liquid two-phase flow, *ExHFT*, pp. 1177- 1188, Brussels, 1997

Sekoguchi, K, and Takeishi, M., Interfacial structures in upward huge wave flow and annular flow regimes, *Int. J, Multiphase Flow*, 15. pp 295-305, 1989.

Sharaf (2011) Private communication

Shoham, O., (2006) Mechanistic Modeling of Gas-Liquid Two-Phase Flow in Pipes, ISBN 978-1-55563-107-9, Society of Petroleum Engineers, USA.

Smith, S.L., (1971) Void Fraction in Two-Phase Flow – A Correlation Based Upon Equal Velocity Head Model. Heat and Fluid Flow. Vol 1 pp 22-39 [Cited in Azzopardi and Hills (2001)]

Szalinski, L., Abdulkareem, L.A., Da Silva, M.J., Thiele, S., Beyer, M., Lucas, D., Hernandez Perez, V., Hampel, A., Azopardi, B.J., (2010) Comparative study of gas-oil and gas-water flow in a vertical pipe, Chem. Eng. Sc. 65 pp 3836-3848

Taitel, Y., Barnea, D., and Dukler, A. E., (1980). Modelling Flow Pattern Transitions for Steady Upward Gas-Liquid Flow in Vertical Tubes, AIChE J., Vol. 26. pp. 345-354

Teixeira, J.C.F, (1988) Turbulence in Annular Two-Phase Flow, PhD Thesis, University of Birmingham, UK.

Tkaczyk (2011) Private communication

Tsochatzidis, N.A., Karapantsios, T.D., Kostoglou, M.V., and Karabelas, A.J. (1992) A conductance probe for measuring liquid fraction in pipes and packed beds. Int. J. Multiphase Flow. Vol. 18. pp 653-667.

Turner, R. G., Hubbard, M. G., and Dukler, A. E. , (1969), Analysis and Prediction of minimum flow rate for the continuous removal of liquid from gas wells. J. Pet. Tech.. Vol. 21.

van 't Westende, J.C.M (2008) Droplets in annular-dispersed gas-liquid pipe-flows, PhD Thesis, TU-Delft, The Netherlands.

van 't Westende, J.C.M., Belt, R.J., Portela, L.M., Mudde, R.F., Oliemans, R.V.A., (2005) Droplet Characterisation in upward annular dispersed pipe flow. 11th Workshop on Two-Phase Flow Predictions, Merseburg, Germany. (through private communication)

Wallis, G.B., (1969) One-dimensional Two-Phase Flow, McGraw – Hill.

Whalley, P.B., Hewitt, G.F., and Terry, J.W., (1979) Photographic Studies of Two-Phase Flow using Parallel Light Technique. UKAEA Report AERE-R9389

Wilkes, N.S., Azzopardi, B.J. and Willets, I. (1982) Drop Motion and Deposition in Annular Two-Phase Flow UKAEA Report AERE-R10571

Zabaras, G., Dukler, A.E., Moalem-Maron, D., Vertical upward cocurrent gas-liquid annular Flow, (1986) AIChE Journal vol.32 No.5 pp 829-843

Zangana (2011) Private communication

Ziadi, S.H., Altunbas, A., and Azzopardi, B.J., (1998) A Comparative Study of Phase Doppler and Laser Diffraction Techniques to Investigate Drop Sizes in Annular Two-Phase Flow. Int. J. Multiphase Flow. Vol. 71. pp 135-143.

Publications and Conference Papers

Van der Meulen., G.P., Zangana, M., Zhao, D. and Azzopardi, B.J., Phase Distribution Measurements by Conductance Probes and Pressure Drop in Gas-Liquid Flows, (2008). Paper presented at The 7th World Conference on Heat Transfer, Fluid Mechanics and Thermodynamics, 28 June- 3 July 2009, Krakow, Poland

Van der Meulen, G.P., Zangana, M., Zhao, D. and Azzopardi, (2010), B.J., Film Measurements in Two-Phase Gas-Liquid Flow by Conductance Techniques in Vertical Large Diameter Pipes. Presented at the International Conference on Multiphase Flow 2010 (ICMF-2010), May 30 - June 4 2010, Tampa, Florida.

Zangana, M., Van der Meulen, G.P and Azzopardi, B.J., The Effect of Gas and Liquid Velocities on Frictional Pressure Drop in Two Phase Flow for Large Diameter Vertical Pipe. Presented at the International Conference on Multiphase Flow 2010 (ICMF-2010), May 30 - June 4 2010, Tampa, Florida.

Mhunir B. Alamu, Barry J. Azzopardi, Gerrit P. van der Meulen and Valente Hernandez-Perez. Investigation of Liquid Loading in Gas Well: Simultaneous Measurements of Drop-size, Film Thickness and Pressure Drop. 29th International Conference on Ocean, Offshore and Arctic Engineering, Volume 4.

Mhunir B. Alamu, Gerrit P. van der Meulen and Barry J. Azzopardi,
Dynamic Drop-Size Measurements in Annular Two-Phase Flow. Presented
at the International Conference on Multiphase Flow 2010 (ICMF-2010),
May 30 - June 4 2010, Tampa, Florida.

Appendix B

Table B1 The PDA experimental matrix [superficial velocities (m/s)]

Liquid								
Gas	0.0045	0.0082	0.01	0.014	0.02	0.025	0.03	0.04
20	X	X	X	X	X	X	X	X
19	X	X	X	X	X	X	X	X
18	X	X	X	X	X	X	X	X
17.5	X	X	X	X	X	X	X	X
16.5	X	X	X	X	X	X	X	X
16	X	X	X	X	X	X	X	X
15	X	X	X	X	X	X	X	X
14	X	X	X	X	X	X	X	
13	X	X	X	X	X	X	X	
12	X	X	X	X	X	X		
10	X	X	X	X				

Appendix C

Extrapolation of drop size distributions

As can be seen from the drop diameter probability distributions, the values do not approach 0 at maximum drop size measured. This is probably due to that there are drops present of sizes larger than the PDA can measure. These missing drops might introduce error in the calculation of mean drop sizes. To examine the effect in more detail, an extrapolation was imposed. A linear fit was applied to the distribution in order to estimate the drop size. This is illustrated in Figure C1 for a gas and liquid superficial velocity of 20.2 and 0.0045 m/s respectively.

As can be observed this provides an estimate of the maximum drop size obtained for a given distribution.

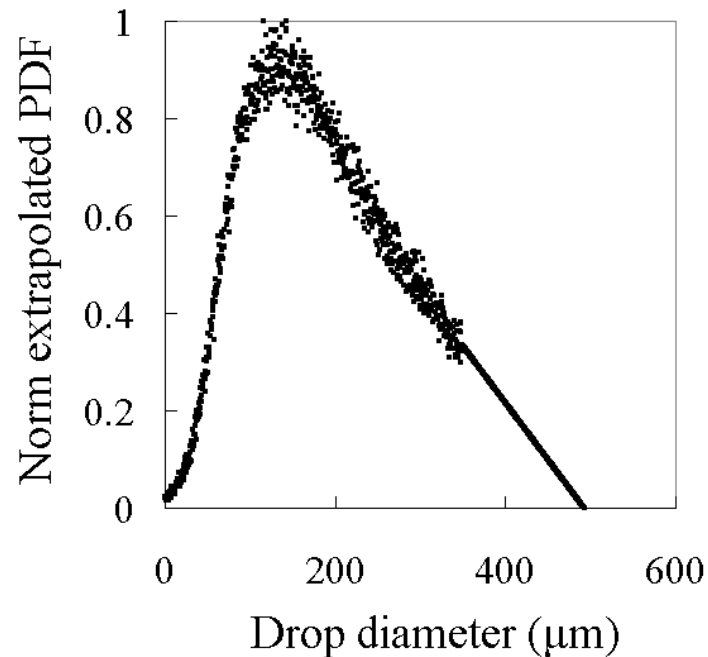


Figure C1 Extrapolated drop size distribution. Gas and liquid superficial velocity of 20.2 and 0.0045 m/s

This linear extrapolation then allows calculation of a corrected Sauter mean diameter. The old and new Sauter mean diameters are compared in Figure C2. There are only small under predictions. A non linear extrapolation (inverse relationship) would perhaps be more correct.

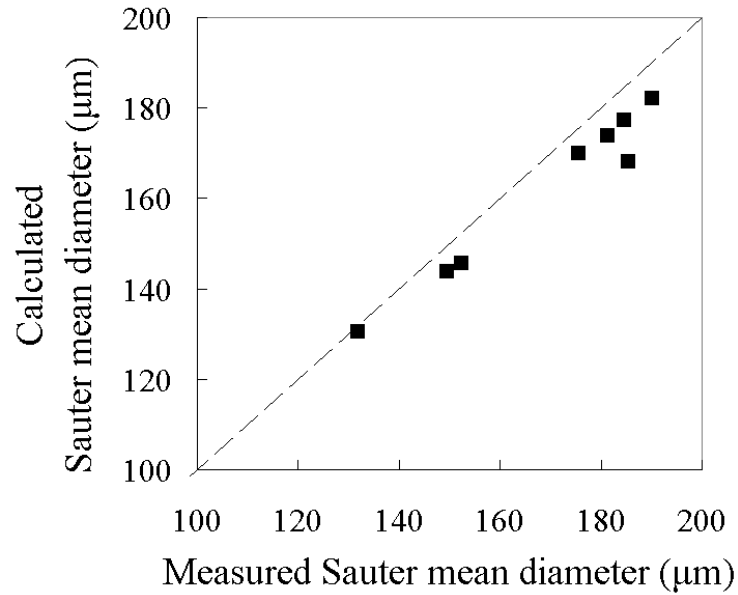


Figure C2 The effect of linear drop distribution extrapolation of selected experiments.

In order to examine the difference between linear and inverse relationship extrapolation, a Weibull distribution was applied to the data. The Rosin Rammler equation, much used to describe size distributions of particles, is a simplified form of the Weibull distribution. Two conditions were selected to be illustrated at a liquid superficial velocity 0.0045 and gas superficial velocities of 13 and 19 m/s.

The goodness of fit of a Weibull distribution depends on its scaling λ (the flatness and width of the distribution) and shape k (the slope) parameters. The sensitivity of the Sauter mean diameter on the Weibull distribution, for the optima extrapolation length and starting points, was first examined. Figure C3 illustrates a typical effect of extrapolation length on the Sauter mean diameter obtained for different starting points of the extrapolation. The vector length for every diameter distribution was iterated until no effect on the Sauter mean diameter was observed. For the majority of data, the most suitable point for vector length was found to be at 550 vector points.

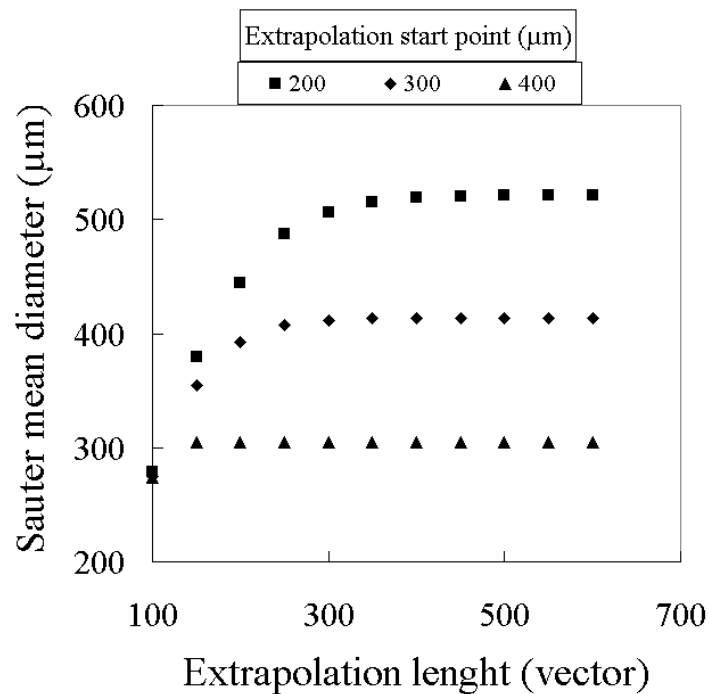


Figure C3 Effect of extrapolation length and start point on the Sauter mean diameter. Liquid superficial velocity 0.0045 and gas superficial velocity 19 m/s

Similar iterations were performed to find the optimum starting point. For the same condition as those in Figure C3, Figure C4 illustrates that the data converges to a constant of the Sauter mean diameter between approximately 280

and 320 μm . This range was found to be similar for the majority of the data and used for iteration.

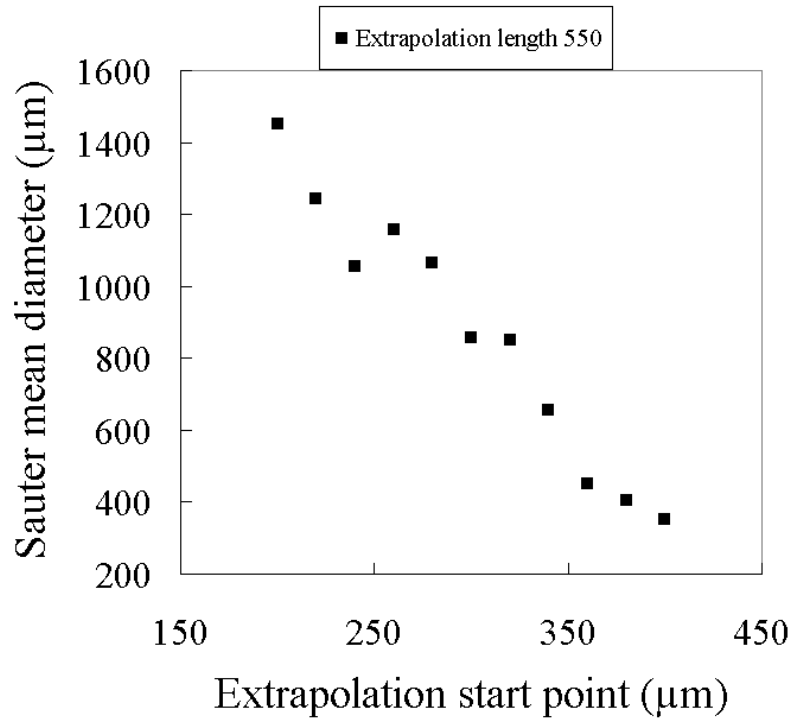


Figure C4 Local minimum to determine extrapolation start point.
Liquid superficial velocity 0.0045 and gas superficial velocity 19 m/s

Figure C5 illustrates the mean drop size distributions and extrapolation results obtained for the flow conditions described above. The results perhaps show a more physically correct behaviour than those by linear extrapolation. In addition it is interesting to see that the extrapolated values show that it is plausible to obtain drops of very large sizes. It should be noted that these events are sporadic considered the occurrence probability. It is perhaps not unreasonable to assume that very large drops can be expected near the gas-liquid interface since the rate of atomisation is smaller. This could link the results reported in the preliminary photography experiments discussed in earlier parts of Chapter 5.

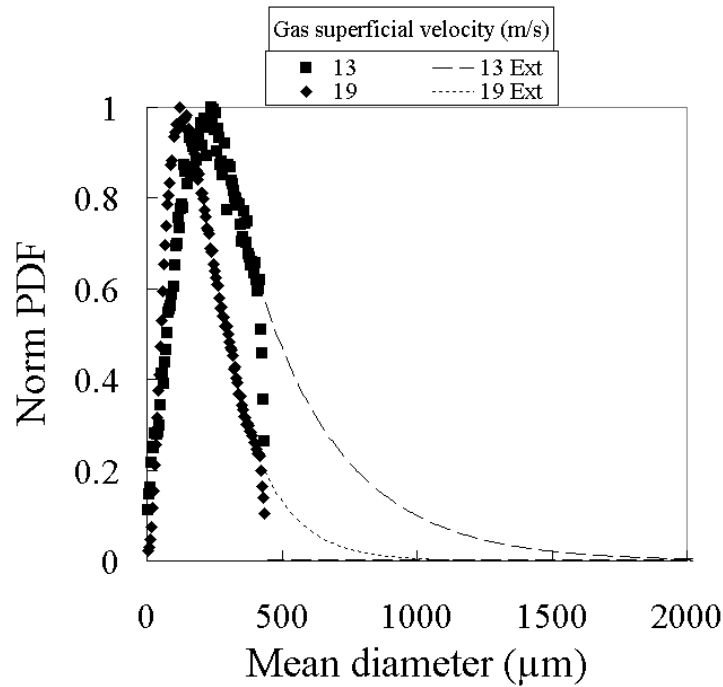


Figure 5.C5 Optimised extrapolation of normalised arithmetic drop size distributions.

A comparison between previous and present data (including Weibull extrapolation) is shown in Figure C6 and a good trend can be observed.

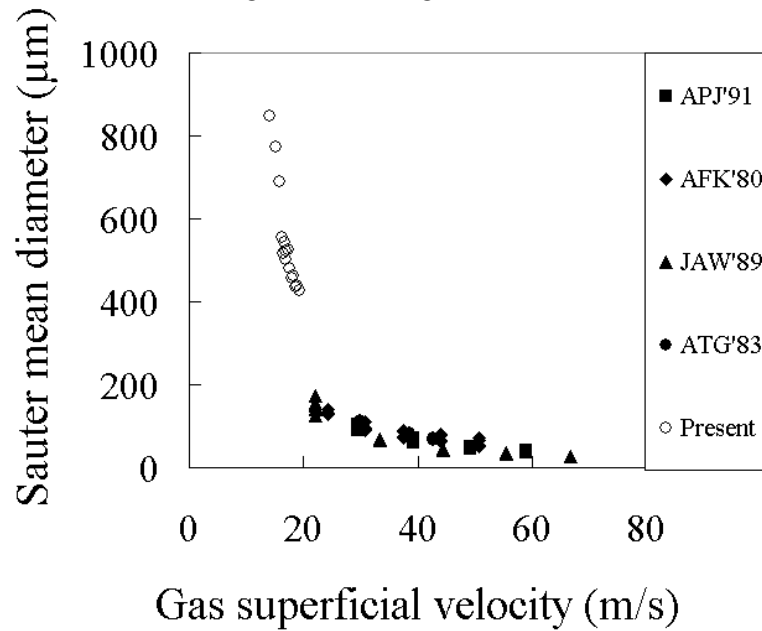


Figure C6 Comparison between previous and present data. Azzopardi *et al.* (1980), Azzopardi *et al.* (1983), Jepson *et al.* (1989), Azzopardi *et al.* (1991).

For the linear extrapolation, the Rosin Rammler parameters were quantified similar to those by e.g., Azzopardi *et al.* (1978). The Rosin Rammler fitting parameters, N and \bar{x} for the present data are illustrated in Table C1 along with values obtained by Azzopardi *et al.* (1978).

Table C1 Experimental conditions and Rosin Rammler parameters

		Present		
Liquid superficial velocity (m/s)	Gas superficial velocity (m/s)	\bar{x} (μm)	N (-)	Sauter mean diameter
0.0045	11.72	396.4	4.4	168.1
	20.19	349.4	4.5	145.6
0.0082	10.83	358.6	4.6	173.8
	20	362.4	4.6	182.2
0.0202	11.52	331.3	4.7	130.5
	19.61	345.4	4.6	143.8
0.04	14.5	353.2	4.7	169.8
	18.8	357.9	4.6	177.4
		Azzopardi <i>et al.</i> (1978)		
0.016	36	255	2.3	162
		253	2.5	170
0.031	36	238	2.2	146
		247	2.4	161
0.047	36	241	2.3	153
0.063		241	2.1	142
		238	2.2	146
0.079	36	235	2.4	154